

University of Leicester
Department of Engineering



EFFECTS OF LONG-TERM HIGH
TEMPERATURE EXPOSURE ON THE
MICROSTRUCTURE OF HAYNES ALLOY 230

*A THESES SUBMITTED FOR THE DEGREE OF DOCTOR OF PHILOSOPHY
IN THE UNIVERSITY OF LEICESTER*

BY

JANA VEVERKOVÁ

MARCH 2010

ABSTRACT

Haynes Alloy 230 is a nickel-based sheet material used for combustor components in a number of small industrial gas turbines manufactured by Siemens. During normal operating service the material is subjected to high temperatures and cyclic mechanical and thermal stresses, which can lead to degradation of the microstructure and mechanical properties of the alloy, and hence limit component design life.

This PhD thesis describes studies of the effects of long-term high temperature exposure on hardness and microstructural changes in creep rupture tested and thermally exposed samples of HA230. Advanced FEGSEM was used for documentation of the microstructural evolution in the temperature range of 500-1170°C following exposure up to 30000 hours. For identification of alloy phases, which could potentially act as indicators of the average exposure temperatures experienced for specific service periods, XRD and analytical TEM techniques were used. Primary carbides $M_{12}C$ and secondary carbides, $M_{12}C$ and $M_{23}C_6$, were identified. No TCP phases were observed within the microstructure of the tested samples, but the secondary $M_{23}C_6$ forms large 'pool-like' precipitates' above 990°C which are very hard and brittle and could be detrimental for the material (*e.g.* reductions in ductility, high temperature strength).

A hardness and microstructurally based model was used for the assessment of an ex-service HA230 transition duct and could be an aid for evaluation of the remnant life of HA230 combustor components.

The tests were carried out as part of the COST 538 technology programme between 2004 and 2009.

ACKNOWLEDGEMENT

First of all, I would like to express my sincere gratitude to my supervisors Professor Helen V. Atkinson and Professor Andrew Strang for their guidance and help with every aspect of the project and to Geoff R. Marchant from Siemens and Dr Gordon McColvin formerly from Siemens for the invaluable help, the meaningful support and the productive discussions.

Special appreciation would like to be given to Tony Forryan for all his efforts to make the things happen as well as for interesting conversations and for special approach to all issues.

It would have been impossible for me to conduct this research alone. For this reason I am indebted to everyone whom I have met during my PhD study for their collaboration, assistance, skills and knowledge. From University of Leicester:

Professor Sarah V. Hainsworth for her help and friendship.

All of the experimental and technical staff involved in this project, namely Graham Clark for his patient help in the laboratory, Barry Kirkland for the help with tensile testing, Paul Williams for the LabView programme, Alan Wale, Ian Bromley, Simon Millward.

Dr Sarah Lee and Cheryl Haidon for the help with XRD technique, Rob Wilson for the help with EPMA and Lin Marvin for ICP results, all from the Dep. of Geology.

Mick Lee from Department of Chemistry for exceptional assistance during the extraction of the phases.

Special thanks go to Dr Michael Phillips from the Department of Mathematics for his excellent help with statistical analysis of hardness results.

Guy Peters for showing me the beauty of the English language.

Many thanks to other PhD students.

I would like to acknowledge collaborators from UK:

Dr Simon Hogg from University of Loughborough for facilitating my progress in XRD.

Dr Crispin Hetherington for his patience over my electron diffraction patterns, Dr Lisa Karlsson and Dr Teck Lim from Oxford Materials.

Anthony Scarratt and his colleagues from Struers for optimising the metallographic preparation of HA230.

I would like also to acknowledge collaborators from abroad:

It is my pleasure to acknowledge Professor Vlastimil Vodárek (University of Ostarva, CR) for his availability to give me precious advice and suggestions.

Dr Giuliano Angella and Mr Maurizio Maldini from CNR IENI Milan (IT) for inviting me to their laboratory, for giving me constructive suggestions and for their kind help. As well as E. Signorelli and the MSc students.

Dr Milan Svoboda, Dr Aleš Kroupa and Miroslav Daniel from Institute of Physics of Materials (Academy of Sciences of the Czech Republic) gave me the opportunity to learn how to analyse the materials in the TEM.

Dr David Koloušek from Institute of Chemical Technology in Prague for the training in 'how to read a diffractogram' and the peak assignment.

Dr D. Klarstrom and Dr Vinay Deodeshmukh from Haynes Intl. for very useful advice.

For the financial support for this project:

EPSRC. The EPSRC is also thanked for funding the access to the TEM instruments in Oxford Materials under the Materials Equipment Access scheme, grant reference: EP/F01919X/1

Siemens

COST organization for supporting my STSM stay in Italy and offering me the opportunity to get involved in the Action 538.

My final thanks go to my husband Vaclav, who motivated me during this period, was giving me support, encouraging me and mostly was there when I needed him.

CONTENTS

1	INTRODUCTION	8
1.1	The Structure of the Thesis.....	9
2	LITERATURE REVIEW	11
2.1	Superalloys.....	11
2.1.1	Nickel-based Superalloys.....	11
2.1.2	Strengthening of Superalloys	18
2.2	Haynes™ 230™ Alloy.....	19
2.2.1	Introduction	19
2.2.2	The development of Haynes 230 Alloy.....	19
2.2.3	Fabricability.....	20
2.2.4	Mechanical Strength	21
2.2.5	Thermal Stability.....	23
2.2.6	Oxidation and Nitridation Resistance.....	24
2.2.7	Microstructural Features.....	29
2.2.8	Identification of the Phases.....	30
2.2.9	Grain Boundary Engineering	33
3	METHODOLOGY	35
3.1	Experimental Techniques and Instrumentation	35
3.1.1	Vickers Hardness.....	35
3.1.2	Nanoindentation.....	36
3.1.3	Optical Microscopy.....	38
3.1.4	Scanning Electron Microscopy (SEM).....	38
3.1.5	Energy Dispersive X-ray analysis (EDX)	41
3.1.6	Transmission Electron Microscopy (TEM)	42
3.1.7	Bragg's Law.....	43
3.1.8	X-rays.....	44
3.1.9	X-ray Diffraction (XRD)	45
3.1.10	Focused Ion Beam (FIB).....	46
3.1.11	Electron Probe MicroAnalysis (EPMA)	48
3.1.12	Inductively Coupled Plasma - Optical Emission Spectrometry (ICP-OES)	49
3.1.13	Tensile Testing.....	49
3.2	Material Characterization	51
3.3	Experimental Procedure	51
3.3.1	Specimens.....	51
3.3.2	Metallographic Preparation	53
3.3.3	Preparation of TEM Specimens	55
3.4	XRD.....	57

3.4.1	Bulk Material	57
3.4.2	Phase Extraction	58
3.5	Tensile Tests.....	58
4	EXPERIMENTAL RESULTS	60
4.1	Vickers Hardness Tests	60
4.1.1	Hardness Results.....	60
4.1.2	Master Curve	62
4.1.3	Microhardness Studies	67
4.2	Nanohardness Studies.....	71
4.2.1	As-received Material	72
4.2.2	Thermally Exposed HA230	74
4.2.3	Creep Tested HA230	77
4.3	Statistical Analysis of Hardness Results	83
4.4	Metallographic Studies	86
4.4.1	Optical Microscopy.....	86
4.4.2	FEGSEM Studies - Imaging	96
4.4.3	Energy Dispersive X-Ray Analysis.....	104
4.5	Transmission Electron Microscopy.....	112
4.6	X-Ray Diffraction	118
4.7	Electron Probe Micro Analysis (EPMA).....	125
4.8	Inductively Coupled Plasma - Optical Emission Spectrometry (ICP-OES).....	130
4.9	Oxidation Characteristics	134
4.10	Tensile Testing	141
5	TRANSITION DUCT – CASE STUDY.....	148
5.1	Introduction.....	148
5.1.1	Background	148
5.1.2	Methodology	149
5.2	Results and Discussion	150
5.2.1	Hardness Studies	150
5.2.2	Microstructural Studies	153
5.2.3	Oxidation Characteristics.....	161
5.3	Conclusions	163
6	DISCUSSION	165
7	CONCLUSIONS	169
8	FUTURE WORK.....	171
9	APPENDICES	172
9.1	Larson – Miller Parameter.....	172
9.1.1	Estimation of Average Operating Temperatures of Service Exposed HA230 Components using Master Hardness v Larson-Miller Relationships....	173
9.1.2	Calculation of Average Service Temperatures.....	174

9.2	Sample Review	174
9.3	Estimation of the temperatures along creep specimen.....	178
9.4	Microhardness Studies	179
9.5	Nanohardness Studies.....	179
9.6	Statistical Analysis.....	180
9.7	TEM	183
9.8	XRD	185
9.8.1	Phase Extraction	185
9.8.2	Calibration of the Diffractometer	186
10	LIST OF PUBLICATIONS	187
11	REFERENCES	188

1 INTRODUCTION

Siemens is one of the world's largest companies specialising in electrical engineering and electronics for a range of industries and applications. Siemens Industrial Turbomachinery Ltd (*SITL*) in Lincoln, designs, manufactures, installs and provides life-time support for world-class gas turbines for Industrial Power Generation and the Oil and Gas Industry.

SIT Ltd in Lincoln produces small gas turbines with an electrical output ranging from 4.35MW to 12.9MW. The material of some components in the turbine is exposed to high temperatures and high stresses. Nickel-based alloys are used primarily for these components, because the high temperature properties of steels are not adequate.

This project focuses on the analysis of Haynes 230 (HA230), a nickel-based superalloy which is used for combustion chambers and transition duct components, where the exposure temperatures can be over 900°C. Creep rupture tests and thermal exposures have been carried out by Siemens in the temperature range from 500°C to 1170°C and for durations up to 50000 hours. The specimens have been examined in this PhD work by various techniques such as optical microscopy, scanning electron microscopy, transmission electron microscopy and X-ray analyses to obtain a general knowledge of changes in the microstructure and also in mechanical properties, in particular the effect of thermal exposure and creep strain. In order to gain a deeper understanding of the behaviour of Haynes alloy 230 in extreme conditions, analyses of the phases and of the mechanisms of their transformation have been performed. In addition, the investigation involved a hardness survey of all tested specimens with an intention to create a Master Curve of Hardness vs. Larson-Miller Parameter (LMP) as the first step in evaluation of service exposed components. In general, the examination is focused on the detection of any possible difference between as-received and tested material, such as carbide size and distribution, growth of secondary carbides, deformation, new phases and composition of both matrix and carbides.

A part of the work was focused on the description of the changes which could be used as 'markers' for the evaluation of the components in service, *e.g.* a transition duct. The use of non-destructive analytical techniques, such as hardness testing, is for the producers more favourable than destructive techniques because former allow the monitoring of the quality and stability during operation.

As is often the case in research, the direction of the project has changed considerably since its beginnings. The project started as part of COST Action 538 in 2004 and as the PhD work initiated in 2006 widened. New techniques were introduced and additional results were obtained.

1.1 THE STRUCTURE OF THE THESIS

The background information and a literature review are introduced in Chapter 2. The first section is concerned with the fundamentals of superalloys, a general description of the composition and phases present in the microstructure and the mechanisms of strengthening. The literature survey on HA230 was mainly focused on the ageing process and on the creep ruptures tests which are the main part of this project. An important part discusses the identification of the precipitating phases as a product of aging.

The techniques and the equipment used in this work are outlined in the Chapter 3. The hardness testing is presented in Section 3.1.1, which introduces the time-temperature parameter, LMP, as a suitable representation of the hardness data. Additionally, nanoindentation was used to determine the hardness of individual microstructural features. The metallographic studies were obtained by optical microscopy (see Section 3.1.3), and FEGSEM (Field Emission Gun Scanning Electron Microscopy) (see Section 3.1.4) imaging. FEGSEM, with its large depth of field and higher resolution, is primarily used to study the surface, or near surface. A brief description of the TEM (Transmission Electron Microscopy) technique is offered in Section 3.1.6. This method provides information about the internal structure of thin specimens. The following sections are addressed to X-ray techniques. Using backscattered electron imaging, XRD (X-ray Diffraction) (Section 3.1.9) and EDX (Energy Dispersive X-ray) (Section 3.1.5) mapping, a qualitative assessment can be readily made regarding the distribution of specific phases within the microstructure, while EDX point and line scan analysis techniques enable the compositions of both the matrix and individual phases to be determined quantitatively. The Focused Ion Beam (FIB) technique is described as it was used in the preparation of TEM specimens. Moreover EPMA (Electron Probe Micro Analysis) and ICP-OES (Inductively Coupled Plasma – Optical Emission Spectrometry) techniques are briefly presented. The final section explains the basics of tensile testing.

Chapter 3 also provides details about the material and the specimens studied, as well as the preparation procedures for each technique. Section 3.3.2

describes the preparation techniques of standard metallographic surfaces of all specimens and Section 3.3.3 is focused on the preparation of TEM specimens. The following section is addressed to the preparation steps of the XRD specimens. The last section explains the miniature tensile testing carried out on HA230.

All experimental results are reported in Chapter 4. The first section summarises the hardness, microhardness, and nanohardness results. Some statistical analysis of hardness data was performed and the conclusions are given in Section 4.3. Section 4.4 presents metallographic studies including optical and scanning electron microscopy and the summary of EDX results. The following sections contain TEM results and the results from XRD analyses. The results from EPMA offer a comparison with the EDX results in Section 4.7. Section 4.8 reviews changes in the matrix composition using ICP-OES. The oxidation characteristics have been investigated by an MSc. student, J. Doucet, under the guidance of the author of this thesis [1] (Section 4.9). The data from tensile testing are summarised in Section 4.10.

Chapter 5 presents the Case Study findings obtained for an ex-service transition duct. This study has been part of COST Action 538 and the data were compared to those of the studies undertaken on laboratory exposed material [2].

Results are thoroughly discussed in Chapter 6 followed by conclusions and the objectives of future work in Chapter 7 and 8. Additionally, Appendices in Section 9, contain detailed hardness and microhardness data, calculations of the statistical analysis and a comprehensive description of the chemical extraction procedure.

Results have been presented at the Parsons 2007 Conference held in Glasgow (UK) [3], at the Superalloy 2008 Conference held in Seven Springs, PA (USA) [4], at the Grain Boundary at High Temperature Conference in Derby (UK) in April 2009 [2] and will be presented at Liège conference on Materials for Advanced Power Engineering in September 2010 [5].

2 LITERATURE REVIEW

The literature review gives a brief general introduction to superalloys, followed by the detailed overview of Haynes Alloy 230.

2.1 SUPERALLOYS

“A superalloy is an alloy developed for elevated-temperature service, usually based on group VIII B elements, where relatively severe mechanical stressing is encountered, and where high surface stability is frequently required.” [6]

The term “superalloy” appeared shortly after World War II describing a group of high performance alloys developed for use in turbosuperchargers and aircraft turbine engines [7]. These metallic alloys are capable of maintaining certain of their room-temperature physical and mechanical properties even after long exposure times at elevated temperatures above about 650°C. In service they can be used at temperatures in excess of 0.7 of the absolute melting temperature. Nowadays superalloys are used in a variety of industries demanding high strength, creep and corrosion resistance. The three major classes of superalloys are nickel-based, iron-nickel-based, and cobalt-based alloys [8-11].

This chapter covers an introduction to nickel-based superalloys. It is concerned with the composition and the phases promoted by the presence of the alloying elements. The last section discusses the strengthening of superalloys.

2.1.1 NICKEL-BASED SUPERALLOYS

Nickel is an ideal matrix element because of its high melting point - 1453 °C, adequate corrosion resistance, and ability to dissolve other elements. The crystal structure of the matrix phase is face-centred cubic (fcc, see Figure 2.1) at all temperatures [12]. The density is 8907 kg/m³ in ambient conditions.

Nickel-based superalloys have been reviewed in reference [9]. They can be used to a higher fraction of their melting points than iron-nickel-based or cobalt-based alloys. Nickel-based alloys are strengthened by solid solution hardening or precipitation hardening (e.g. by intermetallic compound precipitation in an austenitic fcc matrix). In general, the creep rupture strengths of the nickel-base solid solution strengthened alloys are considerably lower than those of the nickel-base precipitation strengthened alloys. Nickel-based superalloys are used in both cast and wrought forms. The wrought form is usually considered more ductile.

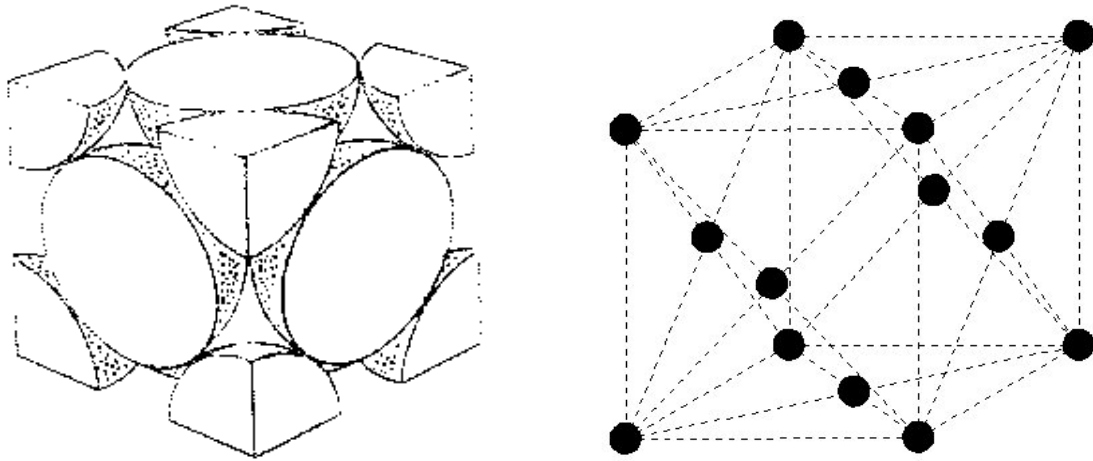


Figure 2.1 The unit cell of the face-centred cubic (fcc) crystal structure.

Among the most demanding applications for a high-temperature material are those in the hot sections of gas turbine engines. Although superalloys have excellent oxidation resistance for such applications as turbine blades and vanes, they must be coated to improve environmental resistance [6].

2.1.1.1 COMPOSITION

The composition of many nickel-based alloys includes more than ten alloying elements. Therefore, superalloys are considered amongst the most complex engineered materials. Most of the nickel alloys contain 10-20 wt% of chromium, up to about 8 wt% of aluminium and titanium, 5-10 wt% of cobalt, and small amounts of boron, zirconium, and carbon are often included. Other common additions are molybdenum, tungsten, tantalum, hafnium, and niobium. Based on the behaviour and the influence on the phase stability, alloying elements can be categorized into three groups [8, 13]:

1. γ formers - prefer to partition to the austenitic γ matrix and stabilise it, their atomic radii are not very different from nickel – cobalt, iron, chromium, ruthenium, molybdenum, tungsten and rhenium (Group V, VI, and VII elements);
2. γ' formers – prefer to partition to the γ' precipitate Ni_3X ; elements include aluminium, titanium, niobium and tantalum (Group III, IV, and V elements), most of which have atomic radii greater than that of nickel.

3. Elements that segregate to the grain boundaries of the γ phase; their atomic sizes are very different from nickel – boron, carbon and zirconium;
4. Carbide formers – chromium, molybdenum, tungsten, niobium, tantalum, and titanium.

Effects of the major alloying elements are listed in Table 2.1.

Table 2.1 Effects of the major alloying elements in nickel-base superalloys [9, 14].

Element	matrix strengtheners	increase in γ' volume fraction	grain boundaries	other effects
Cr	moderate	moderate	$M_{23}C_6$, M_7C_3	improves corrosion and oxidation resistance, promotes TCP (Topologically Close-Packed) phases
W	high	moderate		improves density
Mo	high	moderate	M_6C , MC	promotes TCP phases μ (Mo, W), σ
Co	slight	moderate in some alloys		raises solidus; may raise or lower solvus
Fe				decreases oxidation resistance; promotes TCP phases σ , Laves
Al	moderate	very large		improves oxidation resistance
Ti	moderate	very large	TiC	hardening precipitates, increases hot corrosion resistance
Ta	high	large	MC	improves creep properties
Nb	high	large	NbC	promotes γ' and δ phases
Re	moderate			retards coarsening; increases misfit
C	moderate		carbides	
Y				binds the oxide layer to the substrate
Hf			HfC	improves grain boundary strength
La				improves hot corrosion and oxidation resistance
Zr	moderate			inhibits carbide coarsening; improves grain boundary strength; improves creep strength and ductility
B	moderate			

Chromium and aluminium form adherent diffusion-resistant oxides, which protect the alloys from the environment. 'Tramp' elements, i.e. elements unintentionally included into the alloy, namely, silicon, phosphorus, sulphur, oxygen, and nitrogen must be controlled through appropriate melting practice [6].

2.1.1.2 PHASES AND MICROSTRUCTURE

The microstructure significantly affects the mechanical properties of the alloys. The main changes involve the precipitation of secondary phases at elevated temperatures and for extended exposure times. Their presence can not only radically change the properties but also can impair the material's resistance and life time.

The microstructure of a typical nickel alloy contains different phases which are formed during the fabrication and then react and interact with increasing temperature. The main phases are the gamma matrix, the gamma prime and carbides. Other phase such as TCP (Topologically Close-Packed) phases (σ , μ , Laves) can be found, although their formation is unwanted.

2.1.1.2.1 GAMMA (γ) PHASE

The continuous matrix (gamma) is an fcc nickel-based austenitic phase and can be found in all nickel-based alloys. This phase is nonmagnetic. It usually contains a high percentage of solid-solution elements such as Co, Cr, Mo, and W; W and Mo show the greatest rate in expansion in lattice parameter per nickel solute [15]. Alloying elements are very important in promotion of the creep rupture strength, because pure nickel does not have high elastic modulus or low diffusivity. Superalloys can be used in extreme conditions ($T > 0.85 T_m$ (melting point)) for times up to 100000 hrs) because of the following factors [8]:

- Nickel's nearly filled third electron shell is the reason for its high tolerance for alloying.
- Additions of chromium promote formation of Cr_2O_3 , which has few cation vacancies and restricts the diffusion rate of metallic elements outward and aggressive atmospheric elements (O_2 , N_2 , S) inward.
- At higher temperatures the formation of Al_2O_3 -rich scales provides exceptional resistance to further oxidation.

2.1.1.2.2 GAMMA PRIME (γ') PHASE

The primary precipitate phase in superalloys is called gamma prime (γ'). The basic composition of γ' phase is Ni_3Al and its crystal structure is an ordered ($L1_2$) intermetallic fcc with Ni atoms on the cube faces and the Al atoms at the cube edges [16] (see Figure 2.2).

The major γ' constituents are aluminium and titanium. They are added in amounts and in proportion to precipitate a high volume fraction of a fine dispersion of $\text{Ni}_3(\text{Al,Ti})$ in the matrix. The volume fraction of γ' significantly affects the strength of the alloy; wrought superalloys contain about 20-45 vol % of γ' in contrast to cast alloys which contain up to 60%. Higher content of gamma prime would make difficult the deformation of wrought alloys. Other γ' - formers include chromium, niobium and tantalum [9, 12]. The role of titanium is significant at higher temperatures, where it is stable and less prone to overaging, thus imparting strength [17]. Higher amounts of Ti (or Ti/Al ratio) lead to the precipitation of needle-like particles of the hexagonal Ni_3Ti phase, η , which grows rapidly with additional aging and is deleterious, causing degradation in creep and stress rupture properties [18].

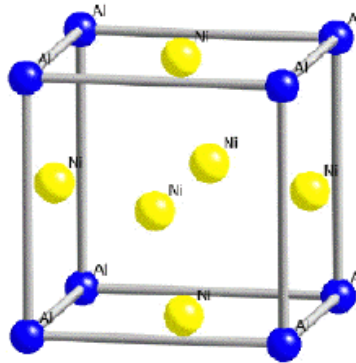


Figure 2.2 FCC gamma prime crystal structure [11].

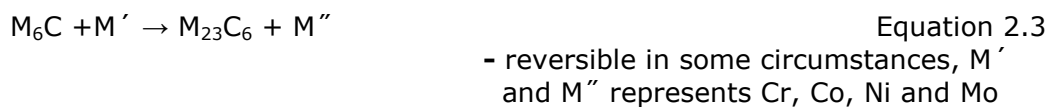
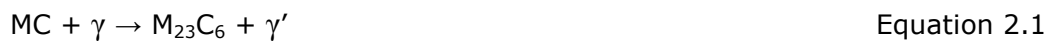
The γ' particles are usually spherical. However, cubic or plate-like particles can be found depending on the matrix/precipitate mismatch. The small difference in matrix/precipitate lattice parameter ($\sim 0-1\%$) in combination with the compatibility of crystal structures allows homogeneous nucleation of the γ' precipitate all over the matrix resulting in a low surface energy and long time stability. This phase is required for high temperature strength and creep resistance [8]. In addition, γ' imparts strength to the matrix without lowering the fracture toughness of the alloy. Many other factors contribute to the hardening imparted by the γ' and include γ' stacking fault energy, γ' strength, coherency strains, volume fraction of γ' , and γ' particle size [7].

2.1.1.2.3 CARBIDES

Carbide formation in nickel-based alloys is desired for stabilising the structure against high-temperature deformation. The most important types of

carbides are MC, M₆C, M₂₃C₆, and M₇C₃ (M stands for one or more metal atoms) with fcc crystal structure (M₇C₃ orthorhombic or tetragonal). Carbon is usually added in amounts of 0.02-0.2 wt%, and reacts with refractory elements such as titanium, tantalum, and hafnium to form the MC carbides (e.g., TiC, TaC, or HfC) which precipitate at high temperature from the liquid phase. MC carbides are a major source of carbon in most superalloys below 980°C. During heat treatment and service, these begin to decompose and form lower carbides such as M₂₃C₆ and M₆C (see Equation 2.1 – 2.3). M₂₃C₆ carbides have a complex cubic structure (when the carbon atoms are removed, the crystal structure transforms in the tetragonal TCP σ-phase), and form at lower temperatures (around 800°C), mainly on the grain boundaries in alloys rich in chromium. Carbides M₆C are formed from about 820 to 980°C in alloys with higher content of tungsten and molybdenum [8-10].

The principal reactions of carbides [8]:



Generally carbides are beneficial because they give an increase of the rupture strength through the inhibition of grain boundary sliding and/or migration at high temperature, and by bonding with reacting elements hence influencing chemical stability [8, 9].

2.1.1.2.4 BORIDES

Boron is an essential element to improve creep rupture strength, but the additions have to be small. Boron forms M₃B₂ tetragonal particles, which are very hard and can be observed on or near the grain boundaries, where boron segregates. Two types of borides have been identified with the M representing a combination of Mo, Ti, Cr, Ni and Co [8].

2.1.1.2.5 TOPOLOGICALLY CLOSE-PACKED (TCP) PHASES

The TCP phases precipitate unintentionally; they are not beneficial in improving properties. Many of them are considered detrimental, and hence the composition of an alloy has to be controlled carefully to avoid their formation.

Excessive quantities of elements such as chromium, tungsten, molybdenum, tantalum and niobium can contribute to the formation of these intermetallic phases. The TCP phases develop during heat treatment or service. The crystal structures of TCP phases are characterised by close-packed atoms in layers separated by relatively large interatomic distances. The layers are displaced from one another by sandwiched larger atoms, developing a characteristic 'topology'. On the contrary, geometrically close-packed phases (GCP) such as the Ni₃Al (gamma prime) compounds, are close-packed in all directions. The general chemical formulae of TCP phases is AxBy, where A and B are transition metals with different electronegativities. The σ , μ , Laves, etc. usually occur in the form of plates, which appears as needles on a cross-section through the microstructure. [8, 13]

Sigma (σ) phase is hard and brittle, and was originally found in the Fe-Cr system. It can be represented in the form (Cr, Mo)_x(Ni,Co)_y, where x and y can vary from 1 to 7. It has a harmful impact on alloy properties particularly the rupture strength of the alloy at elevated temperatures. To develop sigma depletes the gamma matrix of refractory metals, which causes a reduction of solution strengthening and creep strength. The plate-like morphology is an excellent source for crack initiation leading to fracture, thus reducing rupture life. σ often nucleates on M₂₃C₆ because considerable lattice coherency between σ phase and M₂₃C₆ carbide exists. The same reasoning can be used for the μ phase in relation to the carbide M₆C [8].

The μ phase has only been observed in a few superalloys. Precipitates appear in a form of Widmanstätten platelets at high temperatures, but the detrimental effects have to be determined [9].

Laves phase consists of close-packed double layers with a composition of AB₂ type. Most common is its presence in iron-based alloys with benign effect. After longer exposure at high temperature Laves phases precipitate as intragranular platelets or as irregularly shaped globules. At room temperature large quantities of Laves phase reduce tensile ductility and creep properties [9].

The new generation of superalloys contains less chromium to avoid development of TCP phases and thereby degradation of the alloy. Decrease in oxidation resistance is compensated for by protective coatings [11].

2.1.2 STRENGTHENING OF SUPERALLOYS

The chemical composition and the processing conditions determine the microstructure and on this depends the mechanical properties of nickel based alloys. One of the main characteristics of superalloys is the high-temperature strength. Strengthening of nickel alloys can be performed by solid-solution strengthening and/or precipitation hardening of the face-centred cubic (fcc) matrix.

2.1.2.1 SOLID-SOLUTION STRENGTHENING

A solid solution can be defined as a homogeneous mixture of one or more solutes in a solvent in which the crystal structure remains unchanged after substitution of atoms or molecules and the mixture remains a single phase [19].

Solid-solution strengthened nickel based superalloys contain low quantities of precipitating elements such as aluminium, titanium, or niobium, but high amounts of refractory elements, such as molybdenum or tungsten. Typical is an austenitic nickel-chromium-tungsten (or molybdenum) matrix in which other elements can be added, e.g. cobalt, iron, tantalum, rhenium, boron, and carbon. Moreover, carbon is a source of both primary and secondary carbide strengthening. Primary carbides affect initial grain structure. Alongside the solid solution hardening, secondary carbides precipitate on grain boundaries and intragranularly on areas with high dislocation density. The addition of molybdenum and tungsten distort the fcc nickel lattice which causes an internal strain. These elements reduce the stacking fault energy (SFE) while increasing the electron atom ratio. All the characteristics mentioned above reduce diffusion and slow dislocation movement, thus decreasing cross-slip at higher temperatures. [8-10, 12]

2.1.2.2 PRECIPITATION STRENGTHENING

Precipitation hardening is provided by uniform formation of stable intermetallic compounds, primarily γ' [$\text{Ni}_3(\text{Al,Ti})$], and other phases (borides and carbides). Gamma prime is formed during ageing heat treatments when some important factors are: volume fraction γ' , its size, morphology, and distribution. A small misfit guarantees a low surface energy which provides a stable microstructure and improves the properties of the alloy at elevated temperatures. A tendency to keep the lattice parameter of γ' smaller than the parameter of γ , guarantees that a negative misfit facilitates the formation of rafts perpendicular to the direction of applied (uniaxial) stress; thus possibly reducing the creep rate (because the movement of dislocations over the layers is inhibited). [8-10, 12]

2.2 HAYNES™ 230™ ALLOY

2.2.1 INTRODUCTION

Haynes™ Alloy 230™ is a solid solution and carbide strengthened Ni-Cr-W-Mo superalloy originally developed in the early 1980's for industrial purposes for an alloy with a combination of high temperature strength, long-term thermal stability and corrosion resistance in oxidising and nitriding environments at service temperatures up to 1150°C. The alloy design gives distinct resistance to grain coarsening and stability of properties. These properties, together with its good formability and weldability characteristics, have made HA230 an excellent material for many aerospace and power industry applications, including the manufacture of gas turbine sheet metal hardware such as combustion cans, transition ducts etc [20].

2.2.2 THE DEVELOPMENT OF HAYNES 230 ALLOY

Since the occurrence of the cobalt crisis in the late 1970s, effort has been focused on reduction of the cobalt content in existing alloys (HASTELLOY™ X, NIMONIC™ 86, INCONEL™ 617, HAYNES™ 188 (Co-based)) whilst maintaining the properties at an acceptable level or better [21].

The alloy was originally developed from the Ni-Cr-Mo-W system in which the high nickel content provides a stable austenitic matrix with tungsten and molybdenum additions, in the presence of carbon and boron, providing the alloy's high temperature strength [21-24]. Tungsten provides very effective solid solution strengthening whilst carbon promotes the formation of chromium rich $M_{23}C_6$ carbides. The ratio of the primary alloying elements (Cr, W and Mo) is controlled to ensure that $M_{23}C_6$ carbides precipitate out at high temperatures. The lattice parameter of the carbide changes with additions of boron so it is more coherent with the matrix [25]. These precipitates form on grain and annealing twin boundaries, pinning dislocations and thereby contributing to the alloy's creep strength as well as resistance to grain coarsening during prolonged exposure at high service temperatures. Tungsten was also specifically chosen in preference to molybdenum as a major alloying element, since it diffuses more slowly in nickel. It also increases the elastic moduli and decreases the stacking fault energy [26],

HAYNES, HASTELLOY and 230 are registered trademarks of Haynes International, Inc.
NIMONIC, INCONEL are registered trademarks of Special Metals Corporation.

hence impeding cross-slip and promoting high-temperature creep and fatigue strength. One of the objectives during the new alloy development was to design material without the TCP phases which could appear at higher temperatures and cause faster degradation of the properties [25]. Finally, resistance to surface attack in oxidising and nitriding environments is provided by the additions of chromium, manganese and silicon, with the latter element contributing to the stabilisation of the surface protective spinel oxide layer during service exposure. The inclusion of lanthanum improved resistance to oxide spallation [27]. The carbon quantity in the material is kept low, because a content exceeding 0.15% can cause increase in carbide precipitation and thus decrease in ductility [10]. In the case of HA230 the carbon level is 0.1% to provide effective precipitation of $M_{23}C_6$ carbide. The nominal chemical composition is given in Table 2.2.

Table 2.2 The nominal chemical composition of Haynes 230 alloy in weight percent. (*maximum)

Ni	Cr	W	Mo	Fe	Co	Mn	Si	Al	C	La	B
57 (bal)	22	14	2	3*	5*	0.5	0.4	0.3	0.1	0.02	0.015*

2.2.3 FABRICABILITY

Haynes 230, a material used for combustor components, has good workability and weldability, and can be either cast or wrought [21]. As a solid-solution strengthened alloy it has good room temperature ductility. Due to precipitation of intermetallic phases at higher temperatures and long-term service exposures, ductility decreases during cooling process [22].

The wrought product form of the alloy, e.g., bar, plate or sheet, is normally produced by rolling an electro-slag remelted ingot on a reversing mill at a temperature of approximately 1200°C. Thinner gauge sheet products may be finished by cold rolling prior to final annealing. After rolling to the final product size the material is solution annealed within the temperature range 1177 to 1246°C and rapidly cooled or water quenched. This procedure has to be followed for the purpose of the best balance of properties. The result is an equiaxed microstructure with an average grain size in the range of ASTM 4-6 [20]. In this as-received condition (see Figure 4.25 later in the thesis), tungsten-rich primary M_6C carbides, which form during solidification, are present both at grain boundaries and randomly dispersed within the microstructure. These resist resolution during heat treatment thus enabling a grain size range to be achieved which results in the best combination of high temperature creep rupture and LCF (Low-Cycle Fatigue)

properties. Annealing twins are also copiously present within the microstructure which is typical for most nickel-based superalloys. Their occurrence indicates that there is a relatively low value of the stacking fault energy. In addition to the primary M_6C precipitates present in the annealed condition, some chromium rich $M_{23}C_6$ may also be present precipitated at the grain boundaries and on annealing twins within the microstructure [2-4].

2.2.4 MECHANICAL STRENGTH

2.2.4.1 TENSILE AND TOUGHNESS PROPERTIES

The similarity in high strain-hardening properties between HA230 and alloys from the same compositional group (e.g. HASTELLOY X, HAYNES 188) may be attributed to the additions of tungsten which decreases the stacking fault energy of the nickel [21]. The tensile properties of the alloy are: 0.2% offset yield strength of 375 MPa, ultimate tensile strength (UTS) of 844 MPa and elongation at failure of 48% [20]. Klarstrom [23] observed that tensile ductility and Charpy-V impact toughness decline within the first 100 hours of exposure, however after 16000 hours of exposure the alloy possessed a respectable level of these properties. The study revealed ductile fracture characteristics only. Similar observations were reported by Seeley and Srivastava [28]. Wittenberger [29] studied tensile properties after long-term heat treatment at 820°C (1093K) and found the most remarkable effect in the residual tensile elongation at -196°C (77K) in air and vacuum, where dropped from 40 to 5%. Miniature tensile testing at temperatures in the range of 679-752°C for 500 hours in the microturbine environment was performed by Lara-Curzio [30]. The sub-surface degradation and cracking of the material was observed as a result of Cr depletion. Similar observations after cyclic oxidation for 720 days at 982°C have been reported by Gleeson and Harper [31]. The UTS and ductility decreased by 30% and 60% respectively at 752°C, while at 679°C they decreased by 10% and 25%.

2.2.4.2 CREEP-RUPTURE STRENGTH

The creep-rupture strength is an important parameter in designing alloys for high-temperature applications. As mentioned above, one of the reasons why tungsten was chosen as a main alloying element was its slow diffusivity in nickel as high temperature creep is a diffusion controlled process. Also additions of Cr and Mo, based on atom size differences [22], play an important role, as well as the precipitation of fine particles of $M_{23}C_6$ carbide on slip dislocations which is an important strengthening mechanism [32]. The carbides were identified to be of the

form $\text{Cr}_{21}(\text{W},\text{Mo})_2(\text{C},\text{B})_6$ [33]. Furthermore, their precipitation at service temperatures has been shown to restrain sliding of grain boundaries. Klarstrom [22] provides a comparison of 1% creep strengths of three similar superalloys: Ni-based Hastelloy X, Haynes 188 (high Co content) and Haynes 230, (see Figure 2.3). It can be observed that the creep strength of HA230 is significantly higher than that of Hastelloy X and very close to that of 188 alloy.

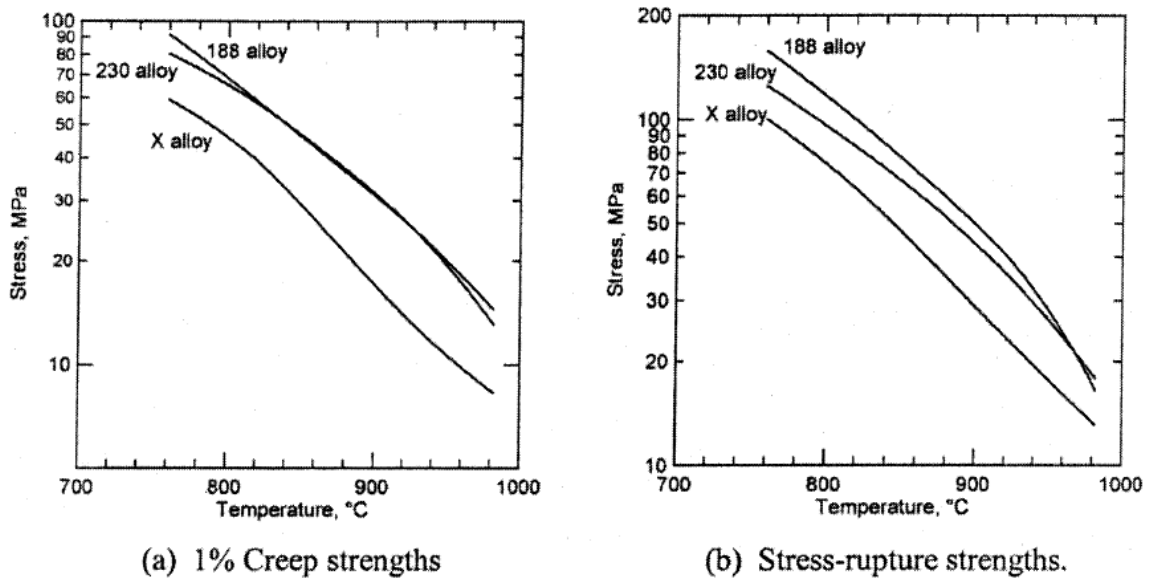


Figure 2.3 Comparison of 1000 hour creep and stress rupture strengths for sheet products [22].

2.2.4.3 FATIGUE STRENGTH

Fatigue resistance is a complex phenomenon and it is not easy to design it into an alloy. The fatigue process consists of crack initiation, growth and propagation. The operating conditions in a gas turbine engine involve thermal cycling which can lead to thermal fatigue failure. The regime for the combustor is considered to be low cycle fatigue (LCF), generally with $<10^5$ cycles. In the low total strain regime (strain rate = 5×10^{-9} /s) HA230 exhibits LCF resistance corresponding to that of Hastelloy X, but in comparison to Co-based alloys it is inferior [21]. Vecchio et al. [34] compared material processed at 1121°C (lower than the carbide solvus temperature) with one fully solution annealed at 1232°C , and reported that subsolvus processing improves the fatigue resistance and refines the grain structure of HA230. The study conducted by Mayer-Olbersleben et al. [35] proved that the main crack initiation mechanism for the thermal fatigue is transgranular cracking on slip bands formed at intermediate temperatures when the mechanical strains reached maximum values. Lu et al. [36-38] report that a hold

time at temperature increases dramatically the cyclic crack-growth rate and, in addition, changes the fracture mode from transgranular to intergranular. This is mainly observed with the increase of the temperature. The overload part of the fractures surfaces of all samples consisted of dimples of various forms. The dimple size decreased as the test temperature increased. The fracture surface at 816°C contained cleavage-like facets and at 927°C had a faceted appearance with fatigue striations. Additionally, Chen et al. [39] report an anomaly in the LCF behaviour of the alloy at high temperatures where the fatigue life is actually longer at 927°C than at 816°C at strain ranges between 1.5-2%. He also observed [40] the reduction of fatigue life at higher temperatures (above 927°C) when oxidation damage assists to crack initiation and its propagation.

Saleh [41] studied the effects of deformation and fatigue using non-destructive techniques. Microcracking and void formation are the primary mechanisms responsible for fatigue damage in tension-tension fatigue. The 0.2% offset yield strength of the materials is 385 MPa in compression and 425 MPa in tension. The tested elastic modulus of 212 GPa is very close to the literature values.

Fatigue-crack-growth experiments with and without hold times (760-927°C) performed by Lee et al. resulted in the change of fracture mode from transgranular (low temperature, no hold) to intergranular and a substantial increase in the crack-growth rate [42].

A plateau in the yield strength between 600 and 800°C is a result of temperature induced carbide formation at high temperatures [25].

2.2.5 THERMAL STABILITY

Thermal stability of HA230 is significantly better than that of Hastelloy X and HA188 (see Figure 2.4) due to its greater resistance to the precipitation of detrimental intermetallic compounds [22]. The only secondary precipitates observed in 230 alloy exposed for 8000 hours between 650°C to 871°C have been chromium rich $M_{23}C_6$ carbides at grain and twin boundaries. Longer term studies (up to 16000 hours) have shown that the Haynes alloy 230 preserves an exceptional level of impact toughness and that only a modest reduction in ductility occurs at intermediate temperatures [23, 43].

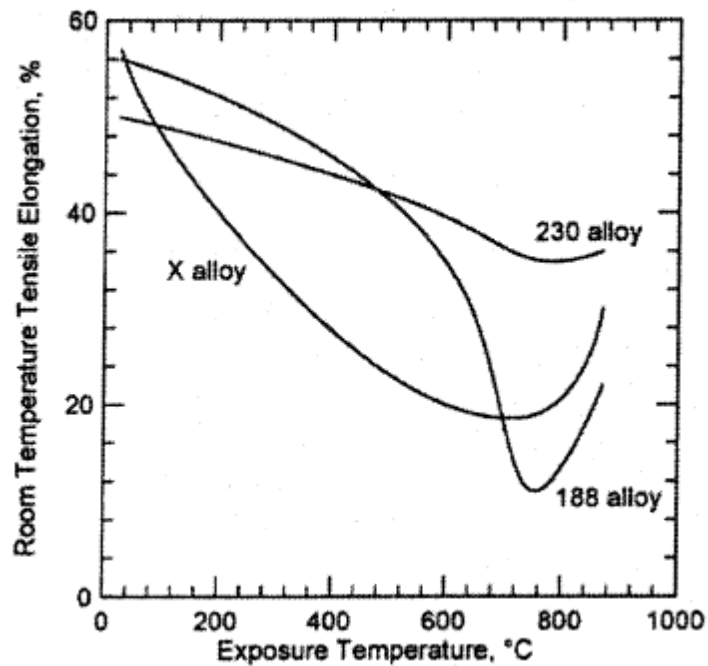


Figure 2.4 Comparison of room temperature tensile elongation after 8000 hours in the temperature range 650°C to 871°C [22].

2.2.6 OXIDATION AND NITRIDATION RESISTANCE

The oxidation behaviour of Ni-Cr alloys has been published in extensive studies [44, 45]. Generally the outer layer is NiO and the inner layer Cr₂O₃. The formation of Cr₂O₃ causes depletion of Cr in the subsurface area. An intermediate layer of the spinel NiCr₂O₄ is formed still with some presence of NiO and/or Cr₂O₃.

Oxidation studies of HA230 have been carried out by various research groups under number of conditions. The protection from oxidation is guaranteed by the formation of Cr₂O₃. [37, 46-48] At the temperatures exceeding 1000°C, the spallation of outer layer and subsequent volatilization (CrO₃) leads to exposure of the surface, attack of the unprotected metal and increase of the internal oxidation. [49-51]

Klarstrom [22] compared 3 alloys with similar composition and use: Ni-based Hastelloy X, Haynes 188 and Haynes 230. Figure 2.5 shows that HA230 suffered the least amount of spallation and of internal attack at 982°C and it is one of the most resistant alloys at high temperature dependent on protective chromium oxide scale. Figure 2.6 compares the changes in the thickness of the oxide layer with increasing time for four nickel based superalloys produced by Haynes Int.

Oxidation kinetics and oxide scale properties were the main issues in the work of England and Virkar [52].

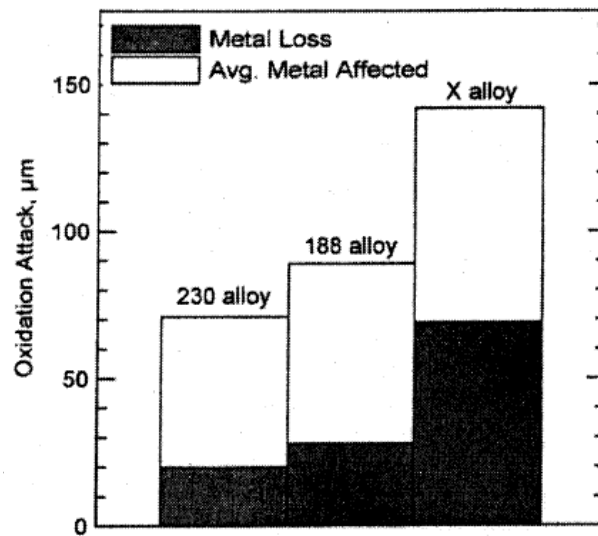


Figure 2.5 Comparison of dynamic oxidation attack at 982°C/1000 hours [22].

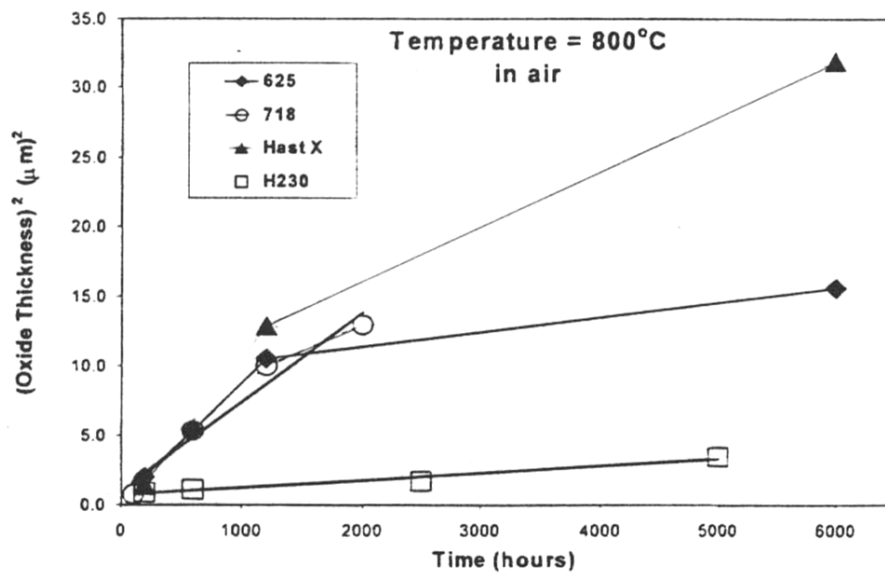


Figure 2.6 Thickness of Oxide Scale vs. Time for Alloys Oxidized at 800°C [52].

Long-term, cyclic-oxidation testing conducted by Gleeson [31] on HA230 in still air for 720 days at 982°C and 360 days at 1093, 1149, and 1204°C exhibited partial (rather than full) scale spallation (attributed to the presence of 0.02 wt.% La in the composition), thus allowing the easier formation of a (semi)protective Cr₂O₃-rich scale during subsequent oxidation. The alloy underwent internal attack in the

form of internal oxidation and void formation, which was, in most cases, significantly greater than the metal loss.

The long term cyclic (every 30 days air cooling at room temperature) oxidation of HA230 coupons in flowing air at 982°C, 1093°C and 1149°C performed by Deodeshmukh and Srivastava [53] for 1 year resulted in the formation of a spinel layer of MnCr_2O_4 above Cr_2O_3 . The higher degree of metal loss is caused by vaporization of Cr_2O_3 .

Lai [54] in his nitridation study exposed the HA230 to cyclic and non-cyclic tests in a combustion atmosphere at 980°C for 1000 hours. The results show the excellent nitridation resistance due to the protective Cr-rich oxide scales, which are very resistant to spallation, formed on the alloy in comparison with other tested alloys. Figure 2.7 summarises his findings. A shallow nitride penetration occurred with blocky nitrides (similar to the 'pool-like' phase observed in this study) identified as Cr_2N formed below the carbide denuded zone and carbide precipitation (M_6C) extending to the centre of the specimen. In a further study, Lai [55] (p. 77) shows that there are no nitrides present after 2000 hours at 870°C. Lai proposed a model for oxidation/nitridation for Ni-Cr alloys which involves the following steps: formation of protective chromia layer, which becomes with cycling/ long-term exposure porous, then O_2 and N_2 molecules penetrate to the metal underneath, nitrogen dissolves and diffuses, and as the concentration rises this leads to the formation of nitrides (CrN , Cr_2N).

Sulphur segregating at the surface at highest temperatures (max at 925°C) might influence the spallation of the protective oxide scale [48]. The depth of the zone depleted in chromium for the specimen repeatedly annealed between 400 and 1100°C was approximately 40 μm from the surface.

Recently a research group in France performed tests with a focus on the high temperature corrosion in helium [56].

At this point it is possible to conclude that the alloy behaves similarly in all the environments, creating protective oxide scale at lower temperatures ($\text{NiO} + \text{Cr}_2\text{O}_3$). With the increase of the temperature, spinels MnCr_2O_4 and NiCr_2O_4 are forming above the chromia layer to replace NiO . At temperatures above 1000°C the outer layer starts to spall/become unstable. Furthermore the oxide/metal interface becomes porous which affects the oxide adhesion. Al_2O_3 forms in the oxide fingers

penetrating into the material. Figure 2.8 shows schematic diagram of an initial stage during the oxidation process in air.

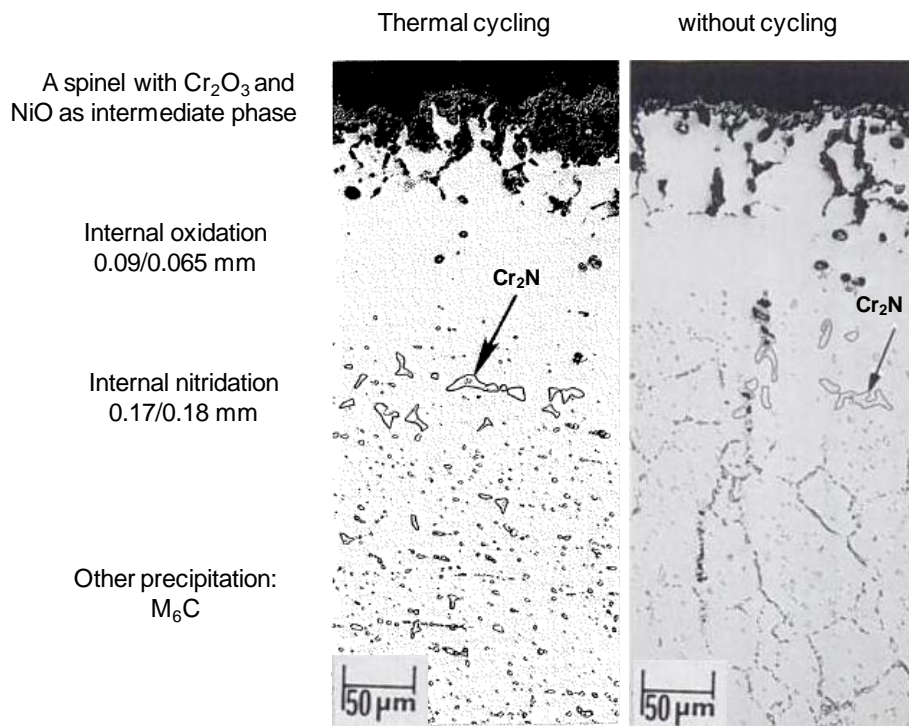


Figure 2.7 Nitridation effect on HA230 during thermal cycling and without cycling [54].

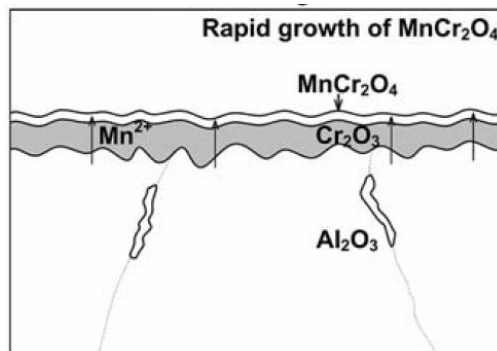


Figure 2.8 Schematic diagram showing the oxidation of HA230 in air at 900°C – initial stage [50].

In all the studies mentioned till now, decarburisation was observed with the zones depleted in Cr close to the surface. On the other hand, the opposite negative effect is the carburization. A carburizing atmosphere introduces carbon into the alloy. Decarburization is linked to reduced creep rupture strength, while heavy carburization leads to loss of ductility and cause low-temperature embrittlement. Alloys then usually fail by cracking because of thermal stresses [57].

If alloy contains elements that form stable carbides, then it is possible that as the concentration of dissolved carbon increases, metal carbides may precipitate in the surface layers when the solubility limit of the carbon is exceeded. This effect is particularly harmful if the metal forming the carbide within the alloy is also the metal whose oxide forms the protective scale. It is also possible that C may dissolve in the metal during reaction [44]:



Lupton [58] exposed high chromium Ni-based alloys (Hastelloy X, Inconel 617 and Nimonic 86) at 950°C and for up to 3000 hours in a carburising environment and observed the vast formation of carbides with a high metal:carbon ratio. He suggests a reduction of chromium content which would lead to the better solubility of carbon in the austenitic matrix. The high volume fraction of carbides at the grain boundaries causes the loss in ductility, however the concentration of C is not high.

Quadackers [59] modified the Ellingham diagram calculated from the results obtained from Inconel 617 behaviour in helium, Figure 2.9. The diagram represents five conditions: *I*-strongly reducing, *II*-highly oxidizing, *III*-stable external oxide with stable internal carbides, *IV*-strongly carburizing internally and externally, and, lastly, *IVa* strong external carburization with stable oxide layer. Zone *III* offers an oxidizing environment yet slightly carburizing and was determined as an area of highest stability.

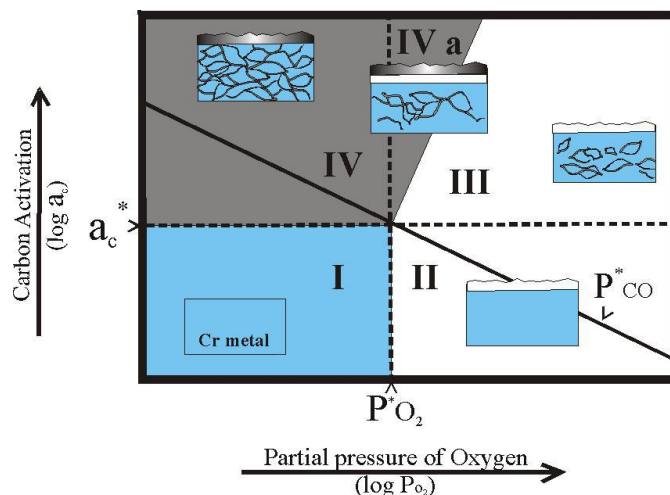


Figure 2.9 A modified Ellingham diagram based on the nickel-chromium alloy's stability calculations (Inconel 617): *I*-strongly reducing, *II*-highly oxidizing, *III*-stable external oxide with stable internal carbides, *IV*-strongly carburizing internally and externally, and, lastly, *IV a* strong external carburization with stable oxide layer. [59, 60]

2.2.7 MICROSTRUCTURAL FEATURES

The matrix of HA230 has a face-centered cubic lattice with a lattice constant of 0.36 nm [21]. The solution-annealed condition contains a relatively small amount of tungsten rich carbide ($\sim 5\%$ volume fraction), referred to as 'primary', dispersed in the matrix. This primary carbide was identified to be of the M_6C -type by X-ray and electron diffraction techniques and is semicoherent with the parent metal [38]. The lattice parameter of the M_6C is approximately three times that of the alloy. Secondary precipitation ($M_{23}C_6$) appears at higher temperatures in the range between 650-980°C. Grain boundaries, annealing twins and pre-existing dislocations are preferred nucleation sites of these chromium rich carbides. The long term studies (for up to 16000 hours) carried out at three temperatures in the range 650°C - 871°C did not reveal any presence of embrittling intermetallic phase such as sigma phase; all precipitated phases are carbides [23,34]. Within this range of temperatures only secondary precipitation of $M_{23}C_6$ carbides at grain and twin boundaries and the peripheries of the primary carbides was observed and these precipitates tend to increase in size with increasing temperature. Long-term air exposures up to 22,500 hours at 820°C (1093K) were performed by Whittenberger [61]. The microstructures observed contained second phase precipitation ($M_{23}C_6$), oxide scales consisting of chromia and spinels, some intergranular porosity, and surface-connected intergranular pits; additionally no change in the grain size was observed at the highest temperature.

A research group in USA is studying materials for use in ultra supercritical conditions (USC - 760°C/35MPa) [62]. Wu et al. performed microhardness testing at 1kg load and some aging for 1-3000 hours in the temperature range of 700-800°C. Considerable scatter in microhardness was observed (200-275 Vickers). Interestingly, primary carbide was identified as WC and secondary Cr-rich carbide, forming networks, as $M_{23}C_6$.

Stefanuto & Pojaghi [63] report the presence of $M_{23}C_6$, M_6C and $M_{12}C$ type carbides in the creep tested specimens at 750 and 800°C, while at 900 and 1000°C only $M_{23}C_6$ and M_6C were observed.

In the design of the alloy, it was crucial to eliminate the presence of TCP phases, which could be precipitating at the high temperatures. One of the most unwanted phases is the sigma phase which has not been observed after any testing.

Several studies have evaluated the hardness of the M_6C carbide in steels [64, 65]. Generally the hardness of this carbide is between 16 and 20 GPa (\sim 1600-2000 Vickers). The microhardness values of M_7C_3 carbides varied between 1050-1500Hv (40g) [66].

2.2.8 IDENTIFICATION OF THE PHASES

In this project, comprising long term high temperature exposure, the new phase, in this thesis called 'pool-like' or transition phase Cr-rich was observed. Therefore a part of this research was focused on the better understanding of the precipitating mechanism occurring in HA230 with time-temperature exposure.

As was mentioned above, two main precipitating phases have been reported in HA230. Firstly there is primary carbide M_6C , W-rich, and then secondary carbide $M_{23}C_6$, Cr-rich. While designing the alloy, the intent was to create the alloy without detrimental phases which could limit the life-time of the components at elevated temperatures. Although any TCP phases have not been reported to date, various long term exposures or testing at high temperatures (around 1000°C) revealed some features in the microstructure which have not been fully identified [62, 63].

The comparison with similar alloys is helpful. The alloys containing high amounts of nickel and chromium with additions of tungsten, molybdenum, as well as iron and cobalt, such as Hastelloy X or Inconel 617, are superalloys with longer history and could offer some similarities. Generally, in this type of alloys with austenitic structure, the following precipitates appear in the microstructure within the whole region of exposure times and temperatures: MC, M_6C , $M_{12}C$, $M_{23}C_6$, sigma phase, mu phase. Tawancy [67] identified the lattice parameter of the matrix in Hastelloy X as equal to 3.6 Å and the primary M_6C carbides as Mo-rich ($a=11.08\text{Å}$). After ageing for 16000 hours at 540°C secondary $M_{23}C_6$ on the grain boundaries and on the primary carbide-matrix interface was observed together with an fcc structure precipitate ($a=10.89\text{Å}$) identified as $M_{12}C$. In addition to these two phases, at 650°C and 760°C a Cr-Fe sigma-phase and at 870°C mu-phase were detected. The morphology of σ -phase was rather blocky-type. The phases were identified by electron diffraction. The same primary (M_6C , Ti(C,N)) and secondary precipitates ($M_{12}C$, $M_{23}C_6$, σ , μ) were identified, for example, by Kirchhöfer et al.[68] and Zhao et al. [69]. In addition to $Ni_2(Cr,Mo)$, M_6C and μ , Raghavan et al. [70] reported the presence of a tetragonal P phase in Hastelloy C-276. The P phase was originally identified by Rideout et al. [71] in the Ni-Cr-Mo system. In modified

Hastelloy XR, besides M_6C , $M_{23}C_6$ and Laves phase Fe_3Mo_2 , $M_{12}C$ was observed after the creep tests at 900°C in an impure helium gas [72].

Li et al. [73] identified three phases in Hastelloy X exposed in air and helium at 900°C. The primary carbide M_6C ($a=10.96$ and 10.94\AA) and secondary carbides M_6C' ($a=10.87\text{\AA}$) and $M_{23}C_6$ ($a=10.69\text{\AA}$).

Similar precipitates can be found in Ni-Cr-Co alloys. Kazdan Zeytin et al. [74] reports the presence of sigma, chi and $M_{23}C_6$ during cooling from the melt. The grain boundaries were decorated by island-like precipitates (σ phase) neighbouring with lamellar $M_{23}C_6$ carbide.

Moreover, Co based alloys show particular similarities. In the Co-Cr-W-C system a variety of carbides can be observed at various temperatures. The M_6C carbide is unstable if the concentration of chromium is less than 5% and decomposes to form tungsten carbide (WC)[75].

M_6C , $M_{12}C$ type carbides were also observed in Ni-Mo alloys. Both could be carbon deficient. M_6C contains 12-16 at% of C, while $M_{12}C$ contains 8 at% of C ($a=10.83-10.98\text{\AA}$) [76]. There is a small difference in the crystal structure of the M_6C and $M_{12}C$ carbides, see Figure 2.10, but quite a significant difference in the lattice parameter. The lattice parameter of Ni_6Mo_6C ($M_{12}C$) is equal to 10.89\AA when the lattice parameter of Fe_3W_3C (M_6C) is equal to 11.10\AA . These carbides belong to the great family of cubic η -carbides where M usually stands for two or more types of metals and can be classified accordingly e.g. the carbon content (η -6-carbide: $M_3M'_3C$, C on site 16c; η -12-carbide: $M_6M'_6C$, C on site 8a [77]). The lattice parameter then changes according to the ratio of the atoms and to the atomic radii of the atoms present. An eta carbide with a diamond cubic crystal structure (Fd3m, $a=10.92\text{\AA}$ and a composition of the form $(Ni,Fe)_6W_6C$ was observed by Muddle in the W-Ni-Fe alloy [78] as well as by Posthill & Edmonds [79] and others.

Very important is the detection of sigma phase in Ni-Cr-W system. Kuo [80] confirmed its presence in the form of Cr_8Ni_5W at a wide range of temperature stability. It has a tetragonal lattice with $a = 8.90-8.94\text{\AA}$ and $c = 4.60-4.62\text{\AA}$. Studies by Kikuchi et al. [81, 82] confirmed the presence of Cr_8Ni_5W in the high W rich alloys, but suggest it as a intermediate phase between 800-1000°C. The ternary diagram of Ni-Cr-W system in Figure 2.11 shows the areas of presence of the sigma phase.

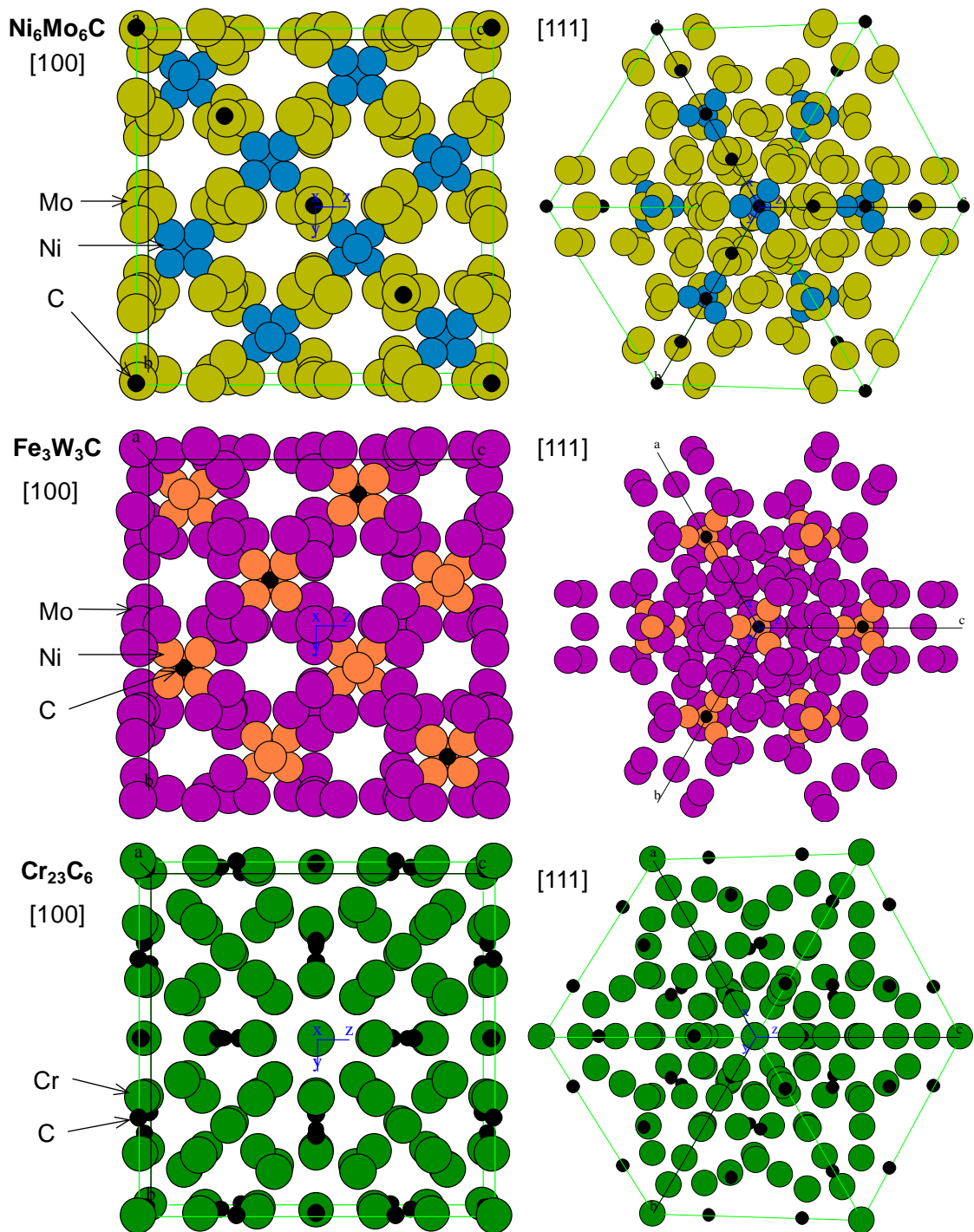


Figure 2.10 Crystal structures of $M_{12}C$, M_6C and $M_{23}C_6$ types of carbides. CaRIne software.

A high temperature phase was reported by Lai [54], who identifies it as nitride Cr_2N . In his nitridation study he observed this phase close to the specimens' surface. Pop and Wolski [48] showed that N is not segregating at the alloy surface above $875^\circ C$; the maximum peak was observed for annealing at $700^\circ C$. Hence, they suggest the formation of W and/or Mo nitrides which was reported previously in Fe-Mo [83] and Fe-W [84] alloys.

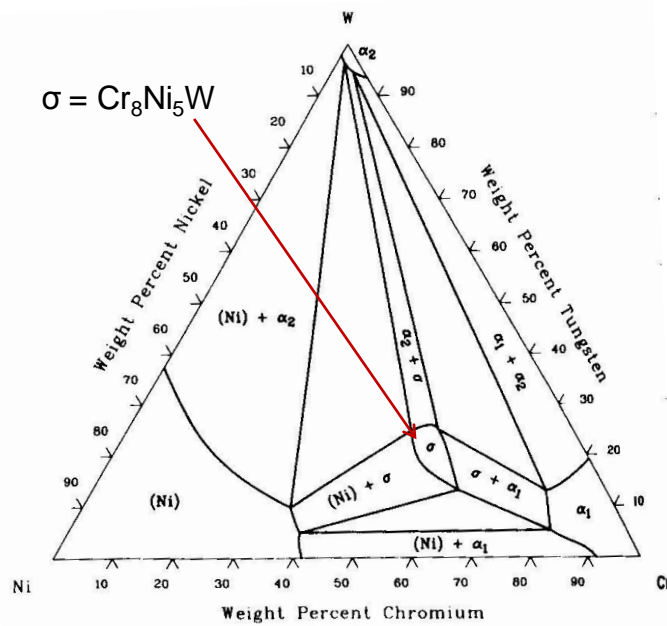


Figure 2.11 Ni-Cr-W isothermal section at 1000°C [85].

Table 2.3 summarises the lattice parameters values obtained by X-ray diffraction technique for HA230 and Hastelloy X during studies carried out by different research groups.

Table 2.3 Summary of the lattice parameters obtained by XRD technique for HA230 and Hastelloy X in different studies.

author	material	Lattice parameters of phases in Å			
		matrix	M ₆ C	M ₆ C' (M ₁₂ C)	M ₂₃ C ₆
Saleh [41]	HA230	3.588	11.09		
Rothman [43]	HA230 8000hrs 760/870°C		10.95	10.80	10.65
Maldini [86]	HA230 creep 750-1000°C	3.57	11.10		10.71
Tawancy [67]	Hastelloy X	3.60	11.08	10.89	
Li [73]	Hastelloy X		10.96	10.87	10.69

2.2.9 GRAIN BOUNDARY ENGINEERING

Grain growth describes the increase in average size of grains after primary recrystallization is complete. Srolovitz et al. [87] used Monte Carlo simulations for grain growth. One of the cases is the grain growth in a particle pinned microstructure in which a sudden decrease of particles occurs (Figure 2.12). Experimental observations in sheet materials showed that the abnormal grain

growth could be associated with grain boundary motion which is opposite to that of the grain boundary curvature (Figure 2.13). Also the recrystallization process might play a role in the changes of the volume energy, when the removal of dislocations modifies the density and the local variation in density result in nonuniform distribution of internal strains.

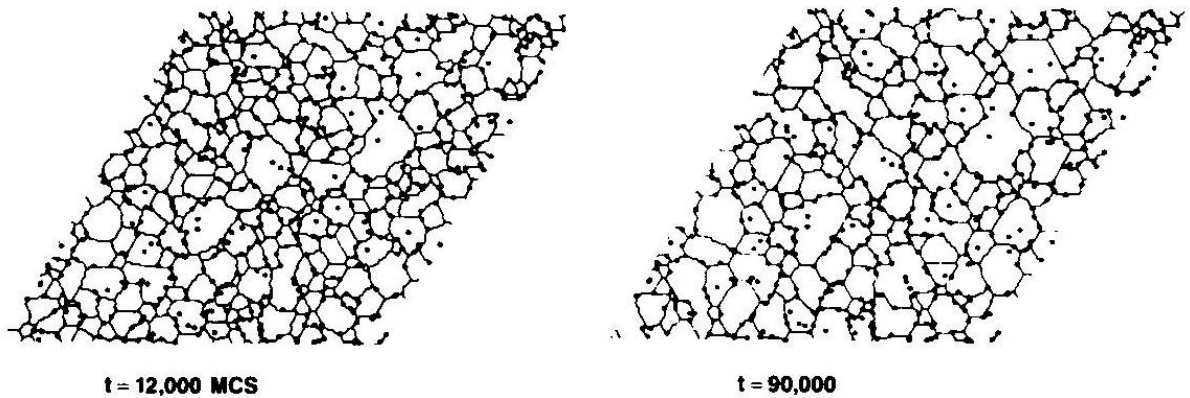


Figure 2.12 Time evolution of a pinned microstructure following a reduction in the particle concentration from 2.5 to 1.5% [87].

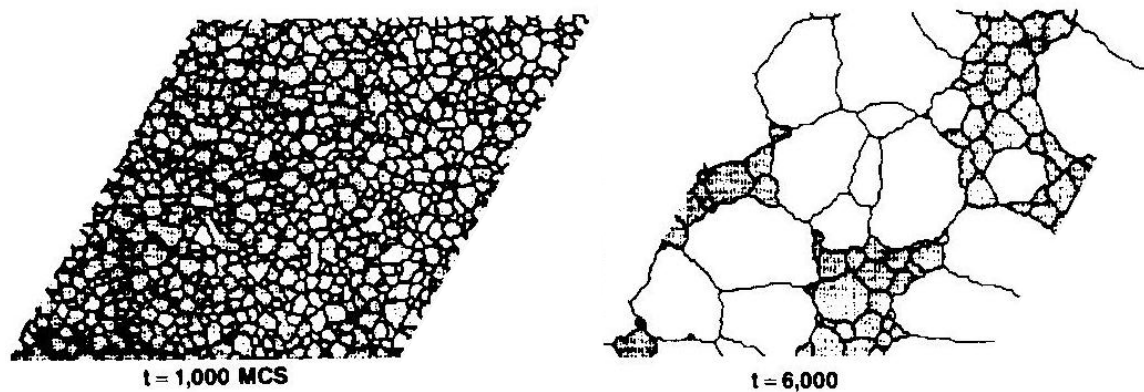


Figure 2.13 Microstructure undergoing abnormal growth. The undashed grains are the secondaries [87].

SUMMARY

In this chapter superalloys have been introduced and a detailed summary of HA230 given followed by an overview of the phase identification. Important points reviewed include the stability of the alloy in all the characteristic aspects at temperatures up to $\sim 930^{\circ}\text{C}$ and the resistance to the precipitation of TCP phases. At higher temperatures the material starts to degrade faster due to the increase of oxidation effect.

3 METHODOLOGY

This chapter covers the experimental techniques and equipment used during this project, a description of the material and its condition as well as the experimental procedures including details about the specimens studied, and sample preparation for each technique.

The aim of this work is to investigate microstructural and hardness changes that the Haynes Alloy 230 undergoes during high temperature (stressed and unstressed) exposure. Optical Microscopy (OM), Scanning Electron Microscopy (Field Emission Gun – FEG SEM, Environmental - ESEM) and Transmission Electron Microscopy (TEM) were utilized to document the microstructural features of the samples, such as the precipitated phases or grain size. Additionally, Energy Dispersive X-ray analysis (EDX), X-ray Diffraction (XRD), Electron Probe Micro Analysis (EPMA), Inductively Coupled Plasma - Optical Emission Spectrometry (ICP-OES) provided information about chemical composition and crystal structures, and led to identification of the phases. Focused Ion Beam (FIB) was employed as a tool for preparation of TEM specimens. Finally, Vickers Hardness (VH) testing was carried out to map the changes in hardness as a function of exposure time and temperature, and to obtain correlation with the observed variations in microstructure.

Certain exposed samples were further tested to get more detailed information about the alloy and its properties. Nanoindentation testing was focused on the difference of hardness of individual precipitated phases. Tensile Testing provided information about mechanical behaviour of the aged material.

To facilitate the identification of the precipitated phases, their extractions from the bulk material were carried out.

3.1 EXPERIMENTAL TECHNIQUES AND INSTRUMENTATION

3.1.1 VICKERS HARDNESS

Hardness is defined as a material's resistance to surface penetration by an indenter under an applied force [88]. Vickers hardness is one of the methods of measuring the hardness of a material. In the test a prescribed load/force (kgf/N) is applied to a diamond indenter, in the form of a square-based pyramid with a 136°

point angle (see Figure 3.1). The diagonal lengths of the resulting indentation are measured through the tester eyepiece and the Vickers Hardness value can be obtained from a conversion table. The Vickers hardness value is a function of the test force divided by the surface area of the indentation.

$HV = \text{Constant} \times \text{Test force} / \text{Surface area of indent}$

$$HV = \frac{2F \sin \frac{136^\circ}{2}}{d^2} \quad \text{Equation 3.1}$$

$$HV = 1.854 \frac{F}{d^2} \text{ approximately} \quad \text{Equation 3.2}$$

F = Load in kgf, d = Arithmetic mean of the two diagonals lengths, d_1 and d_2 in mm.

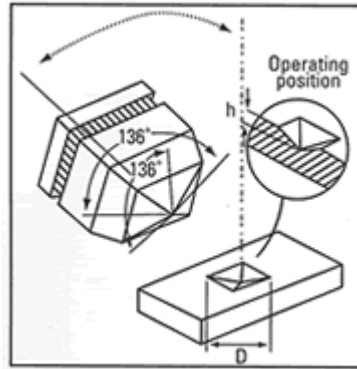


Figure 3.1 Schematic diagram showing the shape of the Vickers indenter and impression [89].

Two different types of hardness testers have been employed in this study. The first one, a Mitutoyo MV-1S, was used to determine the macrohardness. It has a loading capacity of 1-20kg. The other one was a Mitutoyo MVK-G1 microhardness tester with a loading capacity of 10-1000g.

The hardness data from the HA230 material has been analysed using a time - temperature parameter function proposed by Larson and Miller [90]; for details see Appendices 9.1.

3.1.2 NANOINDENTATION

Nanoindentation or Nano-Hardness is generally defined as the resistance of material to permanent or plastic deformation on small length scales [91]. In recent years it has become used as an important technique for characterising the mechanical behaviour of thin films and surface layers of submicron thickness at

loads between 0.1 mN and 300 mN. The Berkovitch indenter is preferred because its geometry facilitates the measurements of hardness and elastic modulus, as well as the fact that the three-sided pyramid produces plasticity at low loads.

As the indenter penetrates the surface, the depth of the residual indentation is measured continuously during the process and the data can be plotted as a load-displacement curve (see Figure 3.2). The most common method for evaluation of hardness and elastic modulus was proposed by Oliver and Pharr in 1992 [92]. It is based on the analysis of the unloading process shown in Figure 3.3. The loading segment of the curve represents elastic, plastic and even phase transformation deformation mechanisms of the material while the unloading segment corresponds to elastic recovery for most materials [93].

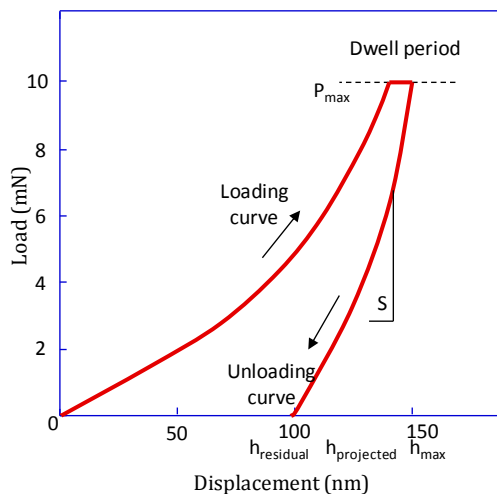


Figure 3.2 Typical load-displacement curve from a nano-indentation test [94].

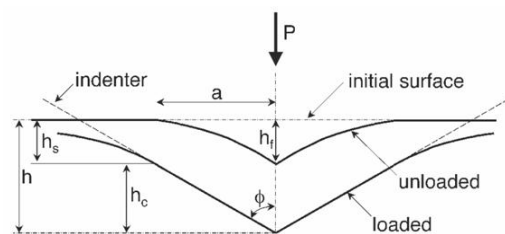


Figure 3.3 Schematic representation of the indentation process [95] where h_f is the plastic depth, h_c is the contact depth, h_s is the displacement of the surface at the perimeter of contact and a is the radius of the contact circle defined by the indenter.

A MTS Nano Indenter G200 was used for nanohardness studies of the precipitated phases and the matrix of as-received as well as tested HA230. The technique is suitable for the characterization of areas a couple of microns in radius; therefore some measurements were carried out to confirm the hardness of the 'pool-like' phase which developed in the microstructure (see Section 4.1.3). Some of the work was part of an MSc project performed by Song Zheng under the part-supervision of this author [96]. The specimens chosen for this study did not require any new surface preparation. Standard metallographic preparation guaranteed surface smoothness which is important for the software calculation of contact areas.

The hardness values of the phases being investigated are determined from the data recorded in Figure 3.2.

3.1.3 OPTICAL MICROSCOPY

Reflected Light Microscopy is suitable for the study of opaque specimens which cannot transmit light. Hence, it is often referred to as metallurgical microscopy. Because the light is unable to pass through the specimen, it must be directed vertically through the microscope objective lens and reflected back up from the surface of the specimen through the objective to an eyepiece, view screen or camera [97].

The initial microstructural evaluation of all specimens was performed using the Olympus Vanox BH-2 microscope, equipped with a video camera (Olympus DP70) connected to a computer for the acquisition of digital images.

3.1.4 SCANNING ELECTRON MICROSCOPY

The scanning electron microscope (SEM) is today a common instrument in various fields of science. The SEM allows the observation of many characteristics of a wide range of materials with the higher resolution than optical microscopy, on a nanometer to micrometer scale [98]. It permits the acquisition of three-dimensional-like images and the determination of many properties of the sample (composition, surface topography, etc.). The interaction of the electron beam with the sample produces different types of signals, *e.g.* secondary electrons, backscattered electrons, characteristic X-rays, and other photons of various energies. The SEM is complementary to the light microscope due to the large depth of field, better resolution, and capability to obtain detailed information from phases observed with an optical microscope.

Figure 3.4 shows a schematic diagram of the main components and the mode of operation of a simple SEM. Located at the top of the column is the electron gun, which contains a filament typically made of tungsten [99]. When the filament is heated, a beam of electrons is generated. The electrons are accelerated to energy usually between 1 to 30 keV. The beam is collimated by electromagnetic condenser lenses into a tight beam, focussed by an objective lens, and scanned over the surface of the sample in a rectangular set of straight lines known as a raster by scanning coils. The interaction of electrons with a specimen results in various secondary emissions from the surface. Figure 3.5 is a schematic diagram showing some of the signals generated from the interaction between the electron beam and the specimen which may be used in the SEM and the regions of electron penetration. Released secondary electrons from the sample are collected by a

secondary detector or a backscatter detector, converted to a voltage, and amplified. The system is under the vacuum of about 10^{-4} Pa.

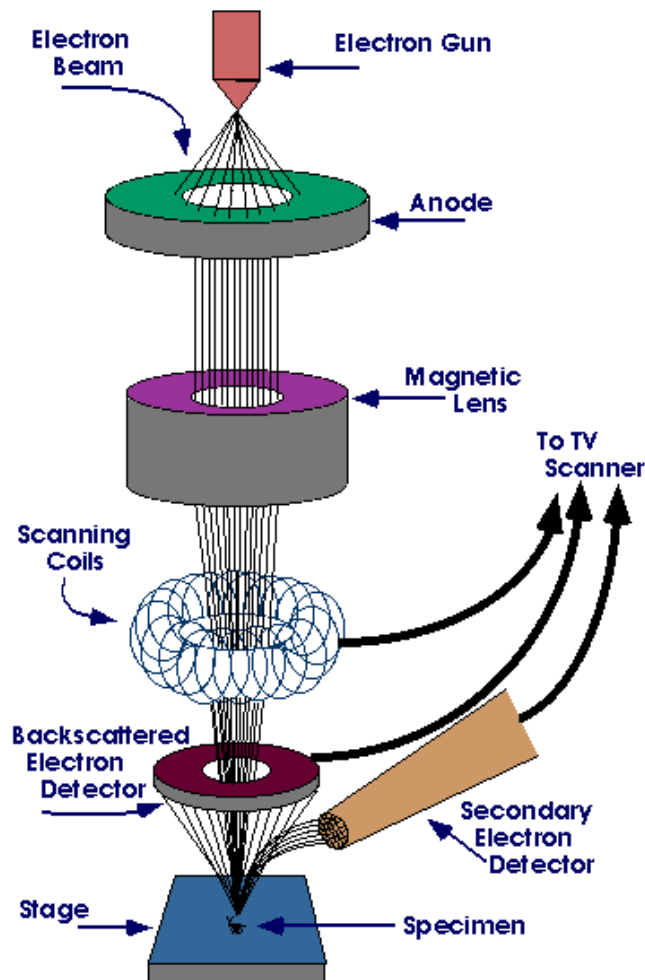


Figure 3.4 Schematic diagram of SEM [100].

Secondary electrons (SE) are emitted from the specimen with energies less than 50eV, and are primarily produced by the inelastic interactions between beam electrons and weakly bonded electrons in metals. An Everhart-Thornley (E-T) detector (with a positive charge) is used to convert the radiation into an electrical signal in most SEM's to generate an image representing surface topography of the sample. [98, 99]

Backscattered Electrons (BSE) are produced by the elastic interactions between the electron beam and nucleus of the atom. These electrons keep their velocity (travel in straight lines) and they come back out of the sample. The number of BSE increases with the increase of the atom number. Therefore the BSE

detector, which is located in the BSE path, can be used to obtain an image showing different elements (e.g. heavier elements will appear lighter). [98, 99]

In addition, contemporary electron microscopes are equipped with an Energy Dispersive X-ray (EDX) detector which allows for both quantitative and qualitative analysis of the specimen. Details are given in Section 3.1.5.

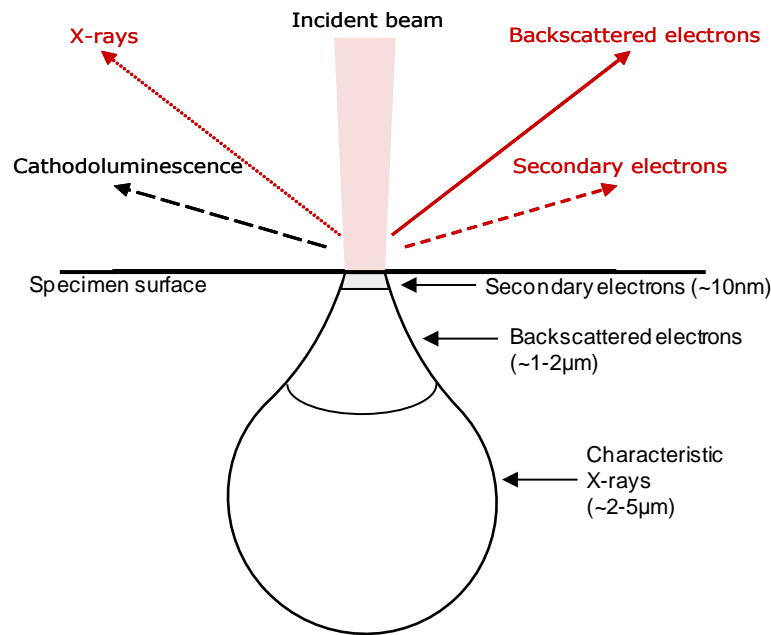


Figure 3.5 Electron beam interaction with sample in SEM and the regions of electron penetration (e.g.[99]).

In this project a Field Emission Gun Scanning Microscope (FEGSEM) - FEI Sirion 200 was used. In addition to ultra-high resolution imaging, it is equipped with an Energy Dispersive X-Ray (EDX) detector and Electron Backscattered Diffraction (EBSD) facilities.

A field emission gun (see Figure 3.6) consists of a sharply pointed tungsten tip and two anode plates placed below the gun assembly. The first anode is associated with the extraction voltage, usually in the range of 3-5 kV, which is necessary to draw electrons from the source, and the second anode with the accelerating voltage which determines the velocity at which the electrons travel down the column. Beyond the accelerating voltage the second factor that determines resolution in the SEM is the initial crossover diameter. To condense the electron beam both of these anodes are employed as electrostatic lenses.

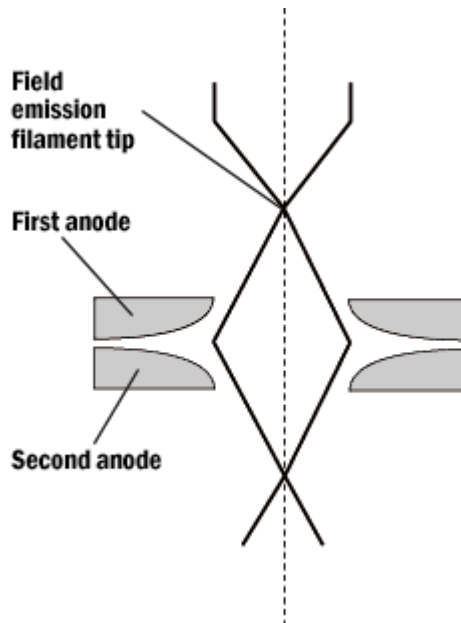


Figure 3.6 A simplified diagram of a field emission gun [101].

3.1.5 ENERGY DISPERSIVE X-RAY ANALYSIS (EDX)

Contemporary electron microscopes are regularly equipped with an Energy Dispersive X-ray (EDX) detector which enables both quantitative and qualitative analysis of the specimen to be obtained.

An EDX system consists of a sensitive X-ray detector, a liquid nitrogen vessel for cooling, and software to collect and analyze energy spectra [99]. The detector is held in the sample chamber as close to the specimen as possible to collect the maximum possible energy of incoming X-rays by ionization. The X-ray entering the detector is converted into an electrical signal of proportional size; the resulting electrical pulses are amplified, registered and can be presented as energy spectra. Every element is represented by characteristic X-ray spectrum. The detector is made of semiconducting silicon or germanium crystals that operate at low voltages to improve sensitivity. EDX system software analyzes the energy spectrum in order to determine the abundance of specific elements, and can create an element composition map showing the spatial distribution of elements in the sample.

In this work, a Princeton Gamma Technology Avalon EDX system was used.

3.1.6 TRANSMISSION ELECTRON MICROSCOPY

The transmission electron microscopy (TEM) is an analytical method which allows detailed examination of microstructure, crystal structures, chemical compositions and orientation of precipitates, through high-resolution imaging, diffraction pattern, and X-ray analysis.

The main disadvantages of TEM are the cost of the equipment, time consuming preparation of samples and destructive nature of this technique.

The transmission electron microscope uses electrons instead of light as a source because their shorter wavelength gives better resolution [102]. The source – the electron gun – at the top of the microscope emits electrons which travel through the vacuum in the column and are focused into a tight beam and directed by electromagnetic lenses and apertures. The unscattered electrons pass through an electron transparent sample and give an image on a fluorescent screen at the bottom of the microscope. This image can be recorded with a CCD camera linked to a computer. Figure 3.7 shows a diagram of the principal TEM features and compares the operation modes of rays.

The acceleration voltage of the latest TEMs is between 120 to 200 kV which defines the velocity and wavelength, and hence the resolution of the microscope.

The objective lens provides the formation of either the image or the diffraction pattern of the specimen [99]. Imaging mode uses the differences between intensities of the electrons after they have interacted with the sample. The contrast images are formed by means of an aperture. A Bright Field Image is created by the transmitted beam and a Dark Field Image by one of the diffracted beams which has travelled through the specimen and the microscope column. Interactions of charged electrons with the periodic crystal lattice are necessary to obtain a diffraction pattern. This provides information on the atomic positions. For usual applications a concept of Reciprocal Lattice, together with Ewald sphere construction, to describe the diffraction conditions is used and Bragg's Law (see Section 3.1.7) or Laue Conditions are adequate approximations. TEMs can produce different types of electron diffraction patterns: spot patterns, ring patterns, Kikuchi patterns, Selected Area Diffraction (SAD) Pattern, Convergent-Beam Electron Diffraction (CBED) Pattern.

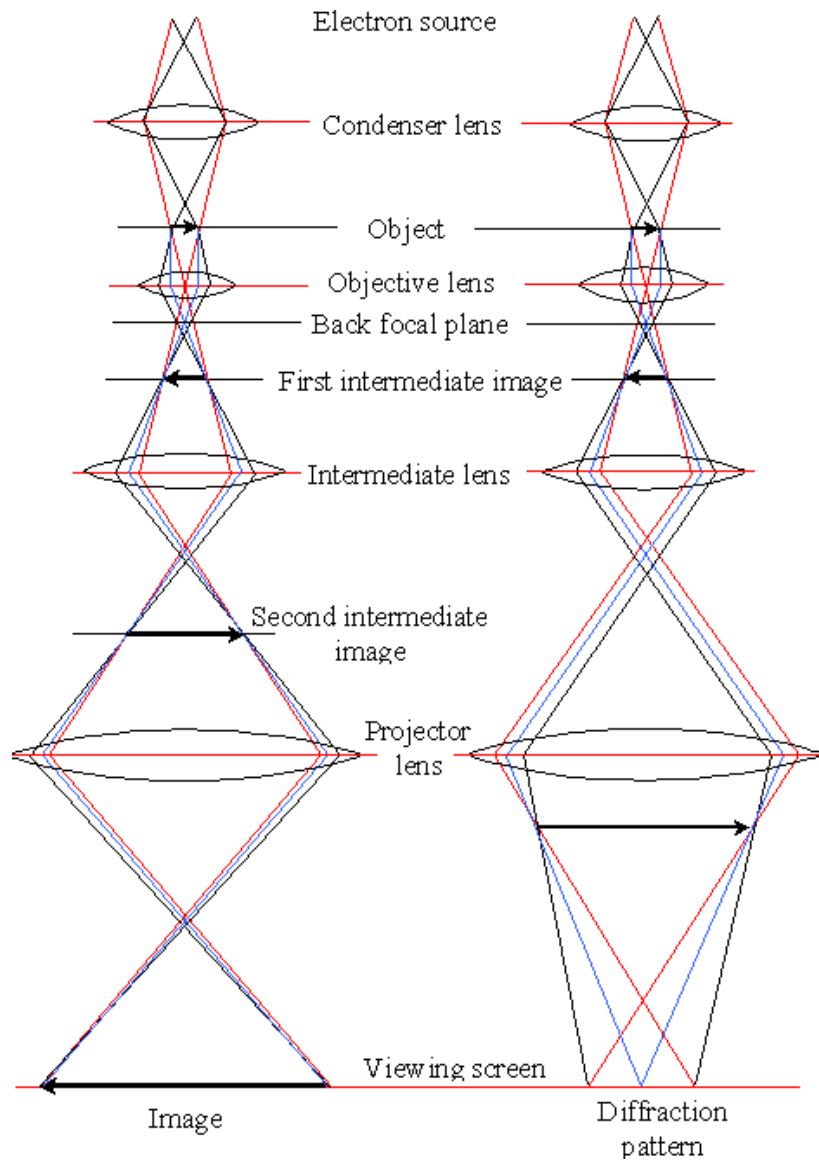


Figure 3.7 Schematic ray diagram of TEM [103].

X-rays generated through the interaction of the electron beam with the specimen can be used to determine the composition and identities of phases from their EDX spectra - see paragraph 3.1.5 above.

In this project the JEOL 2100 transmission electron microscope was used for preliminary analysis of as-received material. It allows the characterization of specimens with a magnification up to 1.5 million and lattice resolution of 0.1 nm [104].

3.1.7 BRAGG'S LAW

In 1912 W. L. Bragg presented his observations about reflections of X-rays of crystals at certain angles of incidence. The geometry of the Bragg condition is

remarkably simple as shown in Figure 3.8. When an incident X-ray beam meets a crystal lattice, scattering in random directions occurs [105]. The distance d between similar atomic planes in a crystal is called d-spacing (interatomic) and is measured in Ångström. The angle of diffraction is θ (theta) measured in degrees. The wavelength λ (lambda) represents the incident X-rays; a copper target is commonly used with $\lambda = 1.54 \text{ \AA}$.

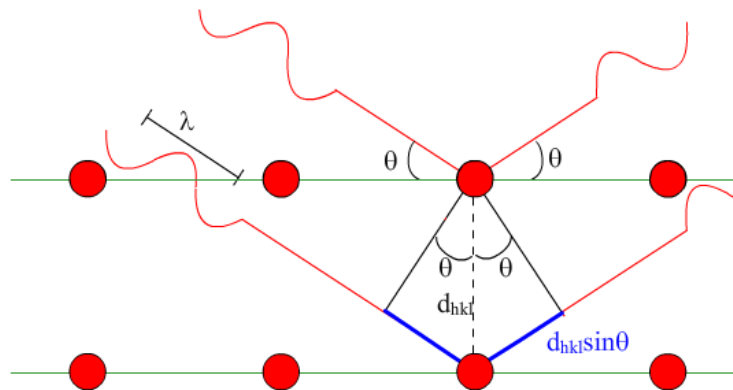


Figure 3.8 Illustration of Bragg's Law [106].

The relation of X-ray diffraction is expressed in Bragg's equation:

$$n\lambda = 2 d_{hkl} \sin \theta_{hkl} \quad \text{Equation 3.3}$$

where n is an integer representing 1,2, 3, etc. wavelength path differences, and index hkl indicates the standard Miller indices.

3.1.8 X-RAYS

X-rays are electromagnetic radiation with short wavelengths in the range of 0.1\AA to 100\AA . Because the wavelength of X-rays is similar to the size of atoms, they are suitable to investigate the crystal structures of many materials [107].

Generally, in the laboratory, characteristic X-rays are produced in an X-ray tube (see Figure 3.9) by bombardment of stationary or rotating solid matter by high speed electrons [108]. Figure 3.10 illustrates the process of emission of characteristic X-rays. The high energy electrons eject an electron from the inner shell of an atom by the ionization (1), the vacancy (2) is filled by an electron from an outer shell (3) and an X-ray photon with specific energy of the target material is emitted (4).

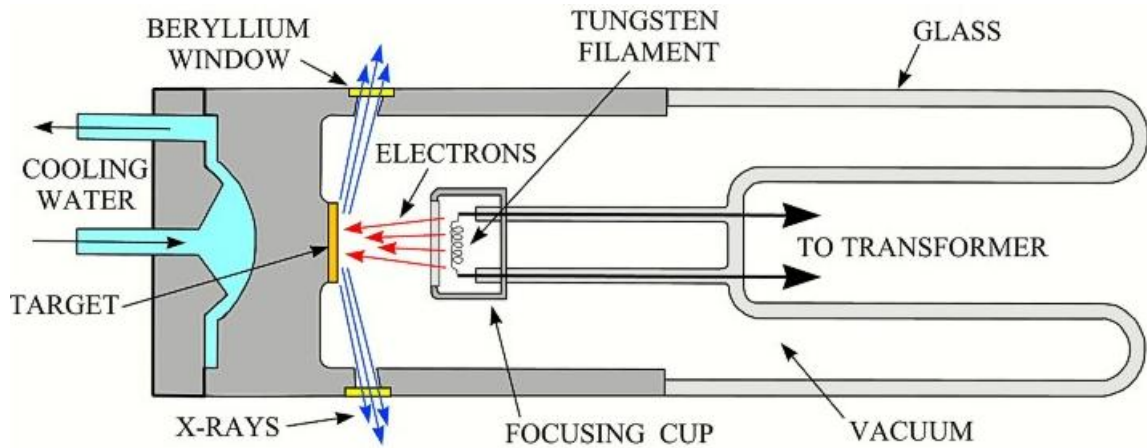


Figure 3.9 Schematic diagram showing X-ray tube [109].

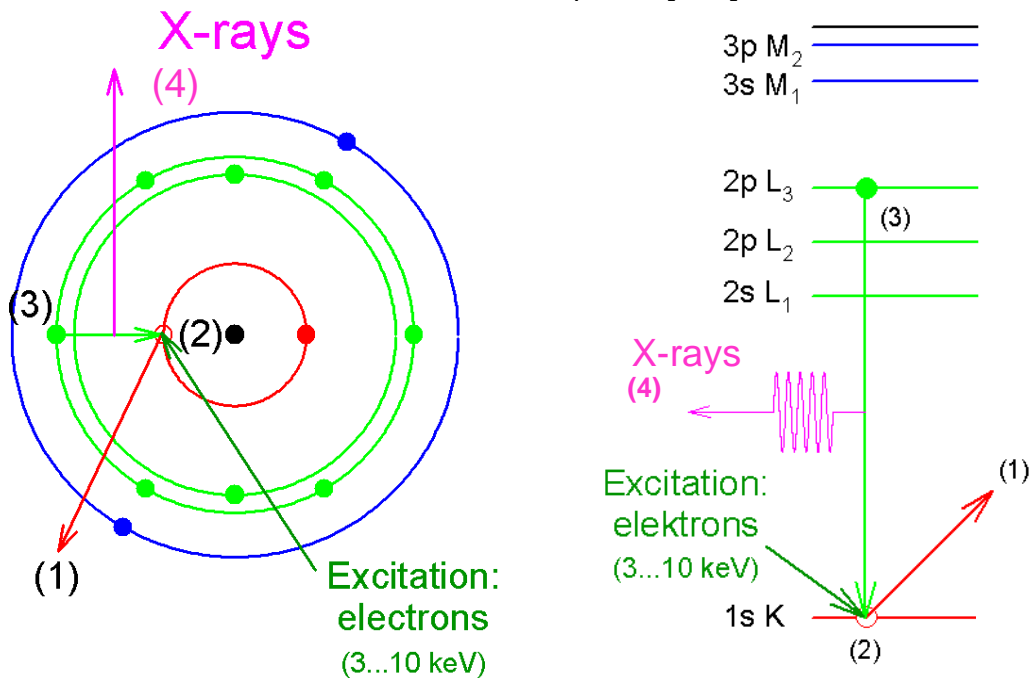


Figure 3.10 A schematic diagrams of emission of characteristic X-rays [110].

3.1.9 X-RAY DIFFRACTION (XRD)

X-ray powder diffraction (XRD) is a non-destructive technique used to identify crystalline material by its diffraction pattern.

X-ray diffractometers consist of three main components: an X-ray tube, a sample holder, and an X-ray detector (see Figure 3.11). X-rays are generated in a cathode ray tube (see Section 3.1.7), then collimated and directed onto the sample. A goniometer maintains the rotation of both the sample, in the path of the collimated X-rays, and the detector at an angle θ or 2θ respectively. The detector collects diffracted X-rays and their intensities, as a function of 2θ , are continuously recorded. Then solving the Bragg equation for the appropriate value of λ the d-spacing of each peak is obtained. Each material has a unique characteristic X-ray

spectrum pattern; therefore matching these d-spacing values enables an identification of the unknown material. Files of d-spacing values for hundreds of thousands of inorganic compounds are available from the International Centre for Diffraction Data (ICDD) as the Powder Diffraction File (PDF). [107, 108]

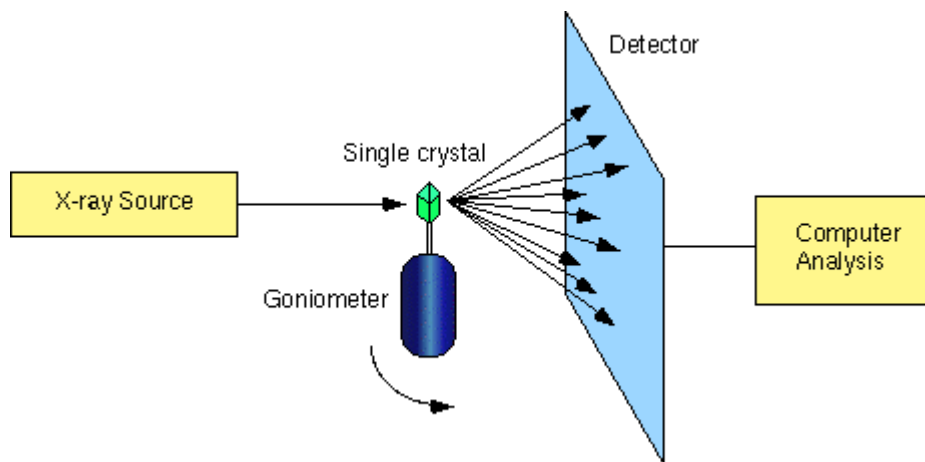


Figure 3.11 Schematic diagram of diffractometer [111].

In this project a Philips PW 1716 diffractometer with a current/voltage stabilised PW 1729 generator and a PW 1050/25 detector was used. The measurements were carried out at the Department of Geology (University of Leicester) by Dr Sarah Lee and Dr Cheryl Haidon. Some of the work was carried out with the author present on SIEMENS D500 diffractometer in CNR, Milan, Italy by Dr G. Angella as a part of COST Action 538.

3.1.10 FOCUSED ION BEAM (FIB)

The Focused Ion Beam (FIB) technique is used particularly for site-specific analysis, deposition, and ablation of materials [112]. Nowadays most instruments combine a SEM (electron) and FIB (ion) column, which allows imaging at higher magnifications and more accurate control during the milling process. Liquid gallium is predominantly used as a source of ions (Ga^+), which are then accelerated to energy of 5-50 keV, and focused onto the sample. Some sputtered atoms and molecules as well as secondary electrons and ions are generated out from the specimen surface after the collision. Optimization of beam currents provides either high imaging resolution or higher amount of material being removed (down to a sub micron scale).

Application: TEM sample preparation

FIB is a very useful tool in the preparation of TEM samples [113]. The nanometer-scale resolution of the FIB allows the precise location the area of interest on the specimen; therefore the exact region for thinning can be chosen. In this project two approaches have been tried.

1. In-situ lift out technique

Method for in-situ lift-out total release technique can be simplified into following successive steps [114] documented on Figure 3.12.

The selected region is plated with platinum. Rapid ion milling steps reveal the inner material, forming lamella. The lamella is then cut underneath and lifted out with a probe which has been fixed to the sample, usually by metal deposition. The sample is lifted-out and attached to an Omniprobe TEM sample holder, again, typically with ion beam-induced metal deposition. The probe tip is then detached using FIB milling. The final step is the thinning of the lamella to electron transparency again with FIB milling.

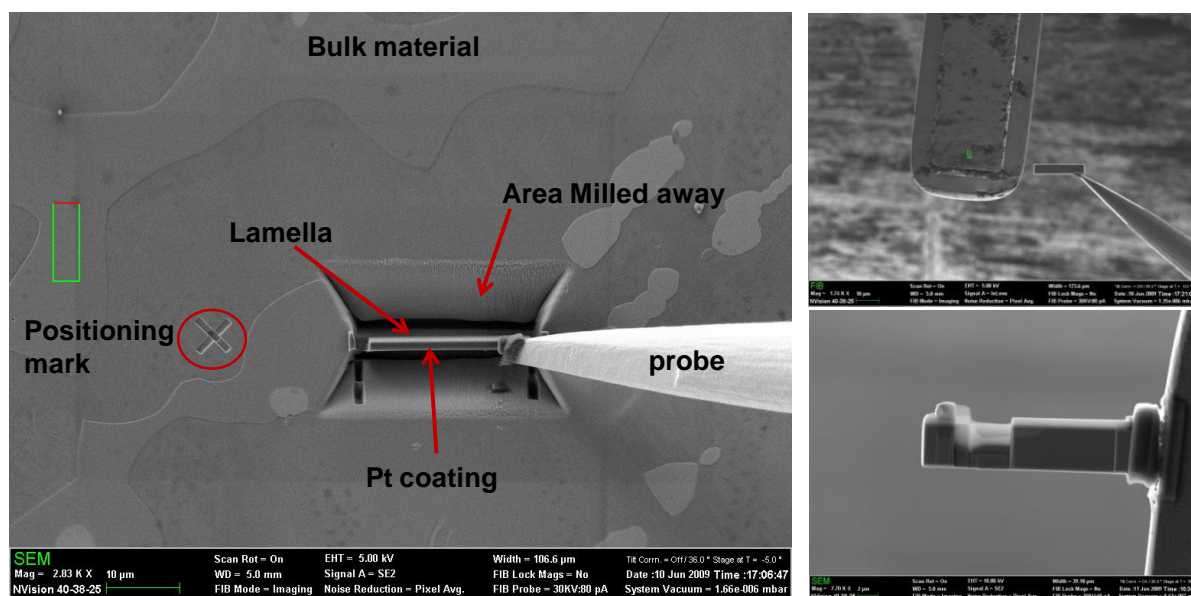


Figure 3.12 In-situ lift-out total release technique.

2. H-bar Technique

The thinned sample (approx. 2.5×1.0×0.5 mm) with fine polished upper surface is mounted on the TEM grid using epoxy glue [115, 116] (see Figure 3.13). Then the specimen is milled in the area of interest from both sides until electron transparency is achieved. There are many advantages in using this technique, e.g. several thinned areas on the

same sample can be prepared, a selection of a specific plane, and the handling is less complicated than in the previous technique.

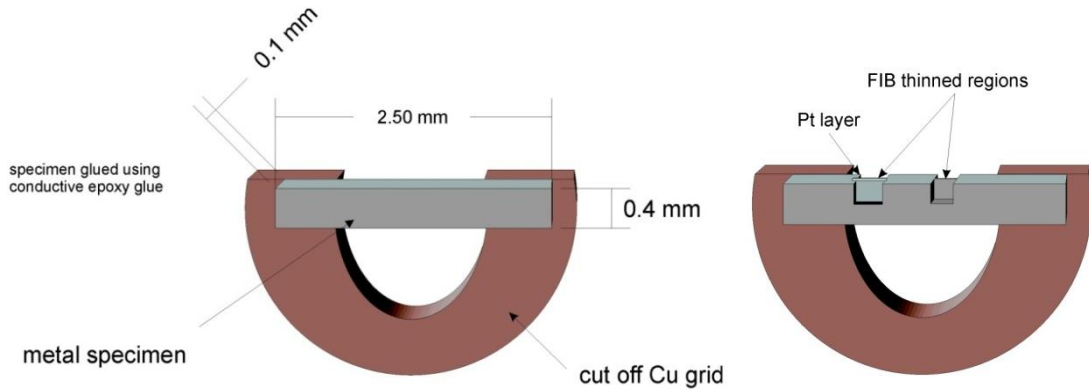


Figure 3.13 Schematic of the process to make a TEM sample – H-bar.

Both techniques were presented/offered by Dr G. Hughes at Materials, University of Oxford, UK under the EPSRC Equipment access scheme and two TEM specimens (see Figure 3.12 and Figure 3.14) were prepared on Zeiss NVision 40 FIB-SEM equipped with a Kleindiek micromanipulator.

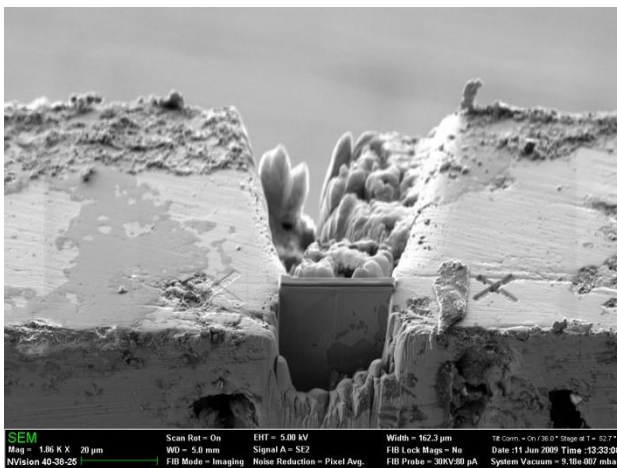


Figure 3.14 The edge milling on the H-bar specimen.

3.1.11 ELECTRON PROBE MICROANALYSIS (EPMA)

Electron Probe MicroAnalysis (EPMA) is a technique capable of producing chemical analyses of small areas at the surface of polished solid samples [117]. It is fundamentally the same as an SEM. A fine focused beam of electrons (1-2 microns) bombards the surface of the sample generating X-rays whose wavelengths

(or energies) are characteristic of the elements present in the sample. The intensities of the X-rays are a measure of the proportions of the elements present which may be quantified by reference to the X-ray intensities of those emitted from standards.

The Electron Microprobe in the Department of Geology (University of Leicester) is a JEOL 8600 S automated instrument. The wavelength-dispersive system (WDS) comprises three crystal spectrometers which allow highly sensitive quantitative analysis of elements from fluorine upwards in the Periodic Table.

3.1.12 INDUCTIVELY COUPLED PLASMA - OPTICAL EMISSION SPECTROMETRY (ICP-OES)

Inductively Coupled Plasma Optical Emission Spectrometry is a technique ideally suited for determining the concentration of a wide range of major and trace elements in solution in a single, short integration period [118]. The liquid sample is atomized into a stream of argon gas, and directed inside the argon plasma flame. The excited elements emit photons which are detected and the light intensity of this emission is proportional to the concentration of the element. Detection limits are low for most elements (typically <10ppm).

A JY Ultima 2 ICP-OES was used in this project. Ms Lin Marvin (Department of Geology, University of Leicester) has assisted with the final sample preparation. The supernatant liquid from the bulk extraction (Section 3.4) has been diluted according to the element concentrations for the analysis: Ni and Cr 1000 times, other elements 100 times.

3.1.13 TENSILE TESTING

Tensile tests provide information on the strength and ductility of materials under uniaxial tensile stresses [88]. Machines used for tensile testing apply uniaxial stresses to the specimen, and the resulting elongation is measured until fracture occurs. This provides a stress-strain curve, from which information on the strength and ductility of the material can be calculated. A typical stress-strain graph for a ductile metal is shown in Figure 3.15.

Grips are used to transmit the measured force applied by the testing machine to the test specimen. Various types of grips are available, depending on the application, ranging from wedge grips to self-adjusting grips.

Depending on the equipment, material properties and material shape, specimens should be specifically designed for each tensile test arrangement. For example, a typical specimen design for plate-type material, along with key dimensional factors, is shown in Figure 3.16.

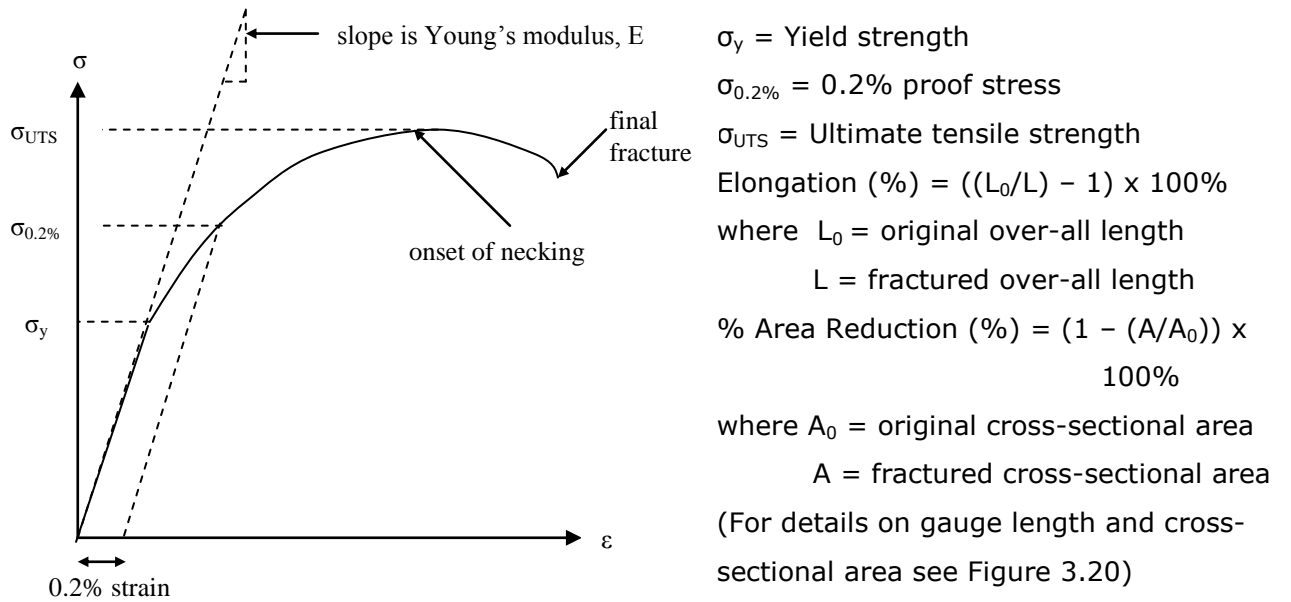


Figure 3.15 Typical stress-strain curve for a ductile metal, along with the appropriate calculation for the information on the strength and ductility of the material [119].

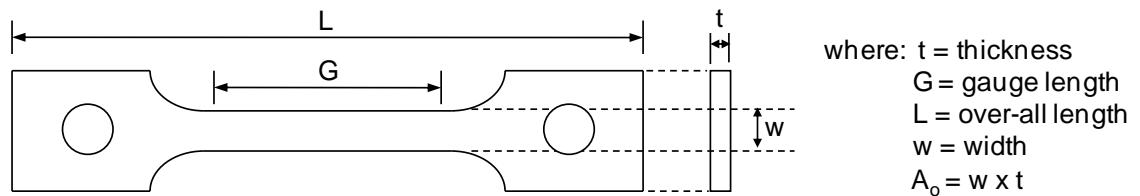


Figure 3.16 Tensile specimen [120].

3.2 MATERIAL CHARACTERIZATION

A single heat of HA230 (No 8305-5-7170) supplied in the form of 2 mm thick sheet in the solution treated and quenched condition to AMS 5878 by Haynes International Ltd was provided by Siemens (SITL) for testing. Comparisons of the test certificate and AMS 5878 specified values for the chemical composition, heat treatment and mechanical properties for this heat indicate that the material met the requirements of the specification - Tables 3.1 and 3.2.

Table 3.1 Chemical Analysis of as supplied material provided by Haynes Intl., (weight %).

Heat	Ni	Cr	W	Mo	Fe	Co	Mn	Si	Al	C	La	B
8305 -5- 7170	Bal	21.75	13.96	1.32	1.40	0.37	0.49	0.36	0.29	0.12	0.013	0.004
AMS 5878	Bal	20.0 <i>to</i> 24.0	13.0 <i>to</i> 15.0	1.0 <i>to</i> 3.0	3.00 <i>max</i>	5.00 <i>max</i>	0.30 <i>to</i> 1.00	0.25 <i>to</i> 0.75	0.20 <i>to</i> 0.50	0.05 <i>to</i> 0.15	0.005 <i>to</i> 0.05	0.015 <i>max</i>

Table 3.2 Heat Treatment and Mechanical Properties

Properties	Test Certificate	Specification
	Heat no 8305-5-7170	AMS 5878
Heat Treatment	Solution annealed at 1230°C and quenched	Solution treat between 1177°C and 1246°C and cool rapidly
0.2% Yield Strength	448 MPa	345 MPa min
UTS	859 MPa	793 MPa min
% Elongation	45	40 min
Rupture life at 927°C and 69MPa	50 hrs	36 hrs min
% Elongation	34	10 min
ASTM Grain Size	5.5	3 max

3.3 EXPERIMENTAL PROCEDURE

3.3.1 SPECIMENS

Three types of specimens plus the as-received solution annealed material were investigated; the thermally exposed specimens (81 samples), the creep tested specimens (22 samples) and miniature tensile tested specimens (18 x 3 samples), see Figure 3.17. All the specimens were cut from the same heat of HA230 sheet

(No 8305-5-7170) and aged at SITL. The full list of the tested material with the values obtained for hardness testing is in Table 9.1 (Appendices).

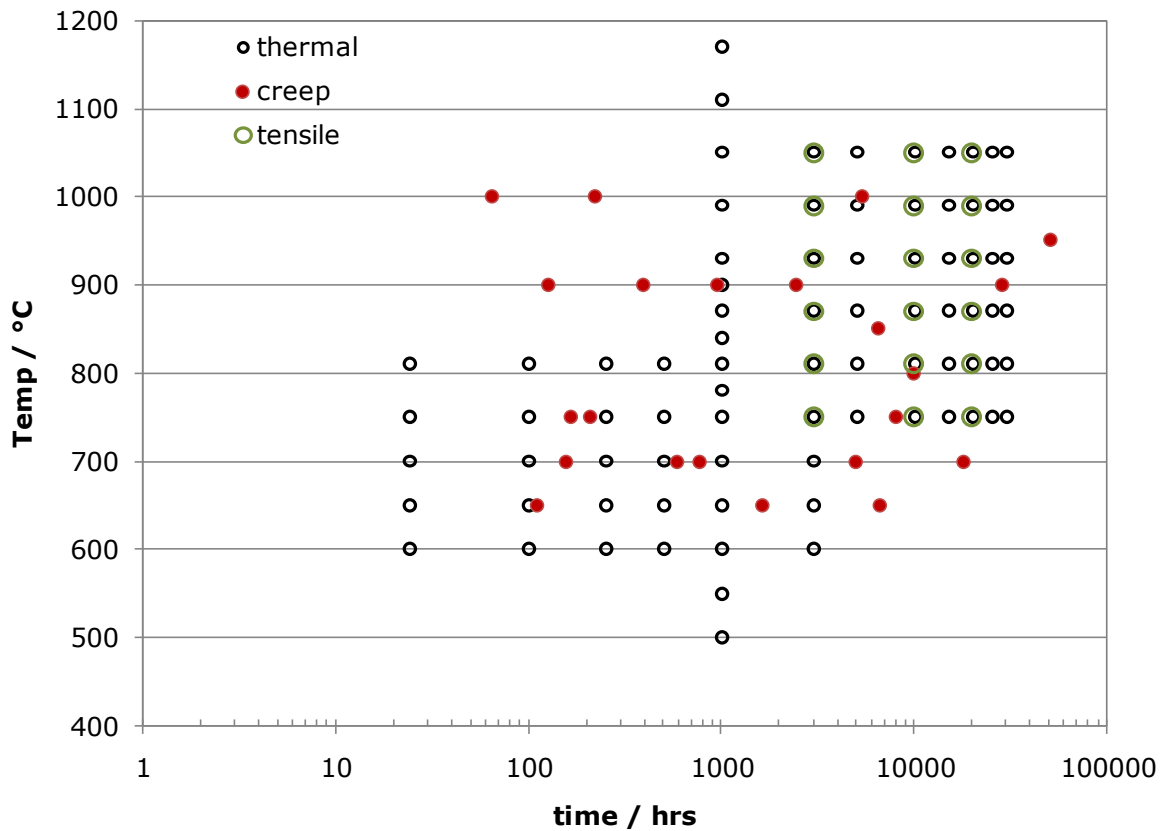


Figure 3.17 Review of HA230 tested specimens.

THERMALLY EXPOSED SPECIMENS

Coupons (30mm x 30mm approximately) were isothermally aged in air in furnaces under various temperatures between 500°C to 1170°C for up to 30000 hours (see Figure 3.18).

CREEP TESTED SPECIMENS

The specimens for the creep tests were cut from the as-received solution annealed material in the rolling direction following the ASTM standards for the dimensions (see Figure 3.18). 22 creep tests were carried out by Siemens in Lincoln at temperatures in the range from 650°C to 1000°C for up to 51000 hours.

MINIATURE TENSILE SPECIMENS

Material for tensile test has undergone isothermal heat treatment for 3000, 10000 and 20000 hours at six different temperatures between 750°C to 1050°C. Then the specimens were milled out, further details will be given in Section 3.5.

3.3.2 METALLOGRAPHIC PREPARATION

During the process of metallographic preparation care must be taken to ensure that the area of interest has not been affected. The standard metallographic technique for HA230 was found to be inadequate to obtain specimen surface of very good quality. Attention was therefore concentrated on improving the grinding and polishing steps. Further an idea of only one preparation procedure for more techniques is going to be discussed.

Two microsections were spark eroded from each sample; one parallel and one transverse to the direction of rolling or one from the unstressed head of the fractured piece and one from the gauge length (see Figure 3.18).

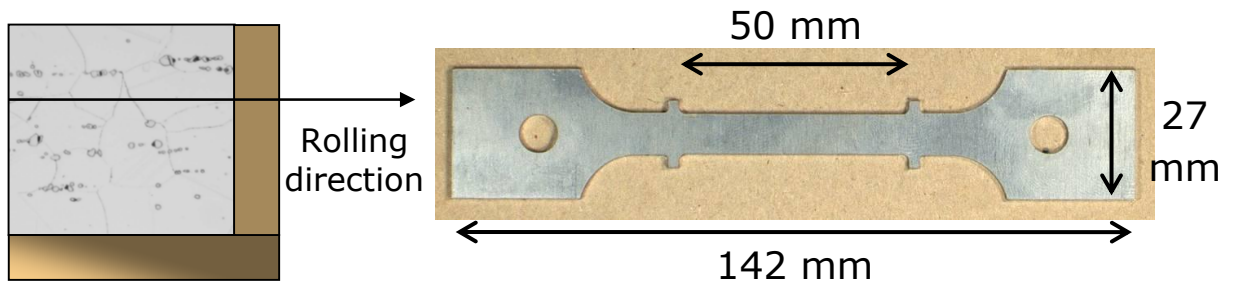


Figure 3.18 Thermally exposed and creep tested specimen showing the direction of rolling. Two microsections were cut from each specimen; one parallel and one transverse to the direction of rolling.

The microsections were hot mounted at 180 °C and 15KN using an automatic mounting press, Struers LaboPress-3, and electrically conducting phenolic resin (Multifast, or the combination of Durofast and Multifast), following instructions provided by the supplier [121].

Mounted specimens were ground with rotating discs of abrasive paper (*e.g.* silicon carbide paper) on the Buehler Metaserv Motopol 8 Grinder-Polisher. This procedure (see Table 3.3) was used as a standard surface preparation for **Vickers hardness testing** (*i.e.* hardness testing was carried out in the ground surface condition).

Table 3.3 Standard grinding procedure for Vickers hardness testing.

stage	silicon carbide paper grade	duration (min)	force lbf (N)	wheel speed (r/min)	coolant
1	240	2	12 (45)	150	water
2	400	1	10 (40)	150	water
3	600	1	10 (40)	150	water

Several studies have been focused on the effect of parameters on the precision and accuracy of the hardness measurements [122-124]. In this study the load time was 15sec, loading speed 50 $\mu\text{m}/\text{sec}$, using the load of 20kg. At least 20 measurements lengthwise along the centre, 2mm apart, were performed on each sample. Microhardness testing was performed at 25g or 50g and at loading time 15 sec. The technique still gives an error about 10%.

Both **Microscopy techniques**, Optical and Scanning Electron imaging, require the microstructural features to be revealed. Therefore surface polishing and etching is necessary.

The 'general' metallographic preparation procedures for nickel-based or similar alloys were not of sufficient quality to produce a smooth surface without any preparation artefacts. The author approached Struers Ltd. and Haynes Intl. to obtain a recommendation to refine the metallographic technique. The first preparation procedure (shown in Table 3.4) was provided by Dr Vinay Deodeshmukh from Haynes Intl, and is used as a general and standard procedure for preparation of Hastelloy and Haynes alloys. The procedure is similar to that previously used and does not meet the requirements. A new preparation procedure was developed in Struers Ltd. as a result of the authors approach and the steps are shown in Table 3.5 which guarantees the true structure without any scratches, excessive pull-outs or artefacts from preparation, and reproducibility. In addition only 7 steps are needed. A thorough cleaning afterwards (soapy water followed by alcohol) is necessary. The procedure in Table 3.5 was used to prepare several sets of the specimens with the TegraSystem (Struers).

Table 3.4 Metallographic preparation of HA230 specimens suggested by Haynes Intl.

		Force	Time
Grinding	SiC Paper 220	low pressure	short
	SiC Paper 400	low pressure	short
	SiC Paper 600	low pressure	short
Fine grinding	SiC Paper 800	low pressure	long
	SiC Paper 1200	low pressure	long
Polishing	Pan-W 9 μm	high pressure	
	Pan-W 3 μm	high pressure	
	Pan-W 1 μm	high pressure	
Oxide polishing	colloidal silica	0.02 μm	

Table 3.5 Metallographic preparation of HA230 specimens suggested by Struers Ltd.

		Force (N) / Ø 40mm	Time (min)
Grinding	SiC Paper 220	30	<1 min
Fine grinding	SiC Paper 800	30	<1 min
	SiC Paper 1200	30	<1 min
	SiC Paper 2400	30	<1 min
Polishing	MD-Plus + AP-A 5µm	30	4 mins
	MD-Plus + AP-D 1µm	30	3 mins
Oxide polishing	MD-Plus + OP-AN 0.02µm	30	2 mins

Electrolytic etching was used to reveal grain and annealing boundaries, and precipitated phases in this alloy. It was difficult to obtain a uniformly etched surface using a solution of 5g of oxalic acid and 95ml of hydrochloric acid using a voltage of 6V recommended by Haynes Intl.. A second solution of 20ml of hydrofluoric acid, 40ml of Glycerol and plus 340ml of H₂O using a voltage of 3V proved to be much more suitable; it was important to avoid over-etching. After etching the specimens were immediately washed in alcohol and dried.

3.3.3 PREPARATION OF TEM SPECIMENS

Specimen preparation for **Transmission Electron Microscopy** is a complex process [125]. Many different approaches were attempted to obtain a TEM specimen which is electron transparent, contains the representative information about the material and does not obtain artefacts from the preparation.

It was decided to start with the preparation of thin foils and not carbon replicas as the HA230 contains large carbides within the microstructure which are difficult to extract. Regrettably these large and hard carbides caused difficulties during the thinning process in any case so the only option was to utilize the Focused Ion Beam technique. A TEM thin foil has to be about 100-300nm thick to get sufficient transparency for the electrons to form both images and diffraction patterns. The following approaches were examined:

1. Thin sheet thickness was mechanically reduced with SiC papers to about 150 µm. Using the Gatan punching machine the maximum number of discs with a diameter of 3mm were punched, then each disc was ground again to smooth the surface and the edges (Gatan disc grinder) and to obtain a highly polished surface with the final thickness of the disc about

60 to 100 μm . The discs were either a) electropolished or b) dimple ground and then ion beam polished to perforation.

- a) **The electropolishing technique** (e.g. [126]) is favourable in the high rate of the final thinning, but the difficulty is in the control of the optimum conditions. Electropolishing was carried using a Fischione (Model 110) automatic twin-jet electropolisher. A broad range of parameters was tried but none of them gave an optimum TEM sample. Satisfactory results were achieved with a solution of 5% of perchloric acid and 95% of acetic acid at 13-15°C and a voltage of between 50-60V [127]. Some of the electron transparent specimens were also obtained with a solution of 10% perchloric acid, 35% butylglycol and 55% methanol at -30°C and 30V [128], and with 10% of perchloric acid and 90% of ethanol at -40°C and 20V [129].
- b) **Dimple grinding** quickly reduces material thickness and thus reduces the time necessary for final thinning to electron transparency but may introduce mechanical damage. Some of the discs were thinned using the Gatan Dimple Grinder down to 10 μm approximately.

Ion Milling is designed to produce high quality TEM specimens having exceptionally large, clean and electron transparent areas and is used to finalize the thinning process. In the Gatan Precision Ion Beam Polishing System (PIPS) Argon gas is ionized and accelerated toward the rotating disc. Ions sputter the material off without any selectivity. Difficulties were encountered with ion milling. In the majority of the samples, on the bombarded surface, an artefactual 'ripple' pattern was created and/or the specimens were still very thick in the region close to the perforation. The following parameters were set in collaboration with CNR IENI Milan (It) [128] (COST Action 538 program): Double Modulation setting, the rotation of specimen was at the minimum rate, the angles of incidence were changed in 20 minutes intervals, decreasing the angle by 1° from 8° to 4° using a voltage of 4.5 KeV, finally to 2° angle at 3KeV. Optimization was required for every sample.

2. FIB-preparation

a) In-situ lift out

A specimen thermally exposed for 15000 hours at 1050°C has not needed special preparation, had adequate condition for metallographic observation, only the height of the mount was reduced to 6 mm.

b) H-bar specimen

A thin foil (disc) of the creep tested specimen COD (60 μm thick) was cut in half and its cut surface was manually polished using 5 and 1 micron lapping discs. The prepared half of the thin foil was epoxy glued on a Cu grid.

It has to be concluded that despite many attempts both Ion Beam Milling and electropolishing techniques have not proved satisfactory and to obtain better results, *i.e.* the representative large electron transparent area, it was necessary to combine both approaches. The technique providing best results was the Focused Ion Beam.

3.4 XRD

3.4.1 BULK MATERIAL

In the case of as-received material, the samples were cut out of the original (2mm thick) sheet of HA230 with a size to fit the XRD holder, *i.e.* 10mm x 15mm. In the case of thermally exposed specimens, the rest of the coupon (without microsections, see Figure 3.18) was used and adjusted to fit the holder. Sequentially the surfaces of the XRD coupons were ground off by about 0.5 mm from both sides, to get the resulting thickness of about 1mm, the maximum depth of the coupon to fit the holder. The coupons were ground from both sides in the same way to obtain the microstructure in the middle of the sheet (see Figure 3.19). Then standard metallographic techniques were used to prepare a smooth and shiny surface, which then, immediately after XRD, could be used for EBSD analyses.

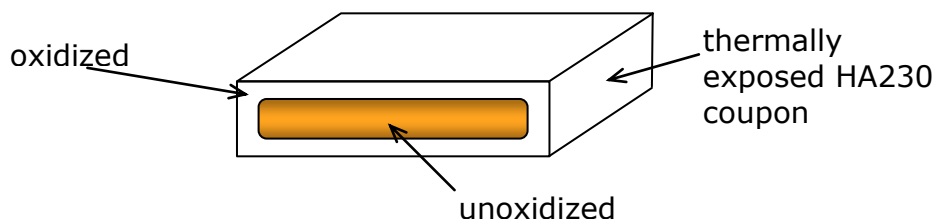


Figure 3.19 Schematic representation of cross-section through thermally exposed HA230.

3.4.2 PHASE EXTRACTION

The chemical extraction of phases from the bulk HA230 material was carried out at the Department of Chemistry under the supervision of Mr M. Lee. To obtain whole picture about the phase transformation, tested tensile specimens have been selected. These specimens have been thermally exposed for 3000 and 20000 hours at six different temperatures (750°C, 810°C, 870°C, 930°C, 990°C and 1050°C). In addition one as-received specimen and a piece from the transition duct were tested. The detailed procedure is presented in the Appendices 9.8.1.

Firstly, the oxide layer was removed from the specimen surface using SiC papers and the material milled to produce fine chippings. During the milling process of the specimens, attention was paid to avoid contamination of the resulting chippings. A known amount of the chippings was dissolved in a 10% bromine + ethanol solution. The residue was washed, centrifuged and dried in an oven at 90°C. The dry powder was provided for X-ray diffraction and the elemental composition was obtained by ICP-OES from the residual supernatant liquid.

3.5 TENSILE TESTS

The tensile testing was performed at room temperature on the 3000, 10000, and 20000 hours thermally exposed specimens. The specimens were exposed at six different temperatures (750°C, 810°C, 870°C, 930°C, 990°C, and 1050°C) for all three exposure times. The heat treated specimens were cut into the form shown in Figure 3.20 below, using a milling machine.

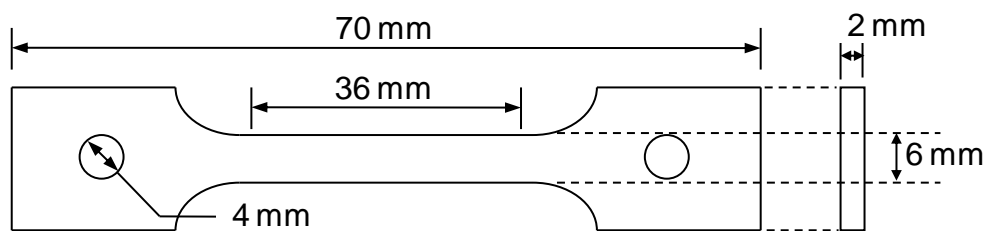


Figure 3.20 Design of the tensile specimen.

Due to the small dimensions of the samples, high toughness and relatively low hardness of the material, the focus was on the development of an effective gripping technique, to prevent slippage of the specimens before yielding. The slippage problem has been encountered during the undergraduate project by Jairath [130]. Initially the specimen was fixed in the grips by a metal pin, see Figure 3.21a. The similar grip configuration was designed for this project, see

Figure 3.22, but other difficulties occurred; thus this set of grips has not been used. After much development and testing, Jairath chose a grub screw configuration to clamp the specimens into place, see Figure 3.21b. Some preliminary testing on HA230 was performed using the grips with grub screws, but the slipping occurred on the specimens. To fasten the grips more and to fix the specimen better inside the jaws, a new design was proposed by Mr Forryan and myself. A new set of grips with a slot for a tensile specimen inside the jaws was fabricated, see Figure 3.23. This gripping configuration was used for all the HA230 tensile tests.

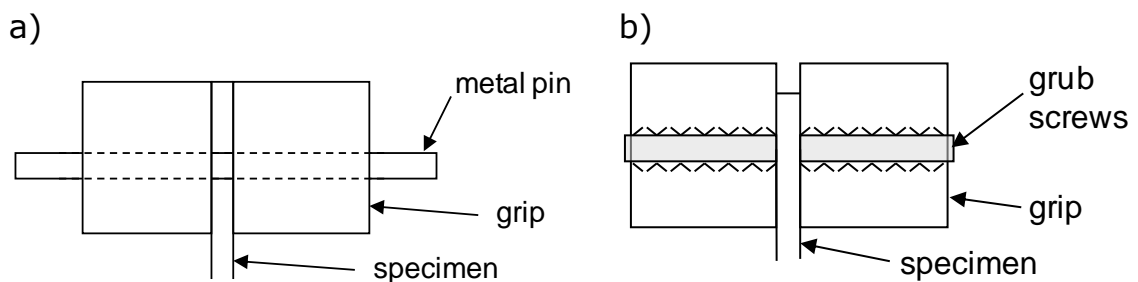


Figure 3.21 Illustration of a) grips with a pin, and b) grips with grub screws.

Tensile tests were performed in an 810 MTS TestStar tensile testing machine, which is controlled digitally through an MTS remote controller connected to a computer, giving the capability to produce accurate force-displacement graphs. The elongation of the tested specimens was measured using an LVDT.

Three sets of tests for each temperature and duration were performed. On some test samples slip still occurred and this has been eliminated by preloading of the machine.

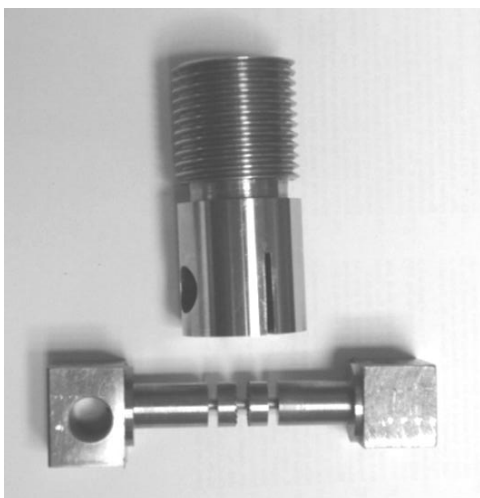


Figure 3.22 Grips with a pin for HA230

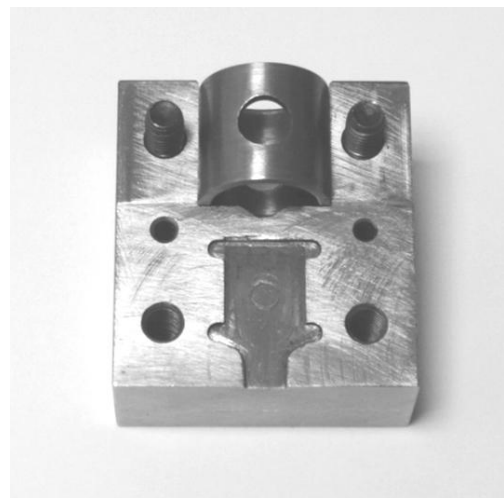


Figure 3.23 Grips with a slot for HA230.

4 EXPERIMENTAL RESULTS

This chapter presents all the results, which have been obtained during PhD project. The results are offered in successive steps following the experimental techniques progress. It is important to have in mind that the work was complex and the results from every single technique must be correlated between each other. This chapter includes initial appraisal of results so that Chapter 6 is very much summative Discussion.

Before the beginning of this project some preliminary work has been carried out by Professor A. Strang and Mr G. Clark which included mainly the samples exposed at the lowest temperatures and short duration (see Appendices Figure 9.2). These results are included here because they form an important part of the data. The results have been obtained on the same equipment.

4.1 VICKERS HARDNESS TESTS

4.1.1 HARDNESS RESULTS

Vickers hardness tests have been carried out at a load of 20kg on the as-received material, on the thermally exposed coupons and on the creep specimens of HA230 in the temperature range from 500°C to 1170°C and after 24-30000 hours of exposure with exceptions of one creep tested sample up to 50874 hours. In the case of the creep specimens, hardness tests have been conducted on microsections taken from the unstrained heads. The hardness values for thermally exposed samples are listed in Table 4.1, a detailed table can be found in Table 9.1 (Appendices), and those obtained for the heads of the creep specimens are listed in Table 4.2. There were at least 20 impressions made on a single sample lengthwise along the centre and the average and the standard deviation values were calculated. The average hardness value of as-received unexposed material was 218 ± 2 Vickers.

The hardness testing provided useful information about the behaviour of the alloy with increasing exposure time and temperature. Figure 4.1 shows a traditional representation of the hardness variation with time. The specimens exposed at 750°C demonstrate stable behaviour with only a small fall obtained for 30000 hours. For the rest of the exposure temperatures the primary drop in hardness occurs after 1000 hours and then for longer exposures the hardness stays rather

stable. The lowest values were obtained for 990°C. In the case of 1050°C the hardness is increasing with exposure time.

Table 4.1 Summary of hardness results on thermally exposed HA230 specimens.

Exposure Temperature °C	Exposure Duration - Hours											
	24	100	250	500	1000	3000	5000	10000	15000	20000	25000	30000
500					218.2							
550					217.9							
600	222.5	221.8	226.3	231.6	244.7	243.4						
650	223.8	244.6	243.2	248.3	250.4	248.3						
700	247.6	248.9	246.7	245	247.7	247.8						
750	240.1	241.3	243.3	239.3	244.5	244.3	243.9	243.4	242.7	242.9	242.3	238.1
780					239.3							
810	239.8	242.1	242.4	236	239.2	233.7	232.1	225.5	226.3	223.3	225	225.3
840					233.6							
870					226.5	216.1	214.5	215.4	217.6	219.6	219.5	216.8
900					218.7							
930					215.6	208.9	210.2	212.0	213.2	216.1	214.8	212.8
990					210.4	207.0	207.4	207.5	212.0	211.0	213.2	209.4
1050					210.5	209.9	212.8	213.6	215.5	214.5	216.9	218
1110					215.1							
1170					203.3							

Table 4.2 Hardness results obtained on the heads of the creep tested specimens.

Creep Test	Temperature °C	Test duration Hrs	Hardness Hv20	LMP P=T(20+logt)/1000
DKZ	650	110.1	237.8 ± 3.64	20.34
DKY	650	1637.5	245.8 ± 1.67	21.43
DKX	650	6576.5	248.4 ± 2.62	21.98
DLA	700	18159.5	246.6 ± 1.58	23.60
DLB	700	4995.0	243.0 ± 2.51	23.06
DLC	700	582.5	241.8 ± 2.48	22.15
DLD	700	156.5	239.5 ± 3.46	21.60
ELM	700	761.0	239.5 ± 2.34	22.26
12722	750	206.3	248.3 ± 2.64	22.83
12784	750	164.9	243.3 ± 2.43	22.73
DLE*	750	8059.0	235.5 ± 1.31	24.46
DLF*	800	9907.0	228.7 ± 2.65	25.75
DLG*	850	6549.0	218.5 ± 2.27	26.75
CNZ	900	124.6	227.9 ± 2.42	25.92
COA	900	389.1	217.5 ± 0.71	26.50
COB	900	951.0	215.4 ± 1.64	26.95
COC	900	2415.5	212.9 ± 3.41	27.43
DLH	900	28775.8	216.5 ± 5.05	28.69
COD	950	50874.0	215.1 ± 1.21	30.22
COE	1000	64.0	210.8 ± 3.19	27.76
COF	1000	221.0	214.1 ± 3.21	28.44
COG	1000	5365.9	208.8 ± 2.66	30.21

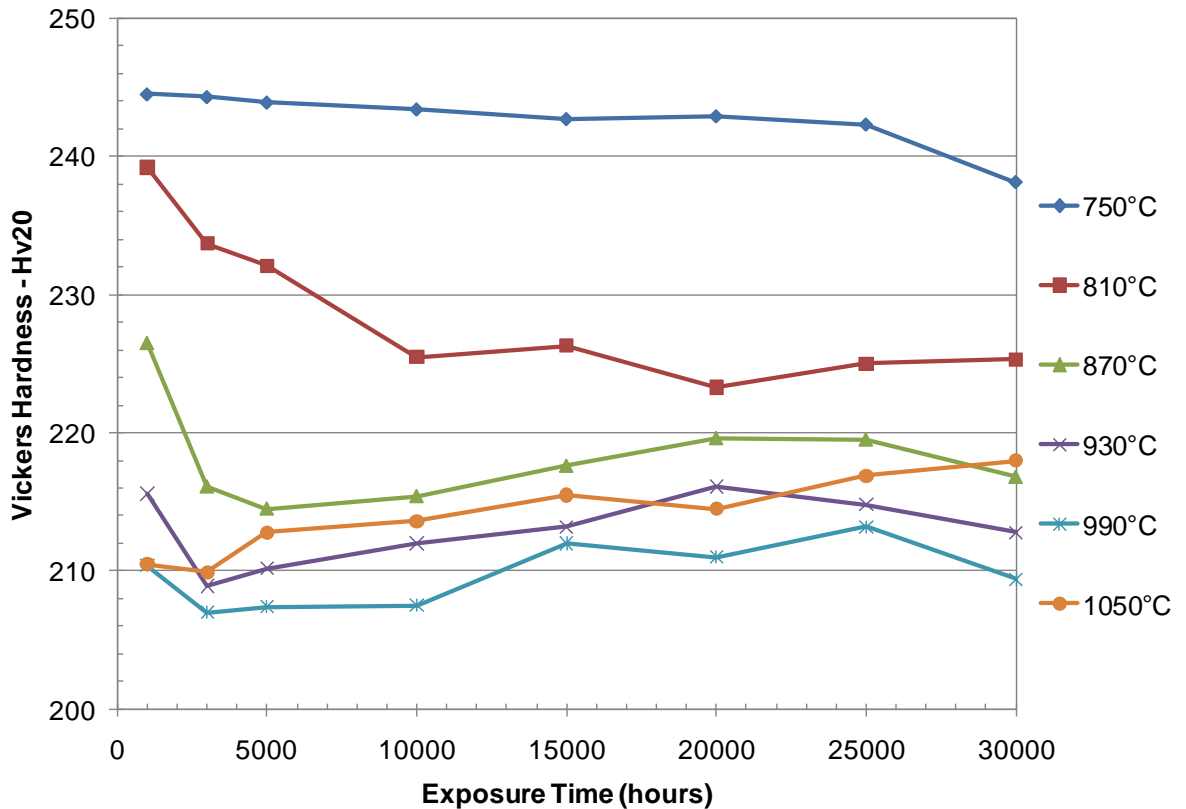


Figure 4.1 Variation of hardness with exposure time for temperatures in the range 750°C -1050°C (Table 4.1).

The relative effects of exposure temperature and duration of thermally exposed samples for six main temperatures is shown in the form of percentage changes in hardness relative to that of the material in the as-received solution annealed condition in Figure 4.2. All the curves have a similar trend. The data curves indicate that following an initial hardening period, re-softening of the alloy occurs reaching its original hardness level (0% hardness change), e.g. at a temperature of about 915°C for 1000 hours duration of exposure, of about 850°C for 10000 hours exposure and of about 900°C for 20000 hours exposure. All curves reach a minimum at a temperature of about 990°C. With additional increase of temperature the material hardens again; the most distinct rise was observed for the specimen exposed for 30000 hours. In addition, the data plotted in Figure 4.2 shows that the initial increase in hardness must occur at exposure times and temperatures less than 1000 hours and 750°C.

4.1.2 MASTER CURVE

One of the aims of this project was to create a Master Curve of Hardness vs. Larson-Miller Parameter (LMP, see Section 9.1) as a first step in evaluation (estimation of average operating temperature (Section 9.1.1)) of ex-service components. The LMP is a physically based time-temperature parameter widely

used also for presentation of the picture of the data. In this work it was used for an illustration of the hardness data variation with time and temperature.

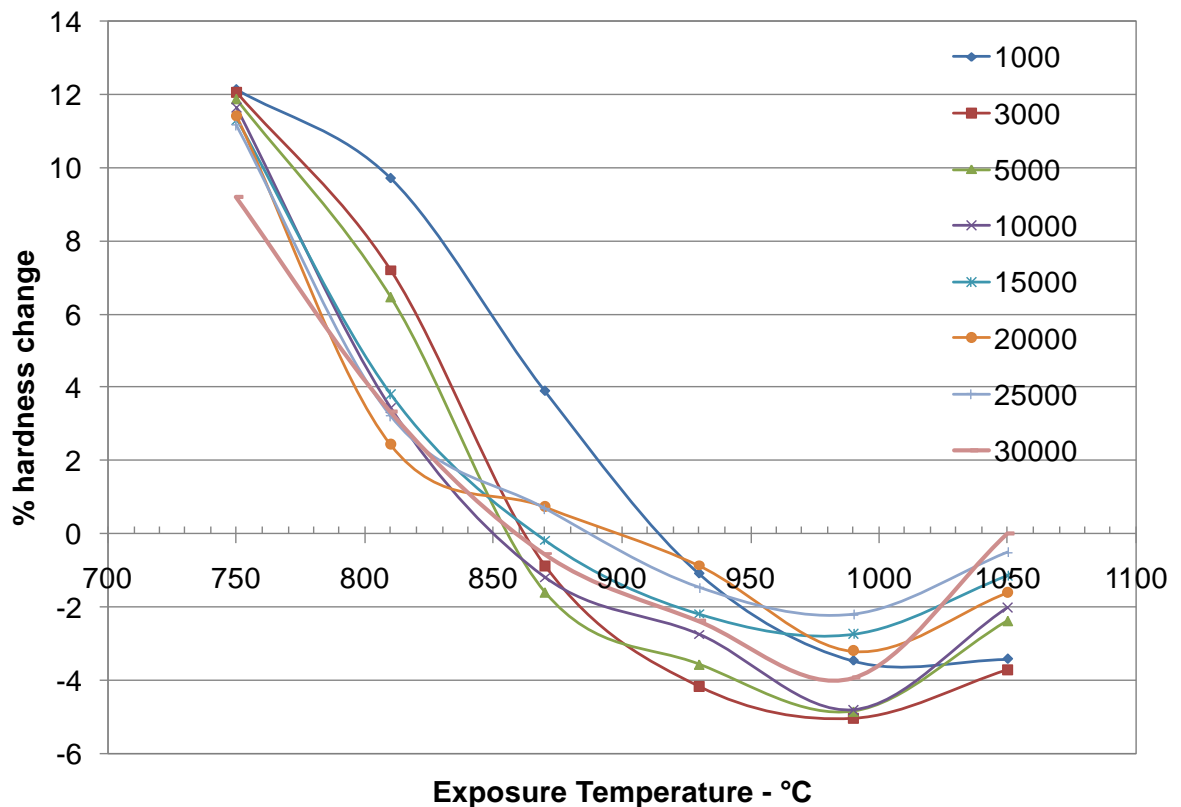


Figure 4.2 Effect of exposure temperature and duration (hours) on the % change in hardness relative to that of HA230 in the as-received solution annealed condition.

The hardness values are shown in the form of a parametric Larson–Miller plot (see Figure 4.3 and Figure 4.4), using a C-value of 20 for the Larson-Miller constant (see Appendices 9.1). The results indicate that systematic changes in the hardness of the HA230 occur with increasing temperature and exposure duration following the same trends for both thermally exposed test coupons of the alloy and unstressed areas in the creep specimen heads.

As is evident from Figure 4.3, the data curve indicates that material initially hardens from the original solution annealed value of 218 Vickers to a peak value of about 246 Vickers and $LMP=22$, then re-softening of the alloy occurs reaching its original hardness value at LMP equal to 27.5 approximately. All the curves reach a minimum at a temperature of about 990°C. The minimum value was of about 208 Vickers and $LMP=30$. With additional increase of temperature the material hardens again. The maximum hardness value was obtained for the specimen thermally exposed for 1000 hours at 750°C and the minimum value after exposure of 3000 hours at 990°C.

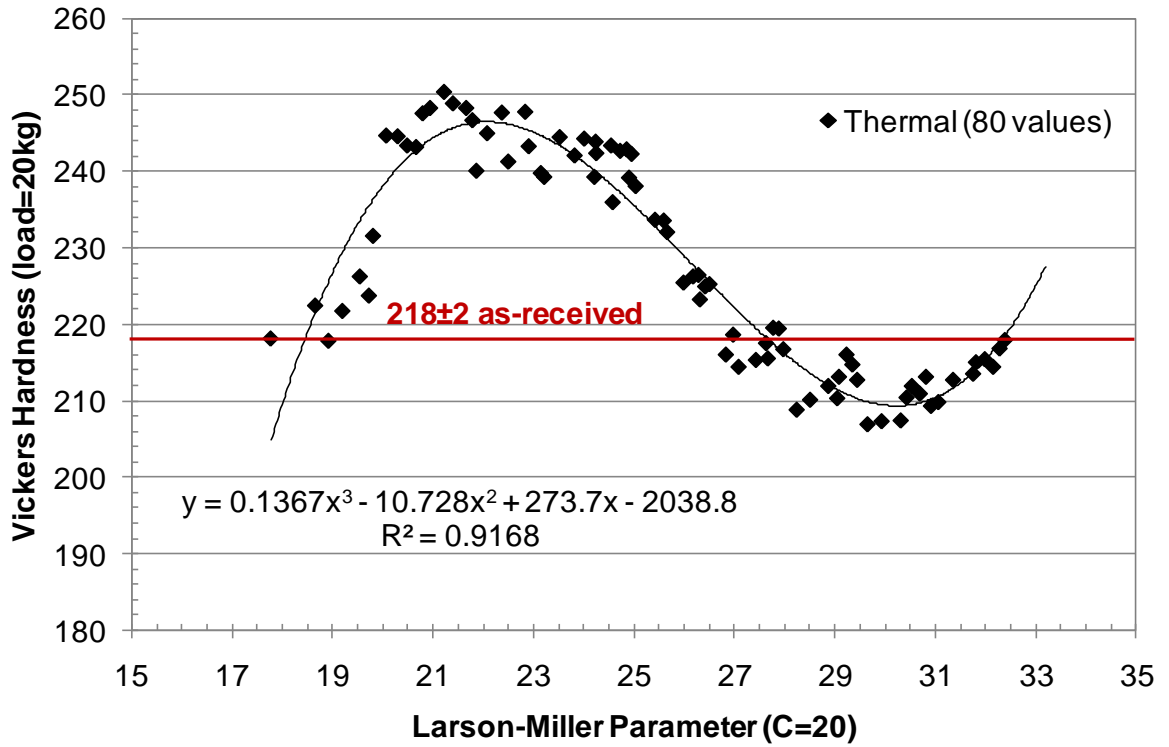


Figure 4.3 Hardness data for HA230 thermally exposed coupons (Table 4.1).

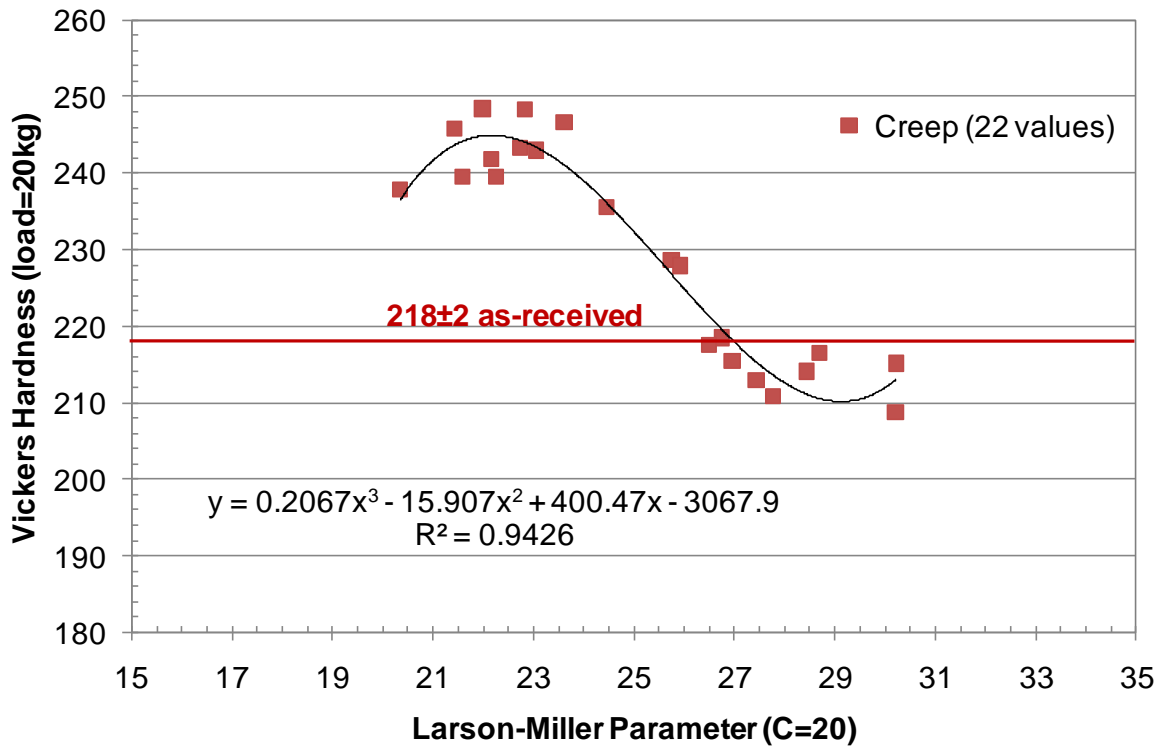


Figure 4.4 Hardness data for HA230 samples from unstrained regions in the heads of the creep specimens tested in the range 650°C -1000°C (Table 4.2).

The hardness data of the unstrained heads follow the same trend as the data of the thermally exposed specimens, Figure 4.4. As before, the initial increase in

hardness is followed by re-softening with the maximum value of approximately 250 Vickers corresponding to a Larson-Miller parameter value of 22.0 and a minimum value of approximately 209 Vickers and LMP=30.2.

The results indicate that systematic changes in the hardness of the HA230 occur with increasing temperature and exposure duration, following the same trends for both thermally exposed test coupons of the alloy and unstressed areas in the creep specimen heads.

To analyse hardness data a least squares regression analysis was used. A good fit for the data set plotted in the parametric shown in Figure 4.3 and Figure 4.4 is obtained using a cubic polynomial of the form:

$$Hv = aP^3 + bP^2 + cP + d \quad \text{Equation 4.1}$$

where a , b , c , and d are constants, Hv is a hardness value and P is the Larson-Miller parameter defined as $P = (273 + T)(20 + \log t)/1000$. Table 4.3 shows regression constants and R^2 value for hardness data obtained in the project.

Table 4.3 Regression constants and values for HA230 hardness data.

Exposure Data	values of regression constants and R^2				
	a	b	c	d	R^2
Thermal exposure	0.137	-10.73	273.7	-2038.8	0.917
Creep heads	0.207	-15.91	400.5	-3067.9	0.943
Combined data	0.137	-10.75	273.66	-2034.6	0.914

On the basis of these analyses and the proximity of the hardness values acquired as is shown in previous figures, it was thought that the data from the thermal and creep exposure tests can be combined for the purposes of analysis to produce a single Master Curve for hardness v Larson-Miller parameter for this alloy. Prior to this it was necessary to perform several calculations.

Firstly, assuming that the values of the unstressed creep heads are shifted by a few degrees of Celsius (see Section 9.3), the calculations of the new Larson-Miller parameter values have been done. This did not have a significant effect on the regression parameters maybe because all values were found within the error range of hardness testing (10%).

In spite of the previous calculations, some laboratory testing has been carried out. The CNR IENI laboratory in Milan has provided the corrections on the temperature of the head part of the creep specimens at 800°C (see Section 9.3).

The calculations of the new Larson-Miller parameter have been made and again no significant effect was observed.

In the next stage of work we considered the statistical difference between two sets of hardness data. For detailed information see Section 4.3. The statistical analysis offered the possibility to combine both sets, although there might be flaws in this approach, *e.g.* the different sizes of the two populations, the different ranges of data in the two populations. Hence a single Master Curve was produced (see Figure 4.5).

The plot combining hardness data for thermally exposed specimens and creep tested samples against the Larson-Miller parameter is shown Figure 4.5. Similar trend can be seen as in single set plots. Maximum values are between 21 to 23 LMP (Larson-Miller Parameter) which corresponds to the temperatures in the range of 650°C -750°C. Minimum values were obtained for 990°C and 3, 5 and 10 thousand hours exposures, corresponding to 29-30 LMP. Using a C value of 20 for LMP gives the best fit with a R² value of 0.914

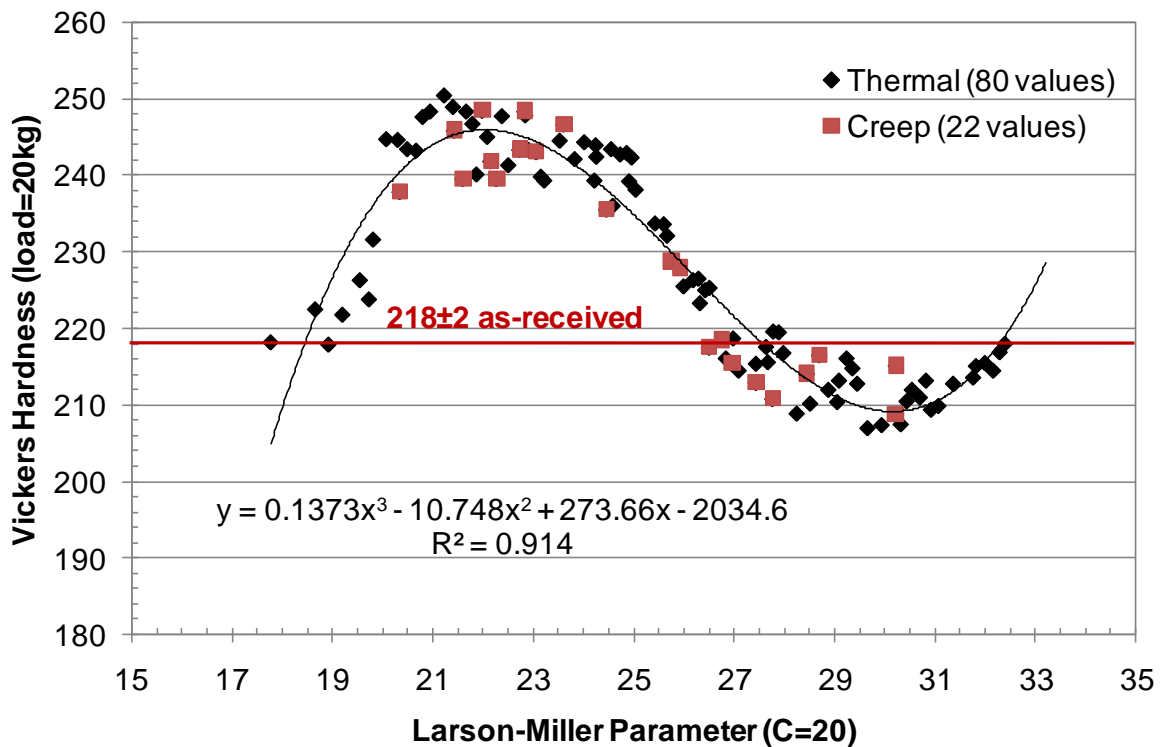


Figure 4.5 Hardness data for HA230 samples combining results from thermally exposed specimens (Table 4.1) with those for unstrained regions in the heads of the creep specimens (Table 4.2) tested in the range 500°C - 1110°C.

The statistical analysis also included an investigation of the optimum C value (LMP constant) for this work. The optimum value for the combined hardness values (thermally exposed and creep tested specimens) was 22.2, but any value between 17.8 and 28.7 would provide good fit within the 95% confidence interval. The convention value of 20 is within this range.

The hardness testing was carried out on HA230 as-received material provided from different batch of the material to have additional information for comparison. The average hardness value was obtained from 40 measurements carried out on two microsections of as-received unexposed HA230. The mean value of hardness of 216 was calculated with the standard deviation of ± 3 .

4.1.3 MICROHARDNESS STUDIES

Microhardness studies were initiated to obtain more information about individual phases, mainly the 'pool-like' phase appearing at higher temperatures. The real intention here was to obtain values which could be compared with those in the literature. For the study two phases were selected because of their reasonably large dimension in the microstructure. These were the gamma matrix and Cr-rich 'pool-like' phase.

The microhardness was studied on the sample thermally exposed for 15000 hours at 1050°C and on the gauge length of two creep tested specimens, COD, tested for 50874 hours at 950°C, and COG, tested for 5366 hours at 1000°C. These specimens were chosen because they contain 'pool-like' precipitates. In the case of thermally exposed specimen these precipitates were observed as forming clusters within the microstructure (see Figure 4.6). In the case of the creep tested specimens the 'pool-like' precipitates form a network shown in Figure 4.7. This phase appears on specimens thermally exposed at more than 990°C and long durations of exposure and on creep tested specimens after 950°C. Table 4.4 lists the test conditions for each sample.

Table 4.4 List of the microhardness test conditions for single samples.

Specimen	Phase	Test loads (gf)		Number of indentations	
Thermal	'pool-like' phase	25	50	6	11
	Matrix	25	50	3	6
Creep	'pool-like' phase		50		15
	Matrix		50		9

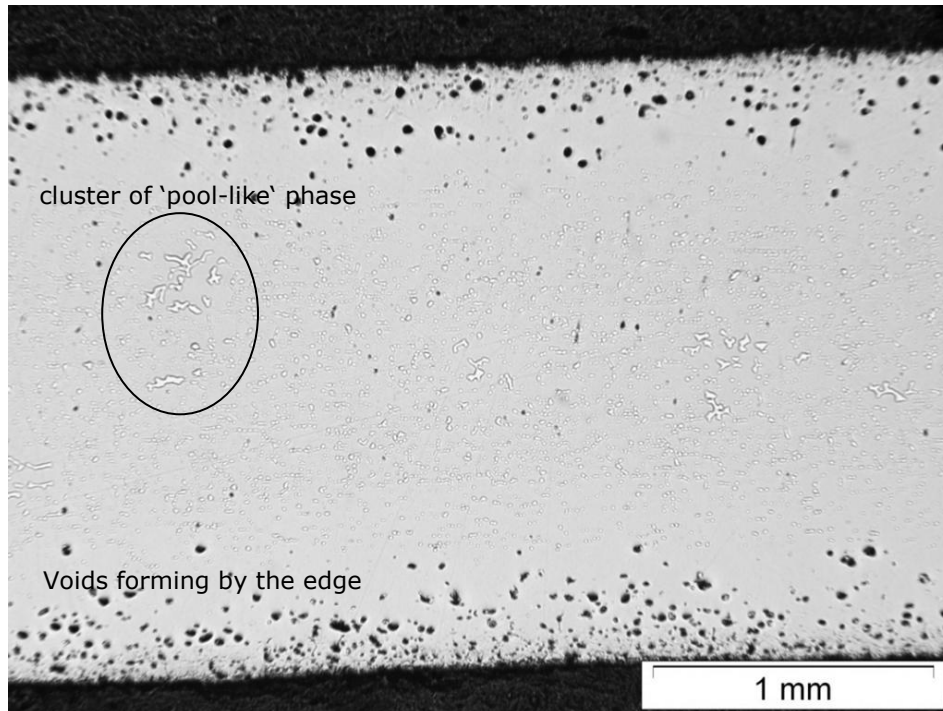


Figure 4.6 The defocused microstructure of thermally exposed specimen for 15000 hours at 1050°C showing the clusters of the large chromium rich precipitates.

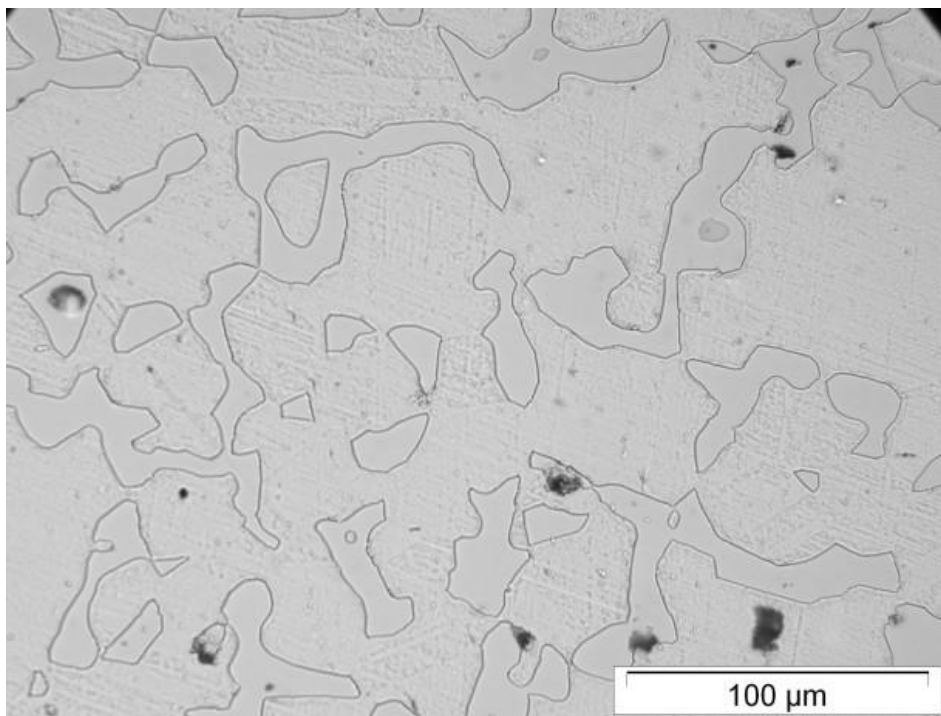


Figure 4.7 The microstructure of the gauge length of the creep specimen COD tested for 50874 hours at 950°C showing the network of coarse Cr-rich precipitates.

The microhardness tests were carried out at a load of 25g and/or 50g according to the expected size of the indentation on the specific phase, and the

loading time was 15s. Even though the 'pool-like' precipitates are large in size (see figures above), it was problematic to centre the indenter accurately in the middle of this phase to obtain the representative impression. Sometimes the impression hits the edge of the phase or is deformed by the effect of the surrounding microstructure. Then the value is completely different from the hardness value perfectly located on the phase or on the matrix. Also it is important to say that the impressions were very small, and that it was rather difficult to measure their dimensions through the microhardness tester eyepiece. It would be more accurate to use the FEGSEM (see Figure 4.8), but then the technique would be more complicated. The comparison and the review of all microhardness values are summarised in Appendices 9.4.

The mean microhardness value of the matrix for thermally exposed specimen for the load of 25 g was 184 Vickers, and for the load of 50g 190 ± 16 Vickers. For the creep tested specimen COG the mean matrix hardness was calculated to be 176 ± 18 Vickers and for specimen COD 174 ± 15 Vickers.

The average microhardness value of 'pool-like' precipitates obtained for thermally exposed specimen for the load of 25g was 653 ± 52 , 735 ± 142 Vickers respectively for the load of 50g. The mean hardness values for the creep specimens at 50g load are 647 ± 120 Vickers (COD) and 698 ± 159 Vickers (COG). The error is very big so it is not easy to say why the values for lower load and for the creep specimens are lower. The number of measurements, from this point of view, is not representative. Furthermore the microimpressions made by the load of 25g are so tiny that every micrometre difference in the size plays a great role in determining the corresponding Vickers hardness number therefore the values could not be accurate.

From the results above it can be seen that two sources of error were encountered. The first one is the sampling error, where the number of impressions is not large enough to obtain meaningful values. The second one is associated with the accuracy of measurements through the eyepiece of microhardness tester.

Latest results show that the difference between the final Vickers hardness values increases with decreasing size of the microimpression. The average microhardness value of 'pool-like' precipitates obtained for thermally exposed specimen measured by eyepiece of hardness tester was 730 Vickers, in comparison with 1200 Vickers obtained by measuring the impressions in FEGSEM (see Appendices 9.4). It should be emphasised that both the hardness tester and the

FEGSEM have been carefully calibrated with a graticule. To conclude, measuring microimpressions has to be more accurate using FEGSEM, where the tips of the diamond impression could be seen more precisely.

Figure 4.8 shows two measurements of microhardness impressions obtained in the FEGSEM. The fact that there are cracks related to the hardness of imprint indicates that the phase is very brittle.

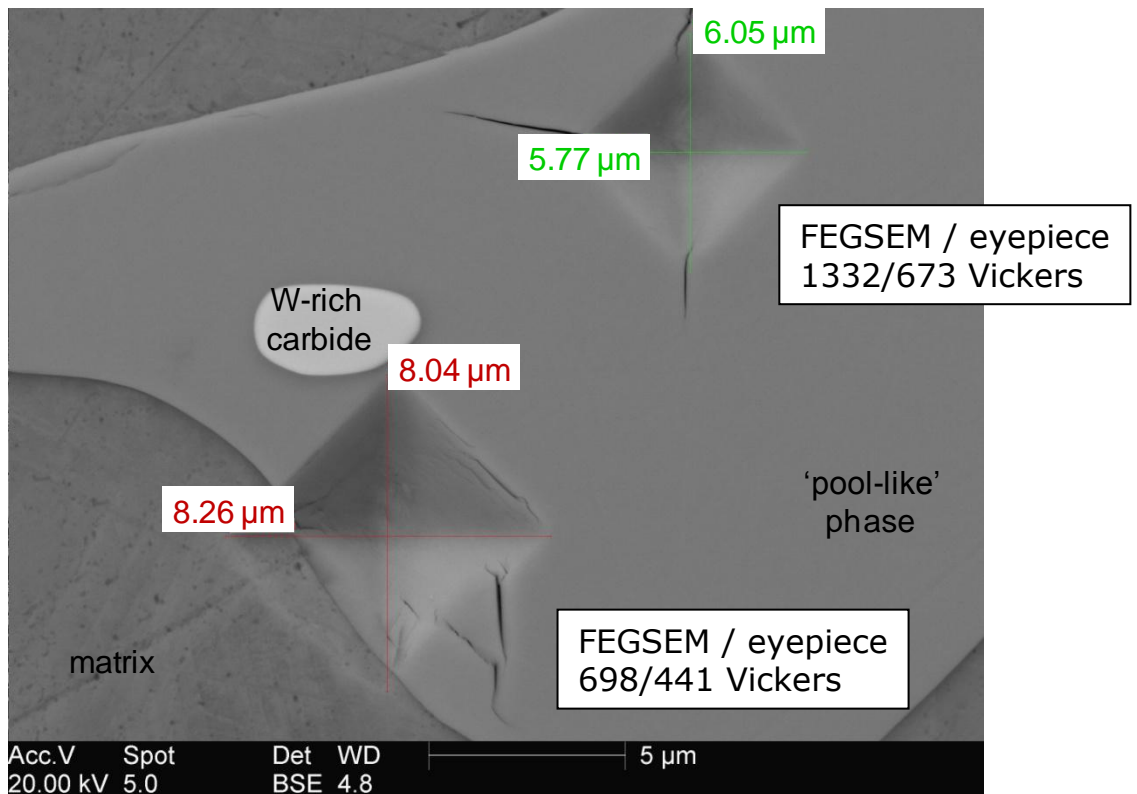


Figure 4.8 Two microhardness impressions on thermally exposed specimen for 15000 hours at 1050°C showing the cracking of the phase.

SUMMARY

Vickers hardness studies at 20kg load showed the same trend for all of the temperatures. After an initial increase in hardness to the maximum (~ 250 Vickers) for the samples exposed between 600-750°C, the material starts to soften. The lowest hardness is reached for exposures at 990°C. Then the hardness starts to increase again due to the precipitation of hard 'pool-like' phase (microhardness at 50gf load ~ 1200 Vickers) within the softer matrix (microhardness at 50gf load ~ 250 Vickers).

4.2 NANOHARDNESS STUDIES

Additional information about the phases' hardness was obtained by nanoindentation. Nanoindentation studies were chosen as another technique to validate the results from microhardness measurements and to confirm the properties of the 'pool-like' phase, such as its hardness and brittleness. Nanoindentation is used when it is desirable to make shallow indentation or to analyse small features.

Nanoindentation was performed on as-received material, on two thermally exposed samples containing 'pool-like' phase (15000 hours at 1050°C, 20000 hours at 1050°C) and on the creep tested sample (COD). This study was partially carried out by S. Zheng, MSc. student under the part-supervision of the author.

Various tested materials require different testing parameters such as the Poisson's ratio and loading time. The hard carbides (such as W-rich, 'pool-like' phase) have Poisson's ratio between 0.2-0.22, the Poisson's ratio for nickel is equal to 0.31 and this value was set up for testing the matrix [131]. The loading time was 15s. The input parameters and the list of data can be found in Appendices 9.5. The results such as the hardness (GPa), the modulus (GPa) and the displacement are calculated directly by the equipment software. The equation for conversion of Vickers hardness at maximum load to Vickers hardness number is:

$$H[\text{GPa}] = 0.009807 \times H_{\text{Vickers}} [\text{kg mm}^{-2}] \quad \text{Equation 4.2}$$

Table 4.5 lists the testing conditions.

Table 4.5 Review of the nanoindentation tests.

Specimen	Phase	Test loads (gf)				Number of indentations			
As-received	W-rich	25	10	5	1	10	10	10	15
	Matrix	50	25			10	10		
Thermal	W-rich		10	5	1		10	10	7
	'pool-like' phase	50	25	10	5	10	10	5	5
	Matrix	50	25			10	10		
Creep	'pool-like' phase	50	25	10		10	10	5	
	Matrix	50	25			10	5		

Nevertheless the tiny size of the nanoindenter meant that the same problem with locating it precisely in the selected phases emerged as with the microindenting. Some of the values had to be rejected for the untypical behaviour.

The results of the appropriate quality for analysis can be selected using the load-displacement curves.

4.2.1 AS-RECEIVED MATERIAL

The hardness of the W-rich carbide and of the matrix was obtained.

Table 4.6 summarises the mean hardness values and the mean elastic modulus obtained for the gamma matrix and W-rich carbide in the as-received material.

The matrix was tested at 25gf and 50gf loads. The mean hardness value obtained for 25gf is about 100 Vickers higher than the hardness value obtained for 50gf which was 300 Vickers approximately with the standard deviation of ± 40 Vickers. This value is much higher in comparison with the microhardness value of the matrix (180-190 Vickers). Possibly it is caused by the stress distribution in the matrix during the indenting process. Figure 4.9a),c) shows the nanoimpressions on the matrix and the load-displacement curves, Figure 4.9b),d), illustrates the process.

The interesting variety in the hardness was obtained for W-rich carbide where the hardness decreases stepwise from above 3200 Vickers at 1gf reaching 400 Vickers at the highest load of 25gf. In this case it can be concluded that the 10gf and 25gf loads were excessive for the size of the carbide. It has been demonstrated that the indentation depth must be shallow in order to obtain the results characterising the feature [132]. A model for separation of the thin film and substrate properties over a wider range of indentation depths has been developed [133, 134]. The model fits the composite hardness against the relative indentation depth, which is calculated as the indentation depth, h , over the (film) thickness, t . Applying the data shown in Figure 4.10b) (load-displacement curves for primary carbide W-rich) for the imprint 2 and the corresponding SEI image (Figure 4.10a)), the indentation depth is less than 400nm and the particle thickness is 4 μm (assuming that the primary carbide is rounded), the relative indentation depth β for primary carbide and the 5gf load is equal to 0.1.

Table 4.6 The mean hardness values and the mean elastic modulus obtained from as-received material. Values obtained from the software on the nanoindenter analysing the load-displacement curves.

Load (gf)	Primary Carbide – W-rich				Matrix	
	1	5	10	25	25	50
Used/total tests	6/15	3/10	5/10	3/10	9/10	8/10
Mean Hardness (GPa)	32.12 ±1.63	15.94 ±1.77	5.72 ±0.8	4.03 ±0.36	4.05 ±0.16	2.89 ±0.34
Mean Hardness (Vickers)	3276 ±166	1626 ±180	583 ±81	411 ±37	413 ±16	295 ±34
Mean Modulus (GPa)	481±33	308±7	183±12	147±8	173±7	160±6

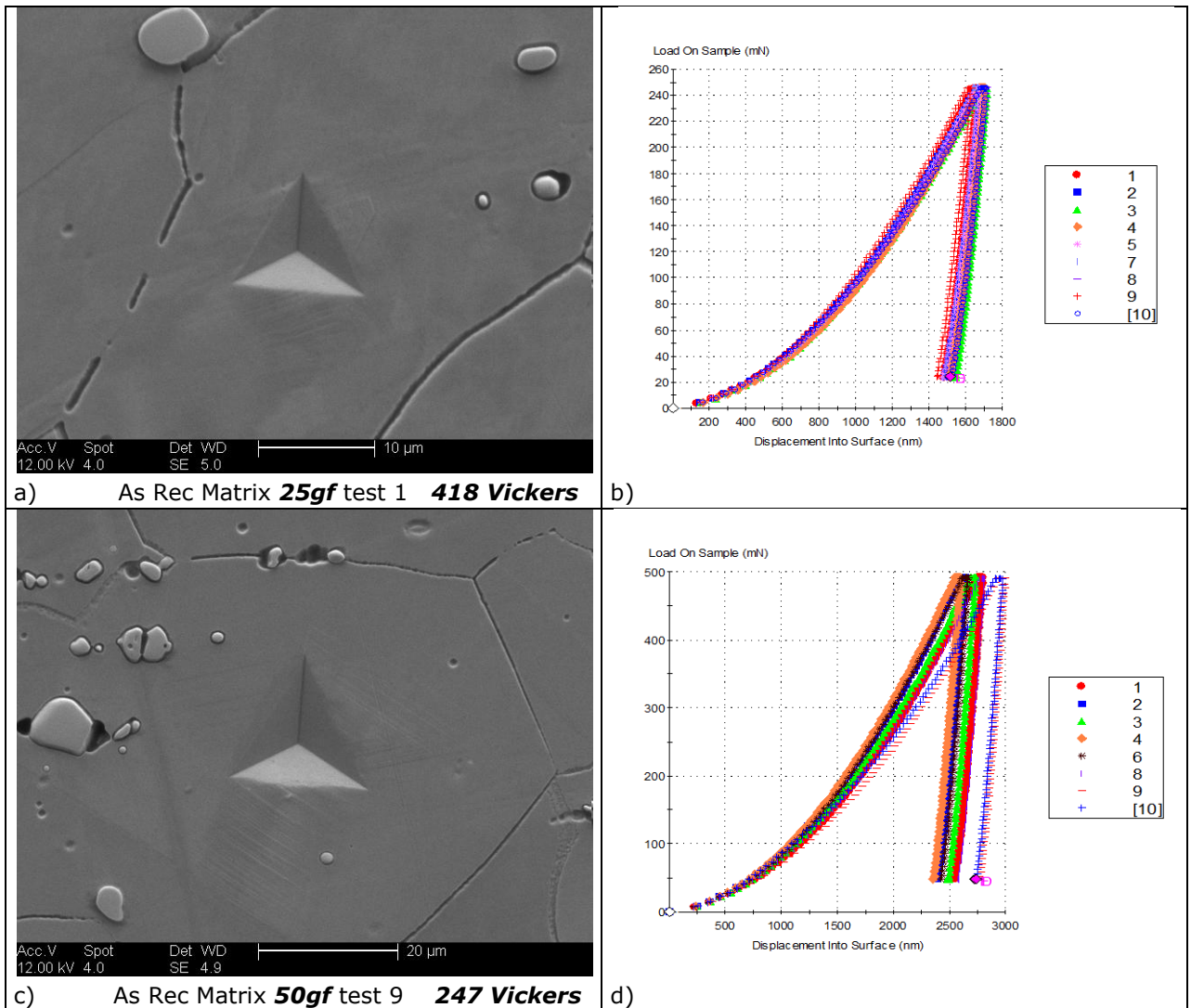


Figure 4.9 As-received material: a),c) the nanoimpressions on the matrix; b),d) the load-displacement curves.

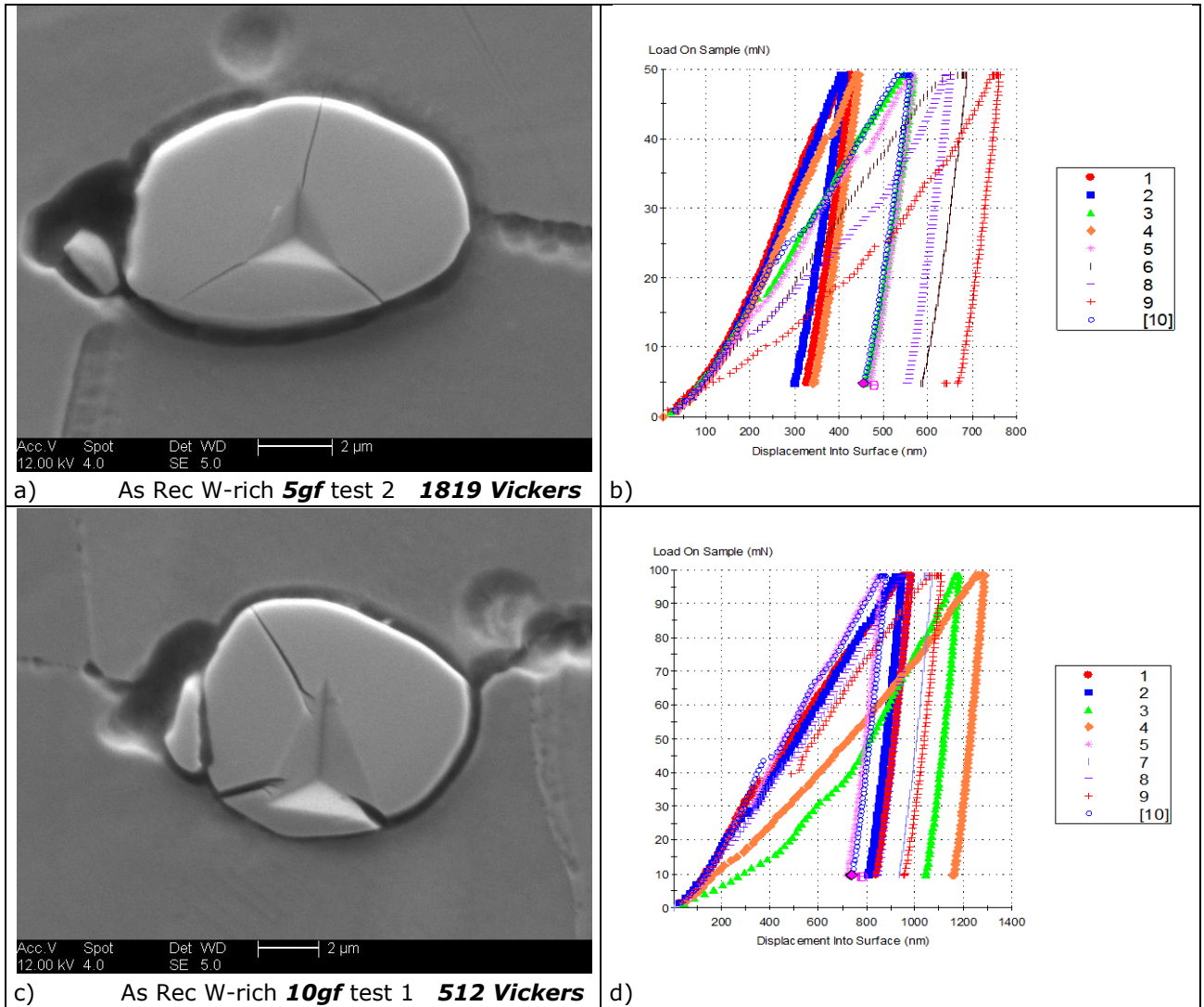


Figure 4.10 As-received material: a),c) the nanoimpressions on the W-rich carbides; b),d) the load-displacement curves.

4.2.2 THERMALLY EXPOSED HA230

Thermally exposed samples at highest temperatures contain three different phases within the microstructure, see Figure 4.11. There are gamma matrix, W-rich phase and Cr-rich 'pool-like' phase. All these phases are relatively large in size; hence meaningful nanohardness values can be obtained.

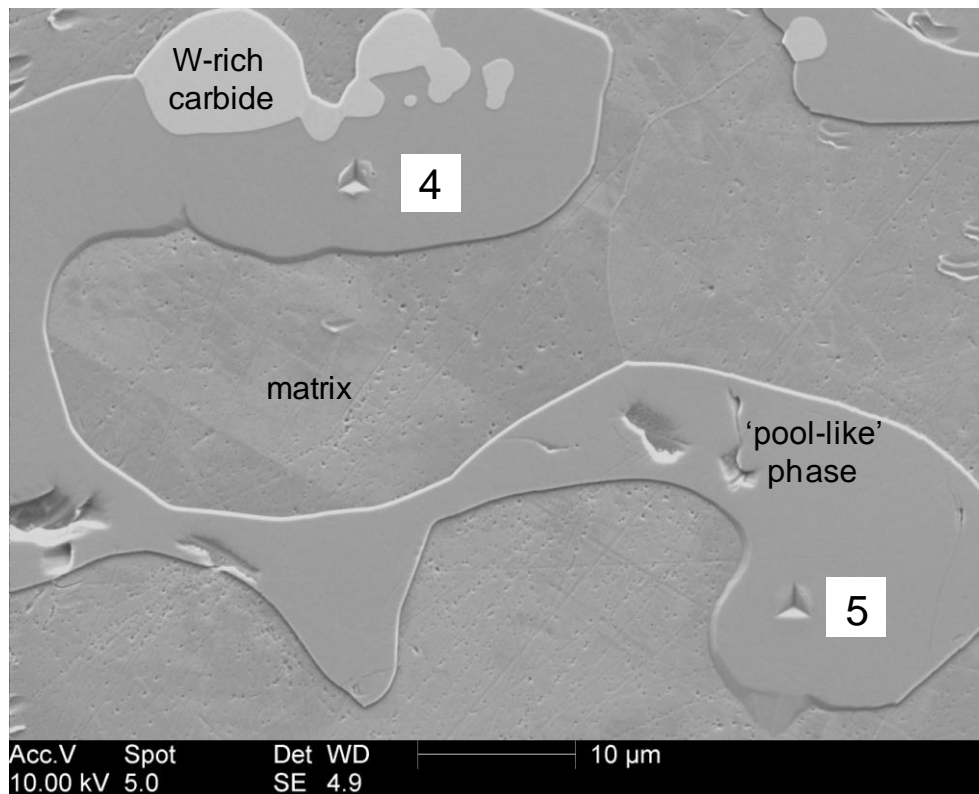


Figure 4.11 SE image of two nanohardness imprints on 'pool-like' phase of the thermally exposed sample.

Table 4.7 summarises the mean hardness values and the mean elastic modulus obtained for the gamma matrix, Cr-rich phase and W-rich carbide in the thermally exposed specimens.

The matrix tested at 25gf and 50gf loads showed the lowest hardness observed. The mean hardness value for 25gf was 249 Vickers and the hardness value for 50gf was 230 Vickers, with the maximum standard deviation of ± 20 Vickers. This value is in the upper range of the macrohardness values and it is little higher than the hardness value obtained for as-received material. Figure 4.12 a),c) shows the nanoimpressions on the matrix and Figure 4.12 b),d) illustrates the process (the load-displacement curves).

Table 4.7 The mean hardness values and the mean elastic modulus obtained from thermally exposed samples. Values obtained from the software on the nanoindenter analysing the load-displacement curves.

	Prim. C - W-rich			Cr-rich				Matrix	
Load (gf)	1	5	10	5	10	25	50	25	50
Used/total tests	3/10	3/10	2/10	29/37	2/5	6/10	3/10	10/10	10/10
Mean Hardness (GPa)	33.08 ±1.01	22.84 ±0.76	20.88 ±1.63	22.27 ±1.51	20.18 ±2.66	17.87 ±1.05	14.02 ±1.52	2.44 ±0.19	2.26 ±0.11
Mean Hardness (Vickers)	3369 ±103	2328 ±77	2130 ±166	2270 ±154	2058 ±271	1823 ±107	1429 ±155	249 ±19	230 ±11
Mean Modulus (GPa)	494 ±19	354 ±51	366 ±4	381 ±24	353 ±28	299 ±13	249 ±9	142 ±6	119 ±5

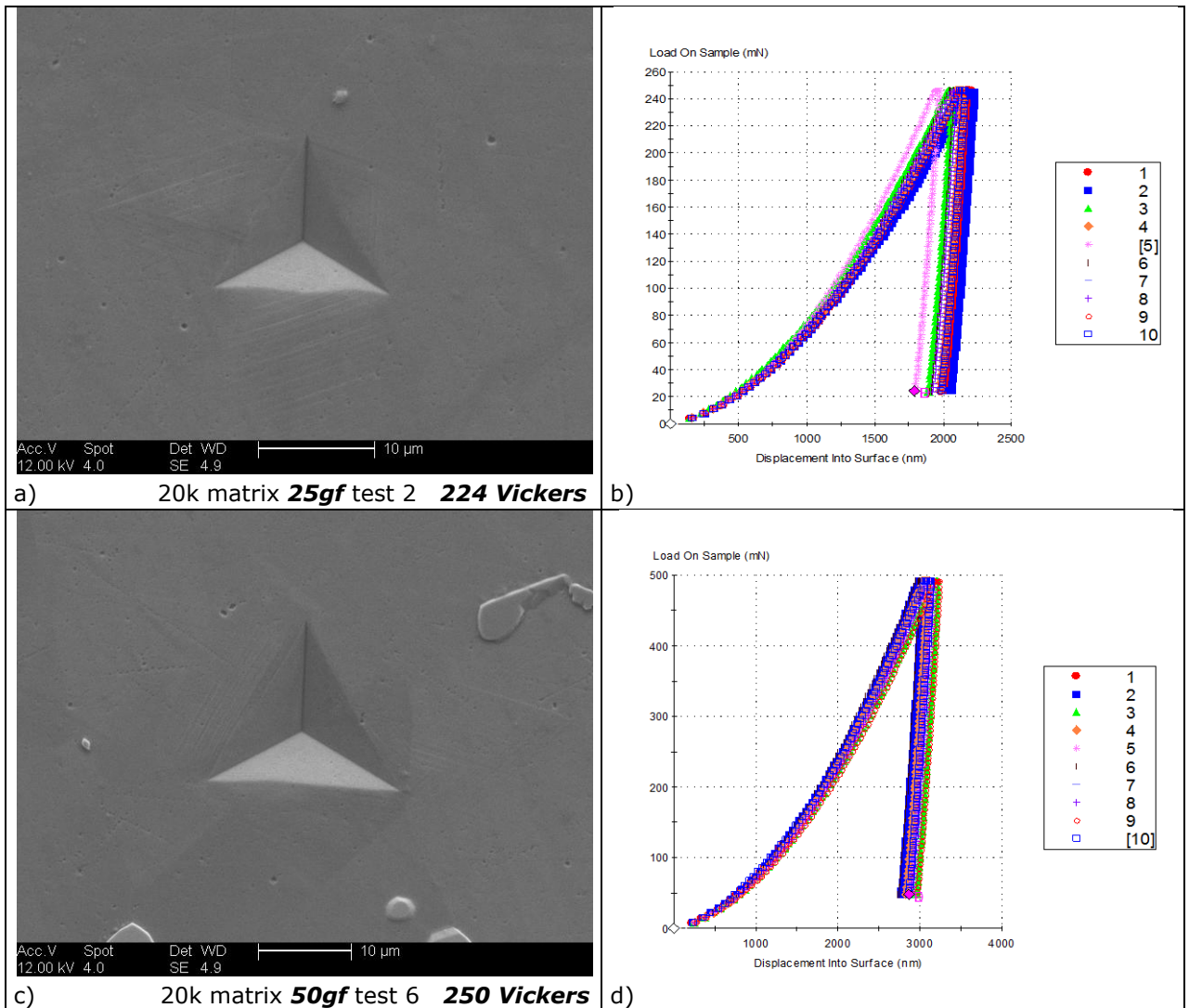


Figure 4.12 Thermally exposed sample: a),c) the nanoimpressions on the matrix; b),d) the load-displacement curves.

The gradual decrease in nanohardness with increasing load was obtained for W-rich carbide. The maximum of 3369 Vickers was calculated for 1gf load, approximately 1000 Vickers lower was the hardness calculated for the load of 5gf and for the load of 10gf the nanohardness was 2130 Vickers. The relative indentation depth β for primary carbide W-rich and the 5gf load can be obtained using the data shown in Figure 4.13d) (load-displacement curves for primary carbide) for the test 3 (2334 Vickers) and the corresponding SEI image (Figure 4.13 c)), where the indentation depth is less than 400nm and the particle thickness is around 4 μm (assuming that the primary carbide is rounded), is equal to 0.1. This corresponds to the result obtained for W-rich carbide in the as-received material.

In the case of the Cr-rich phase a similar trend in the gradual decrease of hardness can be seen (Table 4.7) and in addition, the hardness values for the same loads are similar. 29 measurements were carried out at 5gf load. The mean hardness is equal to 2270 Vickers with an error less than 7%. With increasing load the Vickers hardness starts to decrease reaching 1429 Vickers at 50gf load. Figure 4.14 demonstrates the measurements.

For the estimation of the hardness, the software measures the contact area, which is affected by the amount of pile-up or sink-in developed around the indenter during the indentation process [135]. Consequently, the contact area can be underestimated by as much as 60%, causing overestimations of the hardness and elastic modulus [136]. One of the factors influencing sinking-in or piling-up behaviour of materials is friction. Xu's [137] simulations (FE) showed the reduction of the contact area of indentation as an effect of friction compressing the plastic core of a sharp indentation. The result is decrease of the pile-up for materials with tendency to pile up and vice versa for materials with the tendency to sink-in. The pile-up effect can be observed on both phases, W-rich (Figure 4.13c)) as well as on Cr-rich phase (Figure 4.14i)). However, the relationship between this effect and any other factor cannot be determined.

The increase of cracks growing from the tip area of an imprint with increasing load can be very clearly distinguished, see Figure 4.14 c), e), and h) and again this feature can be observed in both hard phases.

4.2.3 CREEP TESTED HA230

The microstructure of the creep tested specimen (Figure 4.7) should facilitate the positioning of the nanoindenter but on the other hand this type of

microstructure with creep cracks and 'pool-like' shaped precipitates may make the evaluation of the data more complicated.

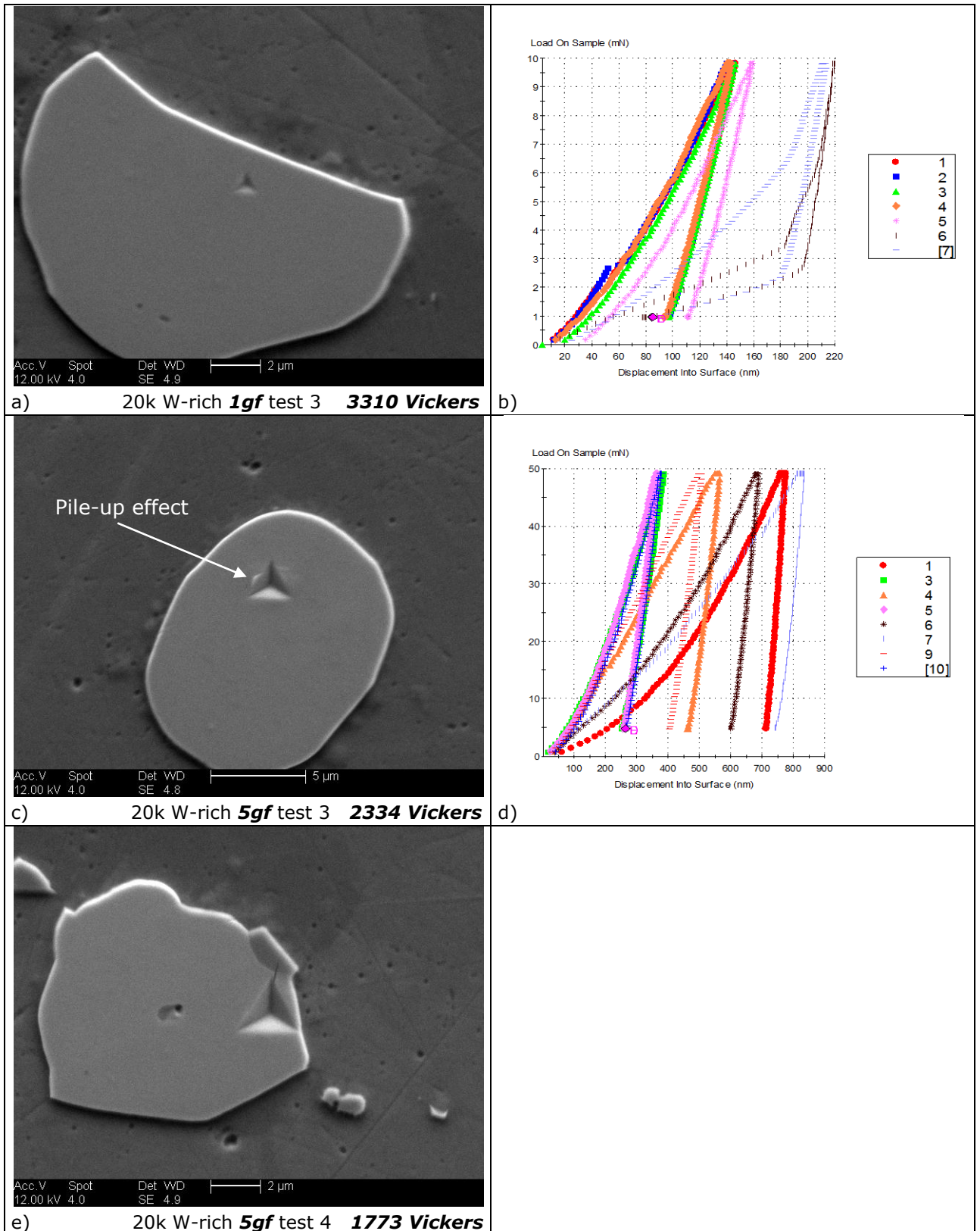
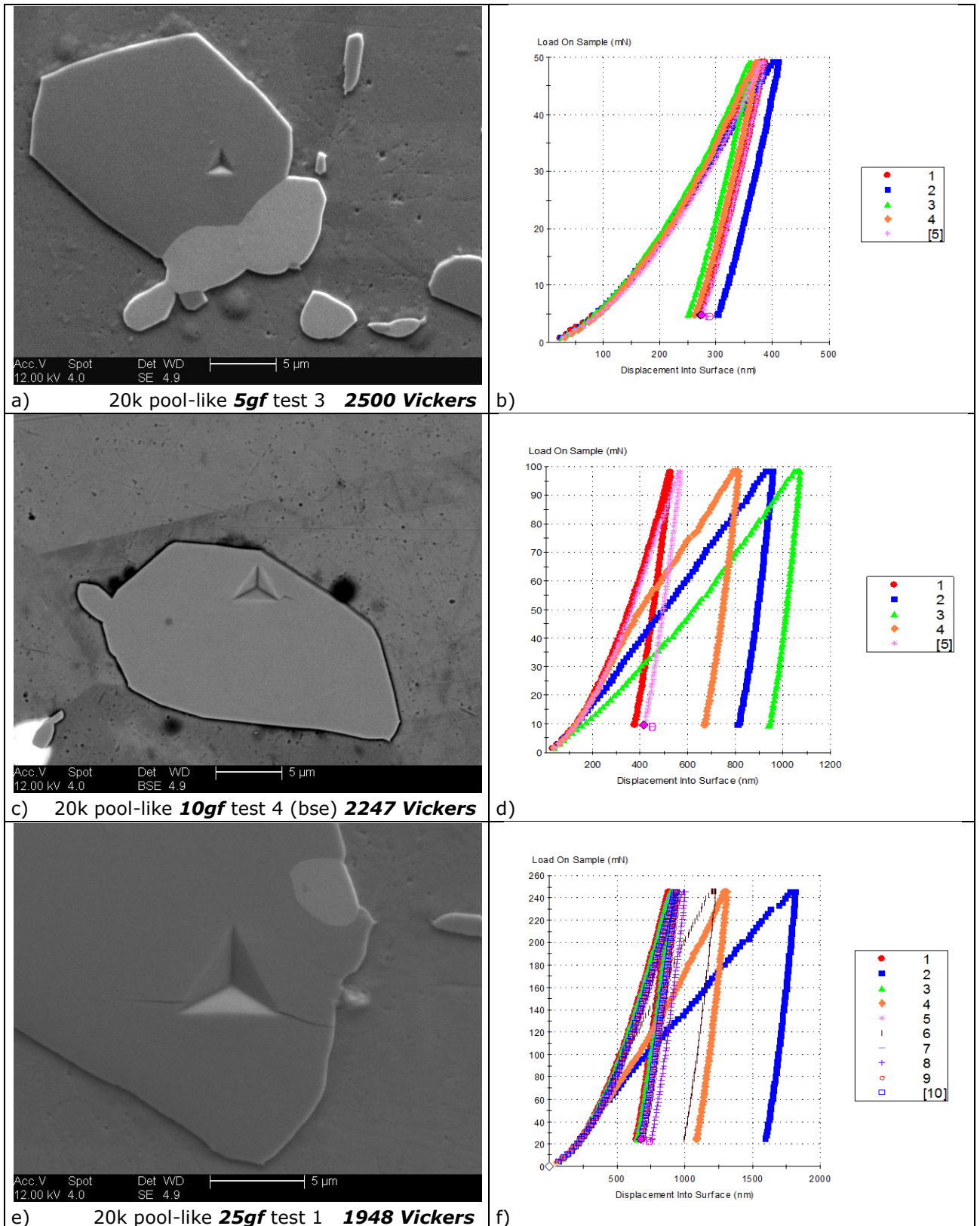


Figure 4.13 Thermally exposed sample: a), c), e) the nanoimpressions on the W-rich carbides; b), d) the load-displacement curves.

The hardnesses of the Cr-rich carbides and of the matrix were obtained. Table 4.8 presents the mean hardness and the mean elastic modulus results obtained for the creep tested specimen.



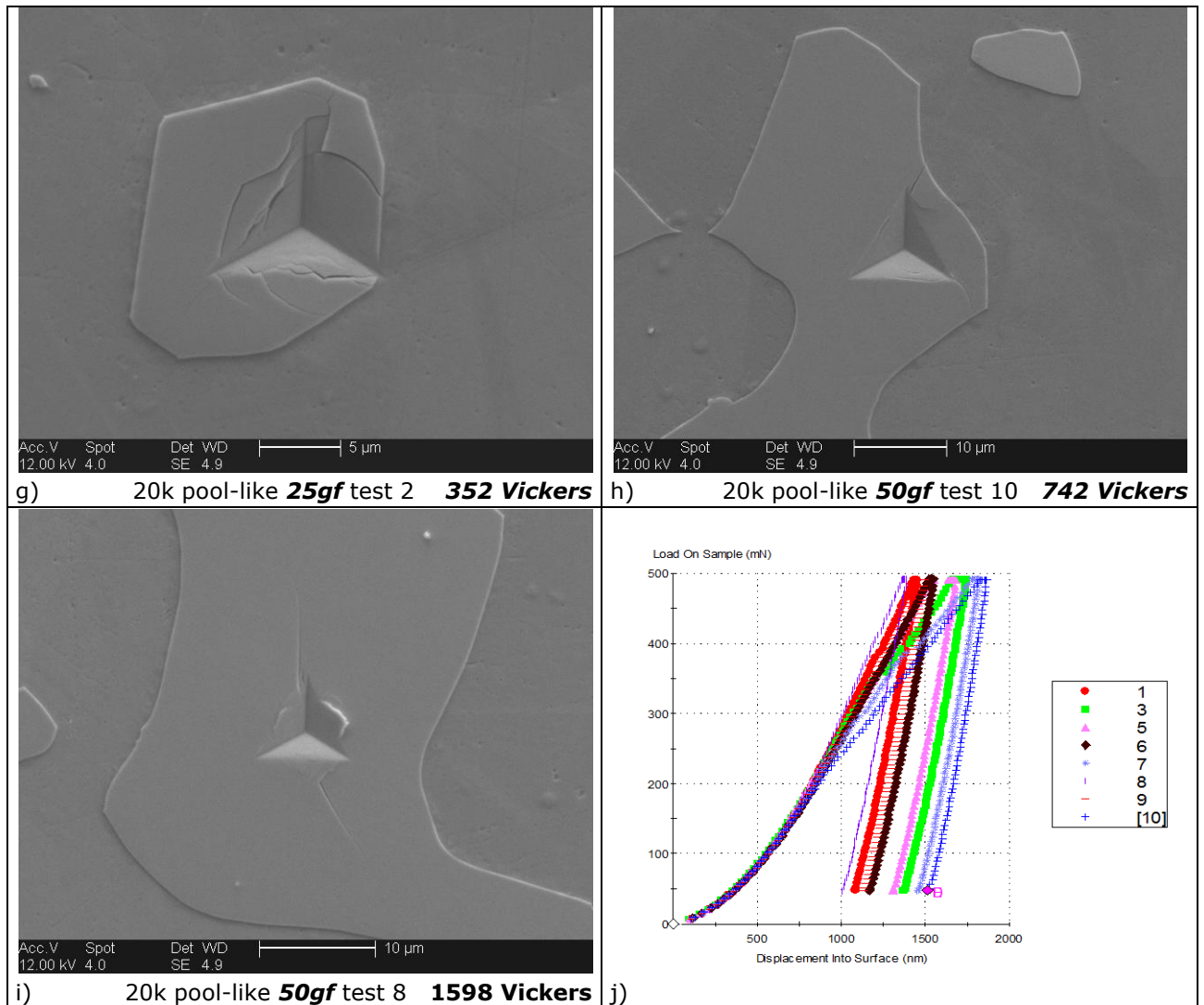


Figure 4.14 Thermally exposed sample: a),c),e),g),h),i) the nanoimpressions on the Cr-rich phase; b),d),f),j) the load-displacement curves; i) pile-up effect.

The matrix was tested at 25gf and 50gf loads. The difference between the mean hardness values is reasonably small; the hardness obtained for 25gf was 276 Vickers and 249 Vickers for 50gf load. Figure 4.15 shows SE images for the matrix imprints and the corresponding load-displacement curves. No pile-up effect was observed.

The Cr-rich ('pool-like') phase was tested at 10, 25 and 50gf loads. A gradual decrease in hardness can be observed which is in agreement with the conditions of testing. Again the 50gf load should be evaluated as excessive for this type of phase. 1855 Vickers is a mean value for 10gf and 1569 Vickers for 25gf load. For the calculation of the relative indentation depth the load-displacement curves, Figure 4.16b), test 5 at 10gf, is used together with the SE image, Figure 4.16a). The indentation depth is approximately 550 nm and the particle thickness is

7 μm (assuming the radius of the 'pool-like' phase in the thinnest area), the relative indentation depth β for Cr-rich 'pool-like' phase in the creep specimen and the 10gf load is equal to 0.08.

Table 4.8 The mean hardness values and the mean elastic modulus obtained for creep tested specimen (COD). Values obtained from the software on the nanoindenter analysing the load-displacement curves.

	Cr-rich			Matrix	
Load (gf)	10	25	50	25	50
Used/total tests	3/5	4/10	2/10	5/5	8/10
Mean Hardness (GPa)	18.18 ± 0.45	15.39 ± 1.62	10.73 ± 0.91	2.71 ± 0.17	2.44 ± 0.23
Mean Hardness (Vickers)	1854 ± 46	1569 ± 165	1094 ± 93	276 ± 18	249 ± 24
Mean Modulus (GPa)	333 ± 13	281 ± 34	242 ± 0	177 ± 4	162 ± 5

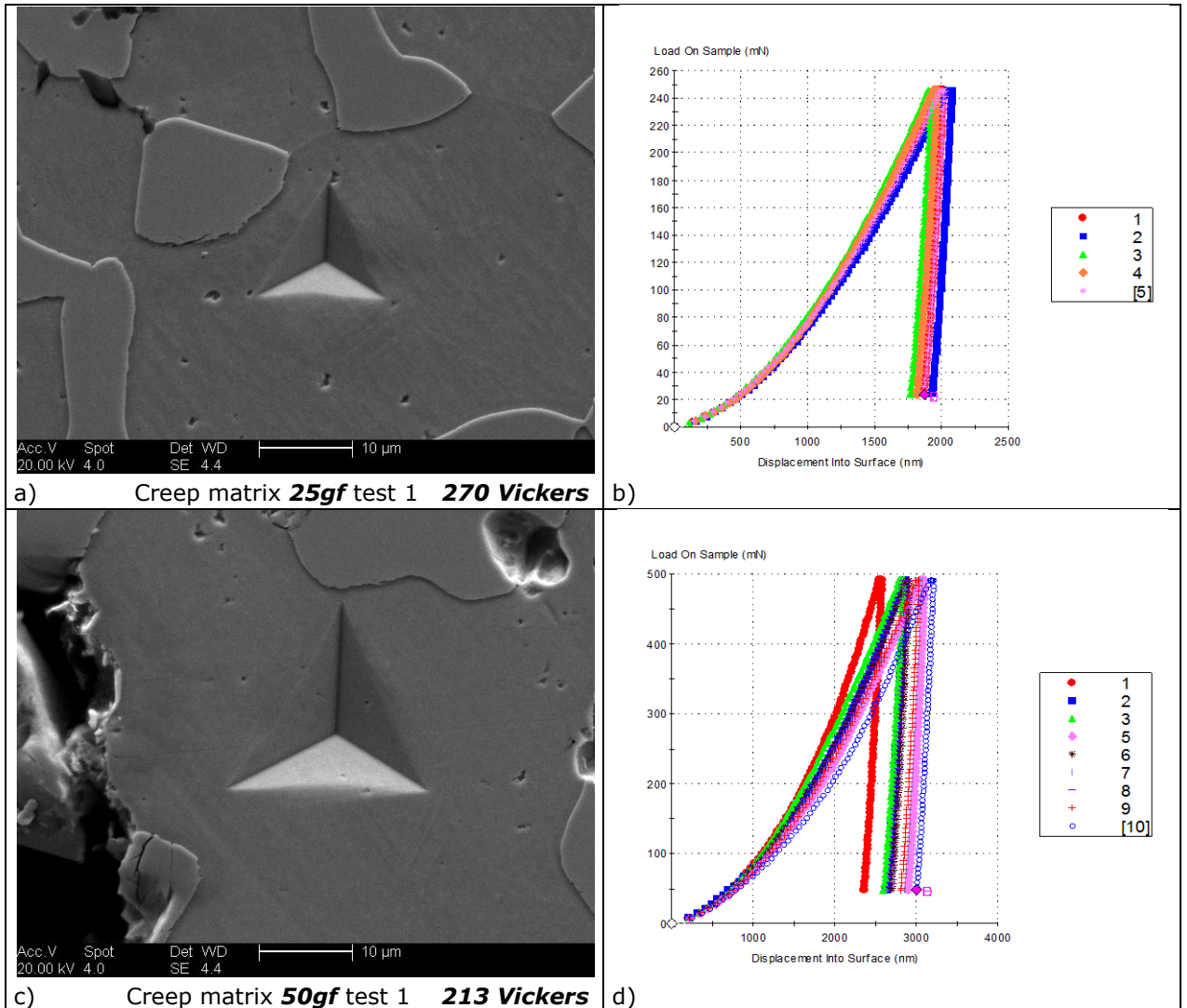


Figure 4.15 Creep tested specimen: a),c) the nanoimpressions on the matrix; b),d) the load-displacement curves.

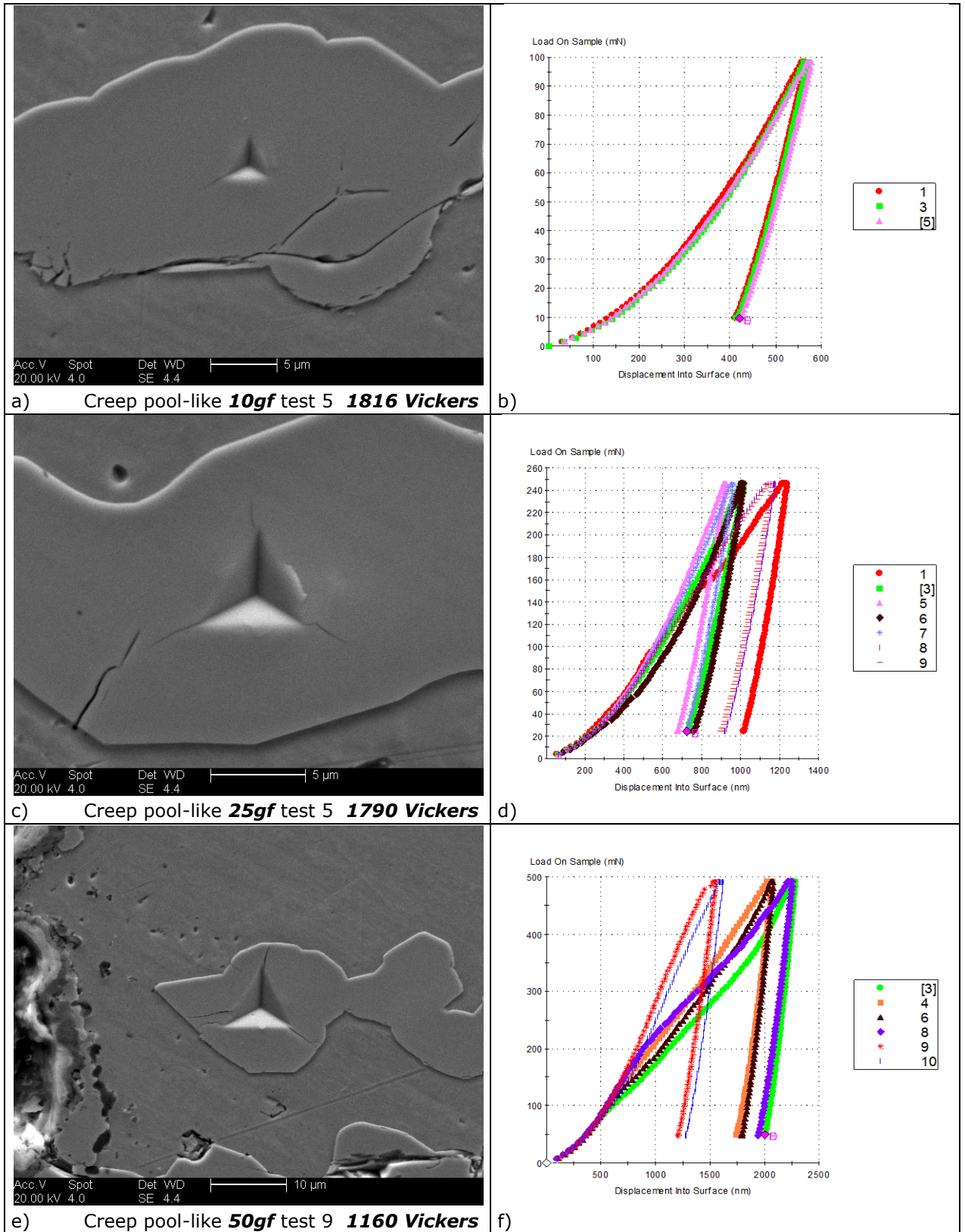


Figure 4.16 Creep tested specimen: a),c),e) the nanoimpressions on the Cr-rich phase; b),d),f) the load-displacement curves.

SUMMARY

The main points obtained in the nanohardness study are the hardnesses of the single alloy phases. Values obtained for the carbides are higher than those from microhardness testing, which was expected. The hardness values of primary carbide W-rich and 'pool-like' phase are in the same range (18-22 GPa) while the hardness of the matrix is generally between 2-3 GPa. There was difficulty with positioning of the nanoindenter and this meant that there was a limit on the number of reliable measurements. However the load-displacement curves used for the calculations clearly show that some tests are reliable.

4.3 STATISTICAL ANALYSIS OF HARDNESS RESULTS

An important aim of this project is to create a single 'master' curve of hardness results to be used as a simple tool for estimation of temperature of the component taken from service. The statistical analysis was performed with the assistance of Dr Michael J. Phillips from the Department of Mathematics, University of Leicester. The task was divided into 3 parts. The first part was to find out if two sets of hardness data, a set of hardness values from thermally exposed specimens ('thermal') and a second set of data from unstressed heads of creep tested specimens ('creep') could be considered to come from the same population. The second part was to calculate a 'master' curve assuming that the two sets of data come from the same population. And the third part was focused on the estimation of the optimum value of the LMP constant C.

The hardness values and relevant Larson-Miller parameters used for statistical analysis of thermally exposed samples and unstressed heads of creep tested samples are listed in Table 9.1. The 'Thermal' set contains 80 values, and the 'Creep' set contains 22 values. The sample thermally exposed for 1000 hrs at 1170°C has been excluded from the calculation. The detailed calculations are offered in Appendices 9.6. The test hypotheses are:

1. Do the two sets of data ('Thermal' and 'Creep') come from the same population?

The F-test was used to answer this question. The $f_{102,4}$ value for the observed data is equal to 2.62 and is greater than the critical value for the upper 5th percentile ($f_{0.05,102,4}$ is equal to 2.47) and therefore the null hypothesis that the sets can be combined has to be rejected at the 5% level. Hence the hardness sets

are statistically different. However, the difference is not very great and in 2. below the two sets of data will be treated as though they can be combined.

2. What is the 'master' curve if the two sets ('Thermal' and 'Creep') are assumed to come from the same population?

The probability value $P(f_{102,4})$ equal to 0.04 (4%), calculated using the F test suggests the possibility of combining the two sets if this can be justified on engineering grounds (see Section 4.1.2).

Using the hardness measurements from both sets of data, so using 102 observations, the 95% confidence (CI) and prediction interval (PI) were calculated (Figure 4.17). For a comparison the same calculation for the 'thermal' set was considered. As can be seen in figure below, the R^2 (coefficient of determination) decreased only slightly with the number of observations ($0.917 \rightarrow 0.914$), and only 2 low temperature observations (LMP=19.48 and 21.76) have untypical behaviour.

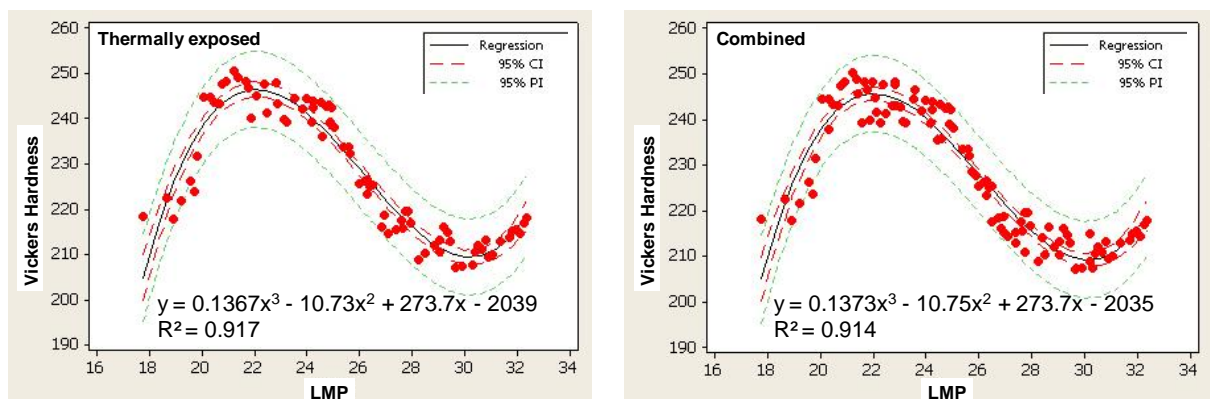


Figure 4.17 The Confidence and prediction intervals for the 'thermal' set and combined set of data.

3. The estimation of the LMP constant C.

The method of maximum likelihood was used for the determination of the optimum value for the LMP constant. For thermally exposed samples (80 observations) the constant C lies within the 95% confidence interval is [15.1, 25.5] with the optimum value equal to 19.3. The optimum value for the combined hardness values of thermally exposed and creep tested specimens (102 observations) was 22.2 with a 95% confidence interval of [17.8, 28.7]. Figure 4.18 shows a graph of the log-likelihood ratio v LM constant values. Any value of C with a loglikelihood ratio greater than -2 would be included in the 95% confidence interval.

The new optimum values of C (LMP constant) were used to replot the hardness values (see Figure 4.19 and Figure 4.20). The R^2 values change little. Any differences can only be observed in the third or fourth decimal place. The LMP constant equal to 19.3 made the R^2 value of the 'thermal' set increase from 0.9168 to 0.9169. The LMP constant equal to 22.2 made the R^2 value of the 'combined' set increase from 0.914 to 0.9147.

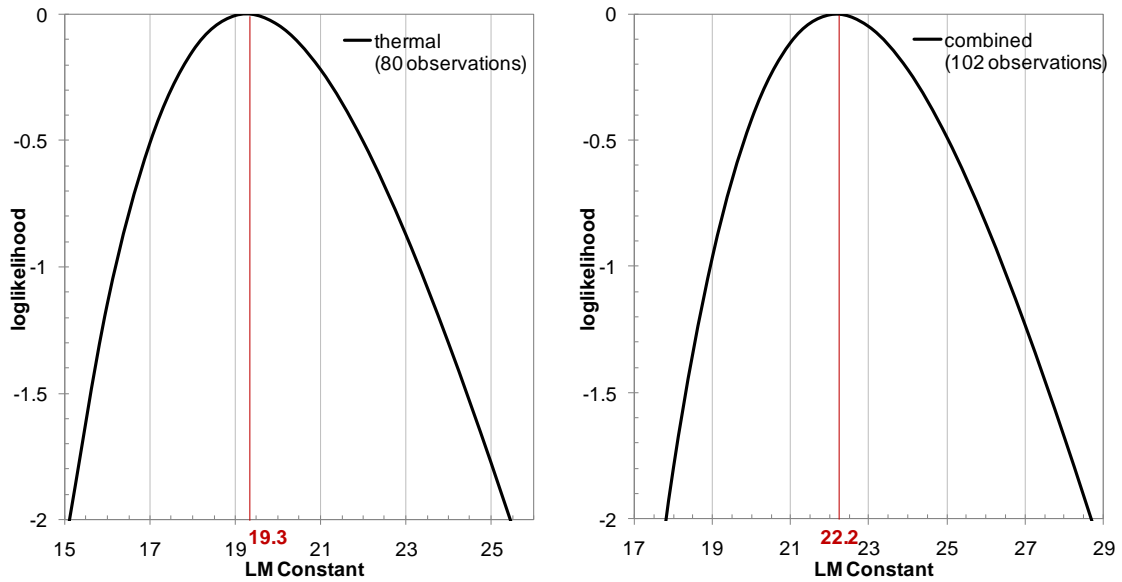


Figure 4.18 Log likelihood ratio showing the interval of values for the LMP constant.

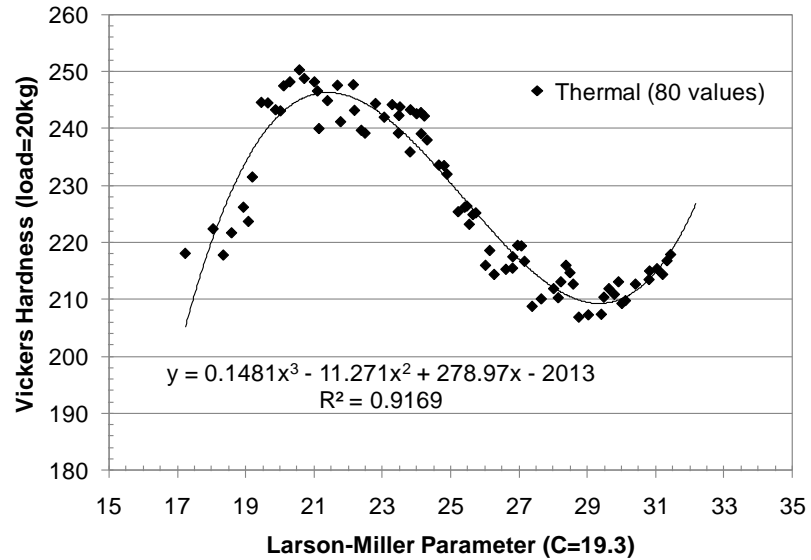


Figure 4.19 Hardness Master Curve for LMP C=19.3.

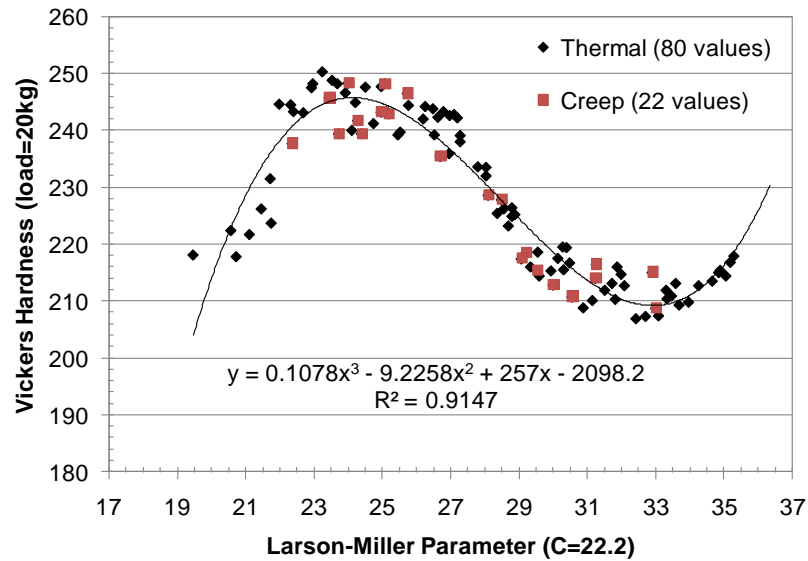


Figure 4.20 Hardness Master Curve for LMP C=22.2.

SUMMARY

Hardness v Larson-Miller parameter curves of thermally exposed and creep tested samples were used for the evaluation of the possibility to create a combined Master curve. Based on the similarity of the behavior of both populations, the Master hardness curve was created with a prediction interval of ± 8.5 Vickers. The new LMP constant C estimated on 22.2 does not affect the R^2 value considerably.

4.4 METALLOGRAPHIC STUDIES

Metallographic studies of the microstructure of HA230 are based on an evaluation of images obtained by the light optical microscopy and the scanning electron microscopy. As was mentioned above, some experiments were carried out before the start of the PhD project (see Appendices Figure 9.2).

4.4.1 OPTICAL MICROSCOPY

Optical microscopy studies were performed on as-received material, on HA230 coupons thermally exposed between 24 to 30000 hours at temperatures in the range 500°C to 1170°C, and on creep specimens.

4.4.1.1 AS-RECEIVED HA230

Figure 4.21 shows the microstructure of the as-received solution treated and quenched HA230 taken from the same batch as for all the coupons for thermal exposure and samples for thermal testing. It contains primary carbides which were identified by X-Ray Diffraction (see Section 4.6) as $M_{12}C$. Primary carbides are

tungsten rich (see Section 4.4.3); cellular in shape, generally associated with grain boundaries (some directionality is evident corresponding with the rolling direction) and range in size from 5 to 20 μm in diameter. Debonding effect can be identified around the primary carbides in the direction of rolling. Any other precipitation has not been identified at this stage. The grain size averages 60 μm and the grains can be identified as equiaxed.

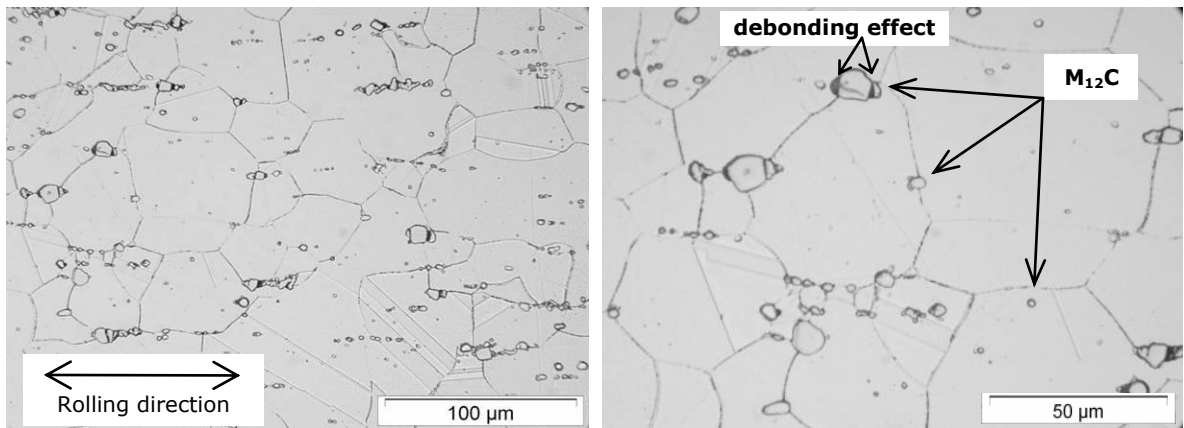


Figure 4.21 Microstructure of annealed and quenched HA230 showing primary carbides.

It is well known that the microstructure of the same material can vary with the form of the final product as well as with different batches of the material. Figure 4.22 shows the microstructure of the as-received solution treated and quenched HA230 but from a different batch. This microstructure contains primary carbides randomly distributed. The etching revealed only a few grain boundaries which are decorated with fine precipitates.

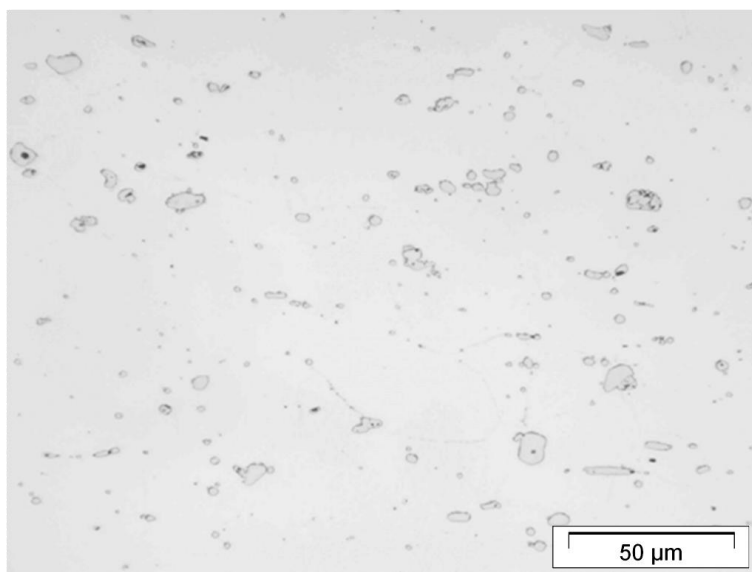


Figure 4.22 Microstructure of annealed and quenched HA230, different batch.

4.4.1.2 THERMALLY EXPOSED HA230

The microstructural examination of the thermally exposed HA230 coupons could be divided into two groups. The first one contains the samples exposed at lower temperatures and shorter times and the second set contains the main body of the thermally exposed samples in the temperature range 750°C to 1050°C and durations between 1000 and 30000 hours.

The effect of temperature is prevailing. Heating of the specimens above 500°C initialises precipitation on the grain boundaries after 1000 hours, but the microstructure, in general, looks very similar to the as-received material (Figure 4.23). All microstructures contain large primary carbides, W-rich (see Section 4.4.3) randomly distributed within the microstructure or aligned as a result of rolling, forming so-called stringers. Already after 1000 hours at 550°C all the grain boundaries are decorated with fine precipitates and some precipitates can be observed on annealing twin boundaries as well. These secondary precipitates are Cr-rich and have been identified as $M_{23}C_6$ type carbide (Section 4.6). Only 24 hours at 650°C are causing rich precipitation on the grain boundaries. With increase of the duration of exposure, the precipitation of the fine carbides increases and there are clusters on some of the boundaries and certain areas with higher number of primary carbides. The temperatures between 650°C and 750°C create the peak in hardness which is caused by the fine precipitation not only on the grain and annealing twin boundaries but also within the grains. This temperature region, from the thermodynamic considerations, is very favourable for the formation of many chromium carbides at grain boundaries. The chromium carbides precipitate close to the grain boundaries, forming so-called cellular discontinuous precipitation, which is perpendicular to a grain boundary. This very efficient way of chromium rich precipitation making the grain boundaries migrate ([10]pg.220) (detail can be seen on Figure 4.29 - 810°C).

Typical optical micrographs documenting the microstructural changes in HA230 in the temperature range 750°C and 1050°C for duration of 1000 hours to 30000 hours are shown in Figure 4.24.

The microstructure of the specimens exposed at 750°C contains some primary carbides randomly distributed within the matrix and the fine secondary precipitation on the boundaries and within the grains. At this temperature, the big primary carbides are 'breaking down' (*i.e.* particles which were previously showing no substructure now appear to be no longer homogenous), see Figure 4.30.

Generally the microstructure of the specimens exposed at 750°C does not change with duration of exposure.

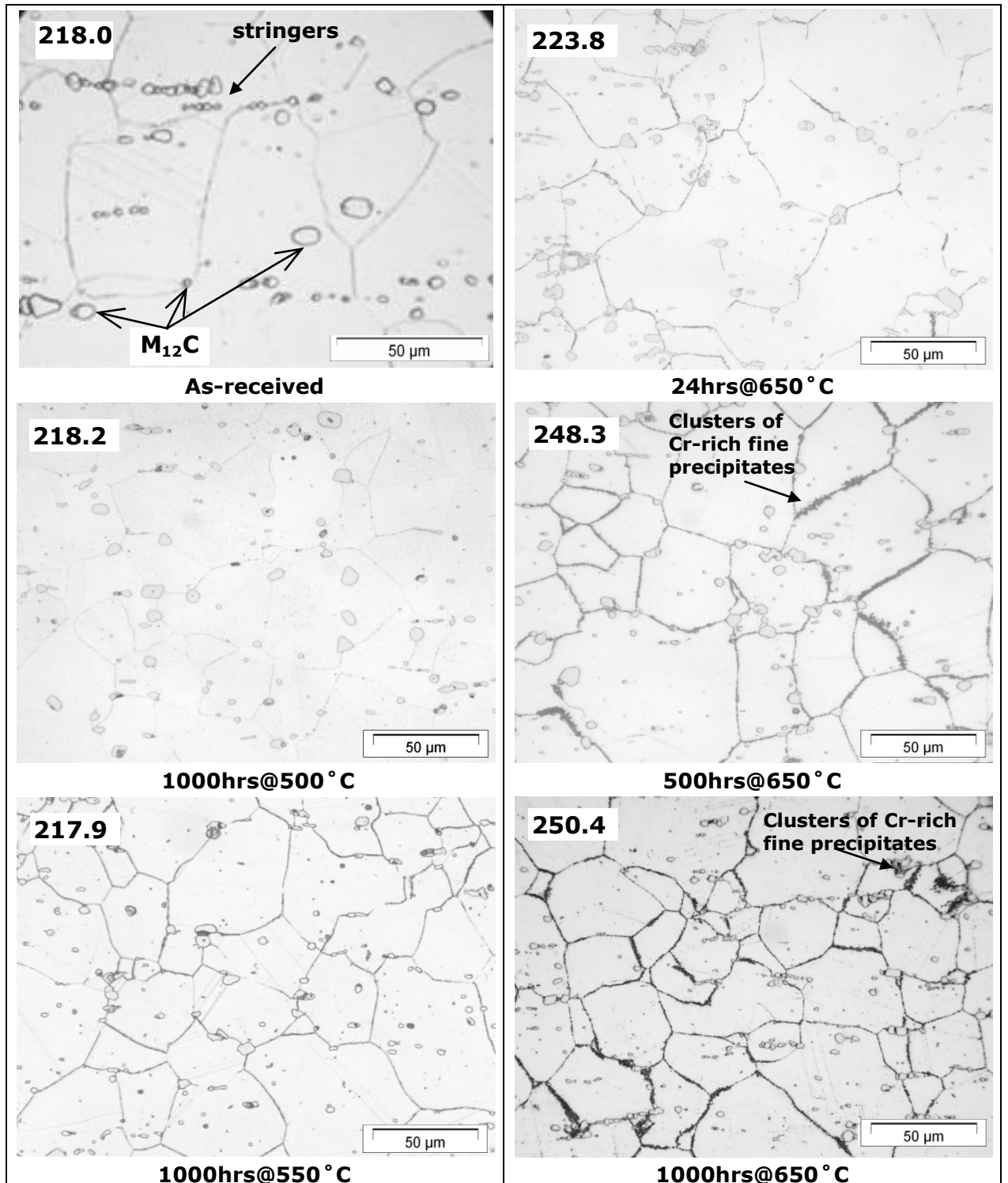


Figure 4.23 Microstructures of annealed and quenched HA230 and the specimens thermally exposed for: 1000 hours at 500°C and 550°C, 24, 500 and 1000 hours at 650°C. Fine precipitates ($M_{23}C_6$) on the grain boundaries.

With increase of the temperature (810°C and 870°C) more and more Cr-rich precipitates are concentrating on the grain boundaries. The composition of these precipitates is not uniform. The microstructure of the specimens exposed for 1000 hours only is slightly different than the microstructures of the specimens exposed for longer duration. The evolution of the precipitates is equivalent to that for the specimens exposed for longer duration but lower temperatures. The longer duration of exposure causes the coarsening of the Cr-rich phase, which still concentrates on the grain boundaries and fewer precipitates are observed on annealing twins and within the grains. The primary carbide starts to transform again in this range of temperatures. They are approaching their original rounded shape, but still some 'cracks' are present.

This evolution proceeds at 930°C when these precipitates continue to grow and coarsen and the primary carbides become more uniform in shape. The hardness of the material at 990°C is a minimum (see Figure 4.1) and this can be associated with the grain boundary phase coarsening; the precipitates do not form continuous precipitation, moreover the phase starts to create 'pools' after long exposures and at 1050°C this 'pool-like' phase creates isolated clusters within the microstructure, see Figure 4.6. This new large phase (Figure 4.24), samples exposed for 20000 and 30000 hours at 1050°C) is mostly chromium rich and also hard and brittle (see Figure 4.8).

In addition, optical studies of the thermally exposed samples indicate an increase of oxidation attack with increasing temperature of exposure, see Section 4.9.

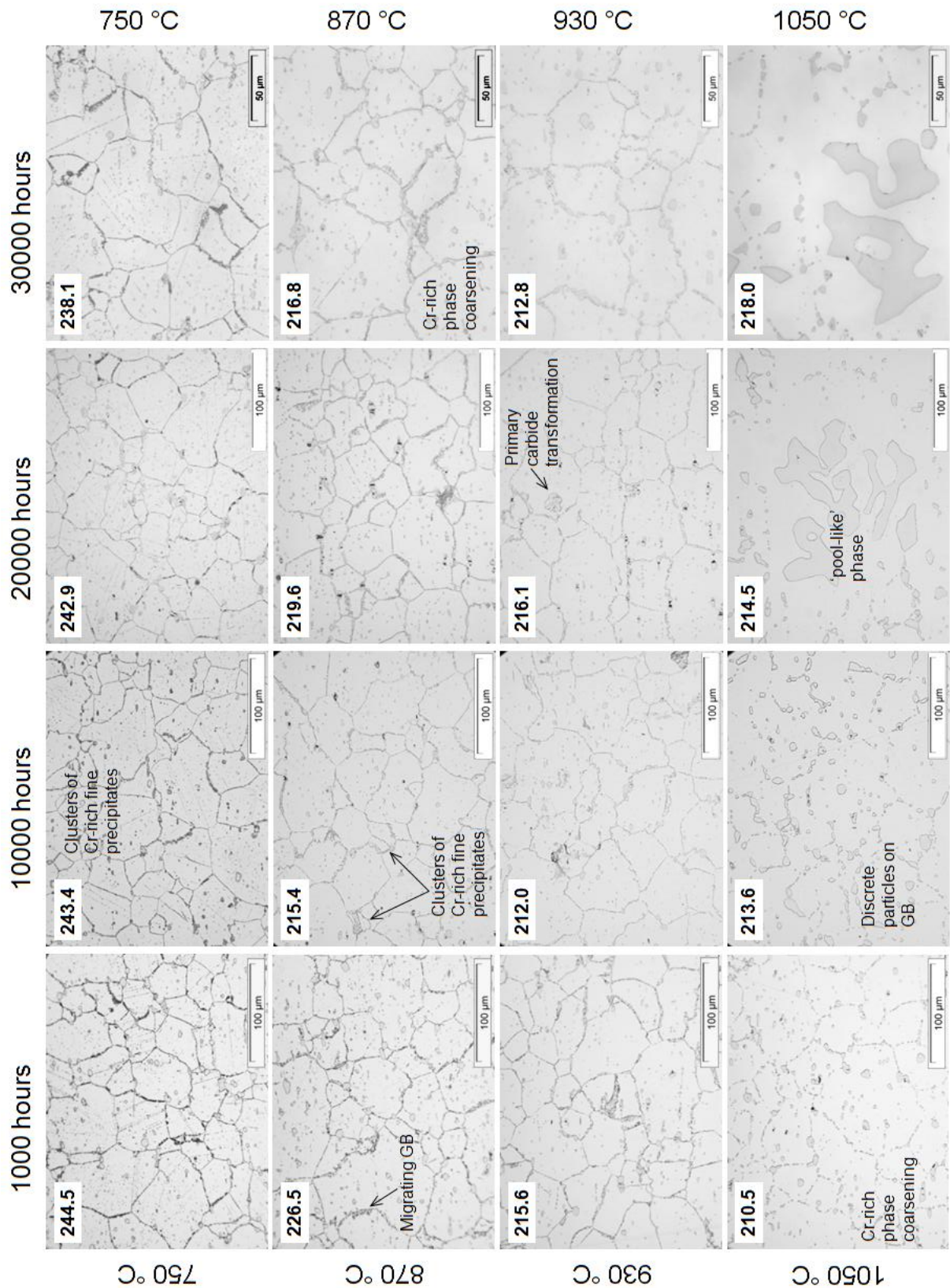


Figure 4.24 Effects of exposure at temperatures in the range 750°C to 1050°C on the microstructure of HA230 showing average Vickers hardness of each specimen (Hv20).

4.4.1.3 CREEP TESTED HA230

Similar optical microscopy studies have been accomplished on microsections taken from selected creep rupture specimens, from areas in the gauge length close to the final fracture zone as well as from unstressed areas of the specimen heads. Details about the creep test pieces are given in Table 4.9.

Table 4.9: Creep rupture test results on HA230

Test piece	Temperature °C	Rupture Life Hours	Elongation %	Larson-Miller Parameter
DKX	650	6577	20.7	21.98
DLA	700	18160	17.2	23.60
DLB	700	4995	-	23.05
DLH	900	28776	~ 35	28.69
COD	950	50874	66.7	30.21
COG	1000	5366	70.8	30.20

The microstructures of the gauge lengths differ from those of unstressed heads of the creep specimens in many aspects. The microstructures of unstressed heads are however similar to those of thermally exposed coupons for the same temperature, in terms of the dimensions of the grains and the precipitates.

Figure 4.25 and Figure 4.26 show typical microstructures of the creep rupture specimens. Unstressed head regions of the higher temperature test specimens contain coarse almost continuous precipitation along the grain boundaries and large particles randomly dispersed all over the respective matrices.

In all instances, the creep damage has been present all along the gauge length and normal to the axial load of the test pieces (see Figure 4.26). In the case of test pieces DKX, DLA and DLB, which have been tested at lower temperature, the creep damage prevails in the form of transverse intergranular cracks. In specimens tested at the higher temperature – DLH, COD and COG - the damage was mainly in the form of large voids located on the grain boundaries. There are also some oxide patches present at cracks and voids.

In general, the microstructure of the low temperature tested specimens is very similar to the microstructures of the unstressed specimens tested for prolonged exposures. This means that the same microstructural features can be recognised viz. large tungsten rich primary carbides at the grain boundaries, which are randomly distributed all over the matrix, and chromium rich carbides $M_{23}C_6$ precipitated at the original grain and annealing twin boundaries, also widely distributed within the grains. In the case of the specimen DKX tested at 650°C,

tungsten rich primary carbides do not break down to the extent that occurs in specimens DLA and DLB tested at 700°C.

At higher temperatures there are big differences between microstructures observed in the heads and in the gauge lengths of the creep rupture test pieces. The gauge length of the specimen DLH exhibits almost continuous precipitation ('pool-like' phase) along the grain boundaries with coarse particles also randomly scattered within the grains. The 'pool-like' phase has a complex composition, it is mostly chromium-nickel-tungsten rich. Primary carbides are very often embedded into the phase or coexist with it. The 'pool-like' phase has not been observed on such a large scale in the specimens thermally exposed for 30000 hours at 930°C nor even at 990°C, hence the stress plays a great role at elevated temperatures.

The specimens tested at 950°C and at 1000°C have comparable microstructures; however the specimen COD fractured after 50874 hours and the specimen COG after only 5366 (see Figure 4.26). This big difference in the tested conditions results in an identical value of Larson-Miller parameter equal to 30.2.

The microstructure of the specimen COD could be described as large almost isolated 'pools' formed by the precipitates. In the case of the specimen COG no discrete particles are present in the microstructure; the precipitation is continuous and formed along grain boundaries.

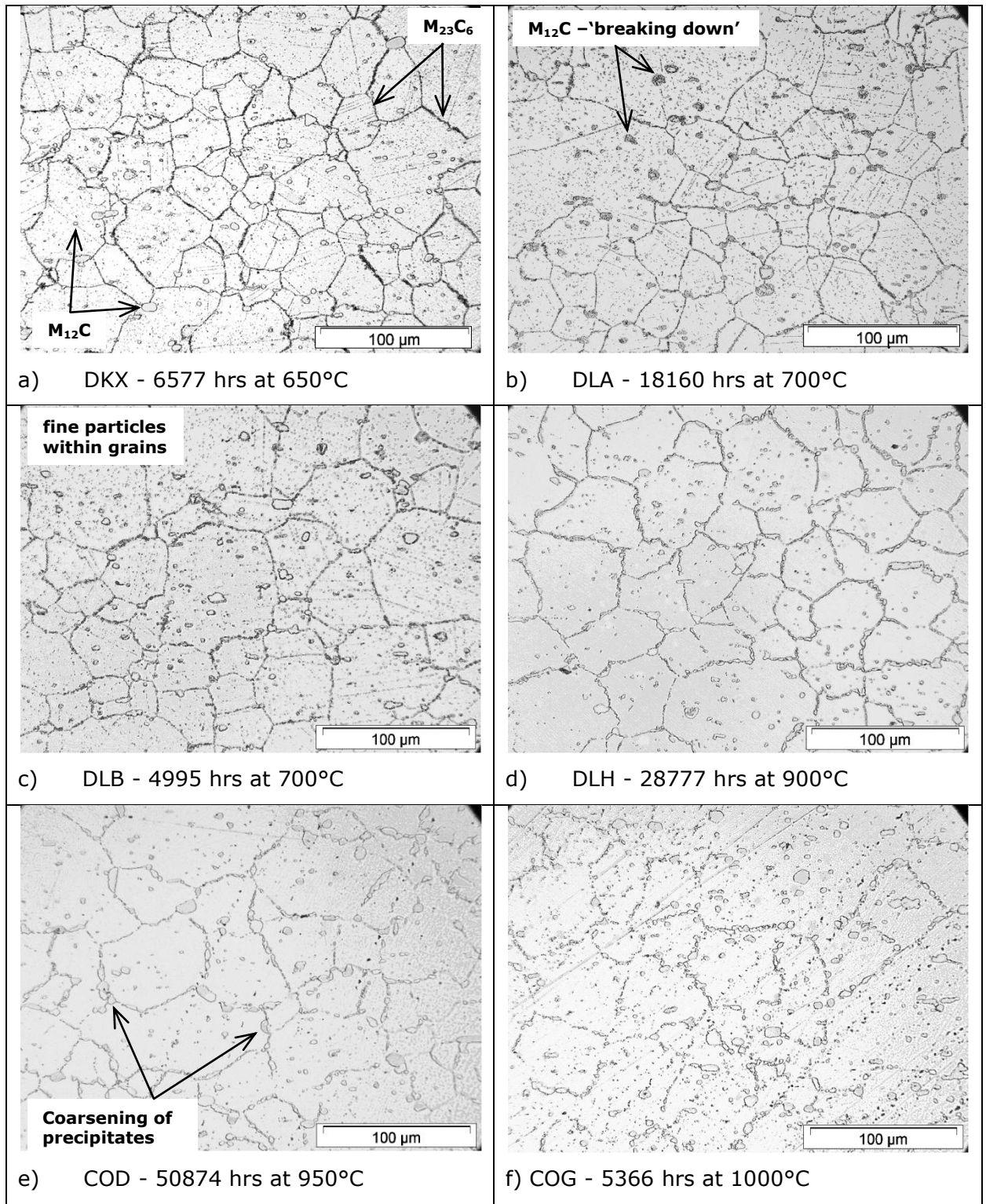


Figure 4.25 a - f: Microstructures of unstressed heads of the creep rupture test pieces.

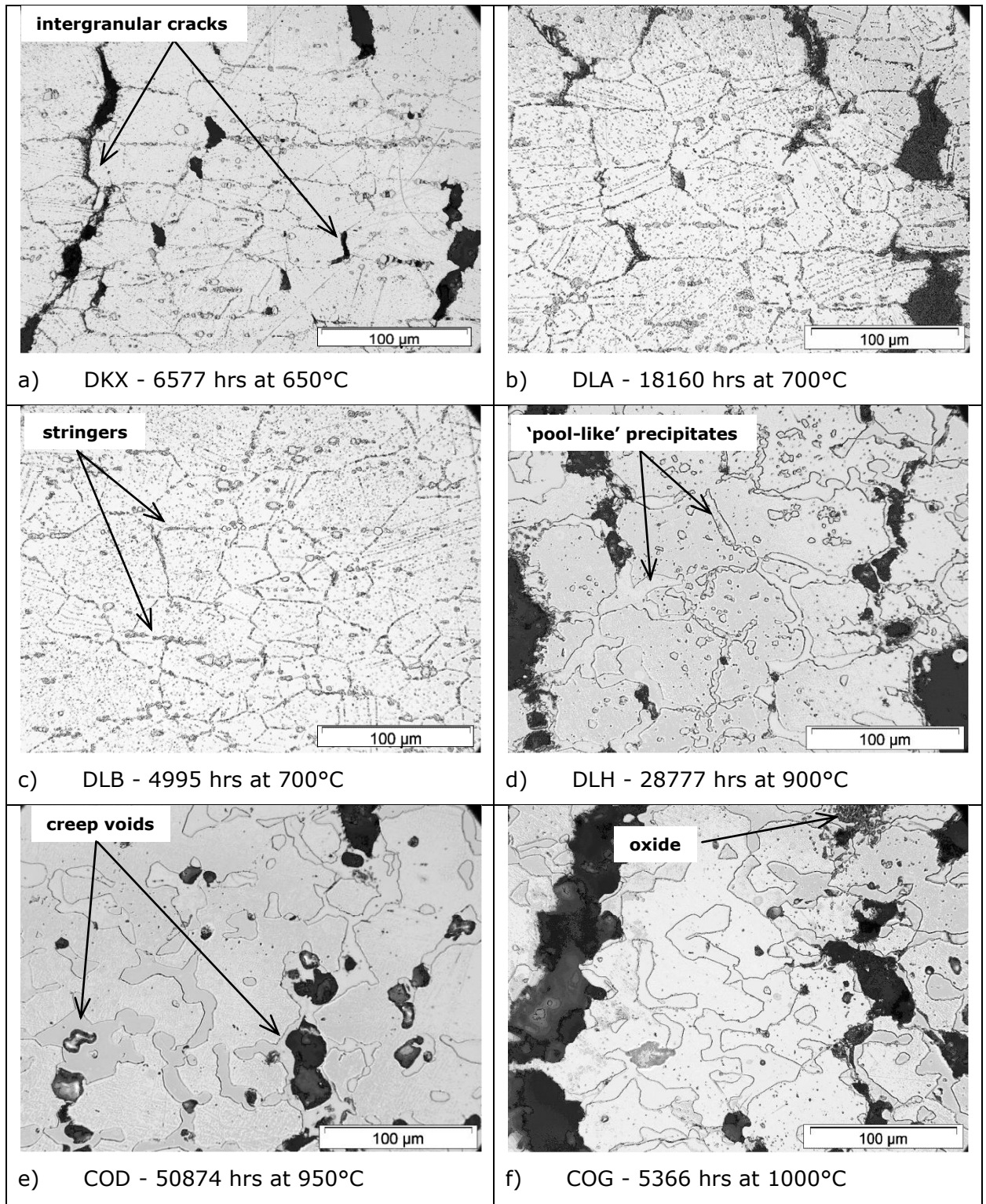


Figure 4.26 a - f: Microstructures of gauge lengths in HA230 creep rupture test pieces (applied stress axes is in the horizontal direction).

4.4.2 FEGSEM STUDIES - IMAGING

FEGSEM studies were based on secondary electron and backscattered electron imaging, and EDX analysis (*e.g.* mapping, point and line scan analysis techniques). FEGSEM studies were carried out on the as-received material, on the thermally exposed specimens and on the selected creep tested specimens. FEGSEM imaging is a very strong tool for detailed analysis of the microstructural features and their mapping on a microscale basis.

4.4.2.1 AS-RECEIVED MATERIAL

In Figure 4.27 individual characteristics of electron imaging and the main features in the microstructure of the as-received solution treated and quenched specimen is indicated. The microstructure contains some annealing twins within equi-axed grains. There are particles lying on the grain boundaries, within the grains and 'stringers' which are corresponding to the rolling direction. These were identified as tungsten rich primary carbides $M_{12}C$, some of which are smaller than 1 μm in diameter (see Section 4.4.3.1). Next to the primary carbides, irregular dark area region, can be observed. Generally, these dark features are found on elongated or on irregularly shaped particles and can be described as an empty space (void) after rearranging of primary carbides during rolling process (debonding effect).

4.4.2.2 THERMALLY EXPOSED HA230

Six specimens that had been thermally exposed for 15000 hours at temperatures in the range from 750 to 1050°C were analysed and Figure 4.28 presents the micrographs (BSI) of the microstructures.

The specimen exposed at 750°C contains the large primary carbides which are transforming ('breaking down' *i.e.* particles which were previously showing no substructure now appear to be no longer homogenous) and secondary fine precipitation which are occurring along grain and annealing twin boundaries. Secondary precipitates are rich in chromium (see Table 4.10), which is a lighter element than tungsten, thus on the image from the backscatter electron detector the particles are grey and not as bright as the primary carbides. Chromium rich precipitates are assumed to be $M_{23}C_6$ type carbides, *e.g.* reference [21] and XRD (Section 4.6). Both types of carbides start to coexist in contact, when darker precipitates can be seen in contact with tungsten rich particles.

At 810°C similar behaviour of all precipitates was observed. The transformation of the primary carbides continues, as well as formation of secondary carbides along grain and annealing twin boundaries. Phases coexist in contact or one pervades the other. It was also observed that the darker phase forms continuous precipitates rather than single particles and in the microstructure a phase (transition phase) whose composition is not uniform but mostly containing identical weight percentage of chromium, nickel and tungsten (see Table 4.10) is present.

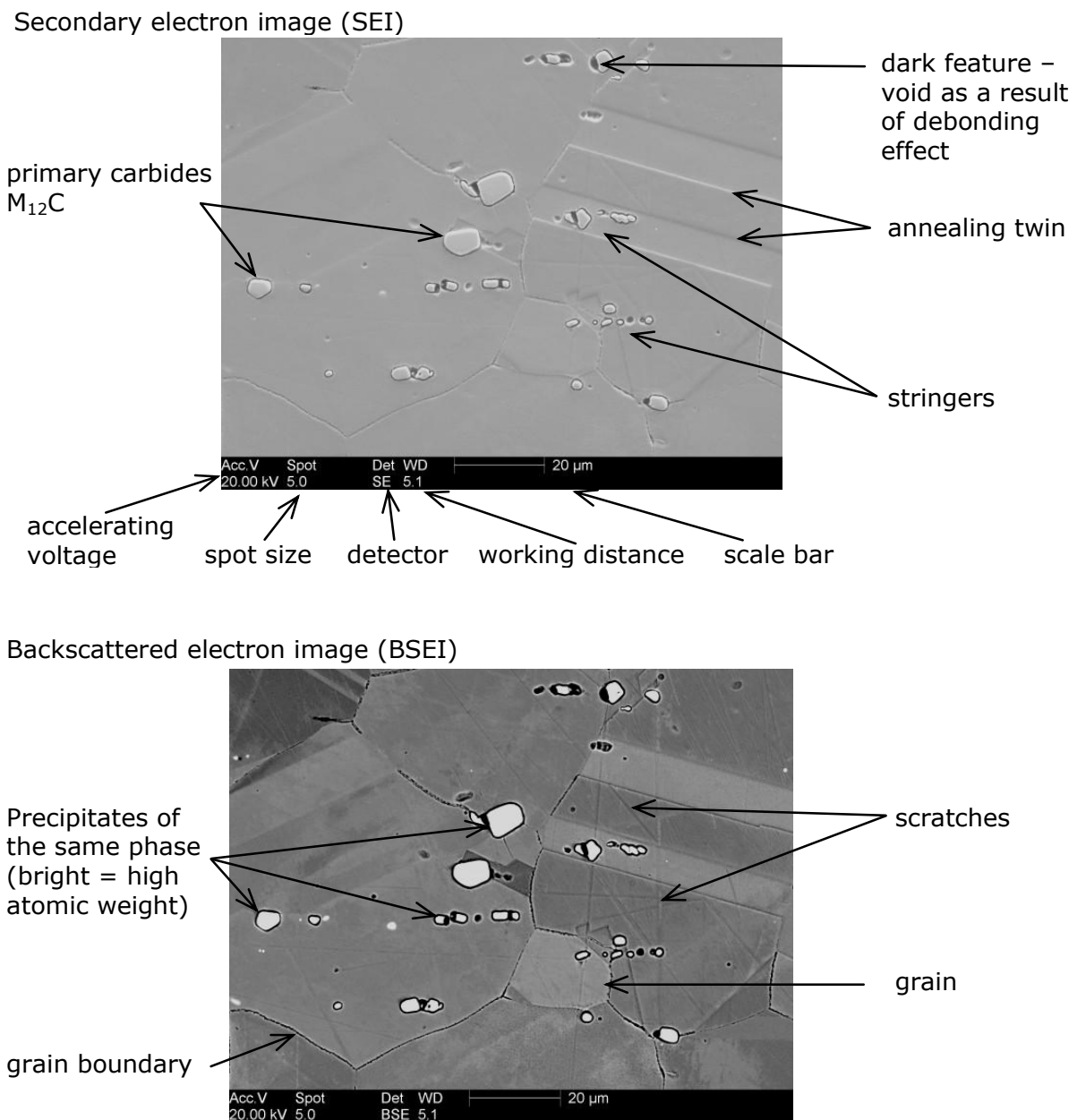


Figure 4.27 Secondary electron image and backscattered electron image of as-received HA230 indicating various features in the microstructure.

The specimen exposed at 870°C according to BSE contrast contains three phases. Within the microstructure tungsten rich, chromium rich and transition precipitates can be observed. Again tungsten rich particles are often large in size, some of them more than 10 μm , furthermore there are dark features (the area showed to have the same composition as the matrix) in the middle of the particles rather than 'break down'. As was observed at lower temperatures, phases still coexist in contact or blend together. Similar coexistence of two carbides was observed by Bhanu Sankara Rao [138] in Inconel 617. Coarsening of the chromium precipitates starts on the grain boundaries. All precipitates are irregular in shape and within the grains only few very small precipitates occur.

With increasing temperature, 930°C, dimensions of both types of precipitates, tungsten and chromium rich, increase. These larger precipitates tend to be less irregular. It seems that the transformation of the primary carbide at this temperature reaches the original stage, i.e. thermodynamically stable shape. There was clearly seen an interaction between the W-rich and Cr-rich particles depending upon the C distribution and the relative stability of the particular carbide in the structure. The phases rich in tungsten are more uniform. The composition of the large precipitates rich in chromium is less uniform as the amount of chromium varies through the particle (see Table 4.10). Smaller particles (less than 1 μm), and some dark features can be observed.

In the microstructure of the specimen exposed at 990°C two different types of particles can be found. The first type is very similar to those observed at 930°C, large particles lying on the grain boundaries and chromium rich phase adjoining the tungsten rich particles. The precipitation on the grain boundaries is not continuous anymore. Coarsening of precipitates continues and a new 'pool-like' precipitate was observed which contained cracks and consumed particles rich in tungsten. Huge 'pool-like' precipitates form at the grain boundaries which are rich in chromium.

At the highest exposure temperature of 1050°C the FEGSEM imaging shows a rise in the dimensions and in the occurrence of the 'pool-like' precipitates. Some of the 'pools' are larger than 100 μm . The other precipitates are growing also and their size is generally between 5-20 μm and the microstructure is very similar to that at 990°C.

For the comparison, Figure 4.29 illustrates the microstructural changes in the specimens thermally exposed for 20000 hours. The features occurring in the microstructure are equivalent to those observed in the specimens thermally

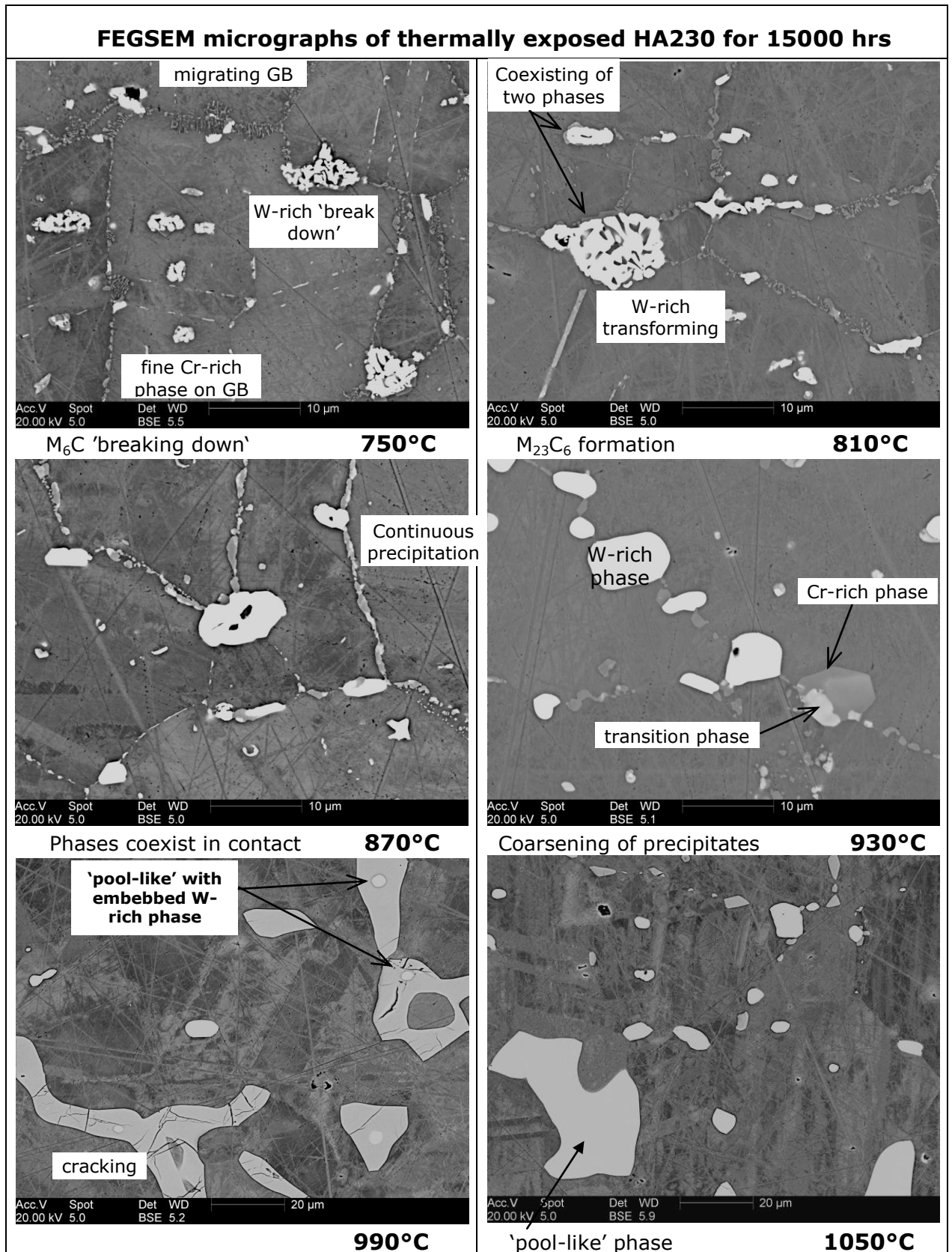


Figure 4.28 BSE micrographs showing evolution of the phases in the specimens thermally exposed for 15000 hours with increasing temperature.

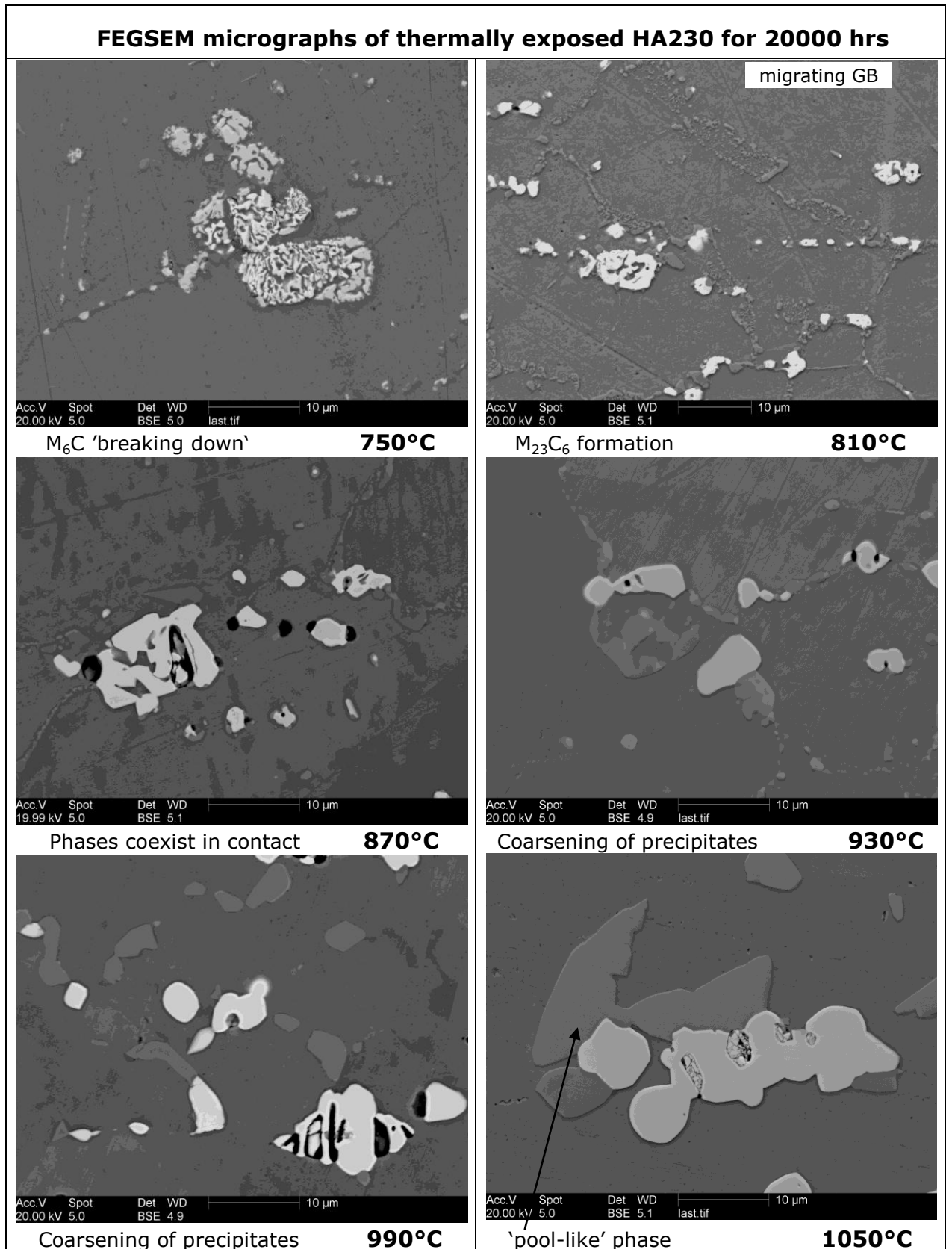


Figure 4.29 BSE micrographs showing evolution of the phases in the specimens thermally exposed for 20000 hours with increasing temperature.

exposed for 15000 hours. At the lowest temperatures (750-870°C), the transformation of primary carbide takes place and the fine Cr-rich precipitates form clusters on the grain boundaries (GB moving) moreover interfere with primary carbide. At temperatures 870-930°C the coarsening of the grain boundary precipitates occurs. At the highest temperatures 990-1050°C the 'pool-like' phase develop from the chromium rich phase which grows in the favourable areas, consuming smaller W-rich carbides and becoming more uniform in the composition. The 'pool-like' phase is very hard (see Section 4.2) and brittle.

Figure 4.30 outlines in detail the transformation of the primary, W-rich, carbide. Originally these carbides are rounded, some of them larger than 10µm. The 'breaking down' initiates at the edge on the uniform and rounded particles, when the Cr-rich phase starts to precipitate in these areas and coexistence of the two phases can be observed. As the temperature increases the W-rich carbide is transforming to its centre and then again, around 850°C, depending on the duration of exposure, gets its original shape still with some 'cracks' in the middle. In the same range of temperatures the Cr-rich phase starts to coarsen. The composition of this phase is complex and varies (transition phase Cr-rich, see Table 4.10 later).

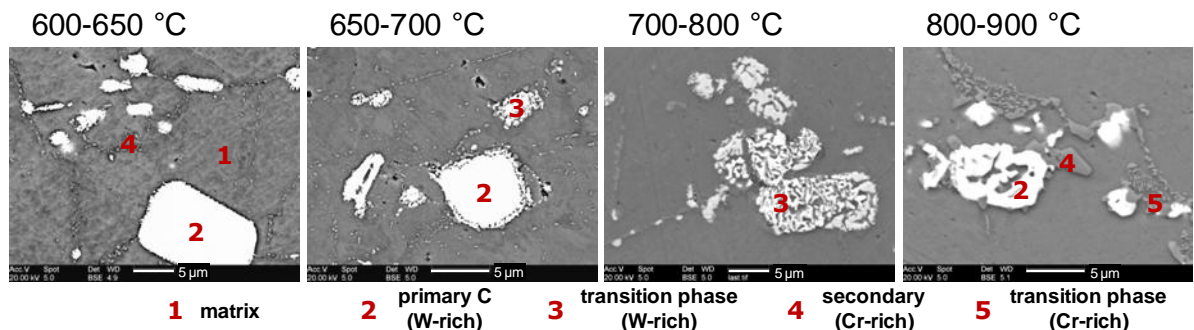


Figure 4.30 Transformation of the primary carbide with increase of the temperature.

4.4.2.3 CREEP TESTED HA230

Six creep tested specimens (see Table 4.9) at temperatures in the range from 650 to 1000°C were subjected to FEGSEM analyses. The shortest duration of testing was 4559 hours and the longest 50874 hours. Figure 4.31 and Figure 4.32 show typical micrographs of the microstructures of unstressed heads and gauge lengths of the fractured specimens.

The specimen DKX was tested at 650°C and the failure occurred after 6577 hours. In the microstructure of the unstrained head (see Figure 4.31) primary tungsten rich carbides can be observed. These are rounded or elongated particles, ranging from a few microns to 15 µm in size. The edges of these carbides are starting to transform ('break down', *i.e.* appear to be dissolving into the matrix). Along grain and annealing twin boundaries some fine secondary precipitates are distributed. In the microstructure of the gauge length cracking is evident. Big creep voids are apparent. Both types of carbides, primary W-rich and secondary Cr-rich, are present. Primary carbides are seen to be 'breaking down', not only at edges but cracks across the particles are also noticeable. Secondary carbides are present along boundaries and their appearance is more frequent than in the head of the specimen.

Two specimens were tested at 700°C; DLA fractured after 18160 hrs and DLB fractured after 4995 hrs. Comparing the microstructure on the head (Figure 4.31) with the longer duration of exposure the degradation of primary carbides (*i.e.* 'break down') is enhanced through the particles. The precipitation of secondary carbides along boundaries is more continuous and precipitates within the grains are in the form of rods. Moreover, a new form of the chromium rich phase can be observed; it is a larger and rounded particle, bigger than 5µm in diameter. The only difference in the microstructure arises from the presence of cracks and voids. Similar features can be seen on the shorter duration sample (see Figure 4.31) where the only difference between microstructures of the unstrained head and gauge length are cracks caused by tension during creep testing.

Whilst the specimens exposed at lower temperatures exhibited similar microstructures in the unstrained heads as in the gauge lengths, the high temperature creep tests showed significant differences between these regions (see Figure 4.32). The specimen DLH exposed at 900°C which fractured after 28776 hours had the same features in the microstructure of the head as the head of specimen COG which was exposed at 1000°C and fractured after 5366 hours. Precipitates in the new form (both chromium and tungsten rich) had formed along grain boundaries, and only a few precipitates were present within the grains. It was observed that these precipitates were large in size (up to 15-20 µm); some were tungsten rich (brighter particles) firstly (at 900°C) with cracks and voids and at higher temperatures uniform in shape. The darker particles (chromium rich) were not uniform in composition (contrast on the BSI) (see Table 4.10 later). It is common to find the chromium rich particles co-exist with the tungsten rich (brighter) particles in contact with each other. The microstructure of specimen COD

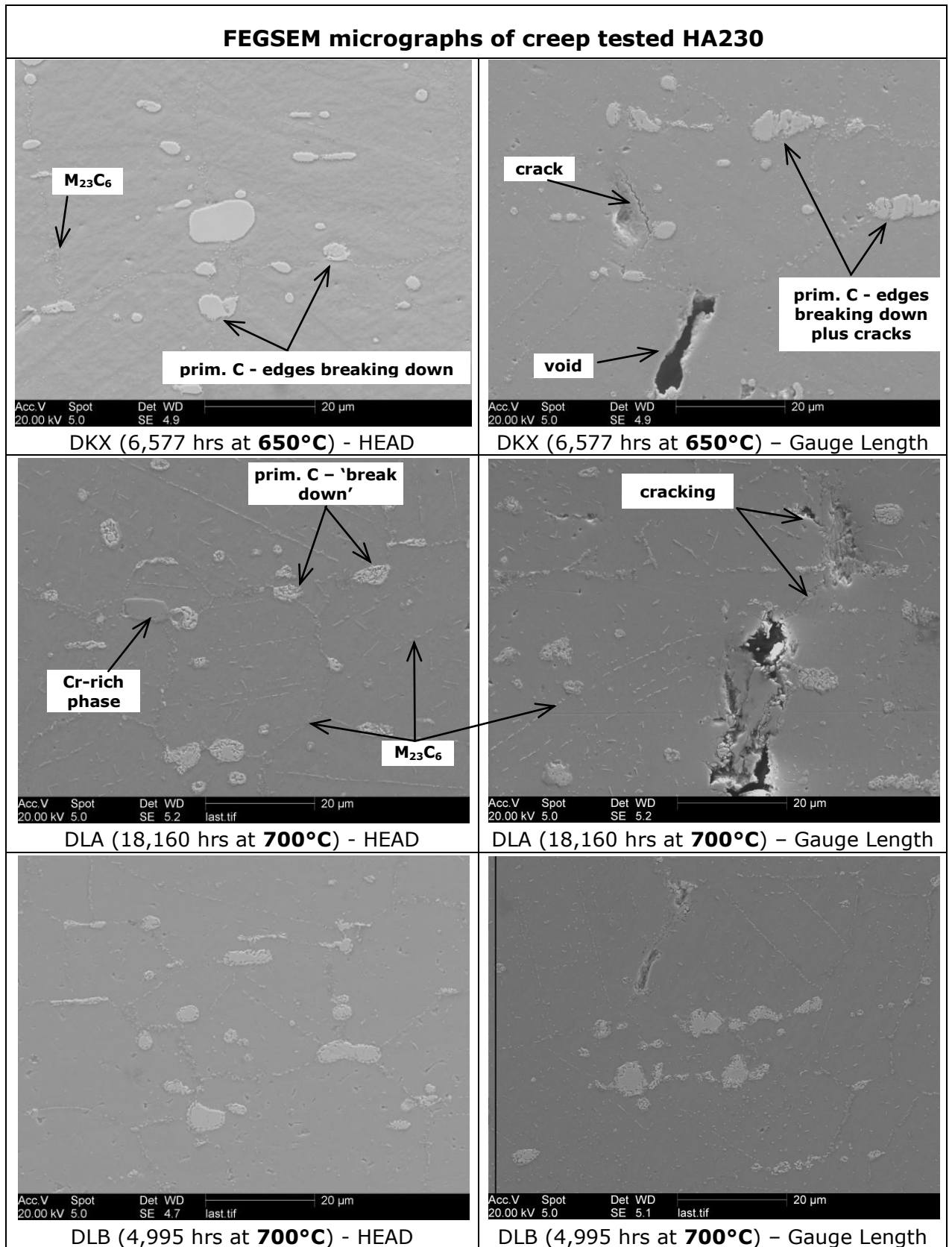


Figure 4.31 SEI of creep specimens exposed at low temperatures, comparison of the microstructures of the unstressed heads and gauge lengths.

tested at 950°C which fractured after 50874 hours is slightly different. The SEM image (see Figure 4.32) shows that the grain structure is no longer clear as in the case of the shorter tests. The microstructures of the gauge lengths of the high temperature creep specimens are characterised by the precipitation of chromium rich phases which are almost continuous along grain boundaries, mainly chromium rich (see Table 4.10) and creep voids are present adjacent to the precipitates. In the case of specimen DLH some coarse particles were randomly present within the grains.

4.4.3 ENERGY DISPERSIVE X-RAY ANALYSIS

The Energy Dispersive X-Ray (EDX) analysis was used to obtain information about chemical compositions of the matrix and of all the phases present in the microstructures of tested specimens. The data facilitated the identification of precipitated phases.

In Section 4.4.3.1 quantitative and qualitative results obtained for as-received material are presented. The results will be presented together with a description of each type of EDX analysis used. To get quantitative results, point analyses and line scans have been used. The qualitative analysis was obtained from mapping scans. The results for specimens thermally exposed and creep tested are given in the following sections.

4.4.3.1 AS-RECEIVED MATERIAL

FEGSEM images and EDX distribution maps for nickel, chromium, tungsten and molybdenum for as-received HA230 are shown in Figure 4.33. These maps clearly show the element distribution in the selected area; in this case the large tungsten rich primary precipitates are depleted in nickel and chromium and enriched in molybdenum. In addition, EDX point analyses give quantitative information about the ratio of the main elements in the primary carbide, as well as the alloy matrix and dark features; also presented in Figure 4.33. The spectra show the differences in the peak distribution. The elemental composition of the matrix and dark features (usually a hole with particle visible at the bottom) is similar which could be sign of the carbide cracking during the mechanical treatment or a result of debonding effect. A typical EDX line scan across a primary carbide precipitate with a dark area region dividing the particle is shown in Figure 4.33. Weight percents correspond to the maximum value of the present element in the line scan.

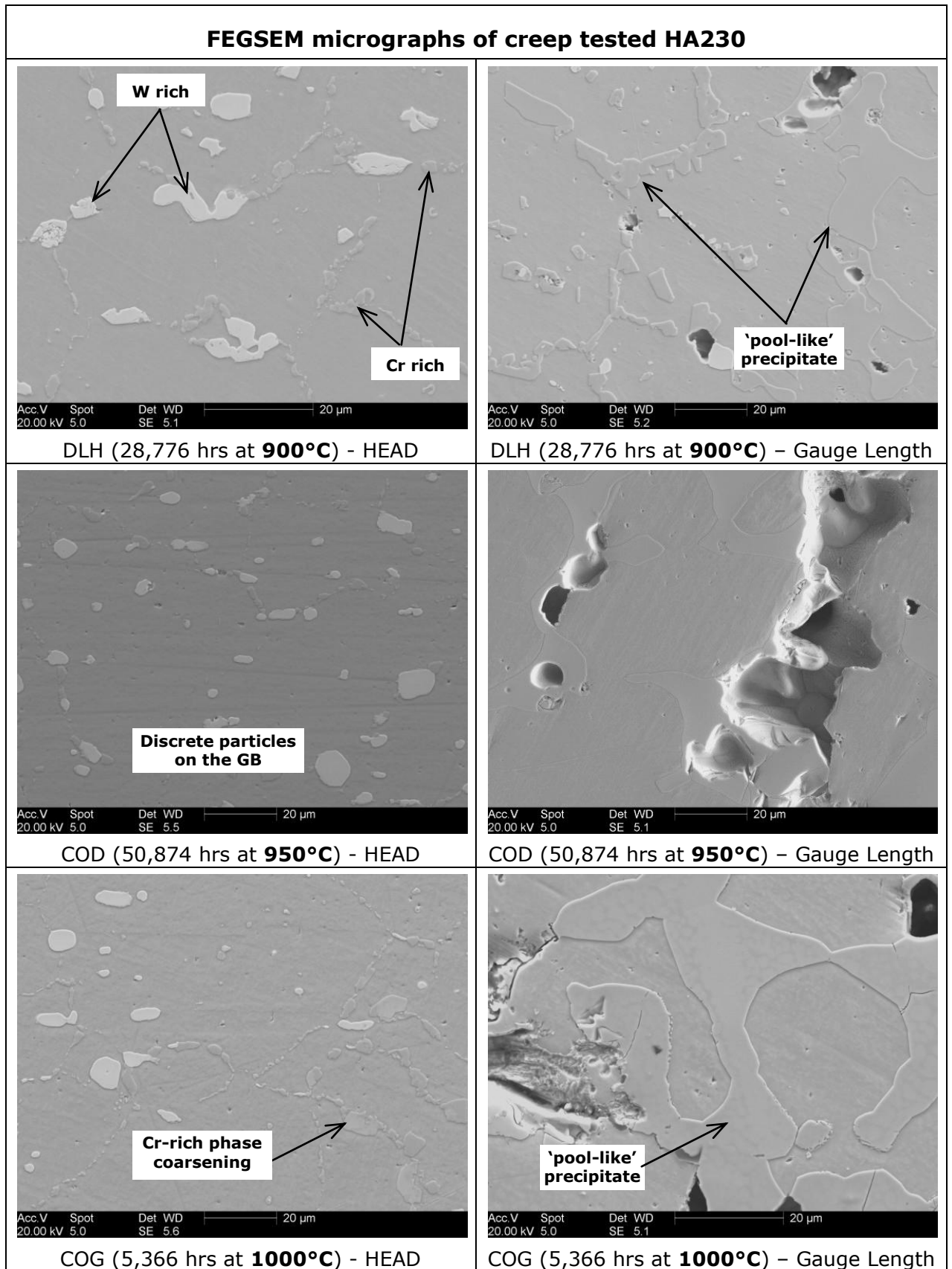
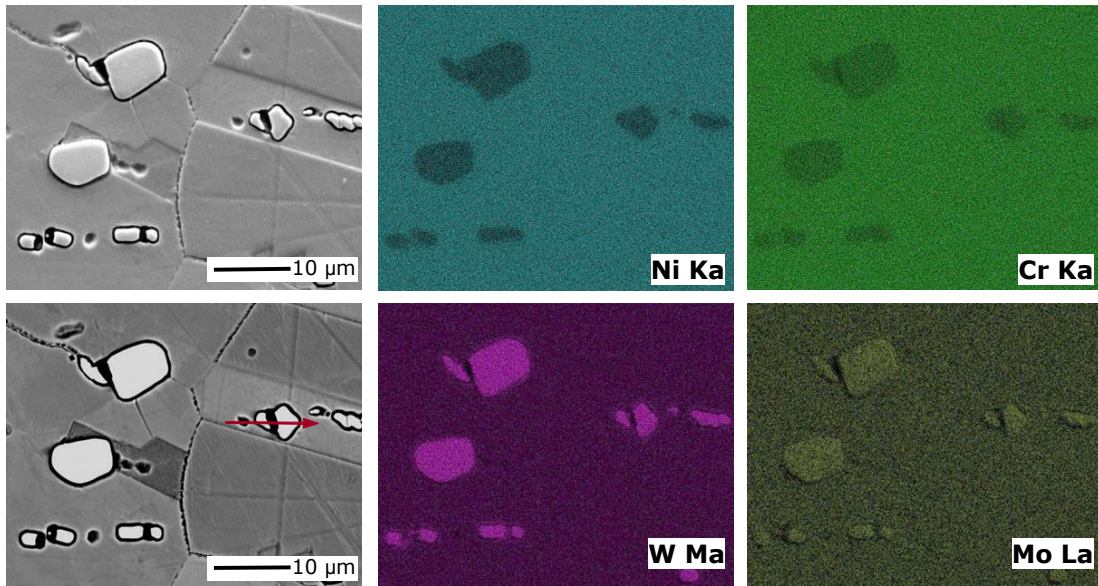
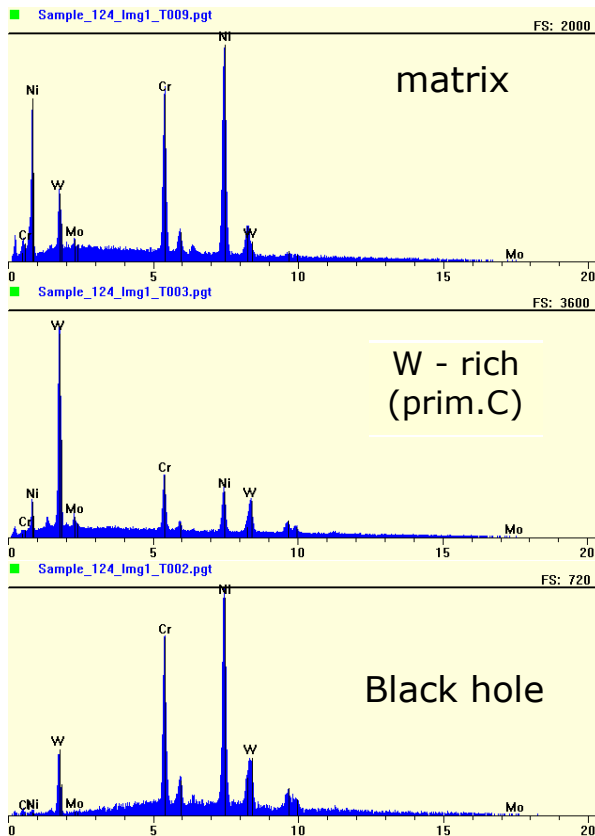


Figure 4.32 SEI of creep specimens exposed at high temperatures, comparison of the microstructures of the unstressed heads and gauge lengths.



EDX Analyses Of The Different Phases (Wt%) – as-received material				
	Ni	Cr	W	Mo
Matrix	54.1	22.3	21.2	2.5
W - rich phase (prim.C)	12.1	10.2	73.0	4.7
'black hole' - void	55.1	23.3	21.4	0.1



Spot and line analysis

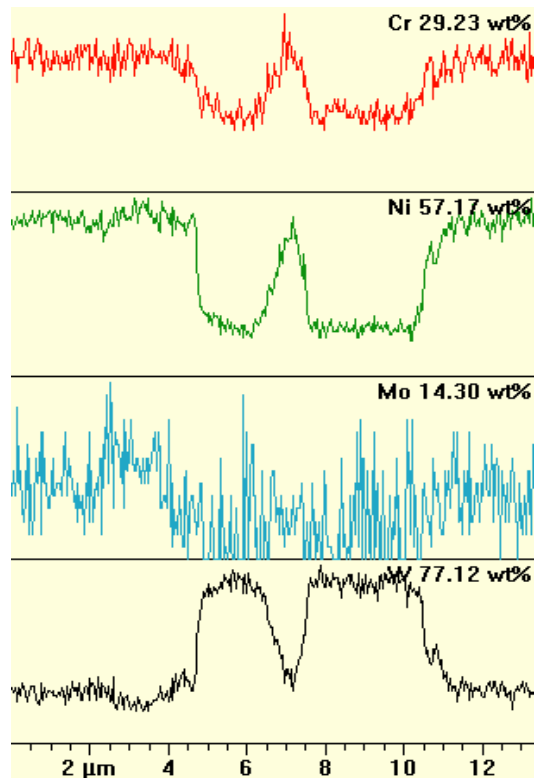


Figure 4.33 FEGSEM images and EDX analyses of as-received material.

4.4.3.2 THERMALLY EXPOSED AND CREEP TESTED SPECIMENS

Most of the thermally exposed samples and six creep tested specimens have been analysed using the EDX technique. The main focus has been on the quantification of the composition of the main precipitates in the alloy. Additionally there has been an interest in compositional changes in the matrix with increase of the temperature of exposure (with changes in the structure of precipitates). FEGSEM images and EDX results for thermally exposed and creep tested specimens follow below. The summary of the quantities of the four main elements (presented as weight percentages) is given in Table 4.10. As can be seen, four different phases plus the matrix were found. Two of them can be categorised as tungsten rich, the first one contains above 70 wt% of W and the second one around 50 wt% of W. A third is chromium rich, containing around 60 wt% of Cr and around 30 wt% of W. The fourth phase, here called transition phase, is rich in nickel-chromium-tungsten and generally contains a balanced ratio between these three elements which is around 30 wt% of each. However as can be seen in Table 4.10 the ranges of the quantities are very wide.

Table 4.10 Summary of the quantitative analyses (wt%) for four main elements in the four different types of precipitates in thermally exposed and creep tested specimens.

	Ni	Cr	W	Mo
Matrix	54.1 – 72.5	12.4 – 26.4	11.8 – 21.2	1.1 – 2.7
W - rich phase (prim.C)	10.9 – 20.2	3.6 – 14.6	61.2 – 76.7	4.6 – 8.0
W - rich phase (sec. C)	16.4 – 33.3	15.5 – 31.3	45.6 – 56.6	2.9 – 11.4
Cr - rich phase ($M_{23}C_6$)	5.1 – 19.5	54.5 – 64.0	21.4 – 36.3	2.8 – 5.1
Transition ('pool-like') phase	26.7 – 40.6	27.0 – 43.8	18.7 – 34.0	2.0 – 7.3

Table 4.11 lists the occurrence of the main phases as they have been detected in the specimens. The results show that the four main phases have not been detected in all samples. For example the Cr-rich phase is absent at lower temperatures, but as the micrographs in the previous sections demonstrate, some Cr-rich fine precipitates are present. Unfortunately the size of these precipitates is not sufficient to obtain a reliable EDX output. In some cases the values were affected by the surrounding area or there was an effect from underneath of the particle. In all such cases the values have been rejected from the analysis. Usually the results represent the average of at least 5 measurements, in many cases 10-15, with standard deviation less than 0.5.

The identification of the phases has been based on the comparison with the micrographs, with the results from XRD and with the literature. The XRD results (see Section 4.6) offered three phases with different lattice parameters only. In the as received material the phase with lattice parameter $a=10.96\text{\AA}$ should correspond to the primary carbide, W-rich, which is in the literature presented as M_6C type.

Table 4.11: The phases found in thermally exposed and creep tested specimens.

Specimen	time hours	Temperature °C	present phases			transition (‘pool-like’) phase
			W - rich phase (prim.C)	W - rich phase (sec. C)	Cr - rich phase ($M_{23}C_6$)	
thermally exposed	1000	780	X	X		X
	1000	840	X			X
	1000	900	X		X	X
	1000	1170	X		X	
	15000	750	X	X		X
	15000	810	X	X		X
	15000	870	X	X	X	X
	15000	930	X		X	X
	15000	990	X		X	
	15000	1050	X		X	X
	20000	750	X		X	X
	20000	810	X		X	
	20000	870	X		X	
	20000	930				
	20000	990	X			X
	20000	1050				
	30000	750	X		X	
	30000	810	X	X	X	
	30000	870	X		X	
	30000	930	X		X	X
30000	990	X			X	
30000	1050	X		X		
DKX	6577	650	X	X		
DLA	18160	700	X	X	X	X
DLB	4995	700	X	X		
DLH	28777	900	X		X	X
COD	50874	950	X		X	X
COG	5366	1000	X		X	X

The second phase referenced in the previous studies as Cr-rich carbide, $M_{23}C_6$ was identified by the XRD technique to have lattice parameter 10.65\AA . As is described in the XRD section, this kind of carbide has been detected in samples exposed for two different durations in all the range of temperatures. The same result has not been obtained by EDX. Sometimes the quantitative analysis is made difficult when the precipitates are not large enough or in the case of coexisting phases. At some temperatures and in some samples; this Cr-rich carbide, containing around 60 wt% of Cr, has not been identified. This fact could be

explained by the appearance of the transition phase. As was mentioned above, the transition phase contains a balanced ratio of nickel, chromium and tungsten and on the micrographs has a slightly brighter shade than the Cr-rich phase (BSI contrast). This discrepancy in contrast reflects the non uniform composition of the phase which corresponds to the variation in the ratio of the elements. The amount of W remains unchanged whereas the amount of Cr decreases and the quantity of Ni increases (Table 4.10). The fact that chromium and nickel atoms are of the similar size results in the conservation of the lattice parameter.

The last phase, secondary W-rich carbide containing between 45 – 55 wt% of W could be assigned to the lattice parameter $a=10.83 \text{ \AA}$. This phase can only be detected at the lower temperatures (750-870°C) which corresponds to the period of transformation of the primary carbide, so called 'breaking down'. The decrease of the amount of W from the original $\sim 70 \text{ wt\%}$ in the primary carbide and its substitution by the smaller atoms in the crystal are causing the shrinkage in the lattice parameter.

The plot on Figure 4.34 documents the effect of the surrounding area on the accuracy of the quantitative analysis in EDX. Some of the point analyses have been carried out on the matrix of the creep specimens in the vicinity of the other precipitates, e.g. in the middle of the Cr-rich precipitates clustering on the grain boundary. It can be seen that the amount of Ni dropped by about 10 wt% and the amounts of the other elements vary.

In addition, the relationship between the composition of the matrix and the precipitated phases has been studied. Figure 4.35 compares the compositions of the specimens exposed at 750°C and at three different durations of exposure with the composition of as-received material. The data show the similar amounts of the four main elements in as-received material and the sample thermally exposed for 15000 hours; in the other two samples the amount of nickel is higher and the amount of tungsten lower. The composition of the specimen thermally exposed for 20000 hours is comparable with the composition of the alloy. The fact that there could be some decrease of the amount of chromium (i.e. precipitation of chromium rich phase on the grain and annealing twin boundaries) has not been observed. The next figure (Figure 4.36) represents changes in the composition in the matrix in the specimens thermally exposed for 30000 hours at six different temperatures. No big changes in the composition can be observed. Generally for the entire set of analysed specimens the amount of nickel in the matrix slightly increases with

increasing temperature, the amounts of chromium are slightly decreasing and the quantities of tungsten and molybdenum stay unchanged.

Cr-rich phase and the transition phase have not been found in all the samples or at least as the whole range of six main temperatures, therefore no trends can be deduced. Only significant changes in the composition have been observed in the case of the W-rich phase, see Figure 4.37a). After 1000 hours of exposure the composition of the phase remains stable, but after longer exposures (Figure 4.37 b)) a distinct drop in the amount of W (about 10 wt%) can be observed while the quantity of chromium rises by approximately the same amount. The quantities of other two elements not change.

Despite the fact that the EDX technique is a rather accurate method for evaluation of the composition and although multiple analyses have been carried out, some ambiguous results have been obtained.

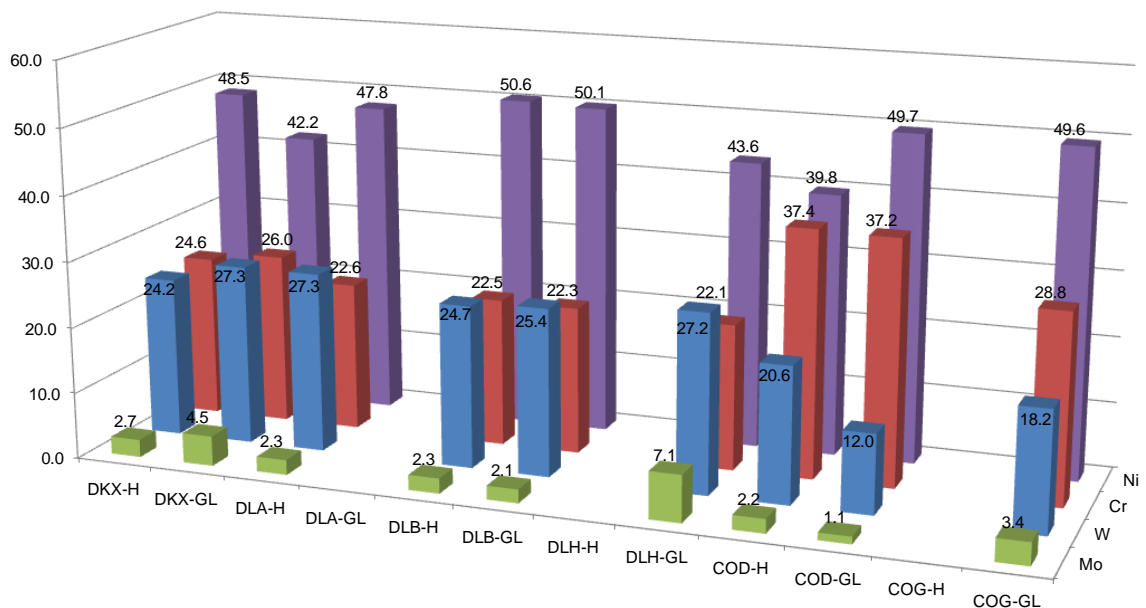


Figure 4.34 EDX quantitative analyses on the matrix of the creep specimens in the vicinity of the other precipitates.

SUMMARY

In this section, the microstructural evolution of the phases in the thermally exposed and creep tested specimens was reviewed. The W-rich primary carbides are transforming with increase of the temperature: at intermediate temperatures they are 'breaking down', depleting in W, and at higher temperatures they are transforming back. At 500°C, a Cr-rich phase starts to precipitate on the grain

boundaries. With increase of the temperature its morphology changes from fine precipitation to coarser particles reaching the 'pool-like' shape at 990°C. The presence of plastic deformation during creep testing makes the coarsening of the secondary carbide faster. Cr-rich carbide was identified as $M_{23}C_6$ with a complex composition which is modifying during exposure.

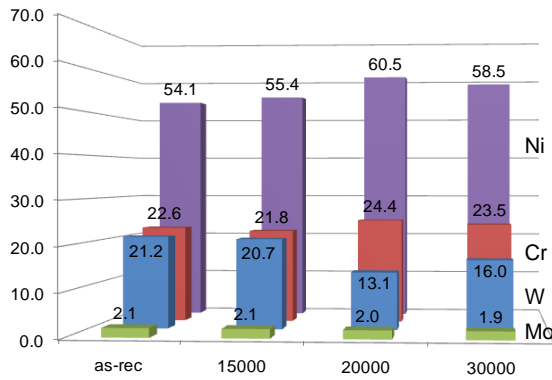


Figure 4.35 The comparison of the composition of the matrix with the samples thermally exposed for 15000, 20000 and 30000 hours.

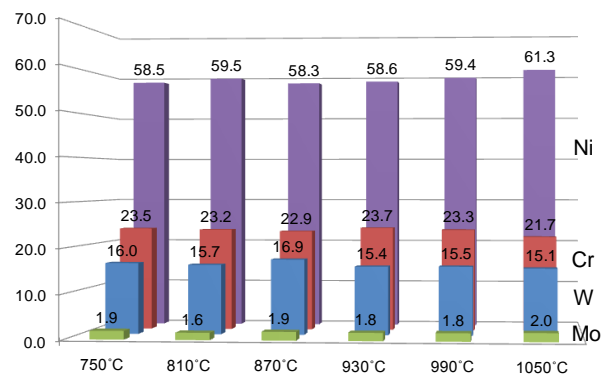


Figure 4.36 The comparison of the composition changes of the matrix with increasing temperature in the samples thermally exposed for 30000 hours.

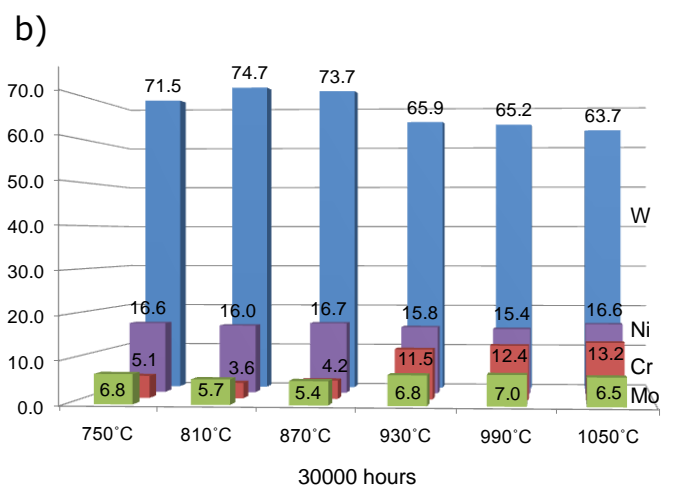
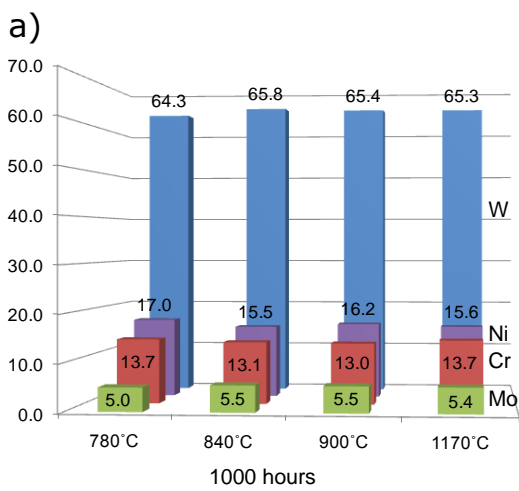


Figure 4.37 The comparison of the composition of the W-rich phase in samples thermally exposed for a) 1000 hours and b) 30000 hours.

4.5 TRANSMISSION ELECTRON MICROSCOPY

The first stage of Transmission Electron Microscopy studies was focused on the as-received material with the aim of developing and optimising the technique before examining the tested samples. The detailed preparation of the TEM specimens was described in Section 3.3.3. Since it is widely recognised that the preparation of the thin HA230 foils for TEM studies is extremely difficult, a number of different preparation techniques has been investigated in order to determine the most suitable procedure to adopt. The most successful approach to date has been the Focused Ion Beam technique.

TEM studies have been focused on the identification of phases formed as a result of a long term thermal and creep exposure on the alloy using electron diffraction and EDX analysis techniques.

The majority of prepared thin foils from as-received (solution annealed and quenched) material were still very thick, with only a narrow area adjoining the perforation transparent. These electron transparent areas were not large enough for more detailed analysis of the microstructure comprising all features and phases. Moreover, the primary carbides $M_{12}C$ (see Section 4.6), which are extremely hard, are absolutely non transparent. They appeared as the large black spots in the microscope images (Figure 4.38).

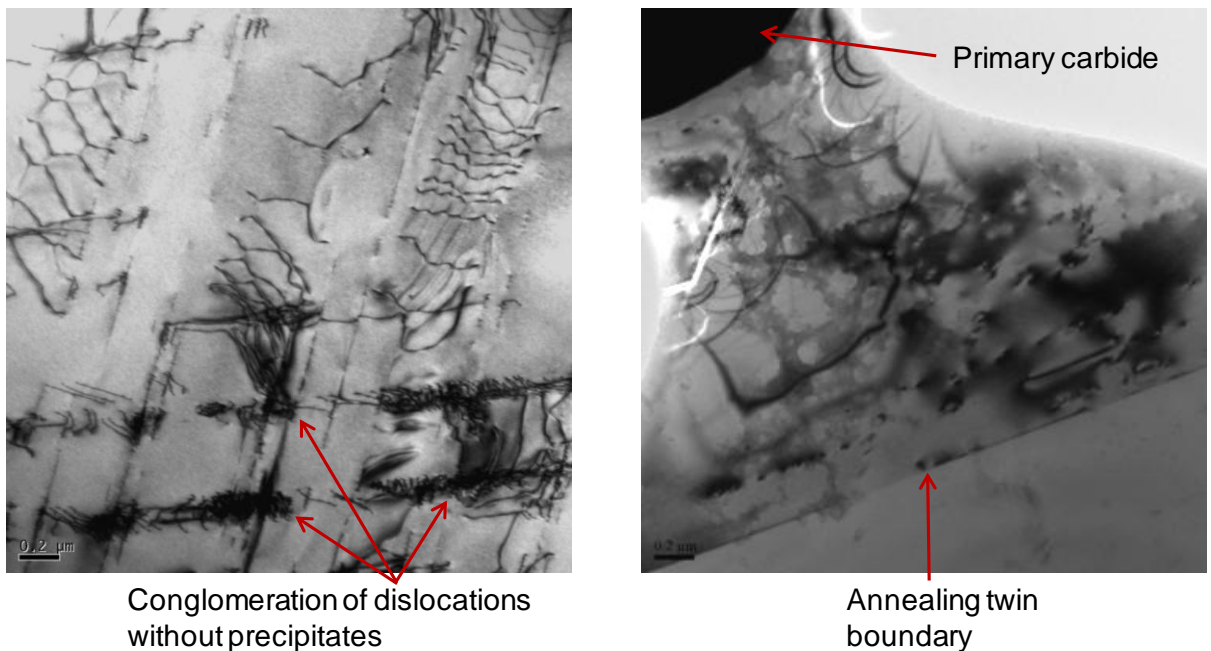


Figure 4.38 TEM images of the microstructure of the as-received HA230 with the systems of dislocations on the slip planes, annealing twin boundaries and primary W-rich carbides.

Figure 4.38 emphasises the microstructure with the systems of dislocations on the slip planes. Because the dislocations lie in the distinct 'slip bands', they were identified as being generated by the flattening operations performed during the sheet manufacture. Their density is not too high, approximately as what would be expected from $\sim 1\text{-}2\%$ stretching [139]. There are no precipitates along the dislocations.

Very fine precipitates, Cr-rich carbides, were found along some grain boundaries, which could be observed in Figure 4.39. Dislocation arrays were also observed often associated with annealing twins within the matrix. However, under this condition no evidence of precipitation was found to be present on dislocations within the microstructure.

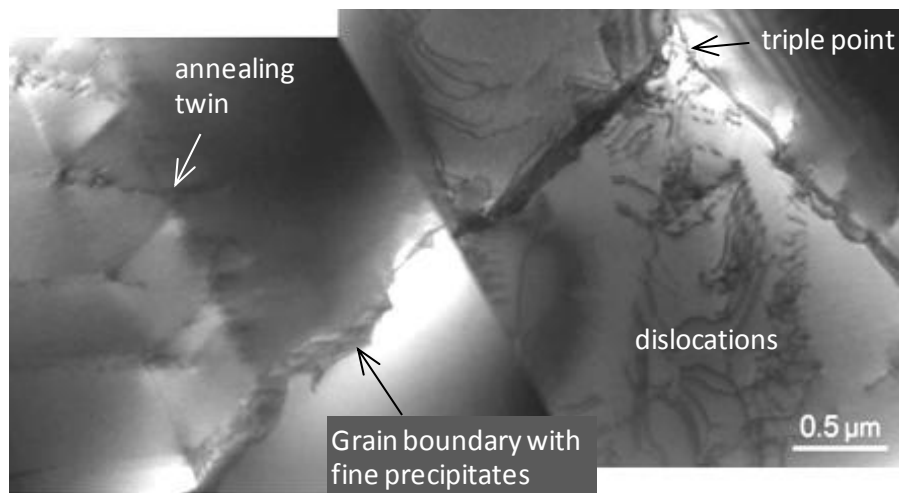


Figure 4.39 TEM images of the microstructure of the as-received HA230 showing triple points, dislocations, annealing twins and fine precipitation on the grain boundaries.

Oxford Materials (University of Oxford), namely Dr C. Hetherington, helped with the TEM sample preparation as well as with a subsequent electron microscopy and data analysis. The help was offered under the EPSRC Equipment access scheme. Two specimens were thinned using the Focused Ion Beam, the first was from the specimen thermally exposed for 15000 hours at 1050°C (Figure 4.40) and the second was the specimen creep tested for 50874 hours at 950°C (COD) (Figure 4.42). Both specimens were preliminarily studied, therefore additional work could bring further information.

Figure 4.40 shows the in-situ lifted out sample from the microstructure of the thermally exposed specimen which was studied in HRTEM 4000 in the Oxford Materials. In the sample three different phases have been found. Numbers 1 to 3 label the secondary phase, numbers 4 and 5 the gamma matrix and number 6 is

another secondary phase. Some diffraction patterns have been obtained, all of them are from the cubic structures. The identification and indexing of the diffraction patterns was performed, and the outcome is summarized in Figure 4.41. As the lattice parameter of the nickel matrix in HA230 is known - 3.573 Å (details provided in Section 4.6), the [110] electron diffraction pattern was used as a calibration for the indexing other diffraction patterns. The scatter of the lattice parameter values calculated from the other reflections varies reasonably. The details are given in Table 9.4 (Appendices).

The estimation of the lattice parameters from other electron diffraction patterns has not provided uniform results. The lattice parameter of the W-rich phase according to the calculation lies between 10.71- 11.72Å and the lattice parameter of the second phase lies between 12.17-12.90Å.

Figure 4.42 shows a SEM image of an H-bar sample of the specimen creep tested for 50874 hours at 950°C (COD) which was studied using the Jeol TEM 2010 in the Oxford Materials. The sample contains three different phases: the gamma matrix, W-rich carbide and Cr-rich 'pool-like' phase. In addition, several fields (dark grey) of an oxide can be observed. Figure 4.43 is a TEM image (HAADF) of the thinned area. The identification and indexing of the diffraction patterns was carried out as described above (see Table 9.5, Appendices). Four different diffraction patterns for the gamma matrix were evaluated and the lattice parameter determined corresponds to the one obtained from XRD (see Figure 4.44 later). The other four diffraction patterns have been indexed but not assigned to any phase because of the variability of the lattice parameter. The $a=8.17\text{Å}$ indicates the possibility of an oxide with a cubic structure, *e.g.* Al_2O_3 often found in the oxide fingers and in the cracks of the creep specimens.

The measurements from TEM images have exhibited scatter due to, for example, hysteresis in the lenses, leading to the actual magnification/ camera length differing from the nominal magnification/ camera length. As a consequence it was not possible to distinguish crystal structures with close lattice parameters as is the case of the carbides in the Haynes Alloy 230.

SUMMARY

The preparation of the thin HA230 foils with a large electron transparent area was extremely difficult. TEM studies confirmed the absence of the Cr-rich precipitates on the dislocations in the as-received material and the presence of two secondary phases with cubic structure at highest temperatures.

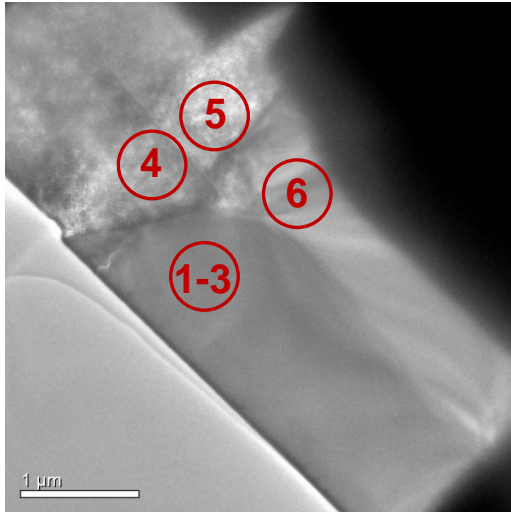


Figure 4.40 TEM image of in-situ lifted out specimen (15000 hours at 1050°C) showing the areas where electron diffraction patterns (Figure 4.41) were taken.

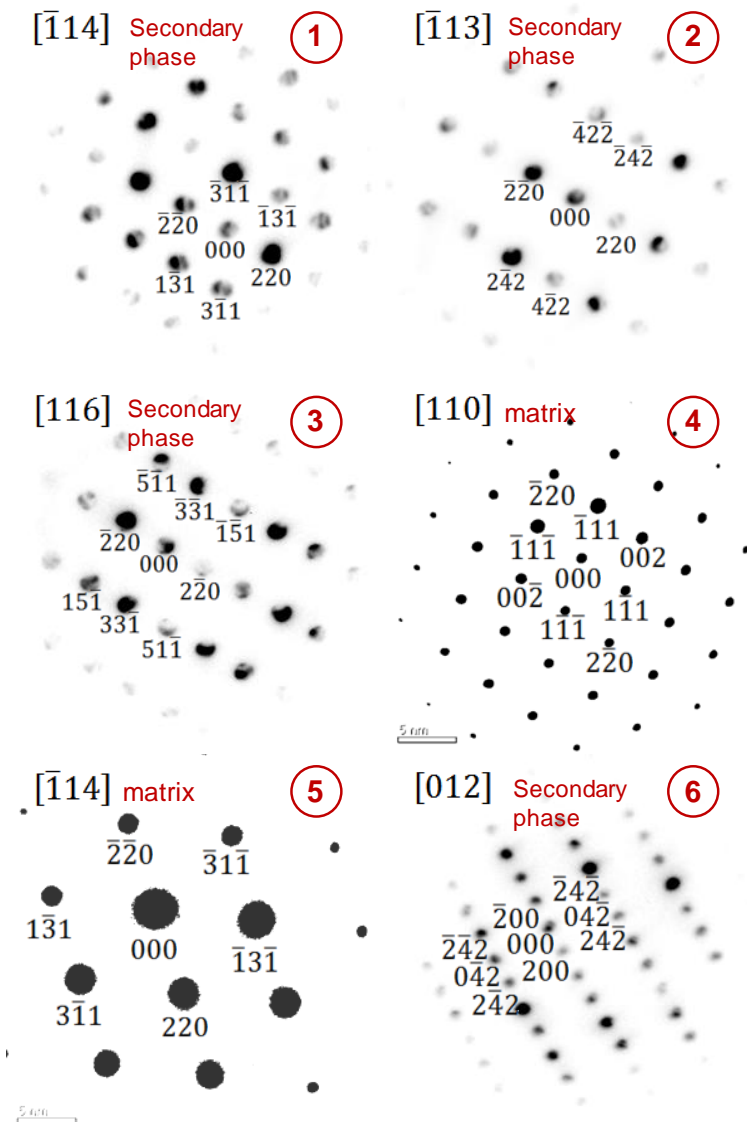


Figure 4.41 Electron diffraction patterns of the thermally exposed specimen (15000 hrs @ 1050°C). Zone axes and indexes are indicated. [140]

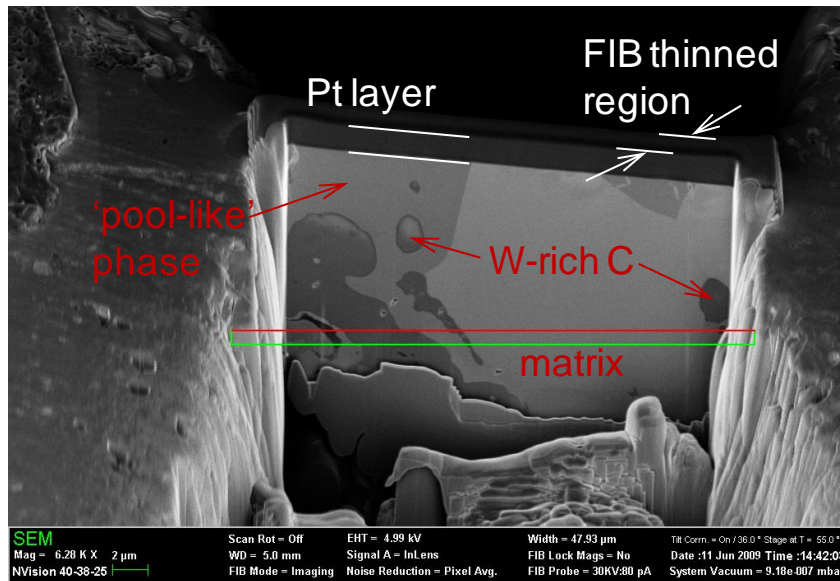


Figure 4.42 SEM image of H-bar specimen (COD) showing the features in the microstructure.

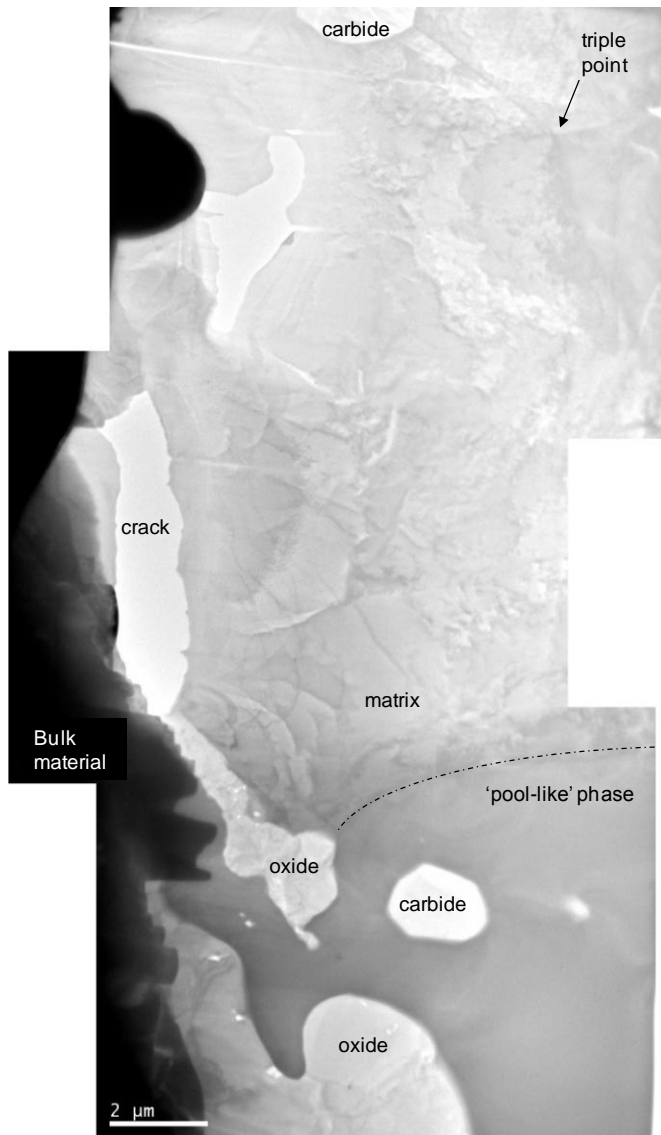
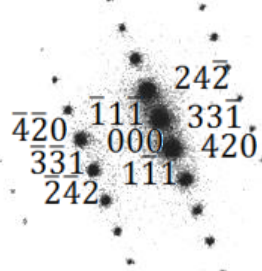


Figure 4.43 TEM image (HAADF) of the creep specimen COD (H-bar).

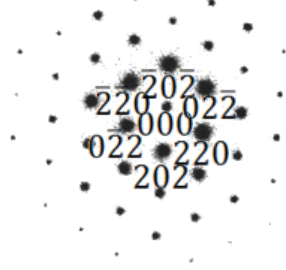
[012] Secondary phase



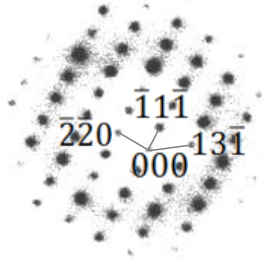
$[\bar{1}23]$ Secondary phase



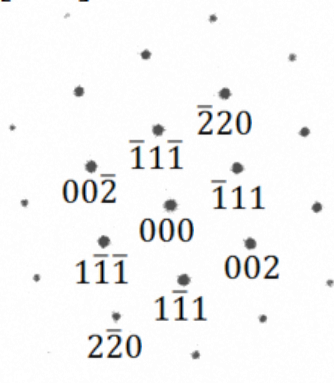
$[\bar{1}11]$ Secondary phase



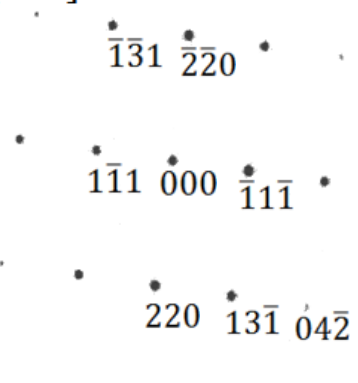
$[\bar{1}12]$ Secondary phase



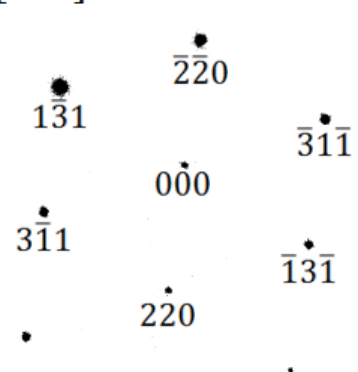
[110] matrix



$[\bar{1}12]$ matrix



$[\bar{1}14]$ matrix



[521] matrix

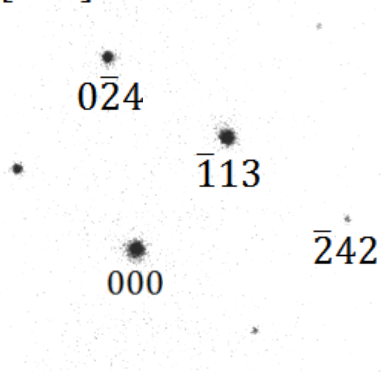


Figure 4.44 Electron diffraction patterns of the creep tested specimen (COD). Zone axes and indexes are indicated. [140]

4.6 X-RAY DIFFRACTION

X-Ray diffraction as a tool for phase identification and structural information has the biggest potential to describe the phase transformation during the thermal exposure. Firstly, the analysis has been carried out on the bulk material taking the advantage of this non destructive technique, but the necessity to map the phase evolution led to the need of phase extraction. Differences between the preparation approaches are summarised in Section 3.4. The following types of samples were studied:

A. bulk material with highly polished surface

1. As-received material
2. Specimens thermally exposed for 3000 hours at 600°C, 650°C, 700°C, 750°C, 810°C, 870°C, 930°C, 990°C and 1050°C.

B. phases extracted from the bulk material

1. As-received material
2. Specimens thermally exposed for 3000 hours at 750°C, 810°C, 870°C, 930°C, 990°C and 1050°C and for 20000 hours at 750°C, 810°C, 870°C, 930°C, 990°C and 1050°C.
3. Transition duct specimen

The X-Ray radiation used for all measurements is that emitted by copper, with characteristic wavelength (λ) 1.5418Å (Cu). The parameters were optimised to obtain sufficient signal response. The step size was set to the lowest possible of 0.016° and the speed to 0.15°/min. The details about calibration of the diffractometer are given in Section 9.8.2.

The tests carried out on the samples from the bulk material revealed some features in the spectra which disallowed the peak assessment. The main problem was the background noise which covers the minor peaks and also the intense Ni-matrix peaks which could cover the peaks of other phases. Relationships between 2θ and intensities (represented by number of counts) were obtained and typical spectra for HA230 '3000 hours set' are shown in Figure 4.45. Figure 4.46 illustrates the comparison of the spectra obtained for as-received material. The bulk material spectrum provided the information about the lattice parameter of the matrix and the spectrum of extracted phases determined the positions of the primary carbide.

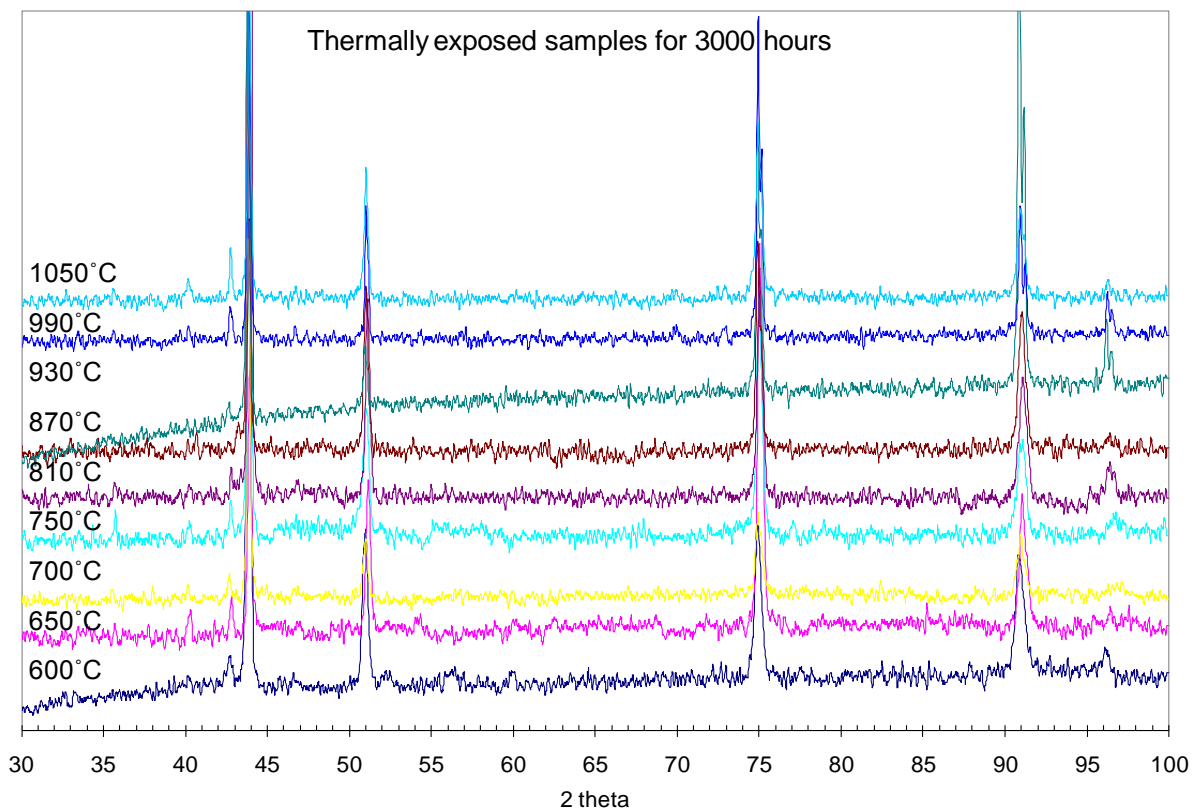


Figure 4.45 XRD spectra of specimens thermally exposed for 3000 hours at various temperatures (bulk material).

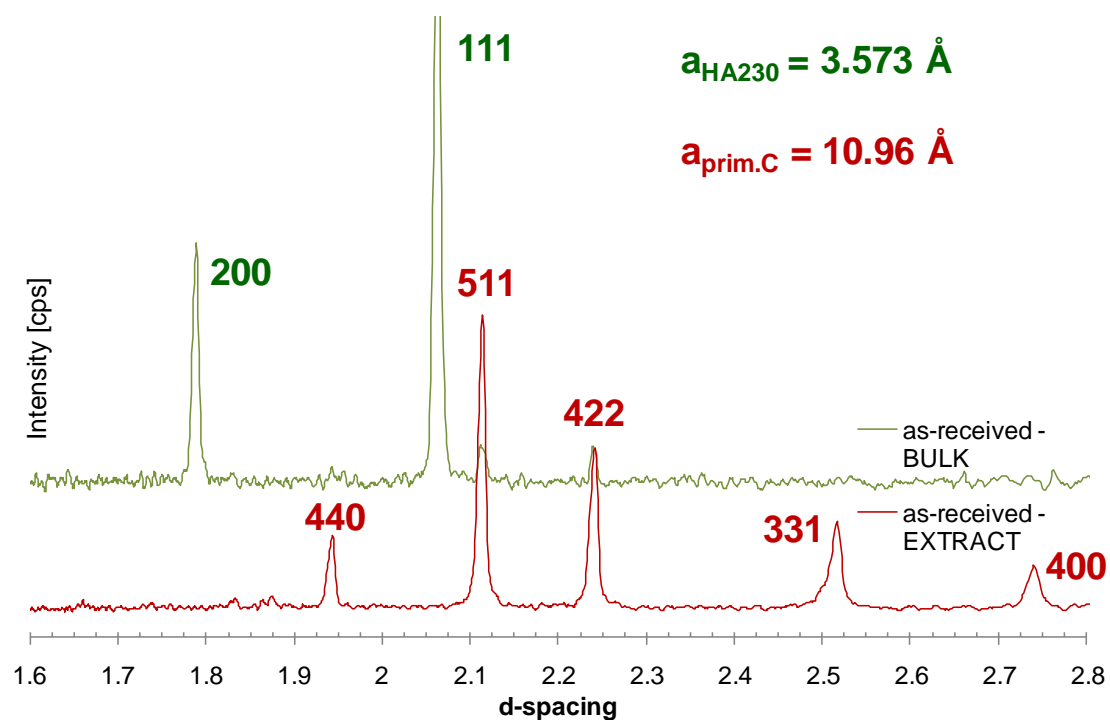


Figure 4.46 XRD spectra of as-received material showing the difference between the spectra obtained from bulk material and from extracted powder with indexed peaks.

The peak assignment was completed manually using the powder diffraction data provided by Professor V. Vodárek [127], by using on-line free databases [141, 142] and the accuracy of the results was consulted with Dr Koloušek [143]. The lattice parameter for Haynes Alloy 230 of 3.573Å was calculated from the diffractogram (see Figure 4.46).

$$a = d * \sqrt{h^2 + k^2 + l^2} \quad \text{Equation 4.3}$$

where d is d-spacing of the peak with Miller indexes hkl. Thus for the strongest (100%) peak 111 the lattice parameter corresponds to

$$a_{111} = 2.063 * \sqrt{1^2 + 1^2 + 1^2} = 3.573\text{Å} \quad \text{Equation 4.4}$$

The lattice parameter plays important role in subsequent phase precipitation (*e.g.* distribution, size) [144]. The lattice parameter of pure fcc nickel is 3.523 Å (JCPDS 4-850). The elements, such as W, Mo, with atomic radii 1.41 Å, 1.39 Å respectively, affecting the macroscopic distortion of the lattice parameter, are present in this alloy. The smaller atoms with comparable size to Ni (1.24 Å) such as Cr, Co, Fe are causing local lattice distortion only (*e.g.* magnetic spin direction).

More unambiguous peak assignment was possible in the diffractograms of the extracted phases. Figure 4.47 shows the spectra for thermally exposed specimens for 3000 hours. Clearly there are three phases present within the range of temperatures between 750°C to 1050°C. The results confirm the presence of the primary carbides with lattice parameter $a=10.96\text{Å}$ in the gamma matrix in the as-received material. The peak assignments determined the peaks of the other two, secondary phases with lattice parameters 10.65Å and 10.83Å.

Figure 4.48 illustrates the assignment of the peaks in the spectra of specimen thermally exposed for 20000 hours at 870°C. The primary carbide with $a=10.96\text{Å}$ is very close to the carbide, generally distinguished as $M_{12}C$ with a lattice parameter equal to 10.95Å and composition Fe_6W_6C (JCPDS 23-1127). The secondary precipitation contains two phases close to the structure of the carbides $M_{23}C_6$ with $a=10.66\text{Å}$ ($Cr_{23}C_6$ JCPDS 35-783) and $M_{12}C$ with $a=10.89\text{Å}$ (Co_6W_6C JCPDS 23-939).

The overlay of the XRD spectra for extracted phases from specimens thermally exposed for 20000 hours, Figure 4.49, documents the phase evolution within the temperature range from 750°C to 1050°C. As was mentioned above, as-

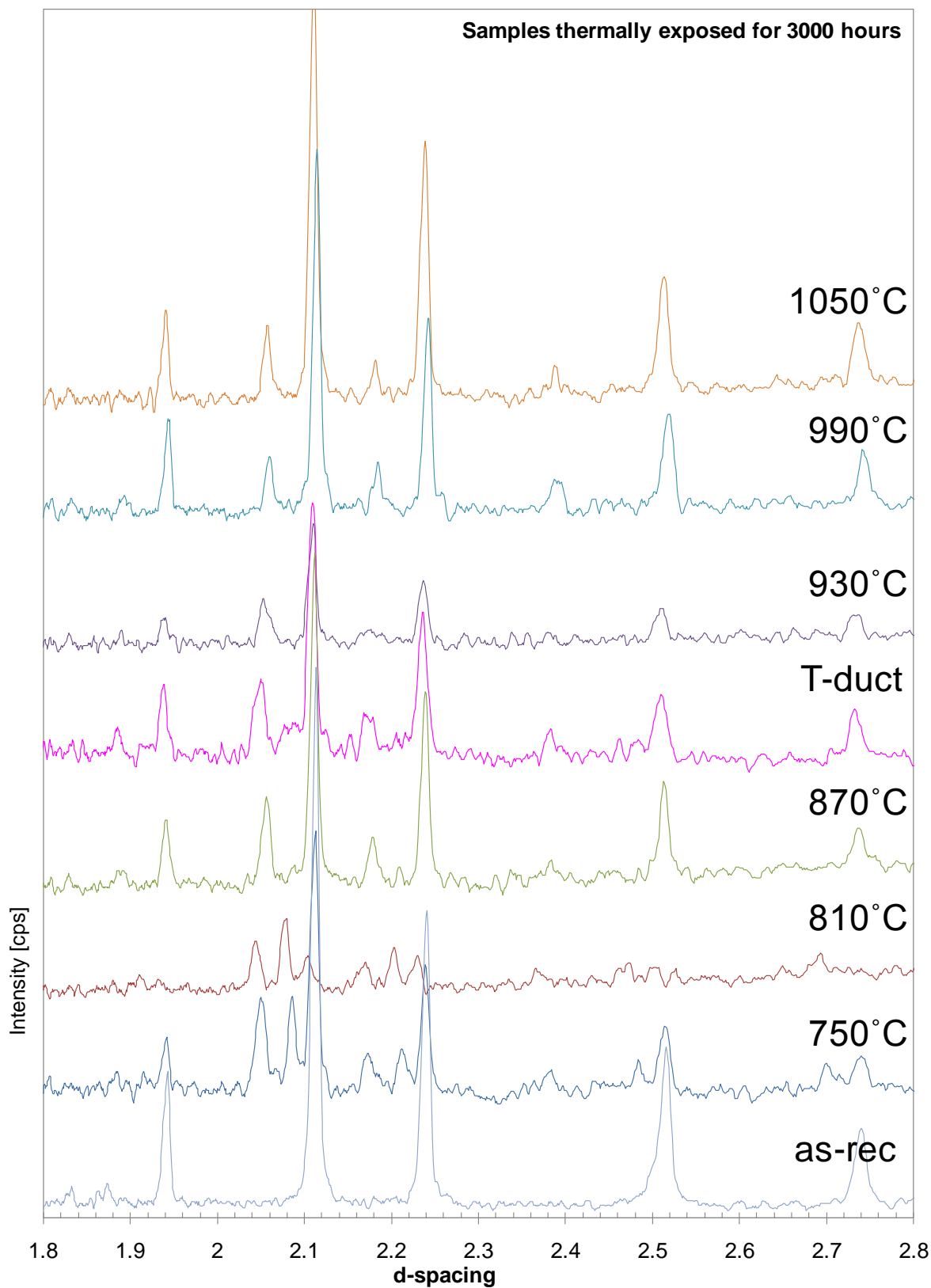


Figure 4.47 Overlay of XRD spectra acquired for extracted phases from the bulk material, samples: as-received, thermally exposed for 3000 hours for six different temperatures (810°C shows lower intensities) and Transition Duct.

received material contains carbide with the lattice parameter of 10.96\AA , called primary $M_{12}C$. This phase was not detected at 750°C and 810°C . The small peak appears again at 870°C and the increase of its intensity can be observed with increase of the temperature. The peaks of two new secondary phases appear at 750°C . One is the carbide with lattice parameter of 10.65\AA which corresponds to $M_{23}C_6$ carbide. Other peaks correspond to the lattice parameter $a=10.83\text{\AA}$ labelled as secondary $M_{12}C$. All these carbides are complex and M stands for Cr, W, Ni, Fe, Co. The composition of the carbides was presented in detail in Section 3.3. Considering the overall intensities of the diffractograms, $M_{23}C_6$ has the lowest intensity at 750°C ; for other temperatures the intensity does not change. Very interesting is the behaviour of the secondary $M_{12}C$. The evolution of this carbide as well correlated with the duration of exposure as shown in Figure 4.50. While at 750°C after 3000 hours the peaks of primary $M_{12}C$ can be observed, after 20000 hours only peaks of secondary $M_{12}C$ are present. At the exposure temperature of 990°C , the duration of exposure does not play such an important role for the primary $M_{12}C$ carbides. Only a slight increase of the intensities of the secondary $M_{23}C_6$ has been observed.

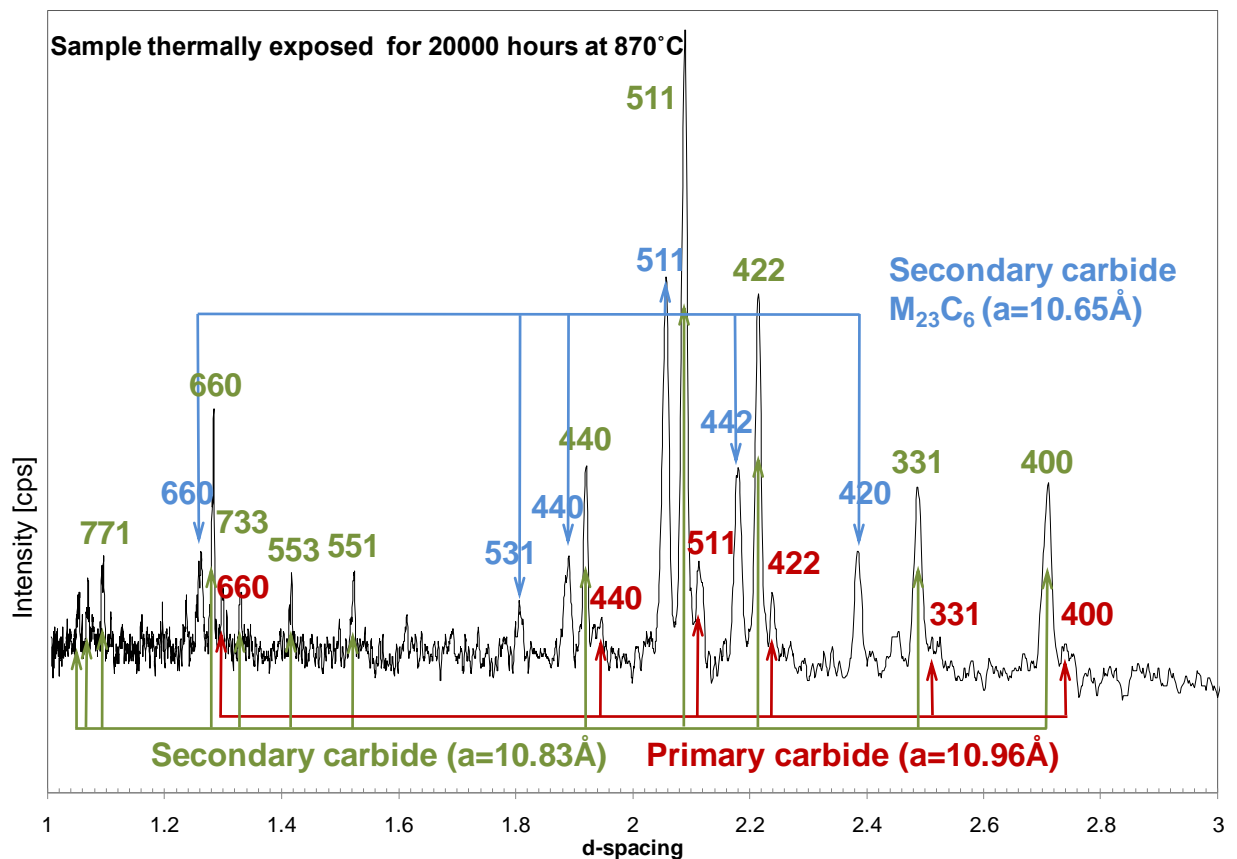


Figure 4.48 The peak assignment in the spectra of specimen thermally exposed for 20000 hours at 870°C – extracted phases.

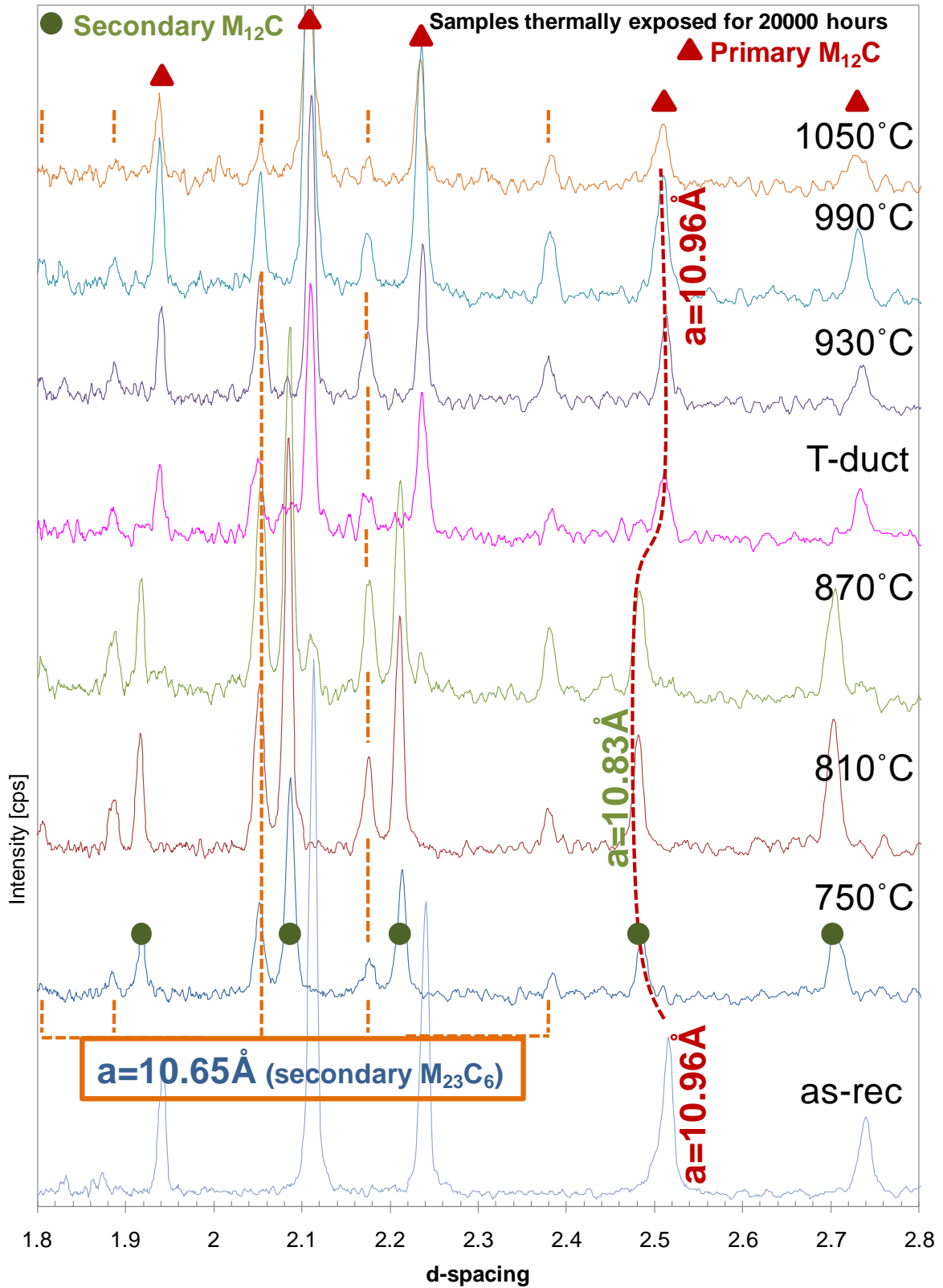


Figure 4.49 Overlay of XRD spectra acquired on specimens thermally exposed for 20000 hours, as-received material and a specimen from Transition Duct – extracted phases.

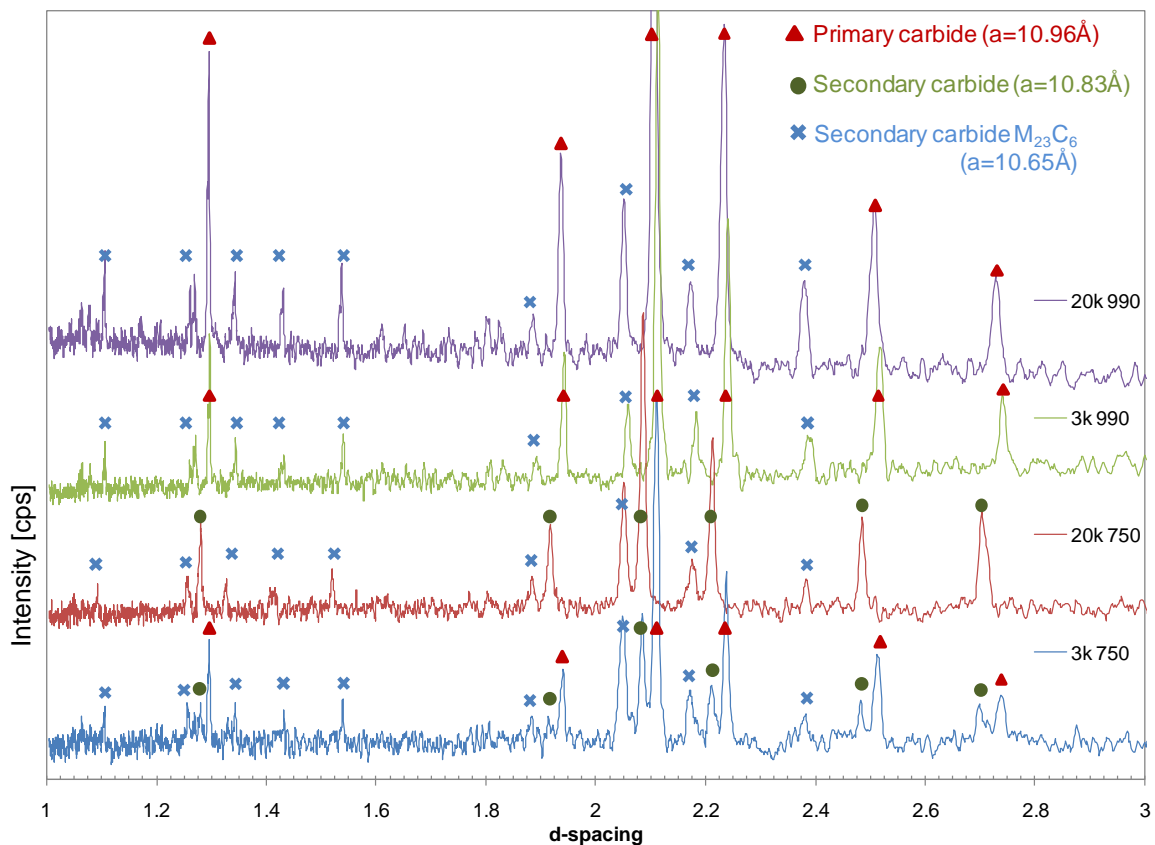


Figure 4.50 Overlay of XRD spectra acquired on specimens thermally exposed for 3000 and 20000 hours at 750°C and 990°C.

In the case of the transition duct, the XRD spectra could help with the mean temperature estimation after approximately 11000 operating hours of this ex-service component, as illustrated in Figure 4.49. The presence of all three phases suggests the temperature range between 870°C and 930°C. The presence of the intense primary carbide $M_{12}C$ peak and vanishing peaks of secondary carbide $M_{12}C$ suggest that the temperature of operation was approximately in the middle of this interval (900°C).

It can be concluded that the amount of $M_{23}C_6$ is constant but the composition varies. The explanation could be that the atomic size difference between Cr and Ni is very small, therefore the atoms are easily exchanged, while in mostly Cr-rich carbide, Cr atoms (probably needed to form protective oxide layer) are replaced by Ni atoms. The powder diffraction data confirm the fact that the difference between the lattice parameters of the two different $M_{23}C_6$ carbides, namely $Cr_{23}C_6$ ($a=10.66\text{\AA}$; 65-3132) and $(Cr, Co, Ni)_{23}C_6$ ($a=10.64\text{\AA}$; 11-545) is insignificant. Table 4.12 provides the summary of the phases detected in the extracted powder from HA230.

Table 4.12 Summary of the phases found in the extracted HA230.

	1° M ₁₂ C fcc a=10.96Å	M ₂₃ C ₆ fcc a=10.65Å	2° M ₁₂ C fcc a=10.83Å
as-rec	X max		
3k 750°C	X	X	X ↑
3k 810°C	X min	X	X max
3k 870°C	X	X	X ↓
3k 930°C	X	X	
3k 990°C	X	X	
3k 1050°C	X max	X	
20k 750°C		X	X ↑
20k 810°C		X	X
20k 870°C	X ↑	X	X
20k 930°C	X	X	X ↓
20k 990°C	X max	X	
20k 1050°C	X max	X	
T-duct	X ↑	X	X ↓

SUMMARY

The lattice parameter of the HA230 gamma matrix was determined by XRD to be 3.573Å. Other three phases (chemically extracted from the bulk HA230) have been identified as primary carbide M₁₂C with lattice parameter a=10.96Å, secondary carbide M₁₂C with a=10.83Å, detected between 750-870°C, and secondary carbide M₂₃C₆ with a=10.65Å.

4.7 ELECTRON PROBE MICRO ANALYSIS (EPMA)

Electron Probe Micro Analysis (EPMA) is in principal similar to an SEM equipped with solid-state energy dispersive spectrometry (EDS). This technique was chosen only to compare the results from the EDS and the wavelength-dispersive system (WDS) used for the quantitative analysis by this instrument.

The analysis was carried out on the samples thermally exposed for 15000 hours in the temperature range of 750-1050°C. The surfaces of the specimens have been highly polished. The focus was on the analysis of the similar phases (features) as during the EDX. In total, 107 measurements were carried out, approximately 20 measurements per sample. Only results providing quantities above 85 wt% in total have been selected for the further calculations.

Tables 4.13 – 4.16 summarise the data for the four main phases observed: gamma matrix, W-rich phase, Cr-rich phase and transition phase. Each table lists

the appearance of this phase in the samples and the average of the composition of the phase over the whole temperature range.

Graphic representations of these data are plotted in Figure 4.51 – 4.55.

The composition obtained for the gamma matrix does not suggest significant fluctuation of the mass fraction of single elements. In the case of the specimen exposed at 930°C the values are slightly lower. This can be observed for all phases; generally the values were lower so this sample has been excluded from the calculations.

Table 4.13 Composition of the matrix (wt%) of the samples thermally exposed for 15000 hours obtained by EPMA.

Wt%	avg	sd	1050	sd	990	sd	930	sd	870	sd	810	sd	750	sd
Ni	59.2	3.8	61.1	2.3	61.6	2.2	51.7	0.0	61.6	2.2	57.4	2.0	55.8	3.2
Cr	21.4	1.0	20.6	0.5	21.9	0.6	19.4	0.0	22.3	0.5	20.9	0.4	21.5	0.9
W	12.5	1.5	11.5	0.1	11.8	0.4	11.1	0.1	12.4	0.6	13.8	2.3	13.7	1.8
Mo	1.2	0.1	1.2	0.0	1.2	0.0	1.2	0.1	1.3	0.1	1.2	0.1	1.4	0.1
Co	0.2	0.0	0.2	0.0	0.2	0.0	0.1	0.0	0.2	0.0	0.2	0.0	0.1	0.0
Fe	1.5	0.1	1.6	0.1	1.6	0.0	1.4	0.0	1.6	0.1	1.5	0.0	1.5	0.1
Total	96.0		96.1		98.2		85.0*		99.4		94.9		94.0	

* this result is out of line with the others and sample should be reanalysed.

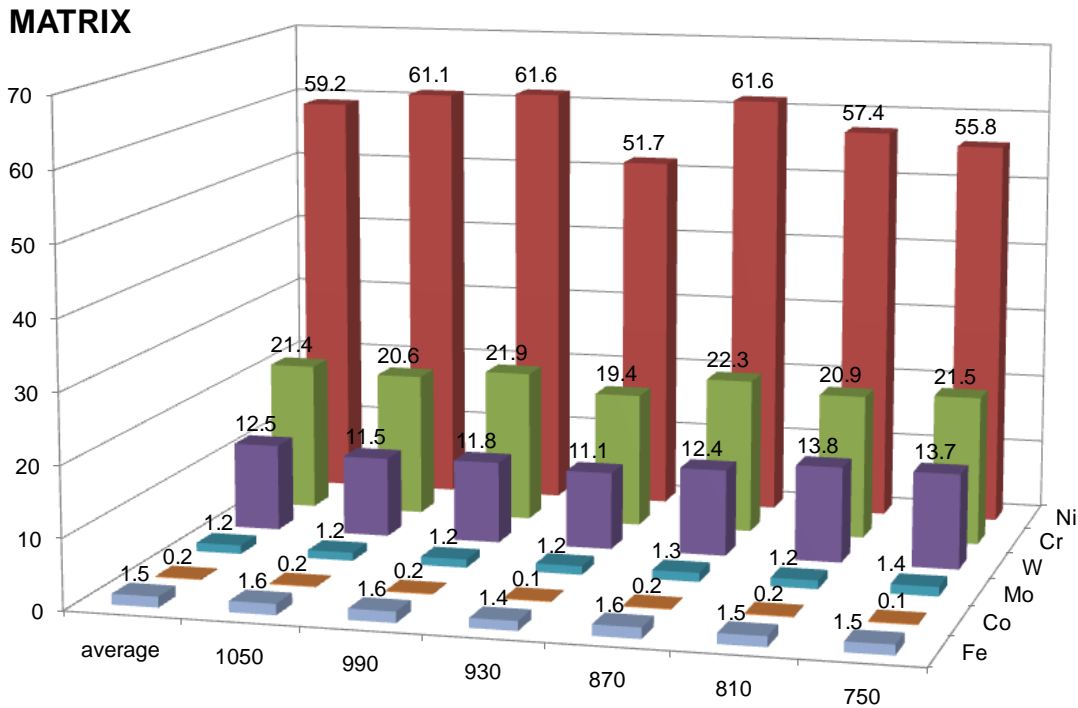


Figure 4.51 Composition of the matrix (wt%) of the samples thermally exposed for 15000 hours obtained by EPMA.

The mass fraction of tungsten in W-rich phase was about 55 wt% in the all samples. Interestingly the amount of Ni and Cr is different in the low temperature samples (750-870°C) and in the high temperature samples (930-1050°C). While the mass fraction of Ni is higher at lower temperatures, approx. 26 wt%, and of Cr lower, approx. 10 wt%, at the higher temperatures the amount of Ni decreases to 20 wt% and the amount of Cr increases to 13 wt%.

Because of the fine structure of the Cr-rich phase, it has not been properly analysed at the lowest temperatures. The high temperature specimens contained more than 63 wt% of Cr, above 5 wt% of Ni, and approx. 23 wt% of W.

Table 4.14 Composition of the matrix (wt%) of the samples thermally exposed for 15000 hours obtained by EPMA.

Wt%	avg	sd	1050	sd	990	sd	930	sd	870	sd	810	sd	750	sd
Ni	22.3	4.1	19.4	0.3	19.5	0.5	17.0	0.1	26.6	2.3	26.1	3.8	25.9	2.0
Cr	11.6	2.6	14.0	0.3	13.2	0.3	12.0	0.1	8.2	2.6	10.4	2.7	10.4	1.4
W	56.2	2.7	56.3	0.9	57.8	0.4	52.2	1.3	58.5	4.3	54.5	2.2	54.6	0.8
Mo	4.9	0.7	5.4	0.1	5.5	0.1	5.1	0.4	4.3	0.7	3.9	0.7	4.5	0.1
Co	0.1	0.0	0.1	0.0	0.1	0.0	0.1	0.0	0.1	0.0	0.1	0.0	0.1	0.0
Fe	0.5	0.1	0.4	0.0	0.4	0.0	0.4	0.0	0.5	0.0	0.6	0.0	0.5	0.0
Total	95.6		95.7		96.6		86.8*		98.2		95.5		96.1	

* this result is out of line with the others and sample should be reanalysed.

W - rich

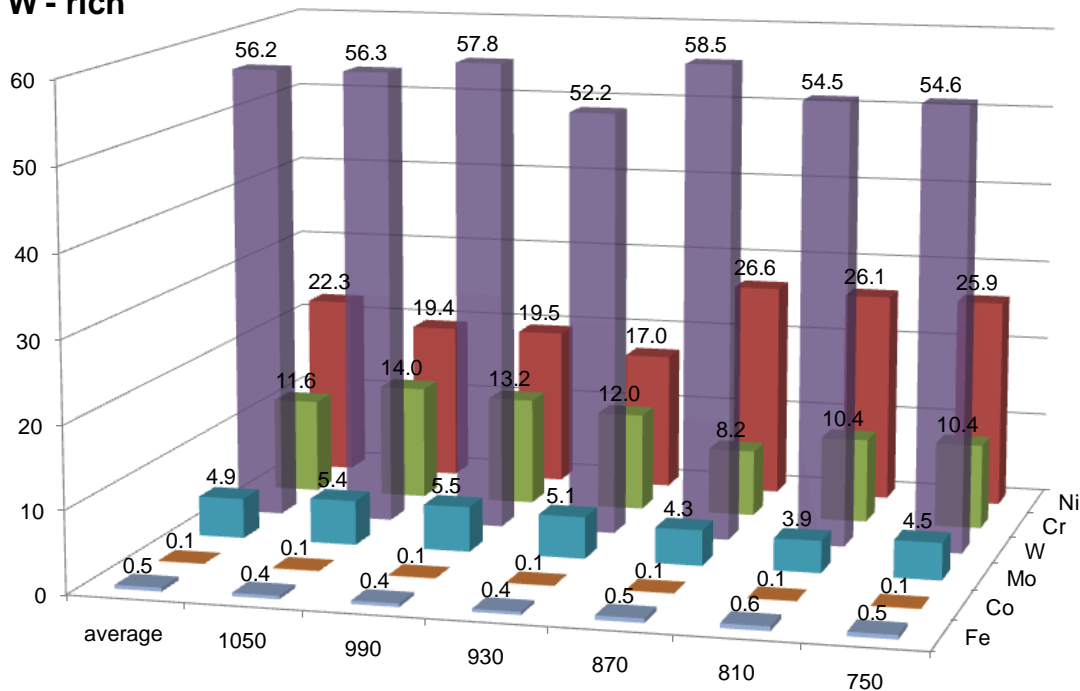


Figure 4.52 Composition of the W-rich phase (wt%) of the samples thermally exposed for 15000 hours obtained by EPMA.

The transition phase has a variable composition. Again at the lowest temperatures it has not been detected. The composition obtained from this analysis is as follows: 38 wt% of Cr, 29 wt% of Ni, 21 wt% of W and 3 wt% of Mo.

As was mentioned above, the Cr-rich phase appears as a complex phase whose composition changes with temperature and surrounding environment influencing the diffusion of the atoms. This phase for its growth uses the Ni atoms, which have the similar atomic radii and easily substitute by, in the future, available Cr atoms.

Table 4.15 Composition of the Cr-rich phase (wt%) of the samples thermally exposed for 15000 hours obtained by EPMA.

Wt%	avg	stdev	1050	stdev	990	stdev	870 Excluded from the average
Ni	5.82	0.90	5.26	0.21	6.56	0.95	13.26
Cr	63.25	0.72	63.09	0.27	63.47	1.14	51.44
W	23.10	0.59	23.55	0.21	22.52	0.27	26.17
Mo	2.45	0.08	2.42	0.04	2.48	0.11	3.02
Co	0.02	0.01	0.02	0.01	0.02	0.01	0.04
Fe	0.29	0.02	0.29	0.02	0.28	0.02	0.39
Total	94.93		94.63		95.32		94.32

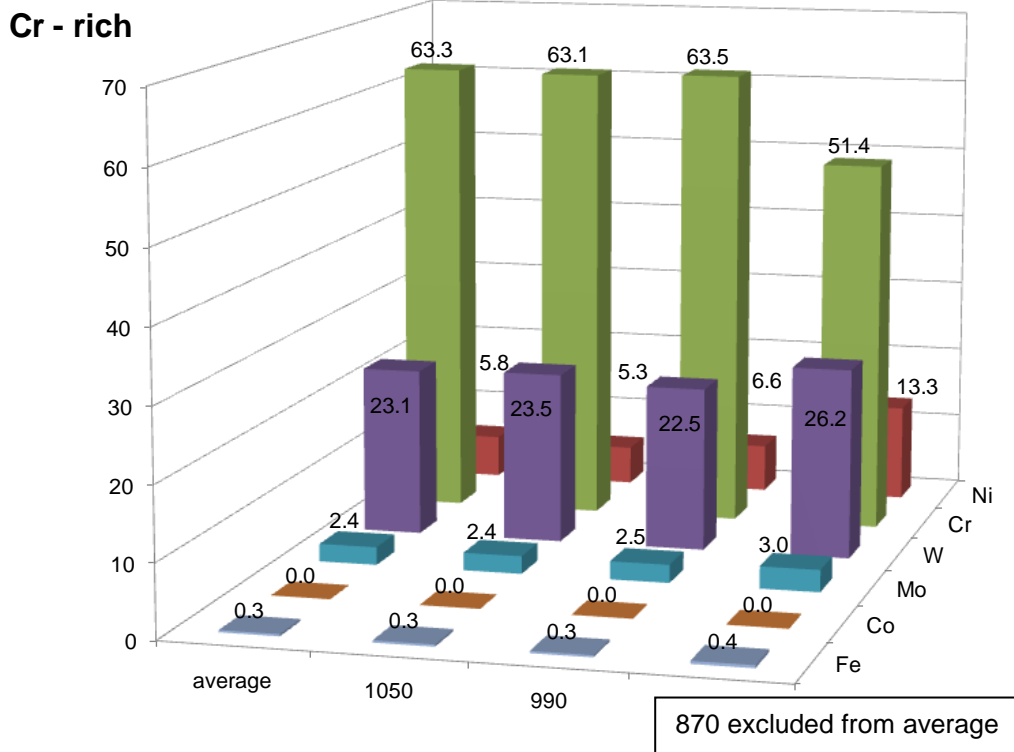


Figure 4.53 Composition of the Cr-rich phase (wt%) of the samples thermally exposed for 15000 hours obtained by EPMA.

Detected amounts of cobalt and iron were very low in all samples (less than 1 wt%).

Table 4.16 Composition of the transition phase (wt%) of the samples thermally exposed for 15000 hours obtained by EPMA.

Wt%	avg	stdev	1050	stdev	990	stdev	870	stdev
Ni	28.97	1.28	29.05	0.36	28.93	0.44	28.81	4.26
Cr	38.40	2.10	37.50	0.38	37.65	0.50	43.02	0.79
W	20.98	1.63	22.50	0.07	20.05	0.27	18.76	1.82
Mo	3.15	0.30	3.34	0.10	3.10	0.09	2.71	0.64
Co	0.07	0.01	0.07	0.01	0.07	0.01	0.08	0.03
Fe	0.40	0.16	0.33	0.01	0.34	0.01	0.75	0.19
Total	91.97		92.78		90.14		94.13	

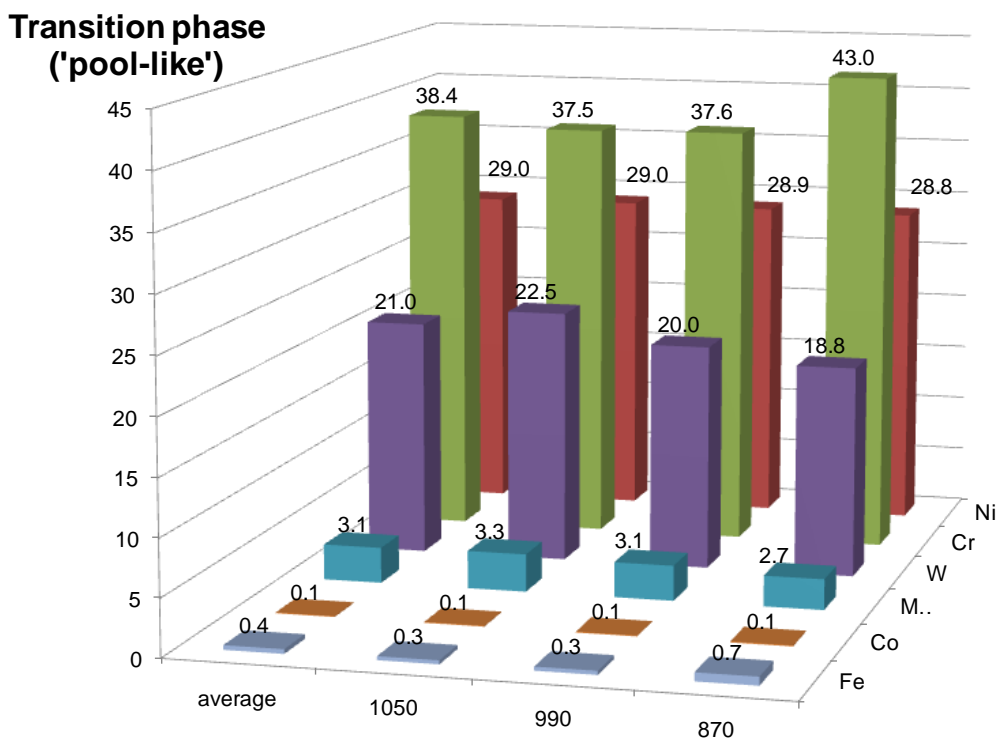


Figure 4.54 Composition of the transition phase (wt%) of the samples thermally exposed for 15000 hours obtained by EPMA.

Figure 4.55 summarises the average values of the all four phases observed in Haynes Alloy 230.

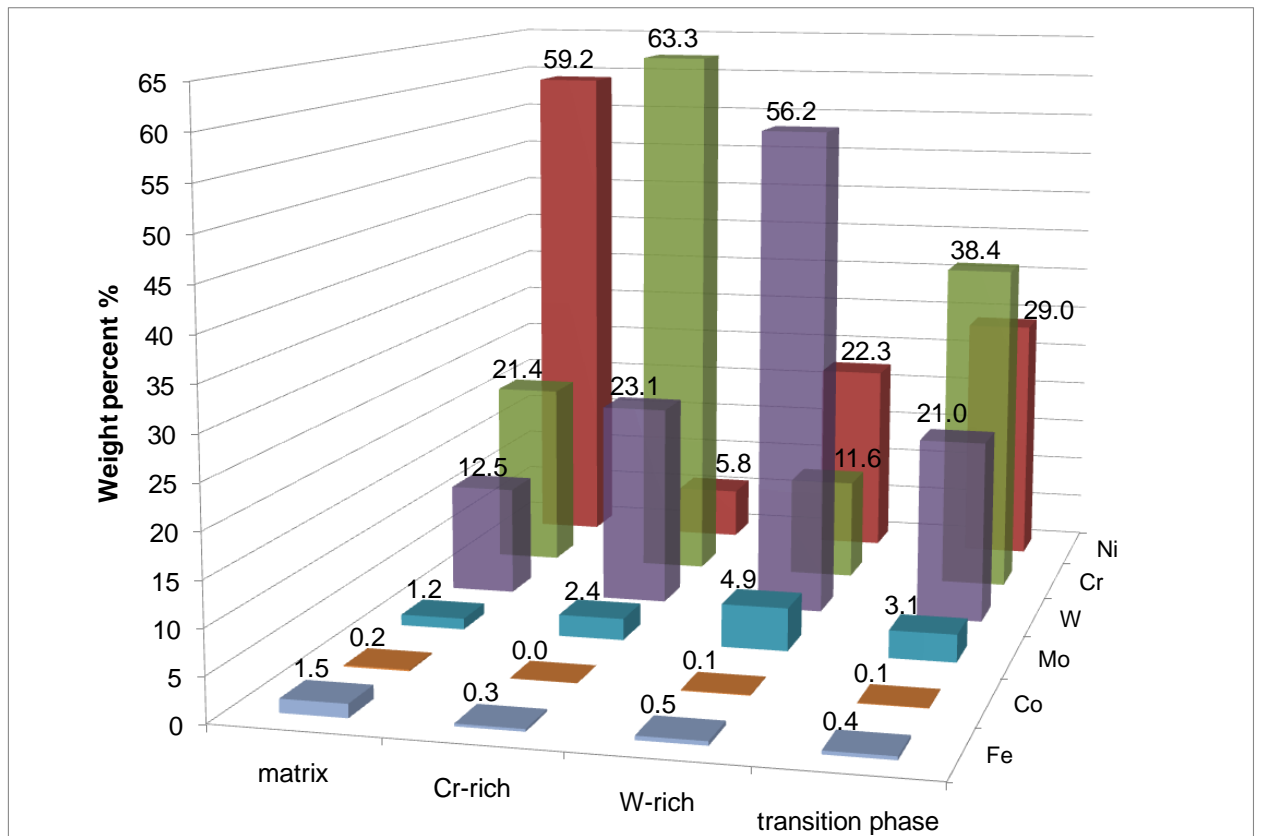


Figure 4.55 Average composition of the main phases (wt%) in HA230 thermally exposed for 15000 hours detected by EPMA.

SUMMARY

EPMA proved the presence and the composition range of the three precipitating phases in HA230 previously described in EDX section. There are no major trends in composition.

4.8 INDUCTIVELY COUPLED PLASMA - OPTICAL EMISSION SPECTROMETRY (ICP-OES)

This technique is suitable for determining of the concentration of trace elements in solution and hence was chosen for analyses of the amount of the main - nine - elements in the supernatant liquid. The supernatant liquid was obtained using chemical extraction of the bulk material. Assuming that only precipitated phases from the bulk material are extracted and all matrix elements are dissolved in the bromine solution, some changes in the composition of the matrix could be observed (as some elements are contributing more to the e.g. precipitation, oxidation).

In total, 14 samples were analysed:

1. As-received material;

2. Samples thermally exposed for 3000 hours between 750-1050°C (6);
3. Samples thermally exposed for 20000 hours between 750-1050°C (6);
4. Sample taken from transition duct.

Firstly, it was necessary to dilute the supernatant liquid to adjust the concentrations of the single elements to the standard. The measuring was made using the standard calibration curves for each element and for the accuracy of the measurement, the concentration of the element must be within the curve's limits. For nickel and chromium the solution was diluted 1000x and for the rest of elements 100x. The values were then converted from ppm to wt%.

The first results obtained showed a distribution of the values and any trend cannot be observed. Plotted values (Table 4.17) are presented in Figure 4.56. The amount of nickel can be distinguished very clearly in the as-received material. The value of over 100 wt% suggests that during the first analysis the diluting process has not been done correctly. This resulted in higher amount of chromium. In general, the major scatter in the values is for nickel. In the first set, thermally exposed samples for 3000 hours, the mass fraction was between 58.2 and 67.4 wt% while in the second set, thermally exposed samples for 20000 hrs, the maximum value reached 73.5 wt%. The lowest value was obtained for the transition duct sample (56.4 wt%). Considering the fact that the HA230 contains 59 wt% of nickel, the majority of the acquired values were higher. In the case of chromium in the '3000 hours set', the values were scattered around 20 wt%, while in the '20000 hours set' the scatter was much bigger (between 18.5 and 25.9). Significant difference was observed for tungsten. The as-received material contains 9.9 wt% of W, which was expected, because the tungsten rich precipitates present in the bulk have been extracted. A similar result was obtained for the '3000 hours set' where the values were fluctuating around 9 wt%. Different results were obtained for the '20000 hours set'. The values around and less than 4 wt% demonstrate an error in the procedure. The other 6 elements were detected and the concentrations were below 2 wt%. Manganese in the '20000 hours set' has not been detected, and therefore the second analysis of this set and of the transition duct sample was repeated.

The second analysis of the '20000 hours set' and of the transition duct sample is shown in Table 4.18 and Figure 4.57. The values of the main three elements are generally lower than in the '3000 hours set'. The new results suggest that there is an effect of extracted phases containing these elements and then the remaining amount was detected in the supernatant liquid. In contrary, there is no

trend which could be observed in the first and in the second analysis of the '20000 hours set'. Certain similarities can be seen in the case of the '20k 1050' specimen and transition duct specimen. In these two the amount of the all three main elements (Ni, Cr, W) decreased with a similar ratio.

It has to be concluded that in spite of the accuracy of the ICP technique, the analysis carried out on HA230 was probably affected by unknown factors and even the repeated analysis was unsuccessful.

Table 4.17 Mass fraction (wt%) of the elements present in the supernatant liquid.

	As-rec	3K 750	3K 810	3K 870	3K 930	3K 990	3K 1050	20K 750	20K 810	20K 870	20K 930	20K 990	20K 1050	T-duct
Al	0.58	0.37	0.34	0.37	0.36	0.37	0.33	0.49	0.49	0.45	0.44	0.45	0.33	0.55
Co	0.32	0.18	0.15	0.16	0.15	0.18	0.17	0.16	0.15	0.17	0.16	0.19	0.15	0.18
Cr	34.4	23.5	19.2	20.9	20.4	21.0	19.5	23.3	20.9	24.5	23.6	25.9	18.5	20.6
Fe	1.09	1.85	1.36	1.55	1.54	1.71	1.61	1.82	1.80	1.92	1.88	2.08	2.15	1.46
Mn	0.43	0.64	0.53	0.57	0.53	0.56	0.49	0.01	0.01	0.01	0.01	0.01	0.00	0.01
Mo	1.87	1.23	1.17	1.28	1.24	1.37	1.30	1.08	1.14	1.33	1.27	1.50	1.19	1.07
Ni	105	67.4	58.2	61.6	59.0	64.9	61.7	64.8	58.5	69.4	66.5	73.5	58.8	56.4
Si	0.56	0.27	0.21	0.24	0.28	0.36	0.37	0.22	0.24	0.31	0.33	0.42	0.32	0.31
W	9.90	8.26	6.89	8.06	9.14	9.68	9.74	2.69	3.36	4.39	4.07	4.35	3.96	3.70

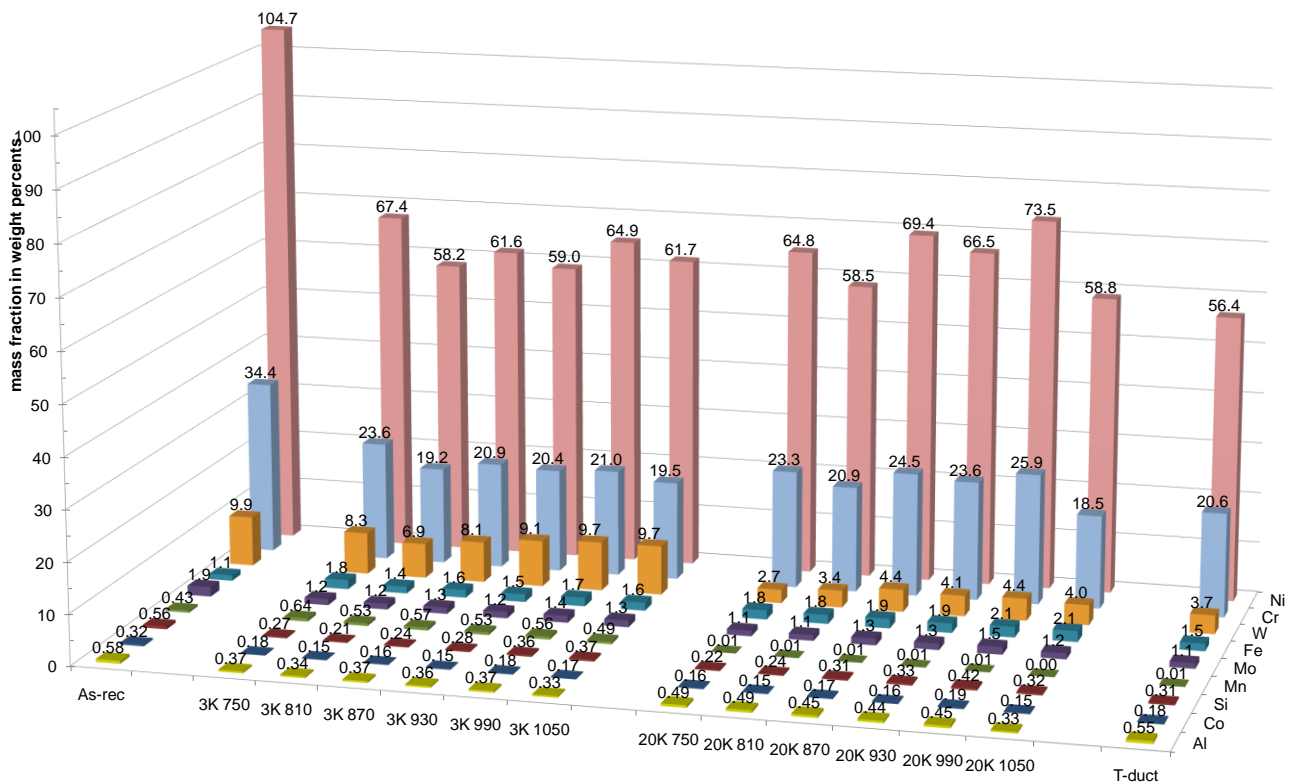


Figure 4.56 Mass fraction (wt%) of the elements present in the supernatant liquid.

Table 4.18 Mass fraction (wt%) of the elements of the '20000 hrs set' (second analyses) present in the supernatant liquid.

	20K 750 (2)	20K 810 (2)	20K 870 (2)	20K 930 (2)	20K 990 (2)	20K 1050 (2)	T-duct (2)
Al	0.76	0.82	0.86	0.71	0.70	0.63	0.89
Co	0.15	0.15	0.17	0.16	0.16	0.14	0.17
Cr	19.25	19.27	21.41	21.05	20.79	15.70	18.27
Fe	1.31	1.27	1.44	1.41	1.38	1.51	0.89
Mn	0.50	0.48	0.53	0.49	0.44	0.28	0.46
Mo	0.50	1.01	1.24	1.20	1.19	1.05	0.96
Ni	53.94	53.72	61.81	59.46	59.79	51.15	51.32
Si	0.31	0.28	0.38	0.28	0.34	0.17	0.24
W	6.03	7.01	8.26	7.18	7.45	7.30	7.46

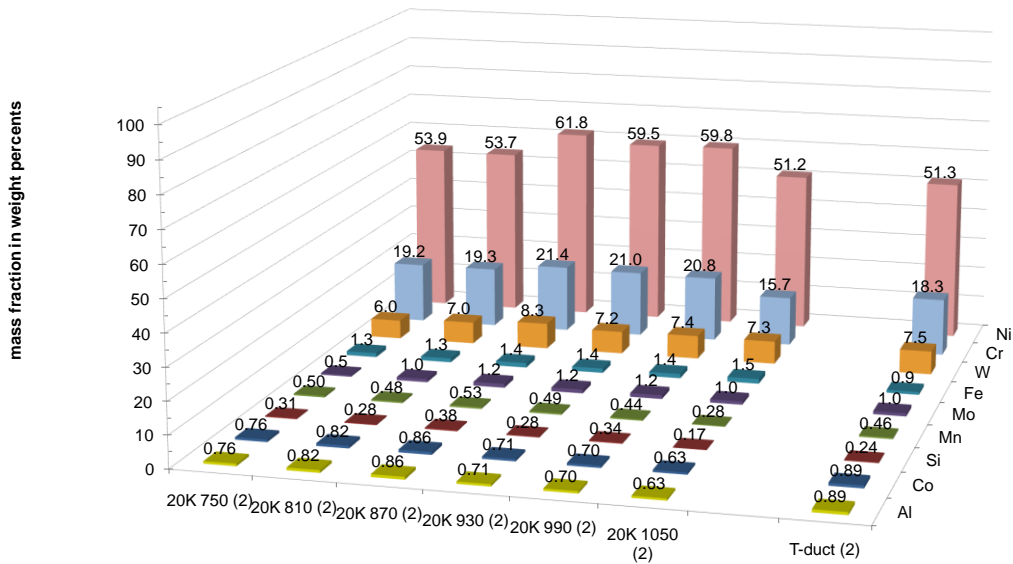


Figure 4.57 Mass fraction (wt%) of the elements of the '20000 hrs set' (second analyses) present in the supernatant liquid.

SUMMARY

The supernatant liquid obtained after the chemical extraction of the phases was analyzed by ICP-OES and the technique offered the possibility to analyze the changes in the composition of the HA230 matrix. The technique is very accurate; no changes in the matrix composition due to precipitation of various phases could be detected.

4.9 OXIDATION CHARACTERISTICS

The project on the effects of oxidation on the microstructure of HA230 was carried out with my assistance and some direction by Jeremy Doucet, a MSc. Student [1].

Doucet's work was focused on the measurements of the oxidation attack on HA230 specimens with increasing temperature (from 750°C to 1050°C) and with increasing duration of exposure (from 1000 to 20000 hours). XRD analysis was performed on the thermally exposed specimens for 25000 hours in CNR, Milan (It) by Dr G. Angella, followed by the peak assessment. FEGSEM studies were carried out on the cross sections of the samples thermally exposed for 10000 and on the oxide layer directly in the case of specimens exposed for 25000 hours.

Figure 4.58 shows an example of the zones in the bulk material affected by oxidation. The measurements of these zones were carried out on the thermally exposed specimens.

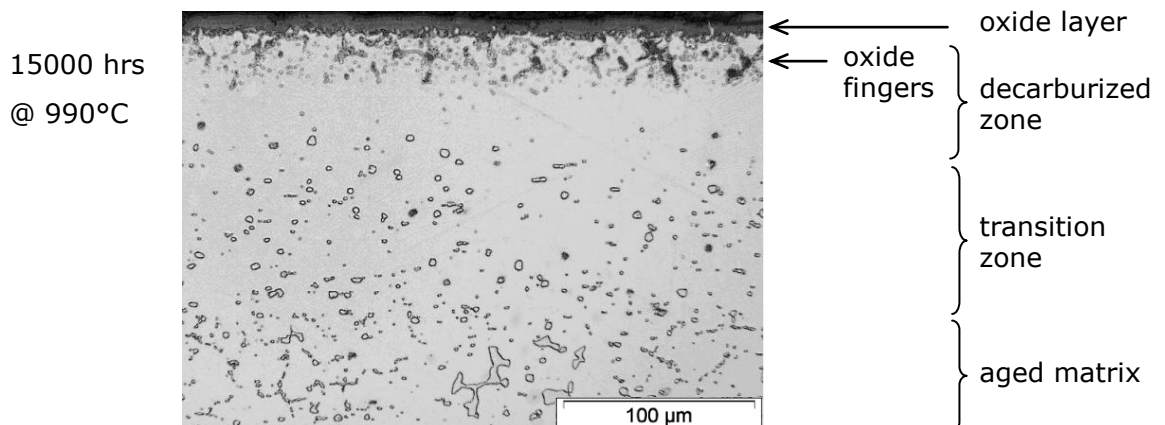


Figure 4.58 Micrograph of 990°C (15000 hours) microsection showing oxidation attack at the material surface.

The effect of oxidation for the case of specimens exposed for 1000 hours at temperatures in the range 750°C to 1050°C is illustrated in Figure 4.59. In addition to the presence of an oxide scale, which increases in thickness with increasing exposure temperature, significant changes in the underlying microstructure of the alloy are evident. These include oxide finger penetration and the presence of a 'decarburised zone' both of which increase, as is shown in Figure 4.60, with increasing exposure temperature.

Similar effects to those shown in Figure 4.59 have been observed for longer exposure durations.

Further measurements on HA230 have shown that further damage to the microstructure occurs due to the effects of oxidation with increasing exposure durations at temperatures in the same temperature range. In addition to 'metal wastage' due to oxide spalling, oxide finger penetration ranging from 0.015 mm up to 0.08 mm respectively has been observed following exposure for 20000 hours at 750°C and 1050°C accompanied by corresponding decarburized zones underlying the oxide layer of 0.025 mm and 0.45 mm respectively.

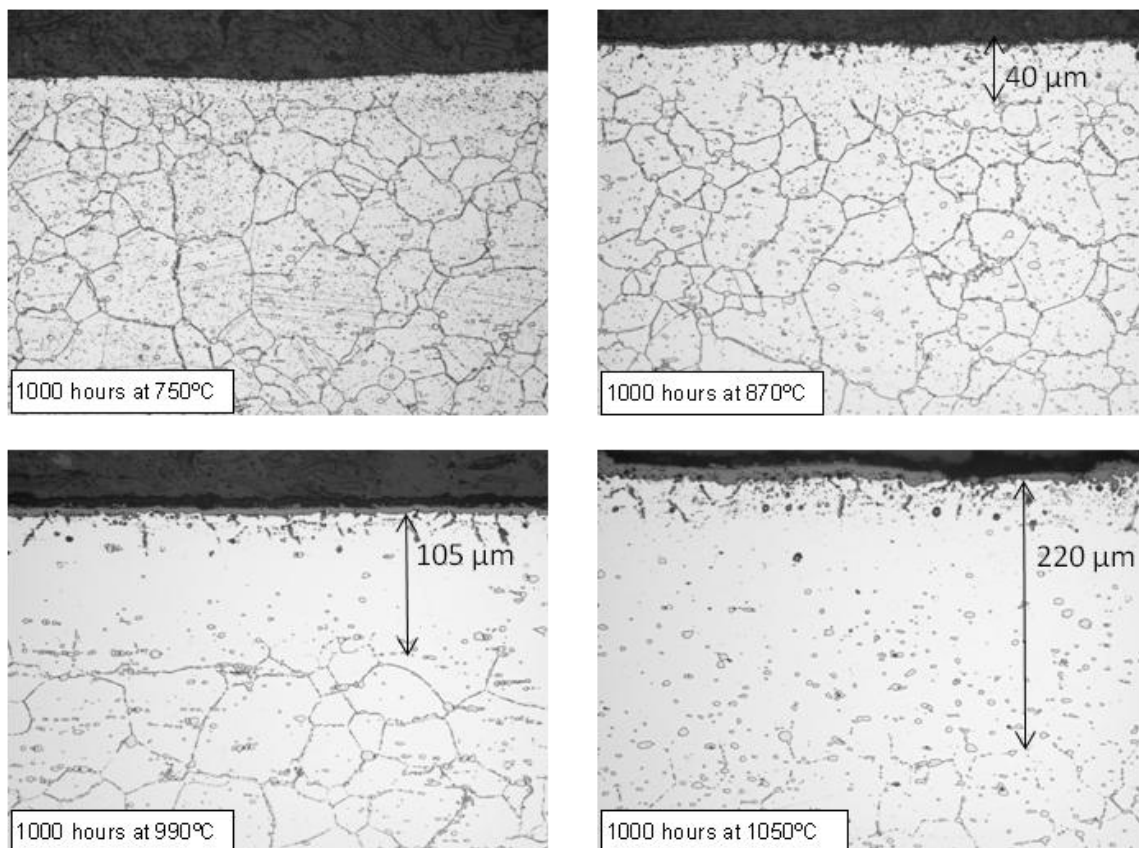


Figure 4.59 Effects of oxidation on the microstructure of HA230 exposed for 1000 hours at temperatures in the range 750°C to 1050°C. The arrow marks the depth of the inner oxidation effect.

Preliminary XRD studies using CuK α radiation have shown that the scale formed during long-term high temperature exposure of HA230 consists of a complex mixture of oxides, typical spectra from which are shown in Figure 4.61 for HA230 samples exposed for 25000 hours at temperatures ranging from 750°C to 1050°C. As shown in the spectrum for material exposed at 750°C the scales consist of a mixture of the following oxides: NiO, MnCr $_2$ O $_4$, NiCr $_2$ O $_4$ and Cr $_2$ O $_3$, Figure 4.62. These have been detected in the scales for all of the temperatures investigated with

chromia being more common at exposure temperatures above 900°C. Al₂O₃ can be found in oxide fingers.

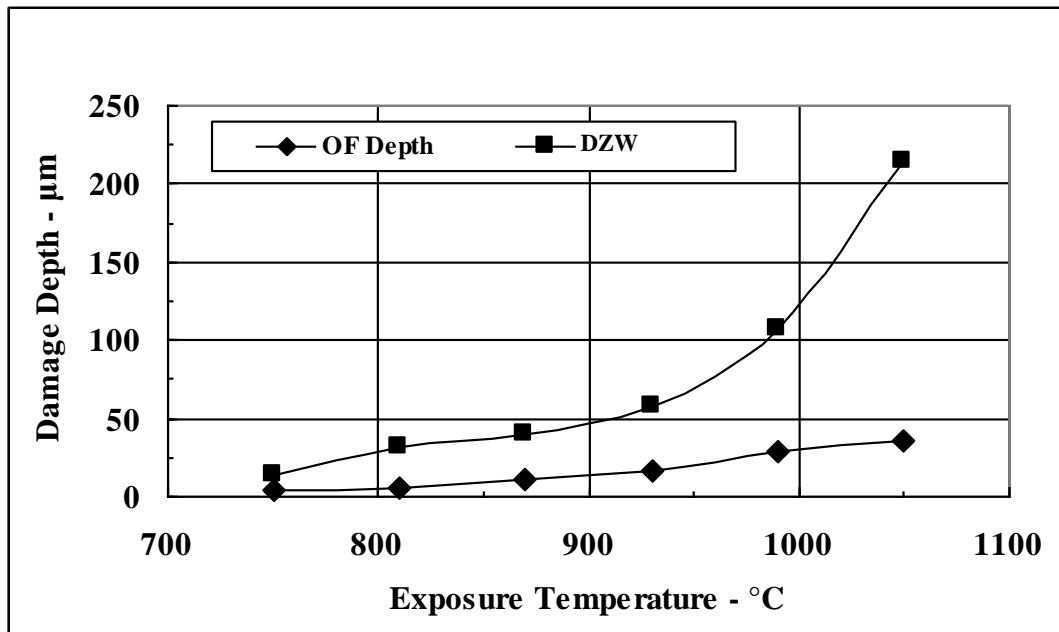


Figure 4.60 Effect of 1000 hours exposure at temperatures in the range 750°C to 1050°C on oxide finger penetration and decarburization zone width in HA230.

Figure 4.63 shows in detail the evolution of the oxide layer on the surface and its 'degradation' with increasing temperature. In addition, it can be observed that the spallation affects the spinels only and the chromia layer tend to remain compact and adherent.

It has not been possible so far to define an oxide evolution model for the range of temperatures and exposure durations in the present study and hence determine whether it may be possible to use oxide sequences as a means of determining average temperatures experienced by components in service. However FEGSEM studies of sections through the oxide scales and of the surface layers suggest that the oxide sequence consists of chromia overlaid with growing spinels MnCr₂O₄ and NiCr₂O₄, and at 750°C the outer layer is formed by compact NiO, see Figures 4.63 - 4.65. The relative proportions of these phases together with the use of quantitative relationships between measurements of oxide finger penetration depth and decarburisation zone widths and time/temperature exposure conditions may be a possible useful exposure temperature indicator for ex-service HA230 components.

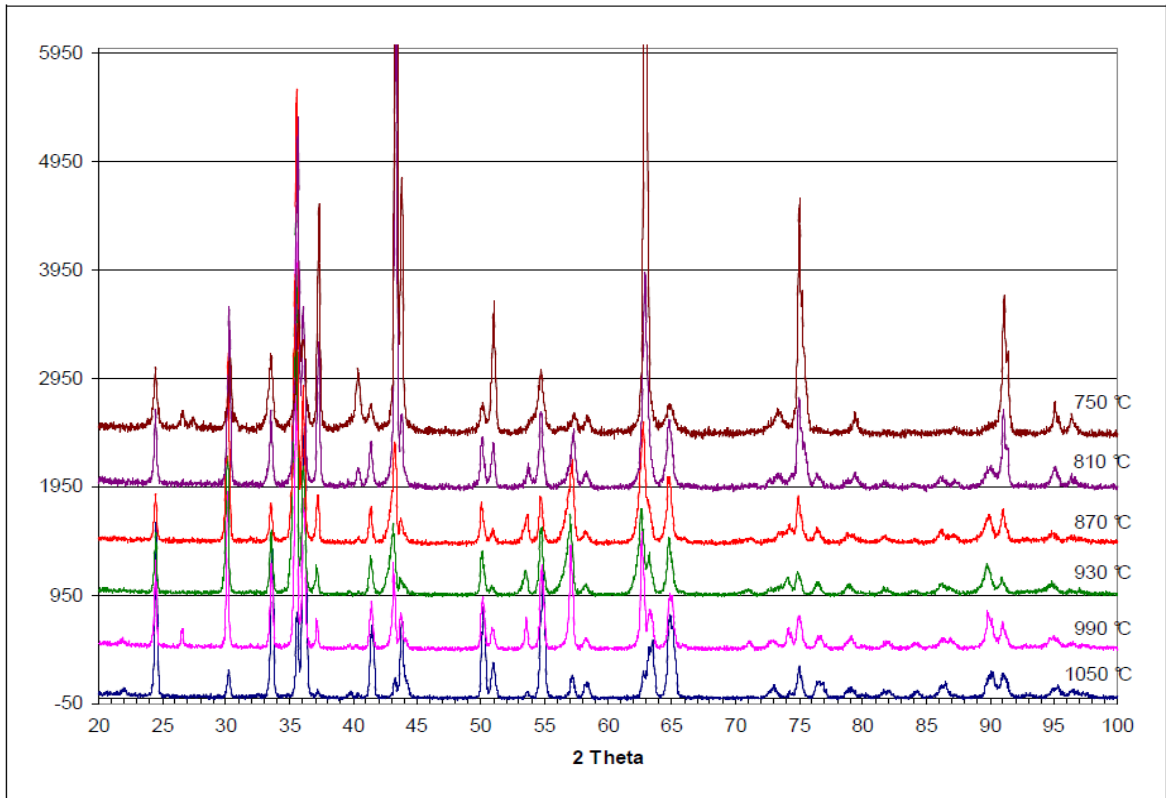


Figure 4.61 X-ray diffraction spectra of oxide scales on HA230 exposed for 25000 hours at temperatures in the range 750°C to 1050°C [1].

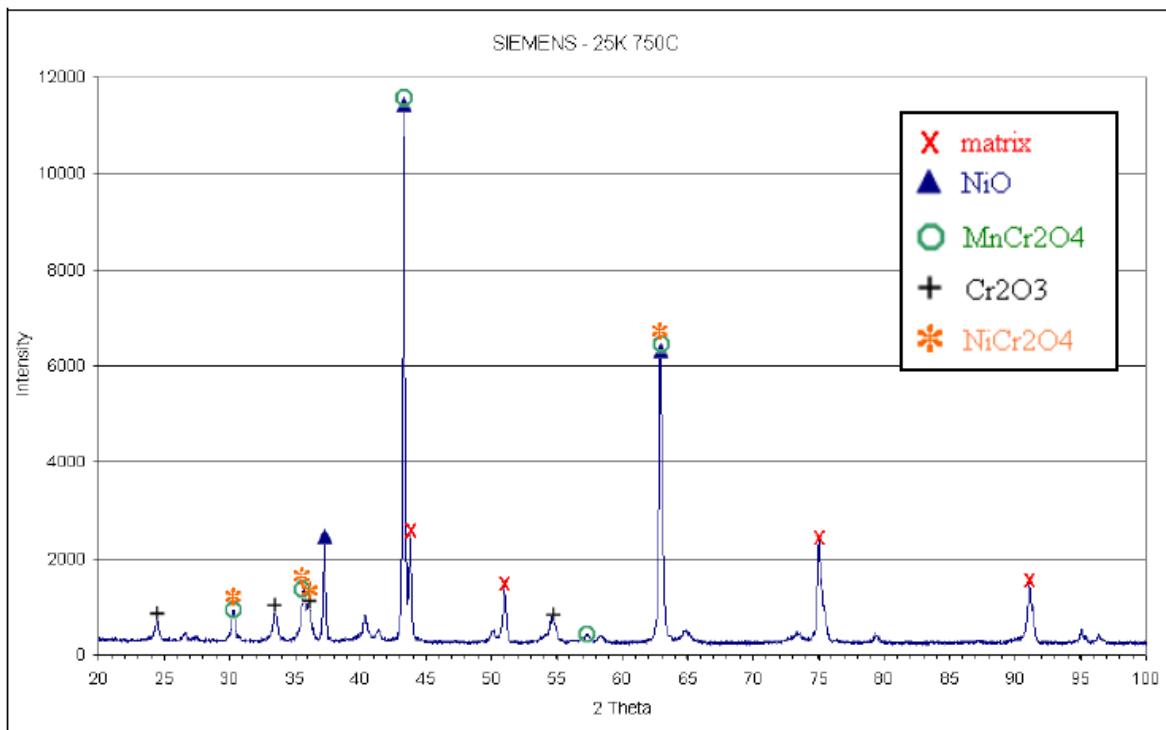


Figure 4.62 X-ray diffraction spectrum of oxide scale on HA230 exposed for 25000 hours at 750°C [1].

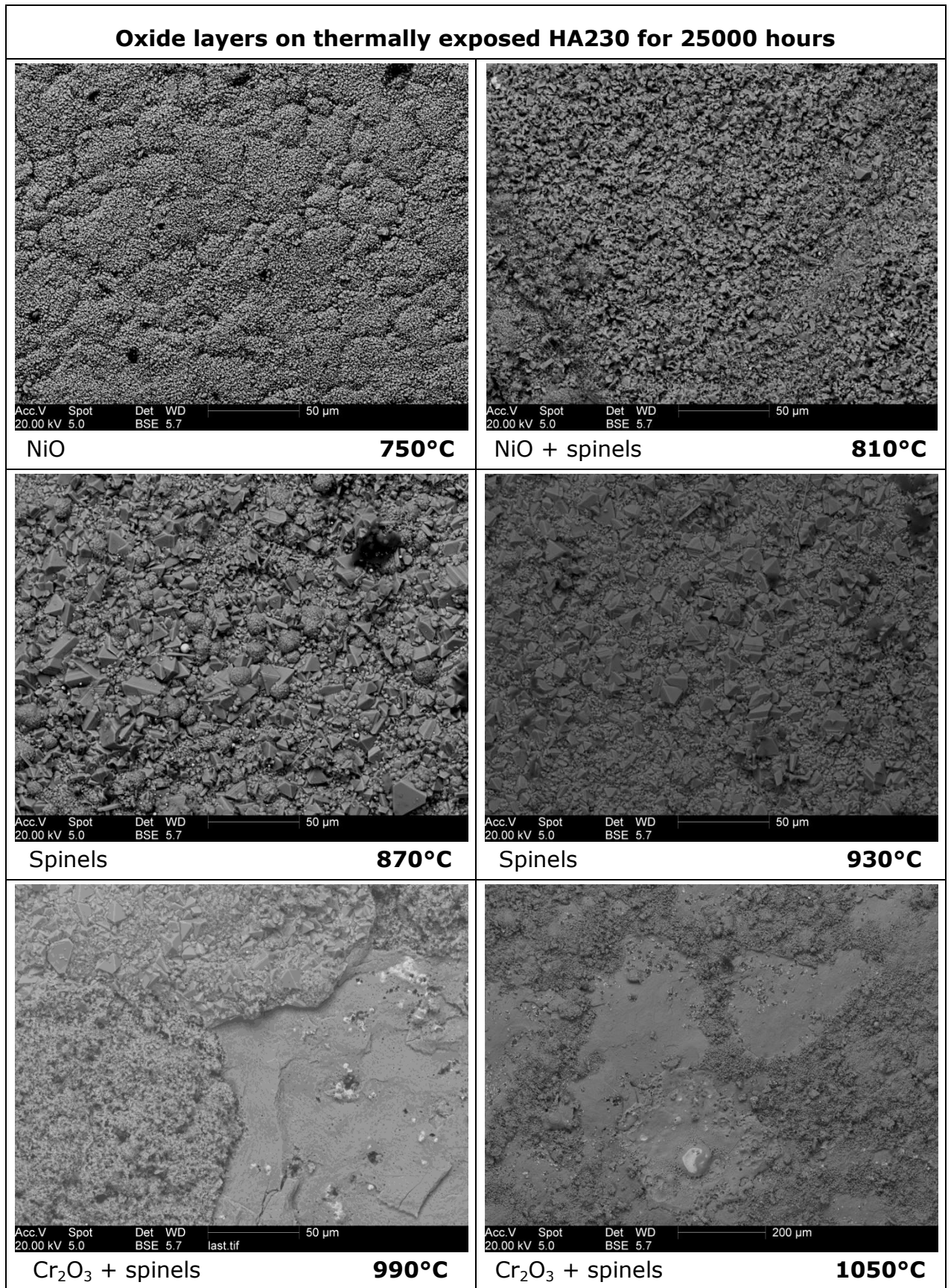
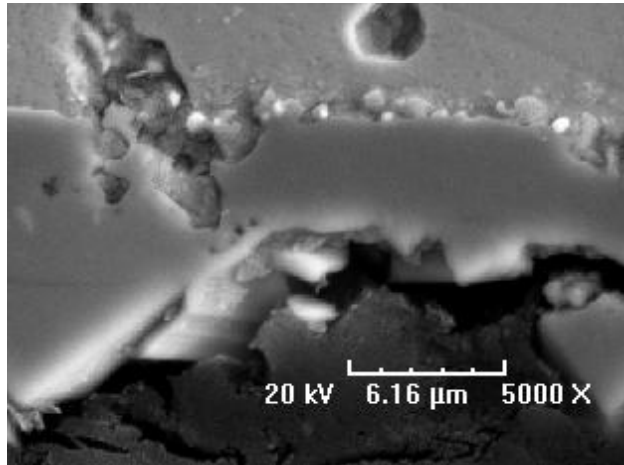
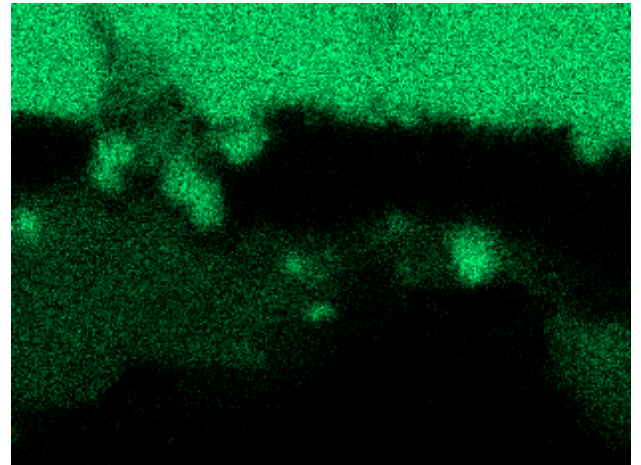


Figure 4.63 Evolution of oxide layer on thermally exposed HA230 for 25000 hours with increasing temperature.

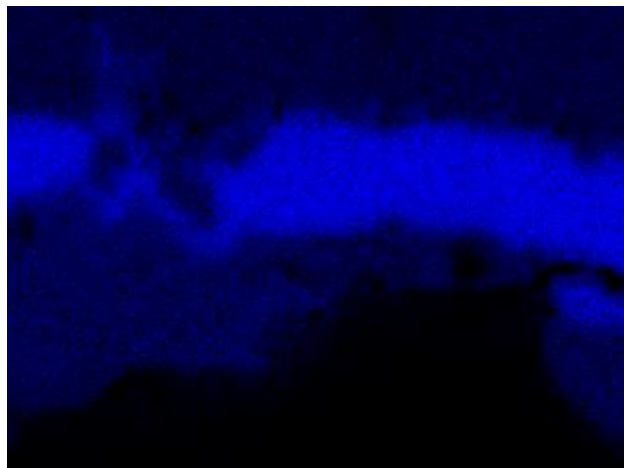
Jana_Oxidation Characteristics of HA230_10000hrs at 870°C



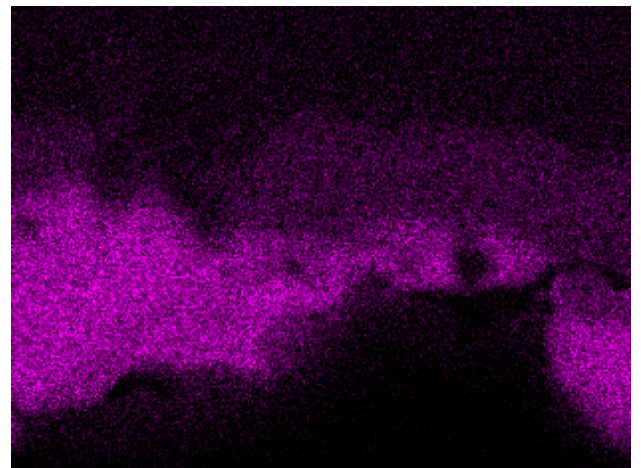
10K 870°C



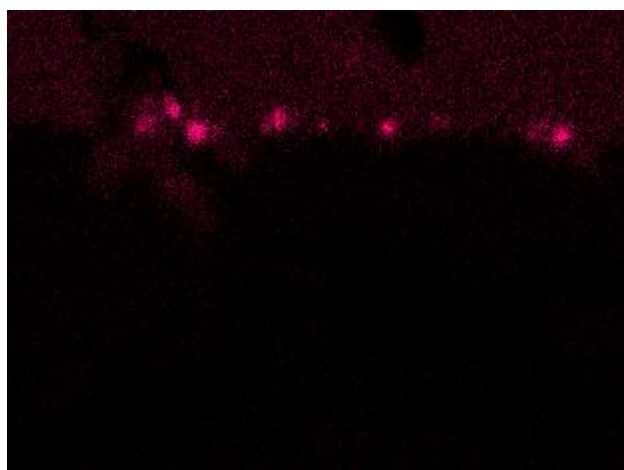
Ni Ka



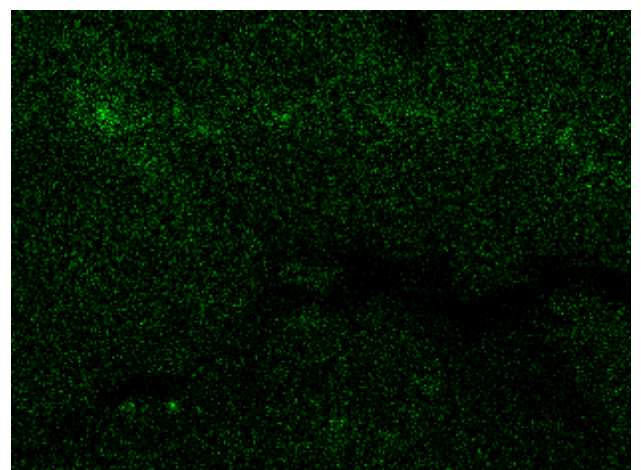
Cr Ka



Mn Ka



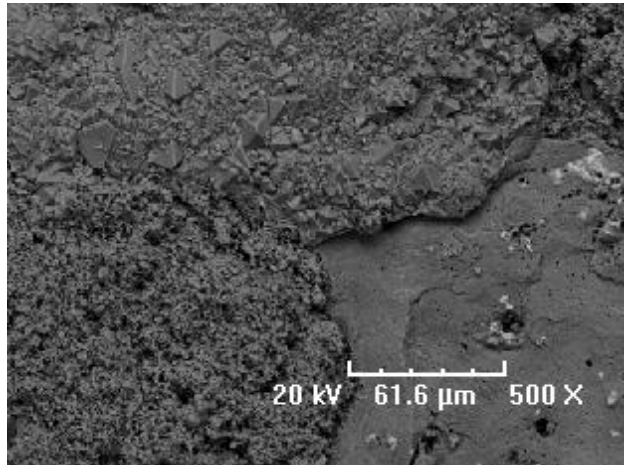
W La



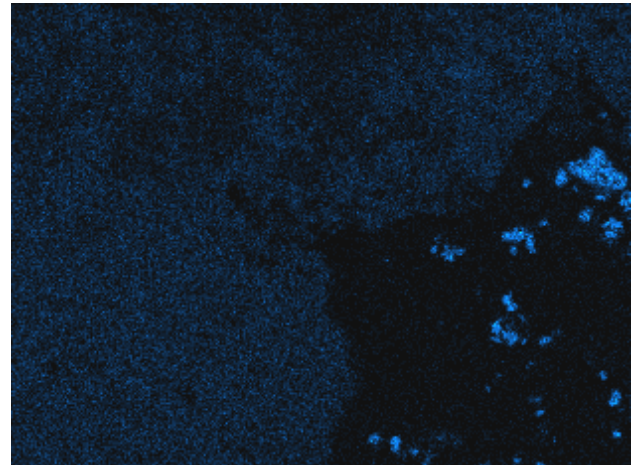
Al Ka

Figure 4.64 EDX mapping describing the structure of the oxide layer in the specimen thermally exposed for 10000 hours at 870°C.

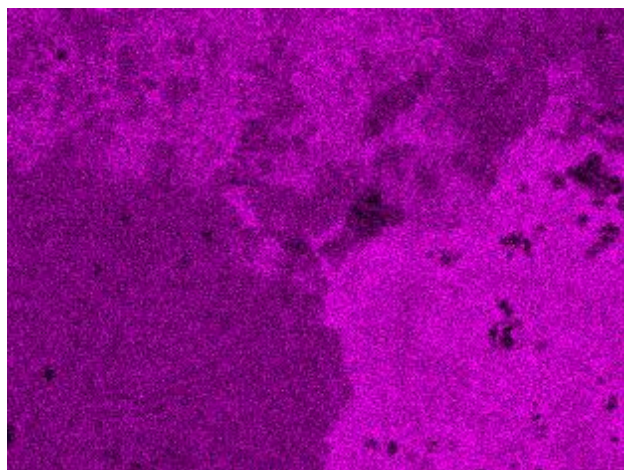
Jana_Oxidation Characteristics of HA230_25000hrs at 990°C



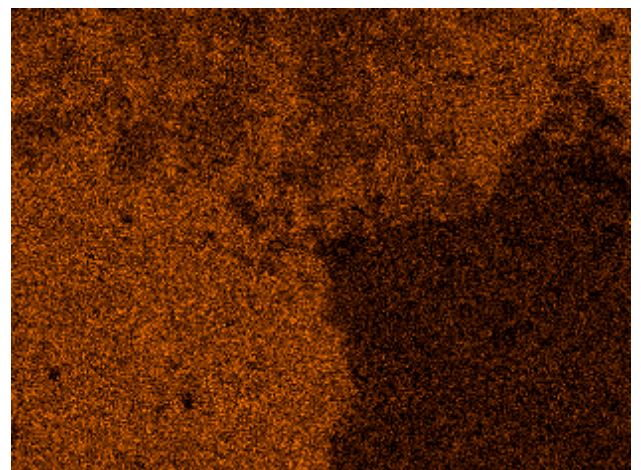
25K 990°C



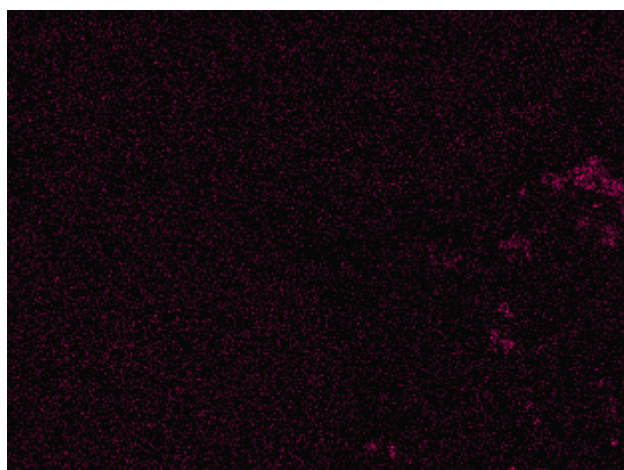
Ni Ka



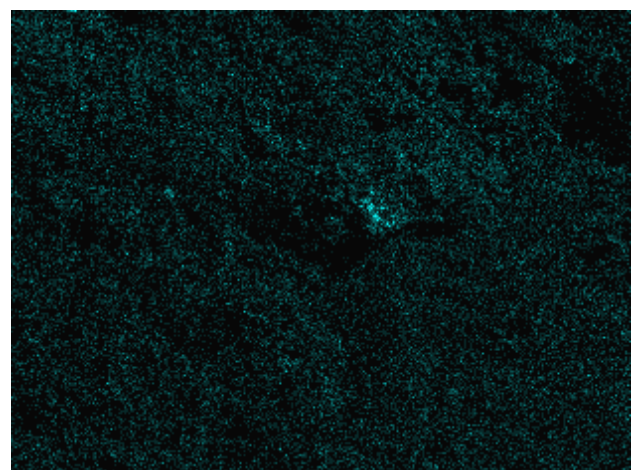
Cr Ka



Mn Ka



W La



Al Ka

Figure 4.65 EDX mapping describing the composition of the oxide layer in the specimen thermally exposed for 25000 hours at 990°C.

SUMMARY

The evolution of the oxidation effect was observed for a number of samples exposed in the temperature range from 750-1050°C up to 25000 hours. At lower temperatures the oxide layer is compact and a protective layer is formed consisting of chromia overlaid with NiO. The increase of the temperature causes the transformation of NiO to NiCr₂O₄ and the formation of MnCr₂O₄. The duration of exposure plays a great role at the highest temperatures when the outer spinel layer is affected by spallation. At highest temperature the inner oxidation effect (width of the decarburized zone) was also predominant.

4.10 TENSILE TESTING

The effects of high temperature exposure on the mechanical properties of HA230 have been investigated by carrying out room temperature tensile tests on HA230 material exposed for durations of 3000, 10000 and 20000 hours at temperatures in the range from 750°C to 1050°C. Details about the procedure and the specimens are described in Section 3.1.13 and 3.5. A plot showing the effects of increasing exposure duration and test temperature on the ultimate tensile strength (UTS) and 0.2% proof strength (PS) of HA230 is presented in Figure 4.66. The results indicate that following an initial increase in tensile strength both the 0.2% PS and UTS decrease linearly with increasing exposure temperature for all three of the exposure durations investigated.

The 0.2% PS and UTS tensile data are shown plotted against the corresponding hardness values for the thermally exposed HA230 material in Figure 4.67. Although there is some scatter in the results present, there is a clear correlation between hardness and tensile strength with increases in hardness corresponding to increases in both the 0.2% PS and UTS in the alloy.

The failure mechanism of the tensile fractured specimen was analyzed using scanning electron microscopy. Figures 4.68 – 4.69 compare the fractographs of the tensile specimens exposed for 3000 hours in the temperature range from 750°C to 1050°C and Figures 4.70 – 4.71 compare the fractographs of the specimens exposed for 20000 hours. The failure mechanism in all the samples was intergranular fracture. Intergranular creep fracture involves the nucleation, growth and subsequent linking of voids at grain boundaries. Two different types of cavities can form: wedge or/and isolated type cavities. Wedge type cavities are associated with cracking at the grain boundary triple points and form by the grain boundary sliding. The formation of cavities is controlled by diffusion-controlled processes.

Triple point cracking is shown in the micrograph. At low temperatures the faceting can be observed. With increase of the temperature the carbide cleavage appears. At the highest temperatures ductile rupture takes place.

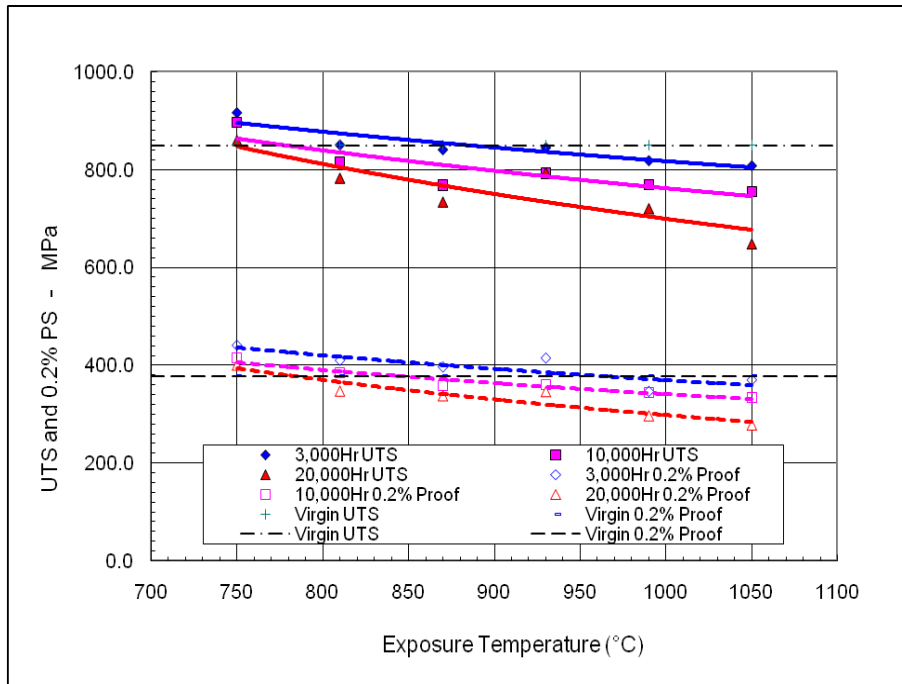


Figure 4.66 Plot of 0.2% PS and UTS tensile data for HA230 material as a function of temperature for exposure durations of 3K, 10K and 20K hours.

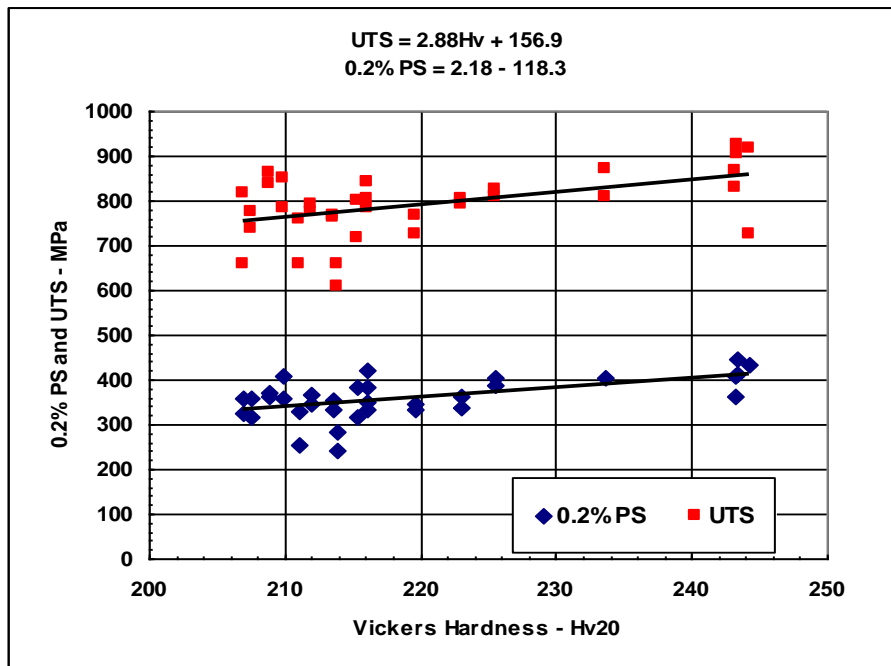
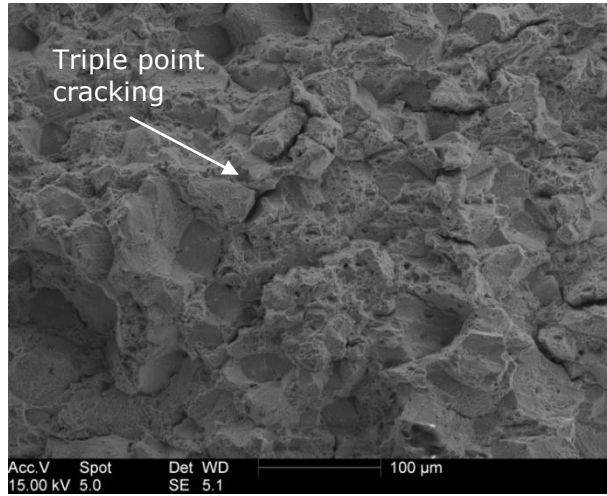


Figure 4.67 Variation of 0.2% PS and UTS with hardness for thermally exposed HA230.

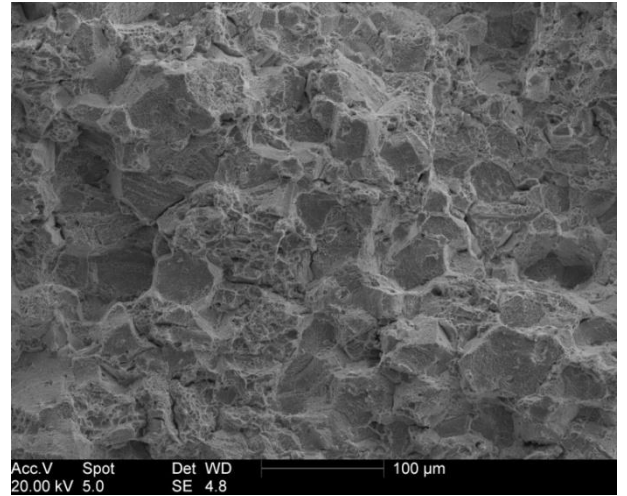
SUMMARY

Ambient temperature tensile tests conducted on HA230 exposed for 3000, 10000 and 20000 hours at temperatures in the range from 750-1050°C indicate the linear decrease of 0.2% PS and UTS with increasing exposure temperature for all three durations investigated. In all the cases an intergranular fracture was observed.

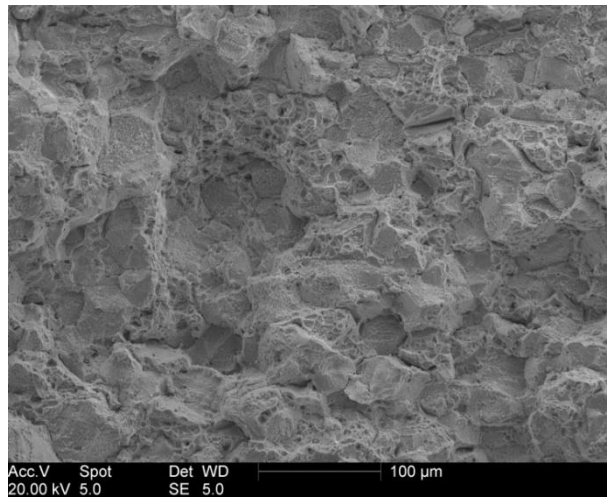
RT Tensile Tested specimens – thermal exposure for 3000 hrs



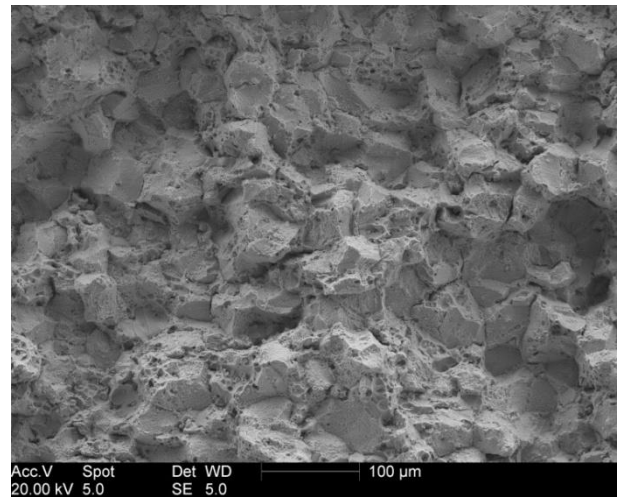
750°C



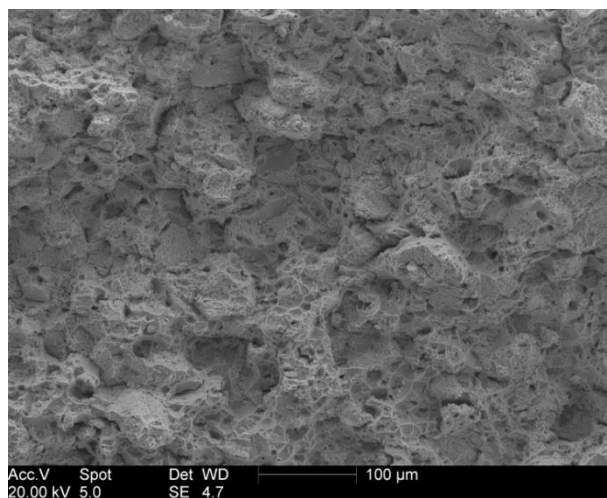
810°C



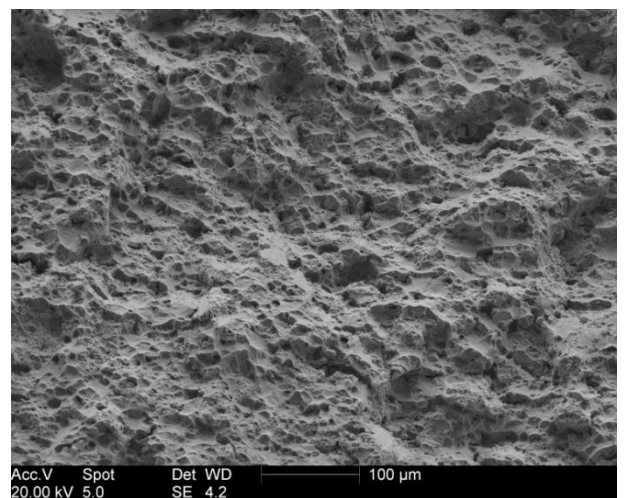
870°C



930°C



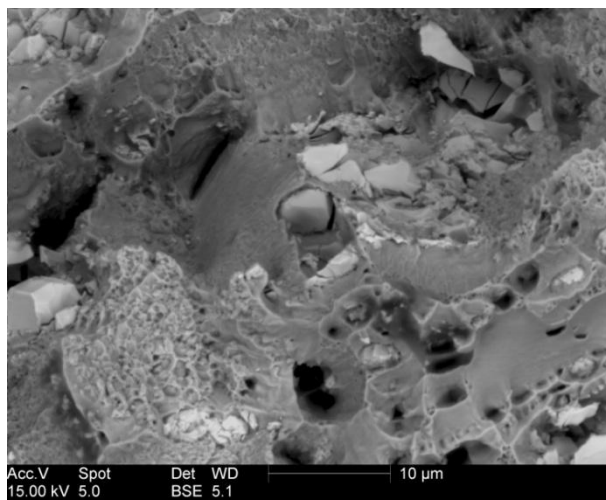
990°C



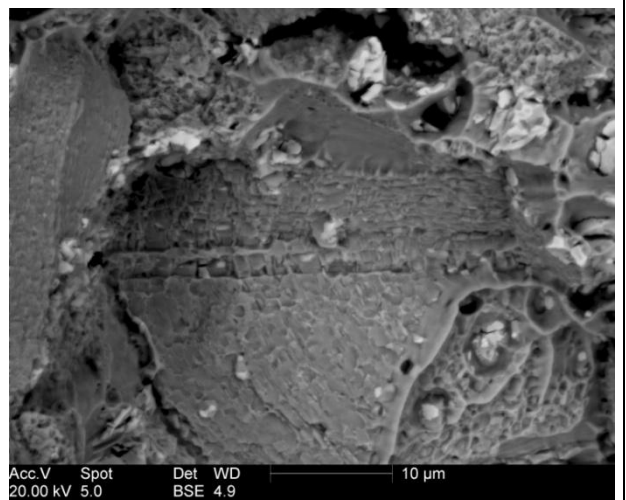
1050°C

Figure 4.68 Fractographs of the tensile specimens primarily aged for 3000 hours in the temperature range from 750°C to 1050°C.

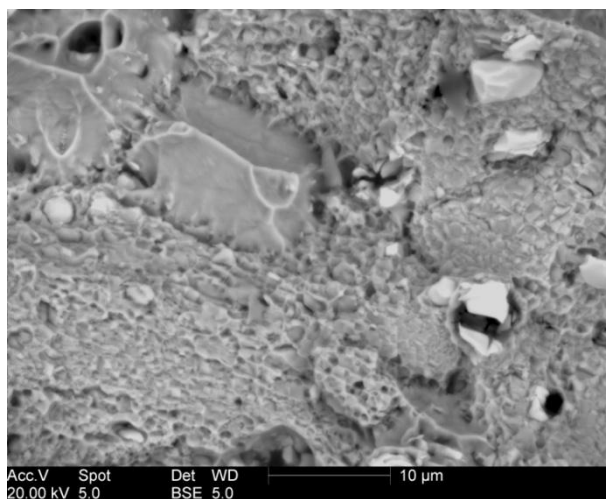
RT Tensile Tested specimens – thermal exposure for 3000 hrs



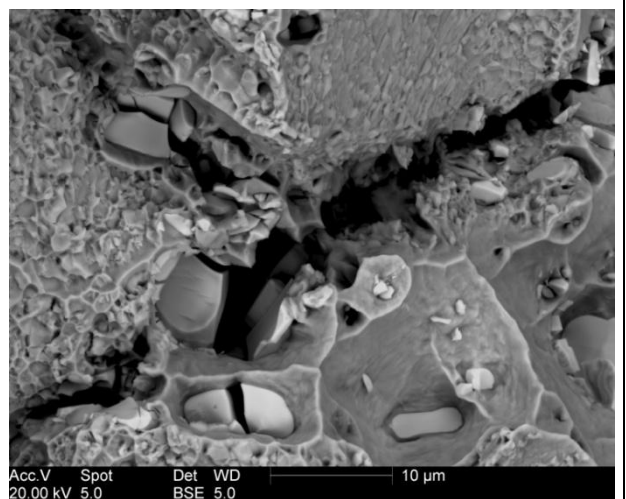
750°C



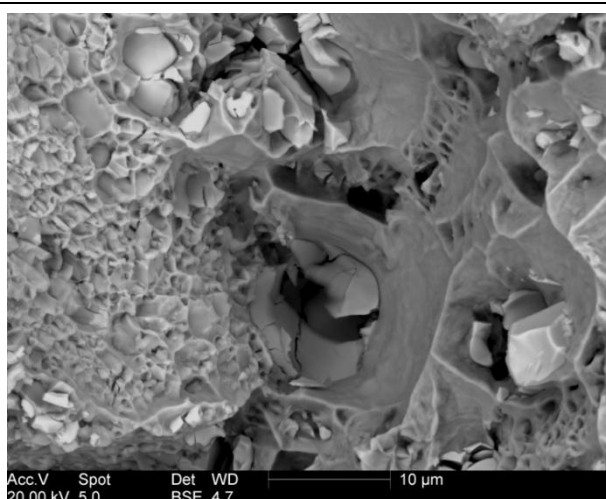
810°C



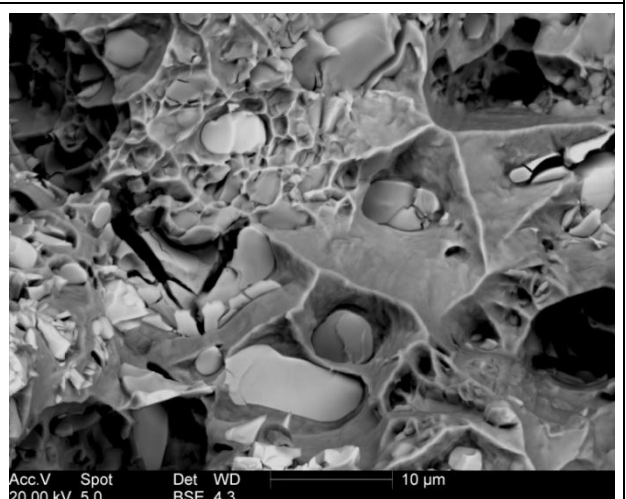
870°C



930°C



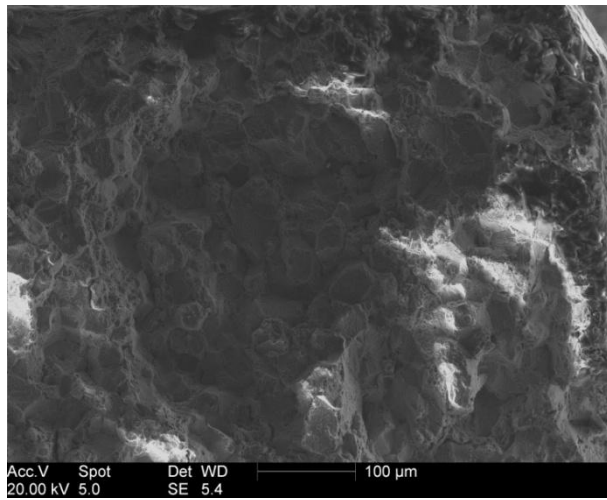
990°C



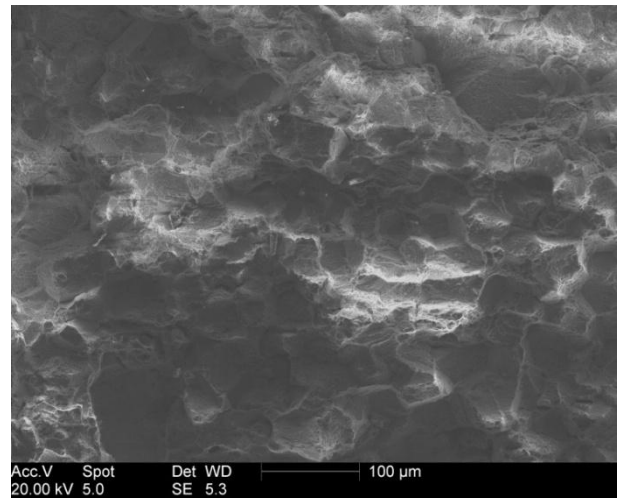
1050°C

Figure 4.69 Fractographs of the tensile specimens primarily aged for 3000 hours in the temperature range from 750°C to 1050°C.

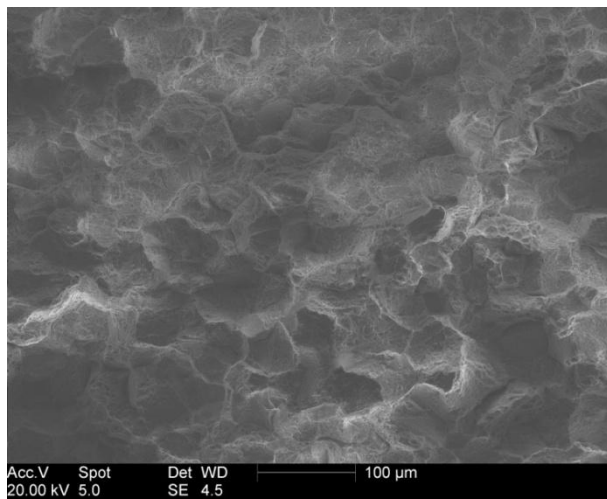
RT Tensile Tested specimens – thermal exposure for 20000 hrs



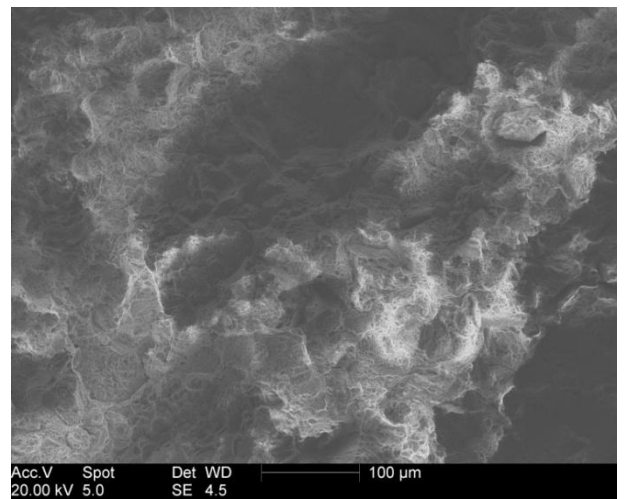
750°C



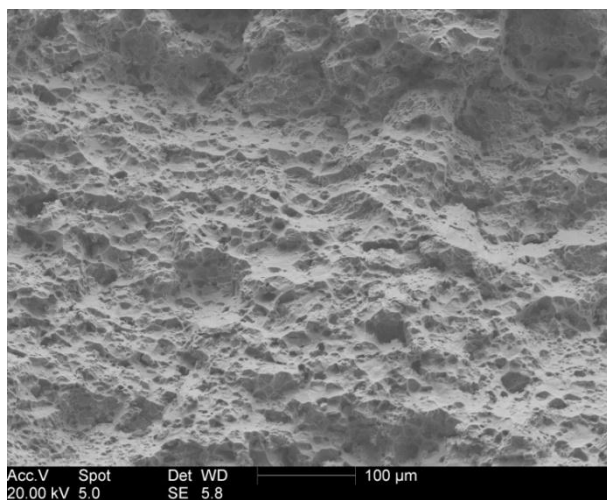
810°C



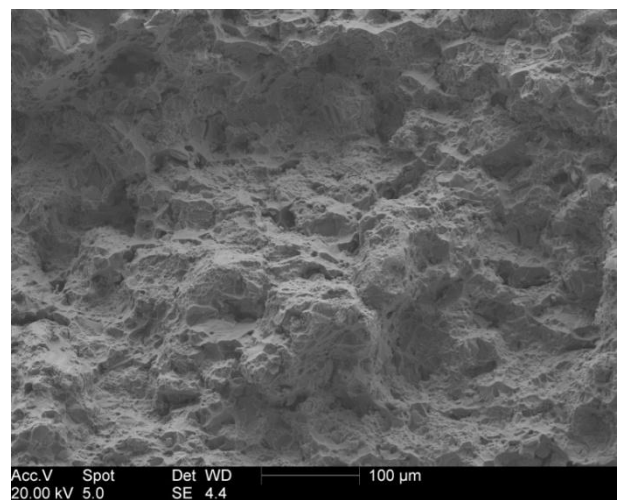
870°C



930°C



990°C



1050°C

Figure 4.70 Fractographs of the tensile specimens primarily aged for 20000 hours in the temperature range from 750°C to 1050°C.

RT Tensile Tested specimens – thermal exposure for 20000 hrs

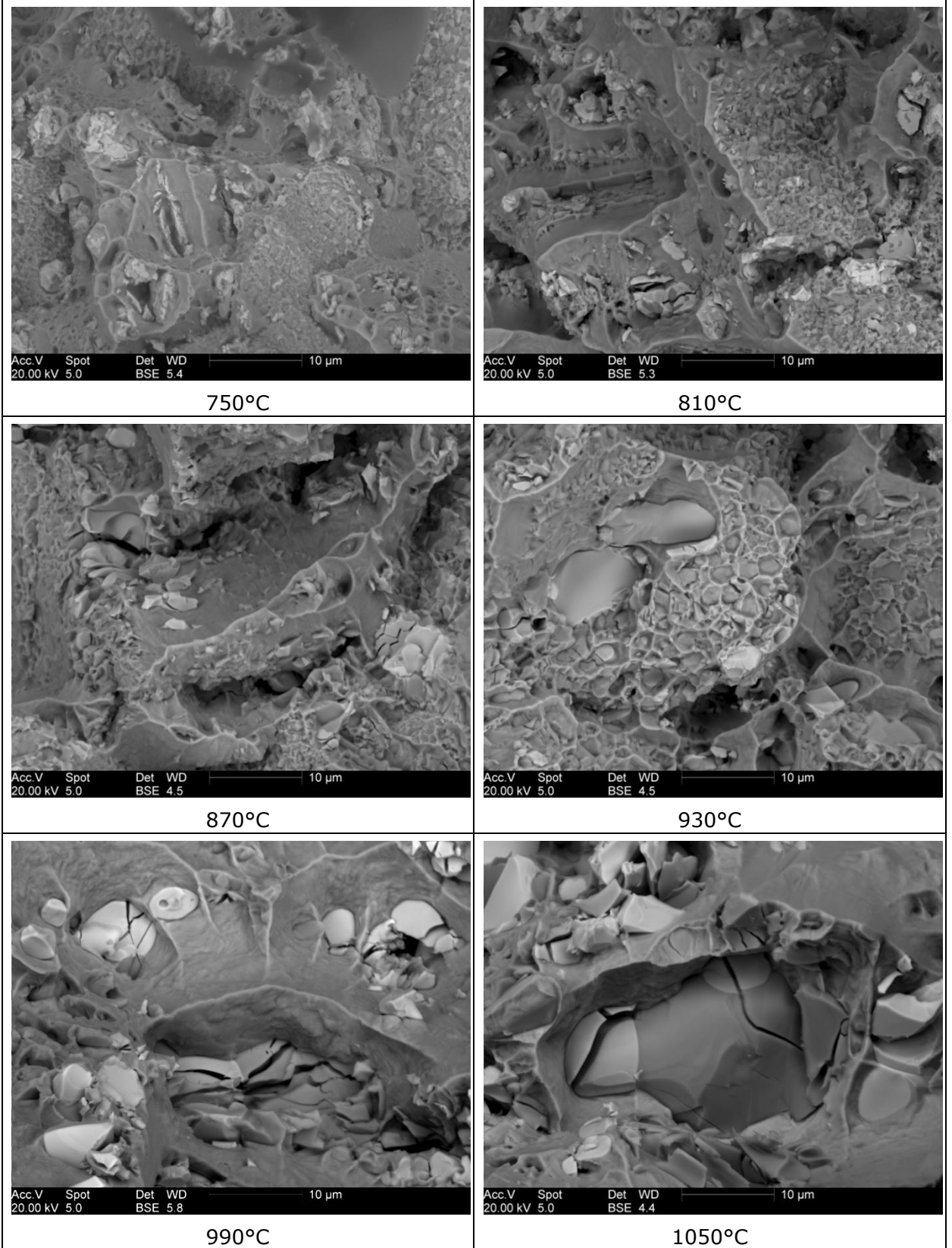


Figure 4.71 Fractographs of the tensile specimens primarily aged for 20000 hrs in the temperature range from 750°C to 1050°C.

5 TRANSITION DUCT – CASE STUDY

5.1 INTRODUCTION

This chapter summarises the results of an examination of a service run transition duct from one of Siemens Industrial Turbomachinery Ltd's (SITL) gas turbines and the correlation between the findings of this, and those of the studies undertaken on laboratory exposed HA230 material that has been ongoing over the last 4 years.

5.1.1 BACKGROUND

The transition duct, shown in Figure 5.1, had been in service for 11000 hours before being removed for metallurgical review. During the overhaul of the engine, the duct had been grit blasted, a routine process applied to remove any deposits/loose oxides built up during operation.



Figure 5.1 Typical views of The Transition Duct.

The ducts are manufactured from two sheet pressings (forming the upper and lower section) which are welded together before being attached (by welding) to the inlet and outlet flanges. These sections are indicated in Figure 5.1. The inlet and outlet flanges are also manufactured from Haynes 230 alloy but in forged ring and thick plate forms, respectively.

During manufacture, the ducts undergo stress relief heat treatments on at least 3 occasions after pressing and between the welding stages. This involves heating to 1170°C followed by rapid cooling. This is a similar (but slightly lower

temperature) heat treatment applied to the sheet material in its as supplied condition.

During operation, the ducts experience a range of temperatures between ~600 °C to >900 °C. Figure 5.2 shows a typical temperature distribution predicted from design analyses which indicates the highest temperatures to be biased towards the outlet flange.

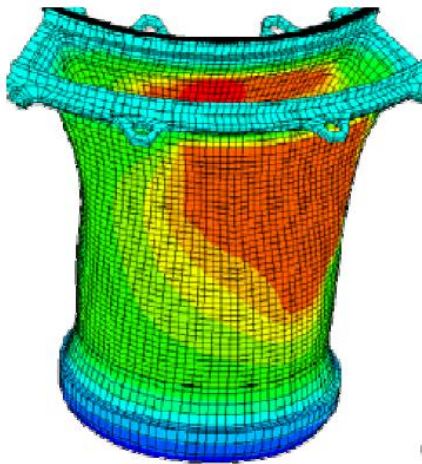


Figure 5.2 FE model of predicted temperature distribution.

5.1.2 METHODOLOGY

Based on the temperature predictions shown in Figure 5.2, a slice of the duct was taken as shown in Figure 5.3 to enable the full range of temperatures experienced by the component's microstructure to be examined.

The microsections were mounted and prepared for metallurgical review by polishing to a 1 µm finish and etching in hydrofluoric acid. The microsections were then examined using optical and scanning electron microscopes in a similar manner to the laboratory exposed material.

In addition, hardness tests were performed along the length of the slice.

The results of the microstructure review and hardness tests were then compared to the laboratory exposed material and temperature estimations made.



Figure 5.3 Location of the slice taken for metallurgical examination and illustration of its sectioning.

5.2 RESULTS AND DISCUSSION

5.2.1 HARDNESS STUDIES

Hardness studies were carried out on metallographic sections cut from the strip. Vickers hardness tests at load of 20 kg were performed in the middle of the cross section along the length of the microsection with 2mm distance between each impression. Two sets of these hardness tests were completed and the results were plotted versus distance along the strip, see Figure 5.4a. The average hardness values fitted with a third polynomial trend line are shown in Figure 5.4b.

When these hardness results were compared with the hardness data obtained for thermally exposed and creep tested specimens (see Section 4.1.2), it was apparent that in general the results are lower. However, some very high values were measured. Thus in order to interpret these figures it was necessary to correlate these results with the microstructures.

The minimum value obtained (193 Hv) was approximately 30 mm from the weld at the warmest part of the transition duct, while the maximum (excluding the first value close to the weld) was found 113 mm from the same weld and is equal to 258 Hv. Interestingly, this maximum value creates a clear peak between previous and following values of 209, and 214 Hv respectively. This peak was seen on two separate hardness traces therefore it is believed not to be an error in measurement.

Figure 5.4 shows that the lowest hardness values were obtained in the first half of the test slice, up to approximately 10 cm from the weld, which corresponds to the hottest part of the transition duct, as predicted by thermal analyses. After the peak value, the hardness increases slowly to a value of 228 Hv in the cooler part in the duct, after which the hardness drops suddenly to 205 Vickers.

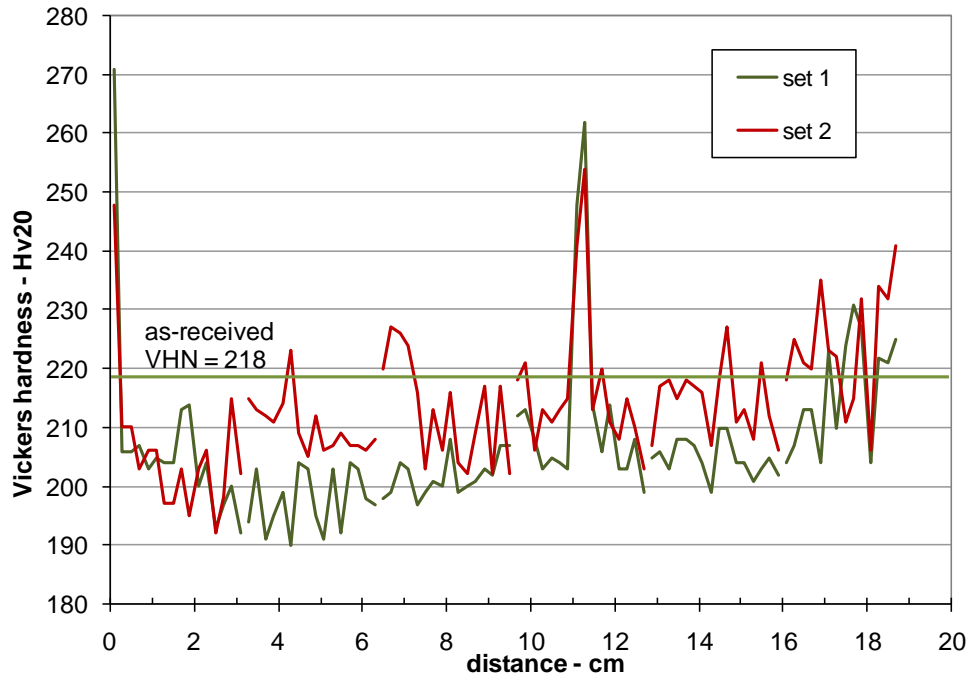


Figure 5.4a Vickers hardness vs. distance along the strip from the outlet flange weld showing two sets of data.

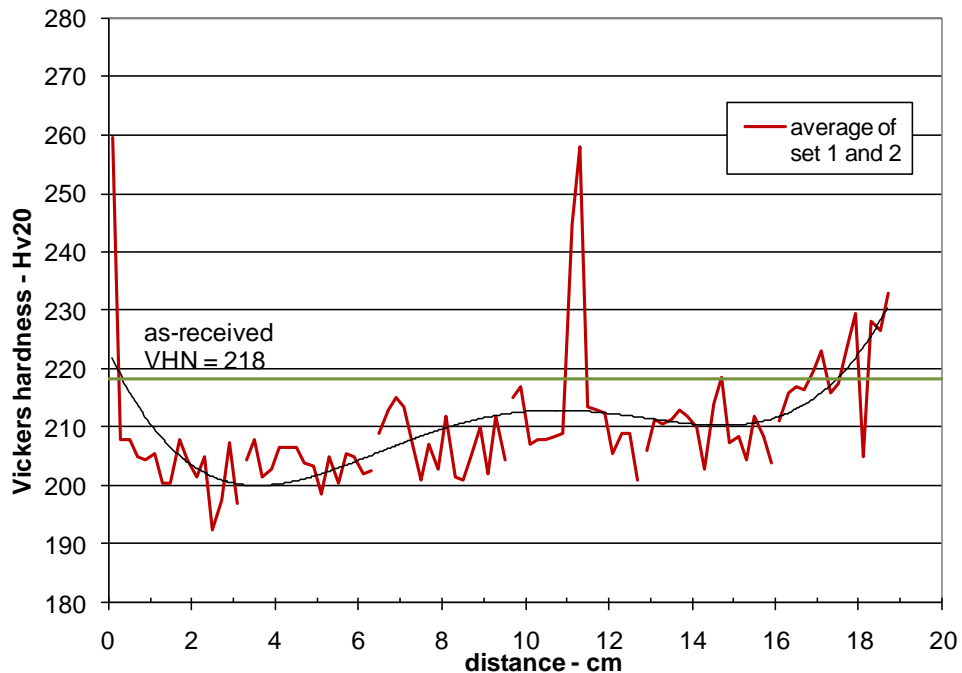


Figure 5.4b Vickers hardness vs. distance along the strip from the outlet flange (warm) weld showing average hardness values for two sets of values and the trend line of the 3rd polynomial.

Applying the data collected from the laboratory studies, see Figure 5.5, to the hardnesses obtained on the transition duct, see Figure 5.6, Table 5.1 determines the estimations of temperatures (for details see Appendices 9.1.1).

Table 5.1 Temperature estimations from hardness values.

Position		
1 cm	Hv = 205	T (°C)
	LMP = 17.8 =	467
2.1 cm	Hv = 201	T (°C)
	LMP = 17.6 =	459
3.5 cm	Hv = 208	T (°C)
	LMP = 17.9 =	472
6.7 cm	Hv = 213	T (°C)
	LMP = 18.2 =	484
	or = 28.4 =	908
	or = 31.6 =	1041
11.1cm	Hv = 244	T (°C)
	LMP = 21.1 =	605
	or = 23.2 =	692
12.3 cm	Hv = 209	T (°C)
	LMP = 18.0 =	476
	or = 30.2 =	983
16.7 cm	Hv = 216	T (°C)
	LMP = 18.3 =	488
	or = 27.8 =	883
	or = 32.2 =	1066
17.7 cm	Hv = 223	T (°C)
	LMP = 18.8 =	509
	or = 26.8 =	842
	or = 32.8 =	1091

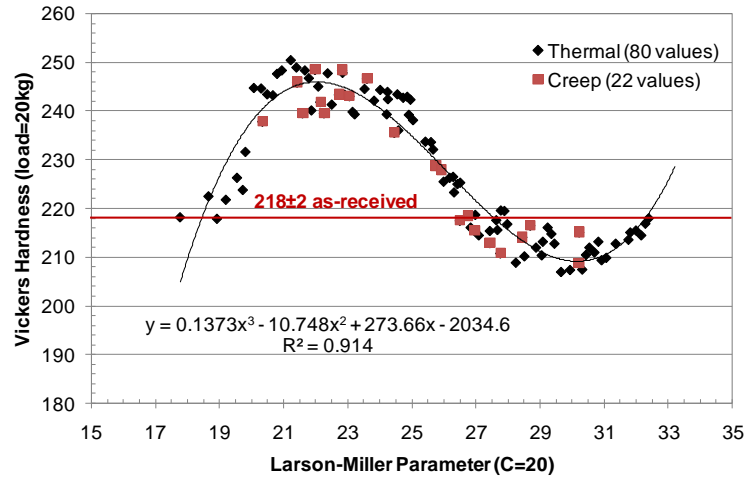


Figure 5.5 Hardness Master Curve.

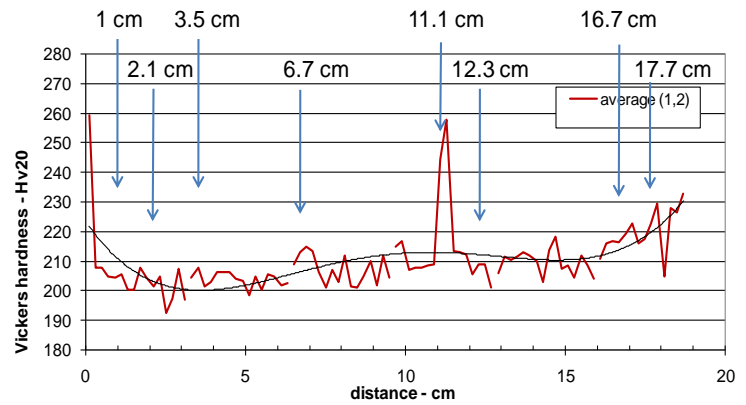


Figure 5.6 Positions of examinations.

It can be seen that, with the exception of the first three positions, two or three potential temperatures can be obtained for a given hardness value. Therefore it is important to use this data in conjunction with the microstructural features to determine which of the temperatures obtained above is the most likely candidate.

5.2.2 MICROSTRUCTURAL STUDIES

Optical microscopy and scanning electron microscopy was used to examine the test strip. The scheme for the correlation between the hardness, the position along the strip and the microstructures is presented in Figure 5.7.

The microstructure of the transition duct showed a number of differences from previous laboratory exposed and creep tested samples. The most remarkable difference is the grain structure as most areas consisted of a very large grain structure with enormous precipitation of chromium rich carbides. Surprisingly within the microstructure many precipitates were present; there were many tungsten rich primary carbides, $M_{12}C$, and also there was a lot of secondary precipitation of chromium rich carbides (smaller in size compared to the $M_{12}C$) within the grains, at the grain and annealing twin boundaries and coexisting with $M_{12}C$. To identify similarities, with the laboratory samples, on a large scale was difficult due the reason mentioned above. But on a smaller scale, 50 μm and less, the same microstructural features can be found in the thermally exposed and creep tested specimens. To confirm our assumption and estimation of the range of service temperatures microstructure images from other studies were used.

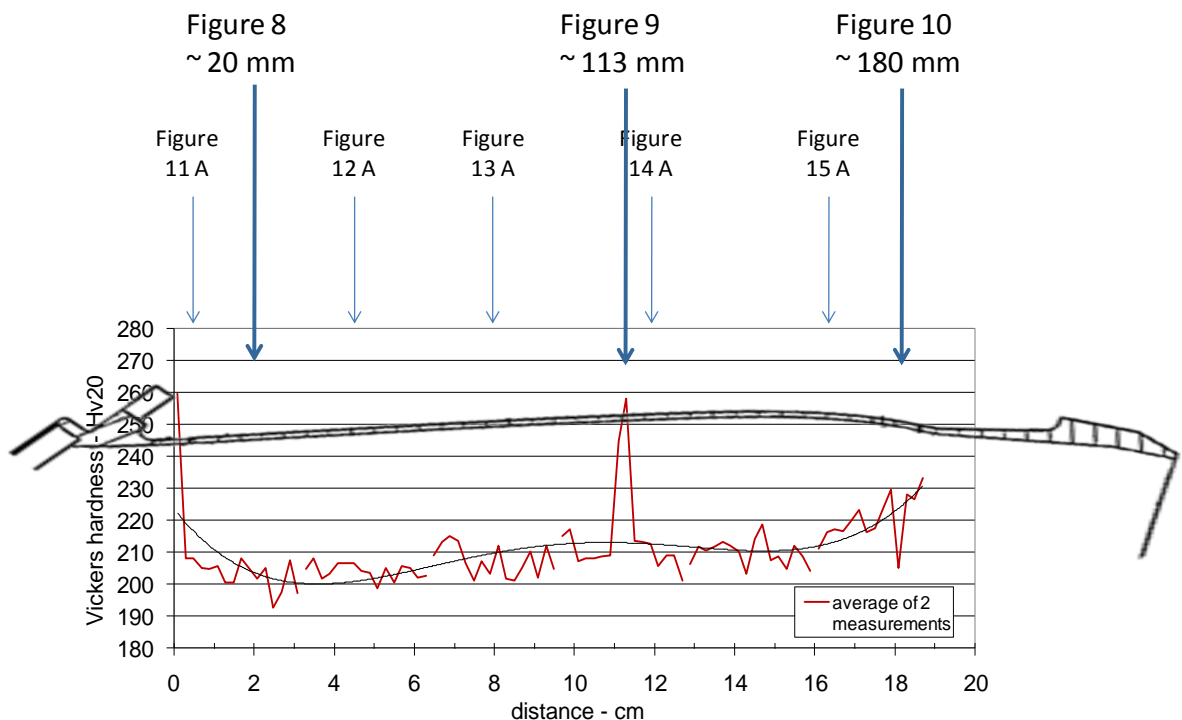


Figure 5.7 The correlation between the hardness, the position along the strip and the microstructures.

Figures 5.8 – 5.10 show montages of optical images of the whole thickness of the T-duct strip in three different places.

Figure 5.8 represents, according to the FE model (Figure 5.2), the warmest part on the component. In this region, distinct grain boundaries are decorated with precipitates, and an abundance of other fine precipitation within the microstructure. Distinct heterogeneity of the grain size can be observed, only a few small grains are present, but the grain boundaries mostly cross the whole thickness of the strip. Also the areas close to the boundaries appear depleted of precipitation which may be caused by the massive precipitation of the chromium rich carbides on the grain boundaries. On the other hand, other areas of the microstructure look completely different (see Figure 5.9 and 5.10 - approximately in the middle of the T-duct strip and the coolest part, respectively).

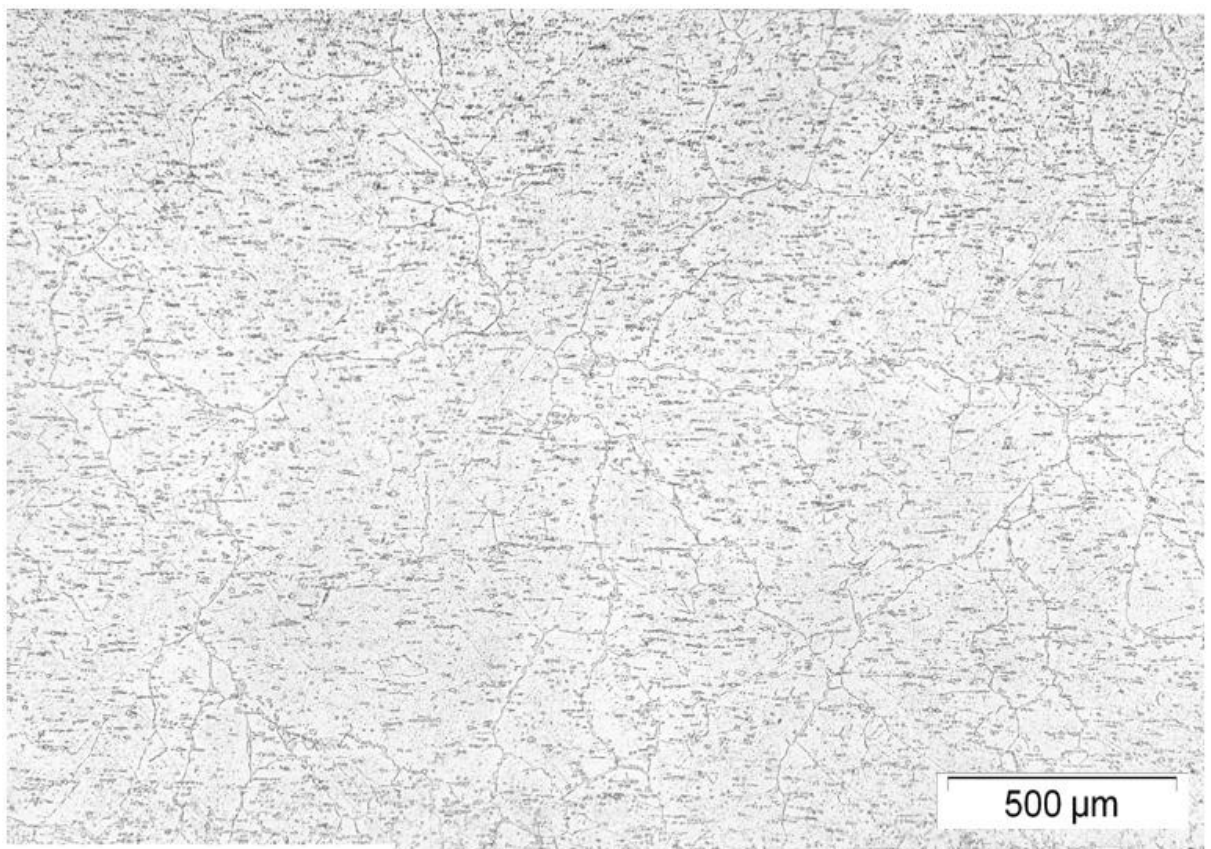


Figure 5.8 Optical image of the microstructure ~ 20mm from the outlet flange weld.

Figure 5.9 shows the position with the highest hardness value (258 Hv) thus can be concluded that the unexpected peak in hardness was very likely associated with the change in the grain size. The smaller grain size can be identified as an ASTM 4-5 which is typical for the as-received material and has been found in the majority of the specimens examined before. This type of grain structure was observed in this area only; close to the inner part of the T-duct (corresponds to a distance of 110-118 mm from the outlet flange weld). Following this there were

large grains with carbide decoration on grain boundaries, but no fine precipitation within the grains could be seen. The 'cooler' part of the T-duct shows a mixture of all the microstructural features mentioned above. There is a mixture of irregular large grains with coarse precipitation, other adjacent large grains filled with fine precipitation, annealing twins and depleted areas close to the grain boundaries, and also localised regions of smaller grains. It might be caused during the manufacturing process, as suggested in models by Strolovitz et al. [87].

The heterogeneous grain structure was not observed before to such a degree. Therefore the correlation with the microstructures seen in the laboratory samples had to continue on a smaller scale, comparing only the precipitation and transformation of the phases present.

Figure 5.11 shows typical microstructural features in the first part of the T-duct strip, 1-30 mm from the outlet flange weld. Image A shows enormous precipitation on the grain boundaries as well as within the grains. Stringers formed by primary carbides indicate the direction of rolling. Images obtained by scanning electron microscope in this part of the strip indicate some similarities with features found for example in the specimen thermally exposed for 15000 hrs at 810°C and specimen B644 creep tested at 800°C, 85MPa [63]. Transformation of the primary carbide $M_{12}C$ can be observed in all areas; with the main 'transformation' on the stringers. Some of the large $M_{12}C$ carbides retain their round shape and coexist with Cr-rich carbide around their edges. In addition, some of the smaller $M_{12}C$ are consumed by the Cr phase. Chromium carbide precipitation is present along grain and annealing twin boundaries, mostly creating continuous precipitation. In addition, migration of grain boundaries was observed.

In Figure 5.12 the microstructures of the area 40 mm from the outlet flange weld are compared with those of the specimen thermally exposed for 10000 hours at 870°C. A large amount of precipitation can be seen within the microstructure together with large primary carbides and clusters of precipitates growing out of the grain boundaries. At temperatures of 870°C, large primary carbides $M_{12}C$ are seen to be transforming around the edges where chromium rich phase can be found. Chromium rich precipitates on the grain boundaries are becoming much coarser, forming a continuous precipitation.

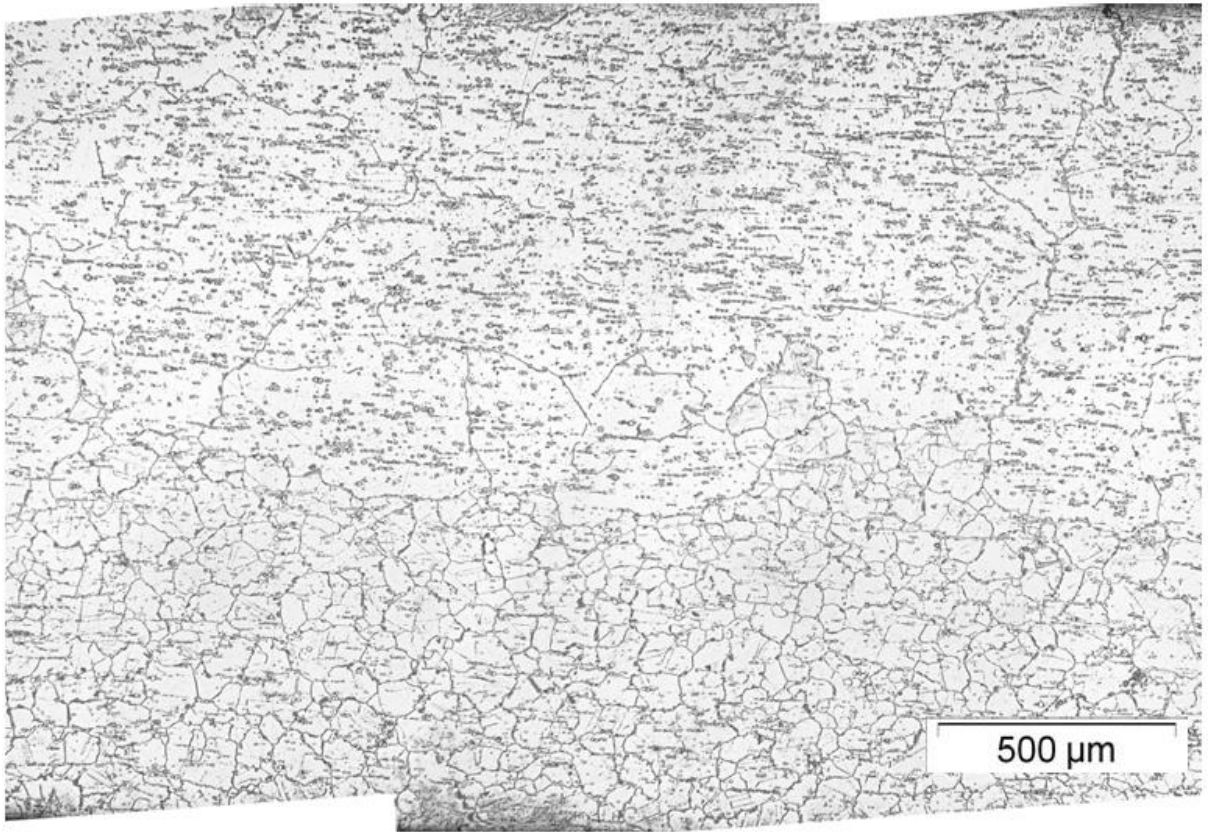


Figure 5.9 Optical image of the microstructure ~ 113mm from the outlet flange weld.

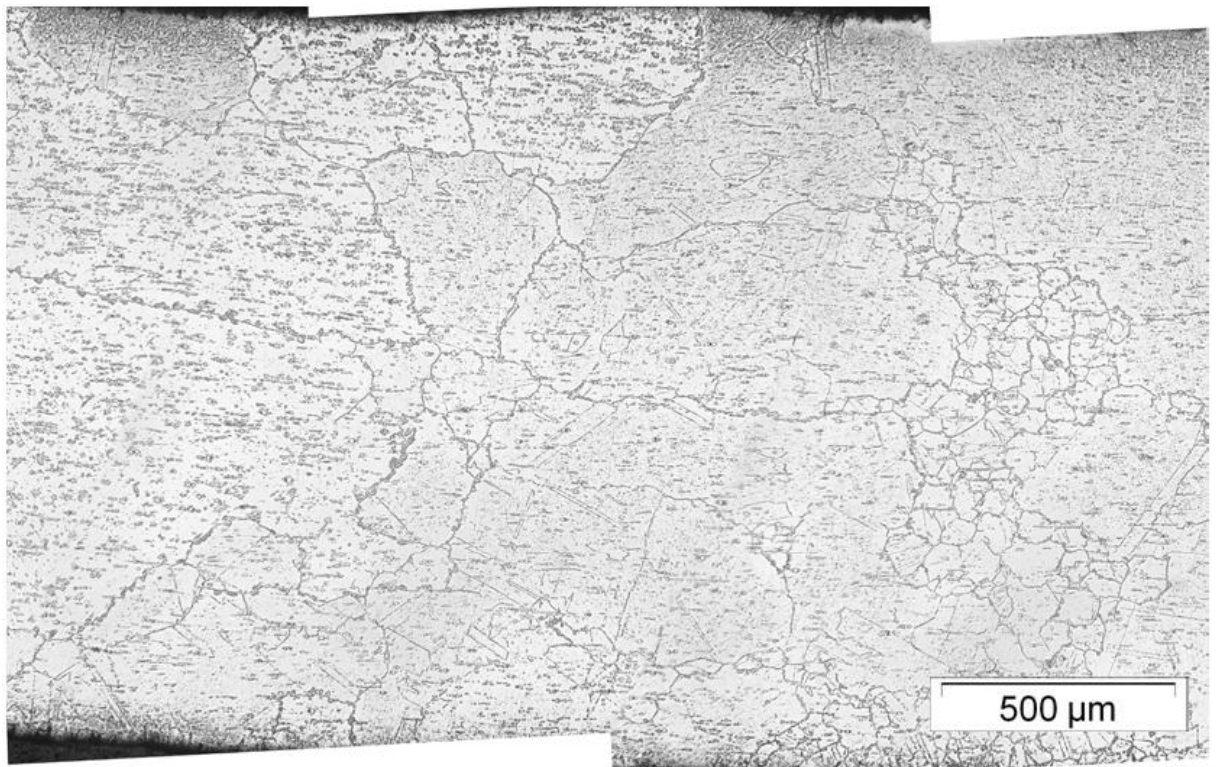
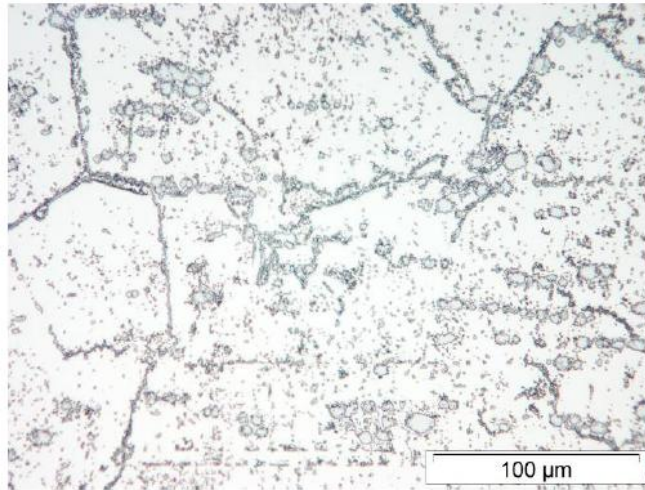
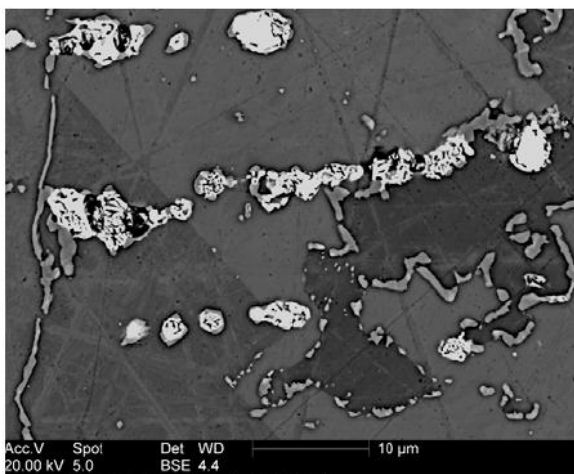


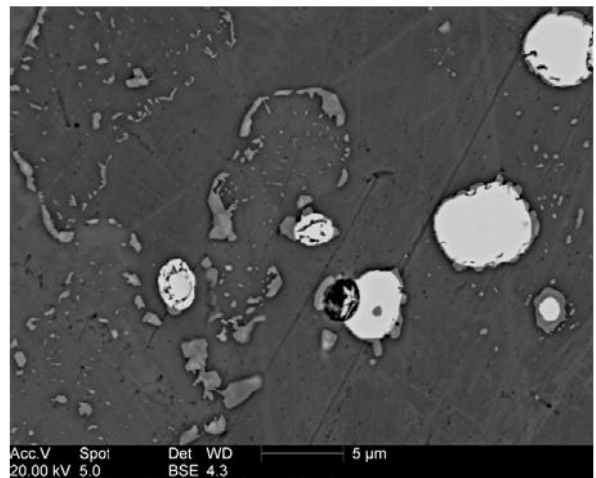
Figure 5.10 Optical image of the microstructure ~ 180mm from the outlet flange weld.



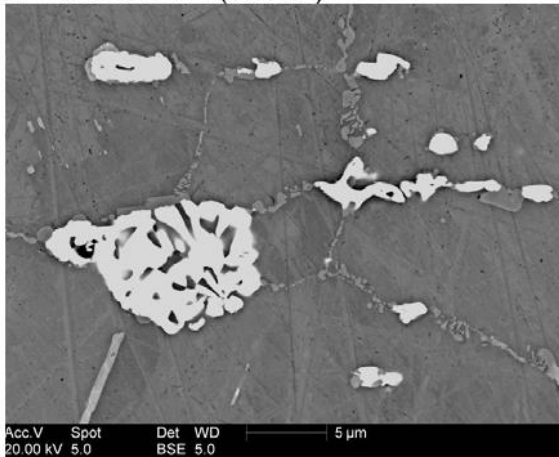
A -



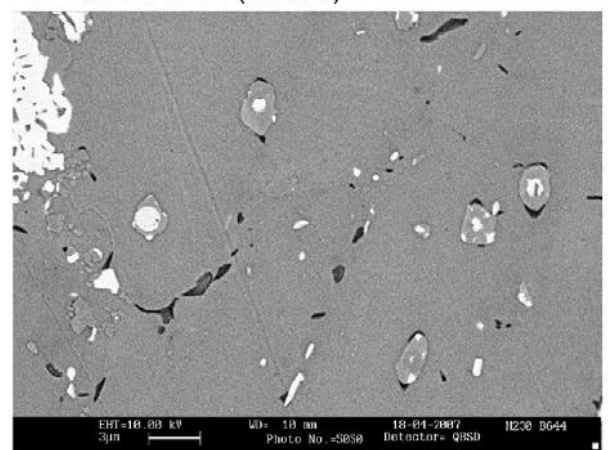
B - TD01 BSE (x2500)



C - TD01 BSE (x3500)

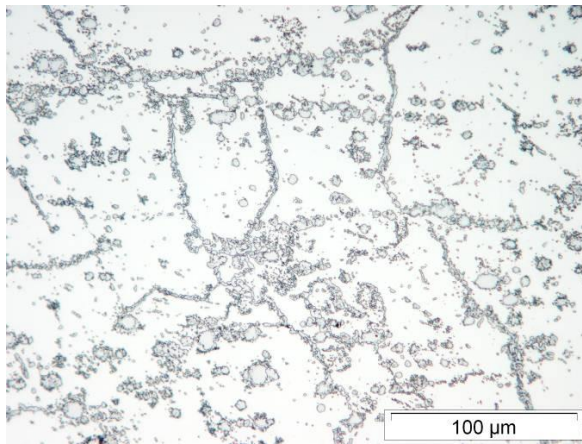


D - 15000 hrs @ 810C

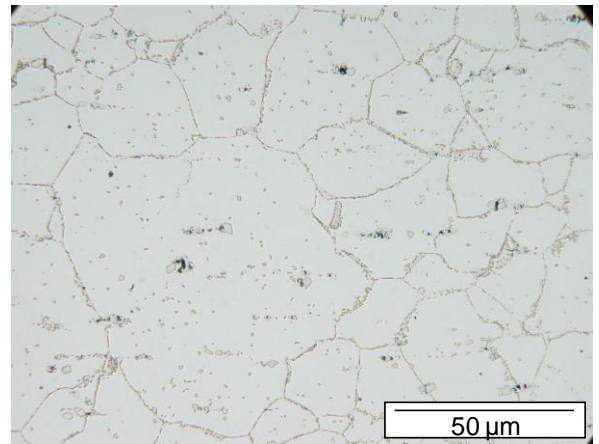


E - Creep tested B644 800°C, 85MPa

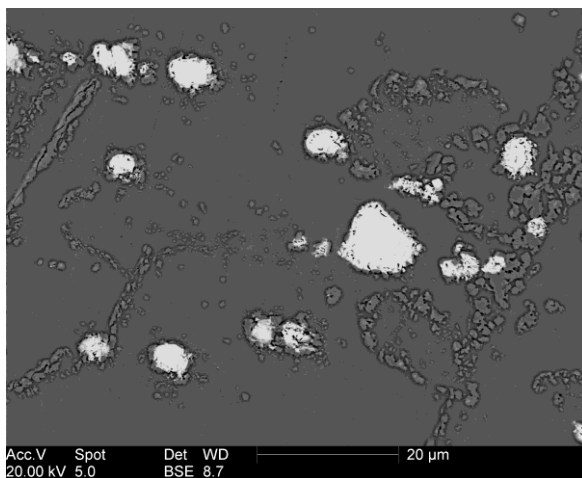
Figure 5.11 A -Optical image of the microstructure ~ 10mm from the outlet flange weld; B, C - BSE images of the typical features in the region; D - BSE image of the thermally exposed sample for 15000 hrs @ 810°C; E - BSE image of the creep tested B644 at 800°C, 85MPa/ MSc thesis CNR-IENI, Milan (It) [63].



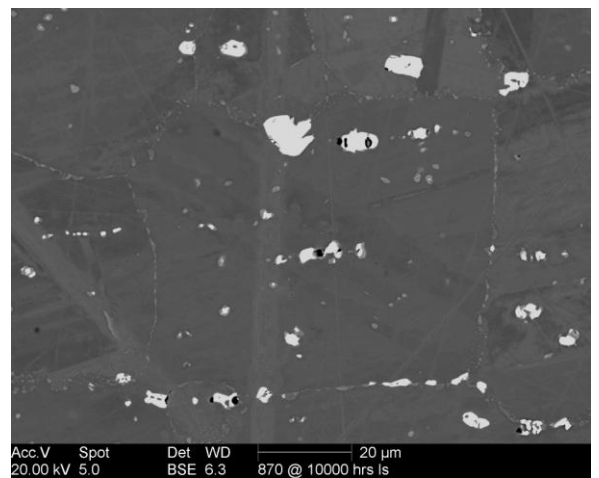
A



B - 10000 hrs 870°C Is 100x



C - TD BSE (1500) 2a_6



D - 10000 hrs @ 870°C Is 1000x BSE

Figure 5.12 A - Optical image of the microstructure ~3.7cm from the outlet flange weld; B - optical image of the thermally exposed specimen for 10000 hrs at 870°C; C - BSE image of the microstructure in the same area of T-duct as mentioned above; D - BSE image of the thermally exposed specimen for 10000 hrs at 870°C.

The microstructure in the area 8 cm from the outlet flange weld (see Figure 5.13) contained similar features to those seen in the previous figures. The microstructure is full of large transforming primary carbides $M_{12}C$, chromium rich precipitates concentrating on the grain boundaries causing grain boundary movement and some fine precipitates can be found within the grains. A new feature can be observed in the warmer part of the T-duct as shown in Figure 5.13A. It is a new small irregular grain, usually about 100 microns in diameter, often with grain irregular boundaries, and within this grain, plenty of fine chromium rich precipitation is present.

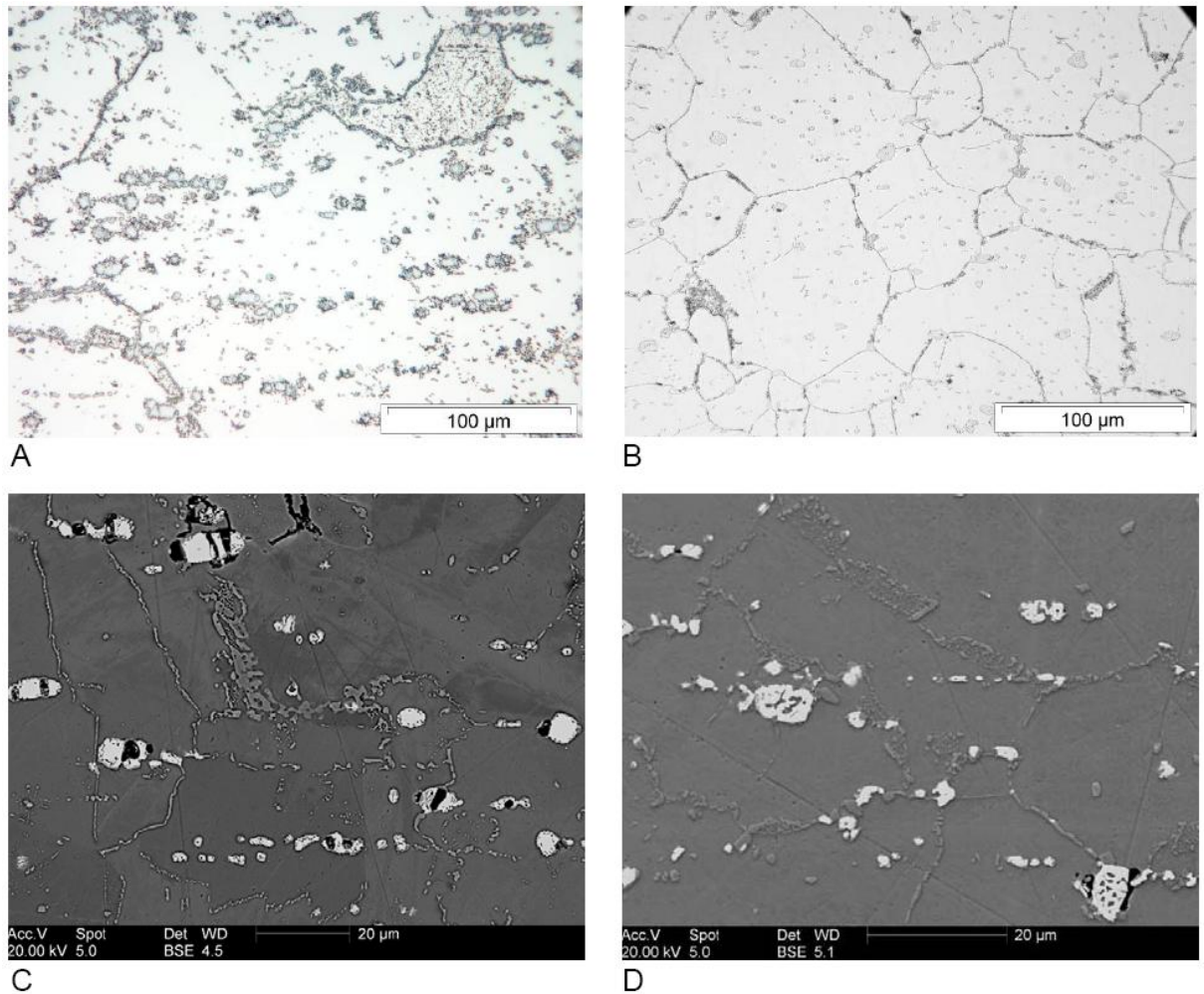
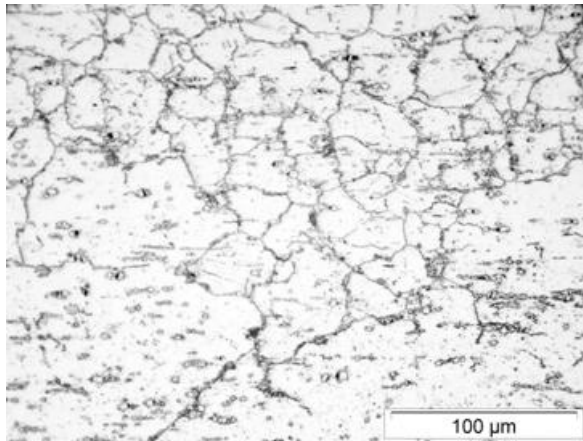
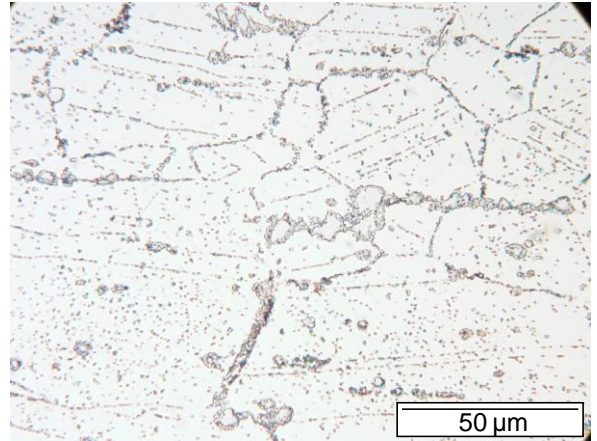


Figure 5.13 A - Optical image of the microstructure ~ 80mm from the outlet flange weld; B - optical image of thermally exposed specimen for 15000 hrs at 810°C; C - BSE image of the microstructure in the same area of T-duct as mentioned above; D - BSE image of the creep tested specimen for 20000 hrs at 810°C.

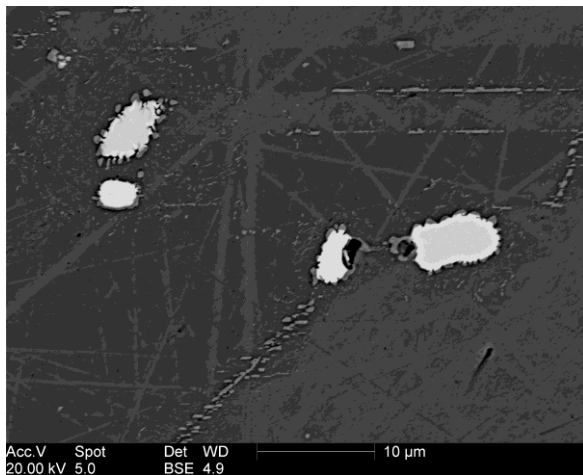
Figure 5.14 shows microstructural features found in the area of the maximum hardness. Very similar microstructure was observed in the creep specimen DLB tested at 700°C for 4995 hours. In the gauge length of DLB, growth of the grains was noticed. Coexisting primary carbides and chromium rich phase, chromium rich precipitation along grain and annealing twin boundaries, and fine precipitation within the grains are the main microstructural features.



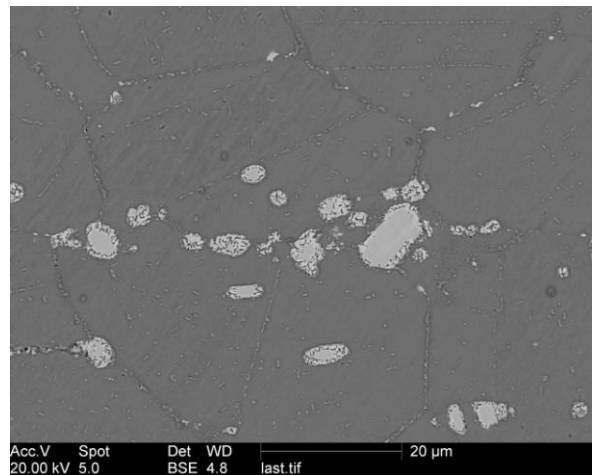
A



B - DLB GL 25



C - TD01 BSE (2500) 4.x_3



D - DLB_GL_BSE_1500_a6

Figure 5.14 A- Optical image of the microstructure ~ 120 mm from the outlet flange weld; B - optical image of GL of the creep tested specimen DLB for 4995 hrs at 700°C ; C - BSE image of the microstructure in the same area of T-duct as mentioned above; D - BSE image of the creep tested specimen DLB.

The microstructure of the coolest area approximately 17 cm from the outlet flange weld is shown in Figure 5.15 together with the images of the microstructures of creep tested specimen DKX tested at 650°C for 6576 hours. In this zone, the transformation of large primary carbides M_{12}C is accompanied by formation of cracks and voids, as well as M_{12}C 'fringed' with chromium rich phase. The chromium rich phase is present on the grain and annealing twin boundaries in some areas. In addition, Cr-rich precipitates are clustered together.

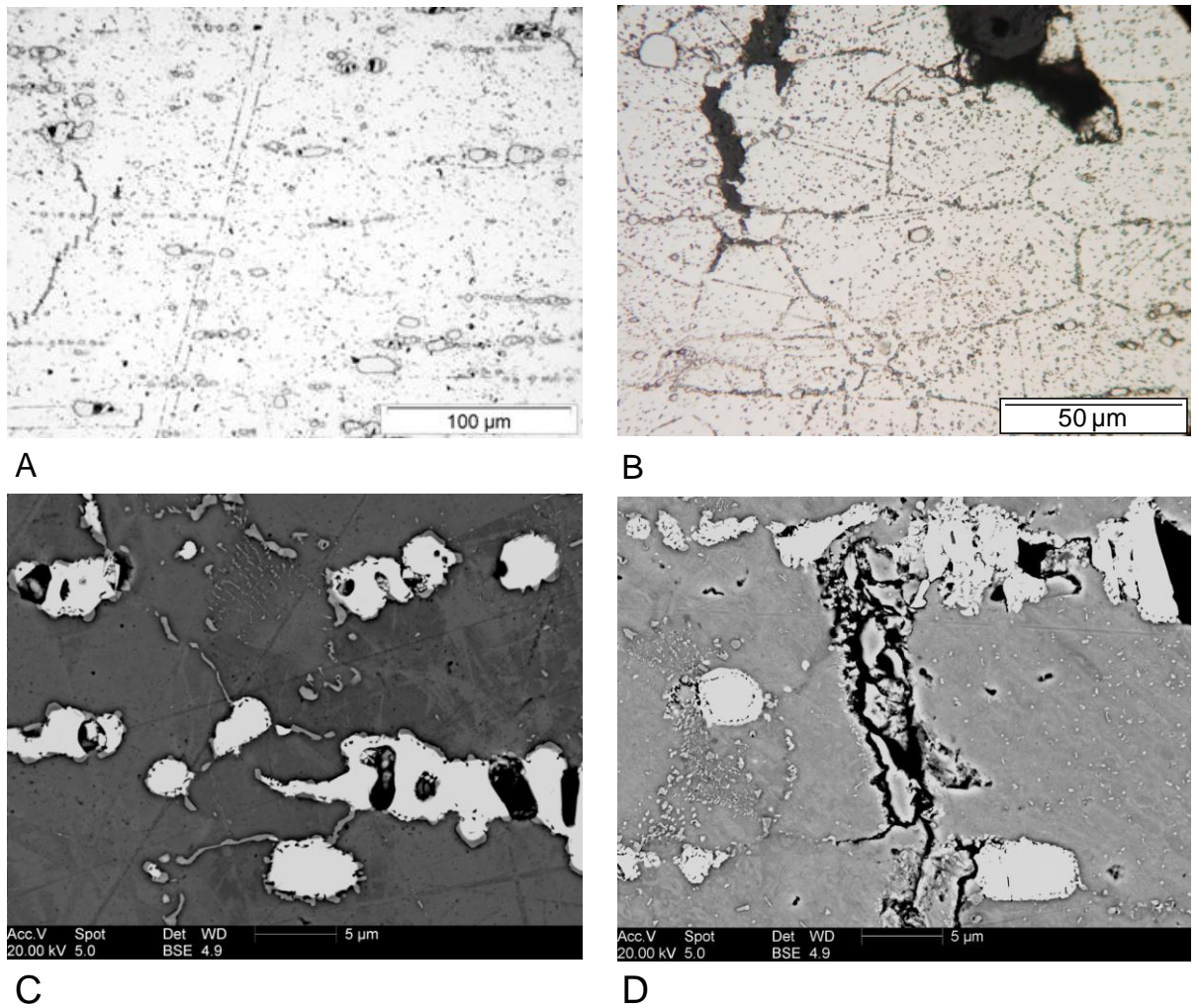


Figure 5.15 A - Optical image of the microstructure ~ 170mm from the outlet flange weld; B - optical image of GL of the creep tested specimen DKX for 6576 hrs at 650°C; C - BSE image of the microstructure in the same area of T-duct as mentioned before; D - BSE image of the creep tested specimen DKX.

5.2.3 OXIDATION CHARACTERISTICS

For the evaluation of the average exposure temperature another microstructural factor may be used - the internal oxidation behaviour. The application of the results obtained on the oxidation attack from the series of laboratory tested specimens is a useful tool for the temperature estimation.

Generally, in the non carburizing environment, the inner oxidation increases with increasing temperature, as presented in Section 4.9. Figure 5.16 shows the comparison of the oxidation attack for the specimen creep tested, thermally exposed and specimen from transition duct. The specimen creep tested for 18159 hrs at 700°C (Figure 5.16a) has the decarburised zone (secondary phase depletion) narrow in contrast with the specimen thermally exposed for 15000 hrs at 810°C

which is approximately 50 μm wide. The decarburized zone on the outer side of the T-duct is narrow or none. More noticeable is the oxide finger penetration which corresponds to that observed on the specimens creep tested at temperatures above 800°C. These facts suggest that the operating temperature in the areas of this T-duct shown in Figure 5.16 c) and d) could not be much higher than 810°C.

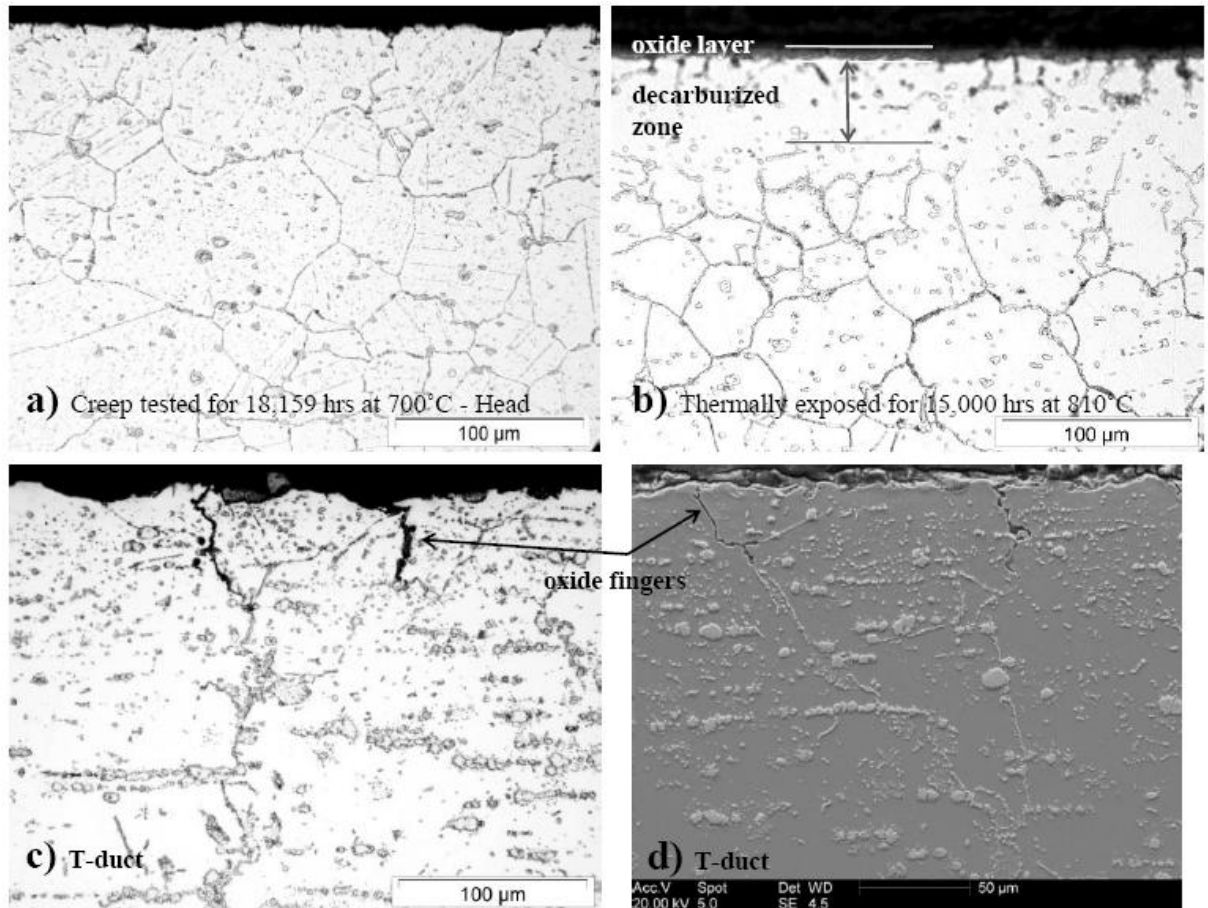


Figure 5.16 Comparison of the internal oxidation between the creep tested sample DLA, thermally exposed sample (15000 hrs at 810°C) and the outer side of the T-duct samples.

The oxidation effect on the inner side of the T-duct is different, see Figure 5.17. On this side of the T-duct the carburization occurs, mostly in the warmest (according to the FE model) part. Needle-like and 'pool-like' Cr-rich precipitates can be observed. The effect of embedding or 'fringing' of W-rich phase by the Cr-rich phase takes place in this area. The networks of the oxide fingers are decorating the edge of the T-duct specimen. This effect has not been observed neither in the thermally exposed or in creep tested specimens, as well as the needle-like precipitates with the composition similar to 'pool-like' phase. In the EDX sections (4.4.3) the varying composition of Cr-rich phase is described. However the

composition of Cr-rich phase varies, the XRD results show clearly that all variations of this phase correspond to the carbide with the $M_{23}C_6$ structure.

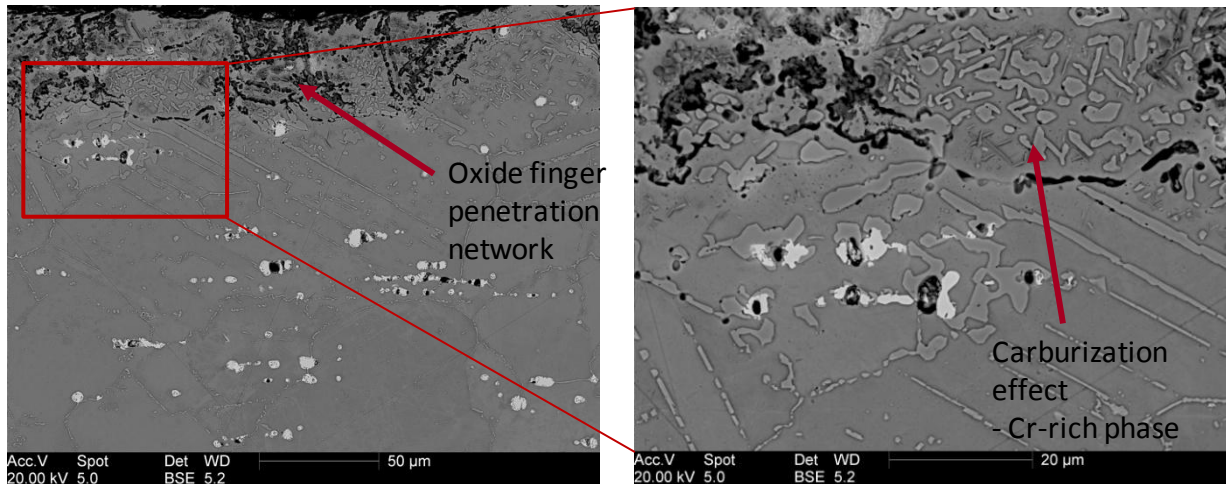


Figure 5.17 Microstructure of the inner side of the T-duct sample showing the carburization behaviour, precipitation of Cr-rich $M_{23}C_6$.

5.3 CONCLUSIONS

Figure 5.18 shows the comparison of the temperature estimations obtained from the hardness tests and the microstructure examination. There are some significant variations between the two sets of results that probably relate to the initial hardness of the manufactured component, as well as processing effects during the manufacturing.

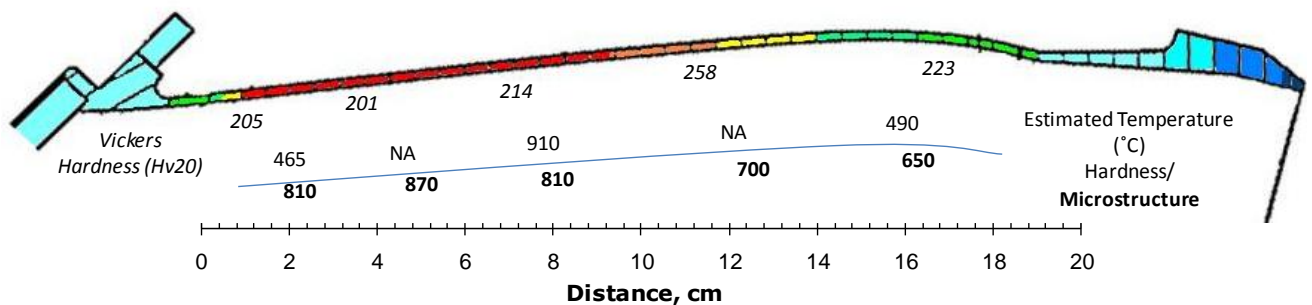


Figure 5.18 Comparison of the temperature estimations from the hardness tests and the microstructures.

The processing of the component during manufacture appears to affect the material grain structure significantly.

This case study showed the potential in application of the model to estimate temperature of operation on components returned from service, in spite of the results revealed a need for further studies to try and refine the process, as well as to understand these changes. For example, assessment of a new component after

the full manufacturing process would give important information about the initial stage of the microstructure (grain size, distribution of precipitation, etc.). These are the factors affecting the behaviour of the material exposed to high temperatures and stressed during the service. Likewise the knowledge of the as-supplied conditions of the material, in our case the hardness at least, would help to create a method of "normalising", e.g. the hardness results. Variations between material and manufacturing batches have to be taken into account, which could have significant effect on the final estimations. In addition, the effects of creep stress on the kinetics of the phase transformation have to be studied in greater detail to gain a better understanding.

6 DISCUSSION

In the Result Chapter some preliminary analysis is given. Here the strands are drawn together.

Optical microscopy and FEGSEM studies on HA230 coupons thermally exposed for up to 30000 hours at temperatures in the range 500°C to 1170°C have revealed microstructural features which can be connected with hardness changes described in Figure 4.3. The initial increase in hardness at lower temperatures can be correlated with precipitation of chromium rich $M_{23}C_6$ carbides at grain boundaries and original annealing twin boundaries within the grains. For example, the specimen exposed for 15000 hours at 750°C (242.7 Vickers) demonstrates a rise in hardness of more than 11% above the value of as-received material (218.0 Vickers) (Figure 4.2). Further exposure results in gradual softening of the material, which can be related with progressive coarsening of $M_{23}C_6$ type carbides and subsequent re-resolution of these precipitates in the microstructure. The material starts to harden again after it reaches its minimum at 990°C. This appears to be due to precipitation of the 'pool-like' phase, which creates clusters within the microstructure and is very hard and brittle.

Previous studies by Jordan et al. [145] and Wittenberger [29, 61] have only been carried out at shorter exposures with unstrained HA230 at temperatures below 950°C (<22500 hours) but the results here are consistent with those previous studies.

It is interesting to note that 'pool-like' precipitates similar to those in material thermally exposed at 990°C and 1050°C for prolonged exposures (10000-30000 hours) (see Figure 4.24) have been observed in the gauge lengths of creep tested samples DLH, COD and COG. This suggests that in the absence of plastic deformation the microstructural evolution occurs at a much slower rate during thermal exposure than during creep testing. This type of precipitation in Haynes Alloy 230 was observed by Lai [54] during his nitridation tests at 980°C for 1000 hours. He identified the phase by XRD as a chromium nitride Cr_2N . In this work, no nitride has been found by X-ray analyses (EDX, XRD). The EDX analyses show the transition phase to contain ~30wt% Cr, ~30wt% W and ~30wt% Ni (see Section 4.4.3). Secondly, comparison of the peaks from X-ray diffractograms with powder diffraction data cards rejects the presence of this nitride and the peaks have been assigned as $M_{23}C_6$ type carbide ($a=10.65\text{\AA}$). Its mechanism of formation has not been reported yet.

The statistical analysis of the hardness results has demonstrated that the data from the thermally exposed coupons and unstrained creep specimens heads can be combined on engineering bases and a Master Hardness v Larson-Miller parameter curve generated. A least squares regression analysis has shown that a third degree polynomial of the form:

$$H_v = 0.1373P^3 - 10.748P^2 + 273.66P - 2034.6$$

gives an R^2 -value of 0.914 using a C value of 20. The C value (Larson-Miller constant) was optimised using the data to be 22.2, but the 'conventional' value of 20 is statistically reasonable. The confidence interval (95%) and the prediction interval have maximal widths equal to 3.6 and 17.1 Vickers respectively.

Nanohardness studies proved that the primary carbide and Cr-rich 'pool-like' phase are hard and brittle. Their hardness is between 18 and 22 GPa when using a load of 10gf. This interval agrees with values in the literature, *e.g.* [64, 65]. More accurate values are difficult to obtain due to limitations such as the number of indentation test and the positioning of the nanoindenter.

The microstructural examination of the specimens thermally exposed as well as of those creep tested demonstrate similar mechanisms of phases formation, though the changes proceed much more slowly during thermal exposure. At lower temperatures (up to 750°C) incipient 'break down' or transformation at the edges of the large W-rich primary carbides can be observed. Between 750°C-810°C the primary carbides contain dark features (usually a hole with particle visible at the bottom, possibly the place from where a primary carbide was pulled out of debonding effect occurred) in the whole volume and secondary precipitates, chromium rich $M_{23}C_6$ carbides, start to coexist in contact with or diffusing into these primary carbides (*i.e.* they precipitate/grow at the peripheries of the primary carbides). With rising temperature, above 870°C, the tungsten rich phases become uniform again, less irregular in shape and often contain dark features within the middle of the particle. At 930°C the sizes of both types of precipitates (tungsten rich and chromium rich) increase, with the phases coexisting, either in contact or merging together. In the microstructures of the specimens exposed at the highest temperatures a new 'pool-like' phase appears. In the case of the thermal exposures 'pool-like' precipitates form clusters within the microstructure whereas in the creep specimens the phase creates almost continuous networks. The 'pool-like' precipitates are not always uniform in composition, containing consumed particles, as well as cracks and some voids.

X-ray analyses (EDX, XRD) confirmed the presence of the primary tungsten rich carbides in the as-received material and in the microstructure of thermally exposed samples. This type of carbide can be found in the whole range of experimental temperatures (750°C - 1050°C) and was identified as $M_{12}C$ type carbide with a lattice parameter of 10.96Å. The presence of secondary $M_{23}C_6$ carbide precipitation is evident firstly as fine particles at grain and annealing twin boundaries and it conforms to the study by Rothman et al. [43]. At increased temperatures the precipitates tend to be continuous and their precipitation appears at the peripheries of the primary $M_{12}C$ carbides as noted by Klarstrom [23]. The lattice parameter obtained for $M_{23}C_6$ was 10.65Å. In addition, the microstructures of the specimens thermally exposed at higher temperature (above 930°C) and longer durations contain coarsened Cr rich precipitates which were confirmed too as $M_{23}C_6$ type carbide with the same lattice parameter. The third phase detected by XRD was identified as secondary $M_{12}C$ with lattice parameter of 10.83Å. All lattice parameters obtained are similar to those reported by Rothman [43] or by Li [73] in Hastelloy X.

Any deleterious secondary phases such as sigma or mu-phase have not been identified. However, 'pool-like' phase precipitating at high temperatures (>930°C) might be detrimental because of its hardness (~20 GPa) and brittleness.

The studies of oxidation attack performed by Doucet [1] agree with the findings by e.g. Deodeshmukh and Srivastava [53], who exposed HA230 to long-term cyclic oxidation in flowing and still air at 982°C, 1093°C, and 1149°C for a year (8640 hours). The formation of manganese spinel $MnCr_2O_4$ above the Cr_2O_3 scale and the presence of 0.02% La were beneficial in improving oxidation resistance.

In addition to the microstructural studies, ambient temperature tensile tests conducted on HA230 material exposed for 3000, 10000 and 20000 hours at temperatures in the range from 750°C to 1050°C indicated that there was a clear relationship between the 0.2% proof and ultimate tensile strengths and hardness of the samples, with in each case increases in hardness being associated with corresponding increases in both 0.2% proof and ultimate tensile strength.

The failure mechanism of the tensile fractured specimen was analyzed using scanning electron microscopy and in all samples was identified as an intergranular fracture. At the highest temperatures ductile rupture also takes place.

The experimental observations on the laboratory exposed HA230 were applied on a service run transition duct. The changes in the hardness and microstructure of the material can be related to temperature and time of exposure and the information gained can lead to estimation of the average component operating temperature. Metallographic studies revealed a high level of heterogeneity of the grains in this transition duct probably caused by secondary recrystallization during the manufacturing process [87].

7 CONCLUSIONS

This research has covered the investigation of the effects of long thermal and creep exposures on the microstructure of Haynes Alloy 230. The microstructural evolution was determined using microscopy techniques (optical, FEGSEM). The alloy phases have been identified by XRD. A hardness and a microstructurally based model have been used for the evaluation of an ex-service transition duct.

The hardness results have demonstrated that hardness data from thermal and creep exposure tests conducted on HA230 for up to 50000 hours in the temperature range 500°C to 1110°C can reasonably be combined to create a single Master Hardness v Larson-Miller parametric plot. The regression analysis has shown that a cubic polynomial gives a good fit to these data with an R^2 value of 0.914.

The Master Hardness v Larson-Miller Parameter equation may be helpful in combination with microstructural observations for estimating the average exposure temperature of HA230 gas turbine components for known periods in service.

The initial increase in hardness, above the value of the as-received material in solution annealed condition, is due to precipitation of fine chromium rich $M_{23}C_6$ carbides at the grain and annealing twin boundaries. The increase in hardness of approximately 15% peaked following exposure for 1000 hours at temperatures between 600°C and 750°C. Subsequent exposure at higher temperatures and/or longer duration provokes softening of the material which is associated with progressive coarsening of these precipitates and the formation of morphologically other phases within the microstructure. This reached a minimum at an exposure temperature of $\sim 990^\circ\text{C}$, with the average hardness being approximately 5% lower than that of the alloy in its original solution annealed condition with the hardnesses increasing again towards the original value following exposure at 1050°C.

Optical microscopy and FEGSEM studies on thermally exposed coupons of HA230 have revealed microstructural features which can be directly correlated with the changes of hardness observed over the range of duration and temperatures investigated. The microstructures observed in the creep strained samples tested at lower temperature (650 - 750°C) were found to be similar to the thermally exposed test pieces. However, the effects of strain at higher temperature results in almost continuous precipitation present along grain boundaries together with coarse particles randomly distributed within the grains. The effects of creep strain on the microstructure were most distinct at the highest testing temperatures (950°C and

1000°C) where significant changes in the appearance and composition of the precipitation was apparent both in the unstrained heads and gauge length regions of the creep specimens. The appearance of continuous precipitation along the grain boundaries and the presence of 'pool-like' particles exhibiting nanohardness values in excess of 2000 Vickers (~20 GPa) characterised these microstructures. Once more these microstructural changes were mirrored in the microstructure of the HA230 coupons thermally exposed for more than 20000 hours at temperatures > 930°C.

X-ray diffractometer studies have confirmed the precipitation of $M_{23}C_6$ in all the thermally exposed and creep tested HA230 samples. It has also been identified what appears to be two variants of $M_{12}C$, corresponding to lattice parameters of 10.93Å and 10.83Å in the exposed materials. The phases present have a closer match to the two different $M_{12}C$ carbides above, rather than the closest lattice parameter for M_6C (11.06Å). $M_{12}C$ has also been identified in the as-received material which is contrary to what has been published previously for this alloy; that is the primary carbides are an M_6C type. No TCP phases, such as σ or μ , have been identified.

The large 'pool-like' phases observed in the microstructures of the highest temperature and longer duration samples have a lattice parameter consistent with that of the $M_{23}C_6$ carbides observed in the lower temperature/shorter duration samples. The studies have shown that the composition of this phase varies with the time and temperature of exposure, and it is believed that as diffusion occurs, Ni atoms substitute some of the Cr atoms in the phase.

The TEM examinations of the precipitated phases have not greatly helped their identification due the closeness of the lattice parameters of the cubic phases present.

The transition duct case study showed the potential of the model to estimate temperature of operation of a service run components. Surprisingly the manufacturing process affected the material grain structure more than was expected.

8 FUTURE WORK

This project offers many possibilities for future research such as modelling work to predict the precipitating phases and the microstructural evolution or detailed description of the precipitating mechanisms.

It would be useful to explore the microstructures and phases of the exposed specimens using TEM. The difficulties faced during the preparation of the TEM specimens should be eliminated and the preparation technique optimised.

The case study opened a good opportunity to develop a simple practical laboratory procedure for determining the average temperature experienced by service exposed HA230 turbine components. Explanation of the processes which the ex-service components underwent and their correlation with the laboratory tests might be helpful in failure prevention.

Moreover using pre-strained specimens for the examination of the microstructural evolution of the thermally exposed and creep tested specimens would have potential to mimic the effect of processing, i.e. to find out why a service run transition duct shows different microstructural characteristics from the thermally exposed and creep samples examined in this project.

9 APPENDICES

9.1 LARSON – MILLER PARAMETER

The Larson-Miller [90] is one of the most commonly used time-temperature parameters to extrapolate creep-rupture data. By running experiments at the design stress, but at a higher temperature, it is assumed that the failure will occur in a shorter time, and the L-M Parameter (LMP) can be calculated. The idea of this extrapolation is based on the observation that creep is thermally activated process and in 1952 F.R. Larson and J. Miller proposed that creep rate could adequately be described by an Arrhenius type equation (see Equation 9.1). In addition, it is necessary to take into consideration premises such as the failure mechanism does not vary and hence is not a function of temperature or time.

$$r = A e^{-\Delta Q / R T} \quad \text{Equation 9.1}$$

where r is the creep process rate, A is a constant, R is the universal gas constant, T is the absolute temperature, and ΔQ is the activation energy for the creep process.

Taking the natural log of both sides gives

$$\ln(r) = \ln(A) - \Delta Q / R T \quad \text{Equation 9.2}$$

which with some rearrangement:

$$\Delta Q / R = T (\ln(A) - \ln(r)) \quad \text{Equation 9.3}$$

Using the fact that creep rate is inversely proportional to time, the equation can be written as:

$$1 / t = A' e^{-\Delta Q / R T} \quad \text{Equation 9.4}$$

Taking the natural log:

$$\ln(1 / t) = \ln(A') - \Delta Q / R T \quad \text{Equation 9.5}$$

which with further rearrangement the relation finally becomes:

$$\Delta Q / R = T (C + \log(t)) \quad \text{Equation 9.6}$$

This equation is the Larson-Miller relation, and the quantity $\Delta Q / R$ is known as the Larson-Miller parameter. Using the assumption that activation energy is

independent of applied stress, the equation can be used to relate the difference in rupture life to differences in temperature for a given stress.

$$\text{LMP} = f(\sigma) = T [C + \log (t)] \quad \text{Equation 9.7}$$

It has been found reasonable for most of the materials when input data are limited to use the value of $C = 20$ (generally in the range between 17 and 21 for metals) and the optimum value is defined by $\log t = C$. (see Figure 9.1) This parameter is plotted against the stress to obtain a Master Curve of the creep rupture behaviour. By knowing the L-M Parameter for a given stress it is possible to determine the time to failure at a given temperature or to predict the temperature at which a given creep strain will be reached in a given time.

Although originally developed as a means of describing multi-temperature creep data the Larson-Miller model is used for representation of other experimental test data so that results at certain temperatures and stresses can be used for the prediction, for example hardness, at other time spans and temperatures within a given time-temperature data set.

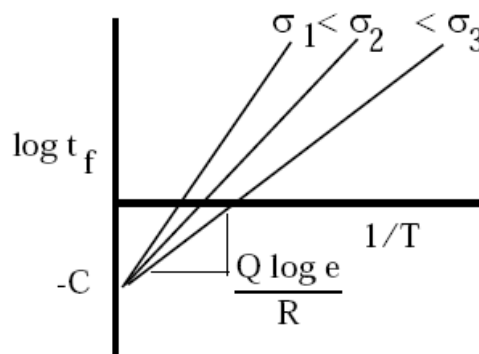


Figure 9.1 Schematic representation of the Larson-Miller Parameter.

9.1.1 ESTIMATION OF AVERAGE OPERATING TEMPERATURES OF SERVICE EXPOSED HA230 COMPONENTS USING MASTER HARDNESS V LARSON-MILLER RELATIONSHIPS.

Master Hardness v LMP Equation

$$H_v = aP^3 + bP^2 + cP + d \quad \text{Equation 9.8}$$

where a , b , c and d are constants, P is the L-M Parameter, C is the L-M constant, K is the exposure temperature in degrees Kelvin, t is the exposure duration in hours and

$$P = K(C + \log t)/1000 \quad \text{Equation 9.9}$$

re-arranging Equation 9.9 gives

$$K = 1000P/(C + \log t) \quad \text{Equation 9.10}$$

Exposure temperature in °C is then given by

$$T = [1000P/(C + \log t)] - 273 \quad \text{Equation 9.11}$$

9.1.2 CALCULATION OF AVERAGE SERVICE TEMPERATURES

Substitution of the measured hardness values of the component, enables the P-value to be calculated from Equation 9.9.

Knowing the component service exposure duration and the C-value used to define the Master LMP for the alloy, the mean service temperature in °C can then be calculated using Equation 9.11.

In the case of the present data set for HA230 thermally exposed material the best fit C-value of 19.3 should be used.

9.2 SAMPLE REVIEW

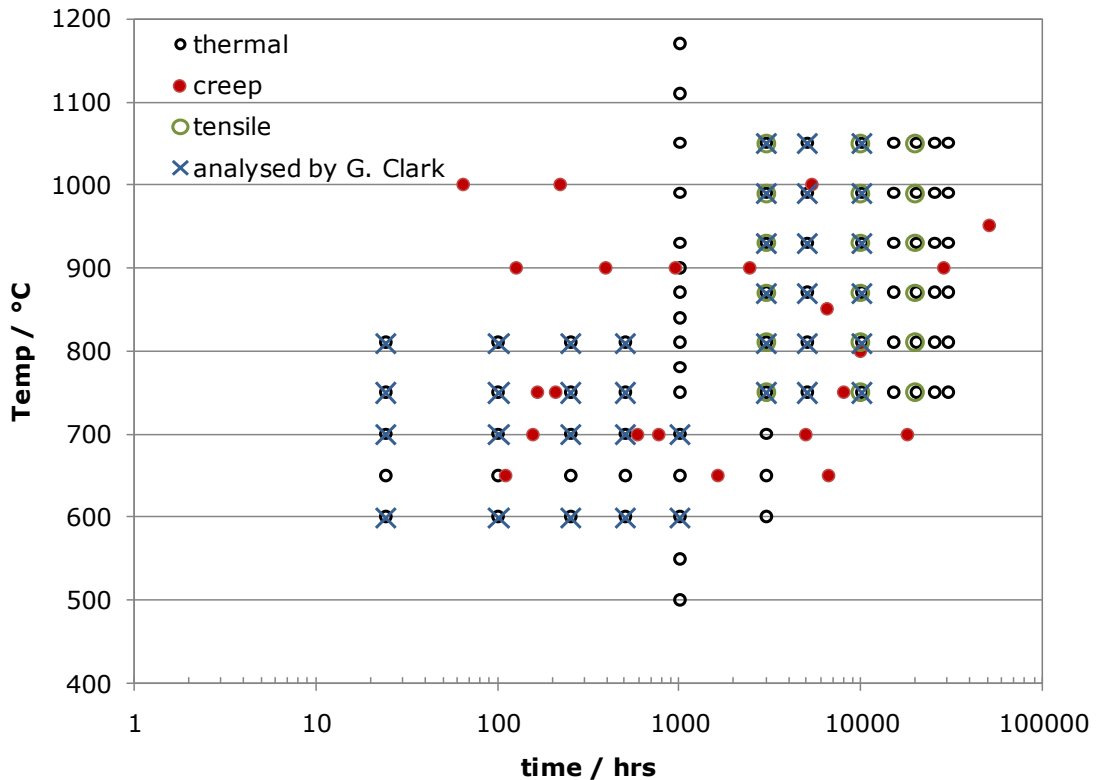


Figure 9.2 Review of the tested samples. The samples highlighted with a cross form preliminary work carried out by Prof A. Strang and Mr G. Clark.

Table 9.1 The list of the specimens thermally exposed and creep tested showing the Larson-Miller parameter, the hardness value and the standard deviation value for every specimen.

Thermally exposed					
Duration - hrs	Temp - °C	LMP (C=20)	Hv20	stdev	
24	600	18.66	222.5		
24	650	19.73	223.8	2.4	
24	700	20.80	247.6		
24	750	21.87	240.1		
24	810	23.15	239.8		
<hr/>					
100	600	19.21	221.8		
100	650	20.31	244.6	2.8	
100	700	21.41	248.9		
100	750	22.51	241.3		
100	810	23.83	242.1		
<hr/>					
250	600	19.55	226.3		
250	650	20.67	243.2	3.6	
250	700	21.79	246.7		
250	750	22.91	243.3		
250	810	24.26	242.4		
<hr/>					
500	600	19.82	231.6		
500	650	20.95	248.3	2.9	
500	700	22.09	245.0		
500	750	23.22	239.3		
500	810	24.58	236.0		
<hr/>					
1000	500	17.78	218.2	4.4	
1000	550	18.93	217.9	3.9	
1000	600	20.08	244.7		
1000	650	21.23	250.4	3.2	
1000	700	22.38	247.7		
1000	750	23.53	244.5	2.4	
1000	780	24.22	239.3	2.3	
1000	810	24.91	239.2	2.4	
1000	840	25.60	233.6	3	
1000	870	26.29	226.5	2.4	
1000	900	26.98	218.7	2.6	
1000	930	27.67	215.6	2	
1000	990	29.05	210.4	2.4	
1000	1050	30.43	210.5	3	
1000	1110	31.81	215.1	3.3	
1000	1170	33.19	203.3	4.1	
<hr/>					
3000	600	20.50	243.4	2.1	
3000	650	21.67	248.3	2.6	
3000	700	22.84	247.8	3	
3000	750	24.02	244.3		
3000	810	25.43	233.7		
3000	870	26.83	216.1		
3000	930	28.24	208.9		
3000	990	29.65	207.0		

3000	1050	31.06	209.9	
5000	750	24.24	243.9	
5000	810	25.67	232.1	
5000	870	27.09	214.5	
5000	930	28.51	210.2	
5000	990	29.93	207.4	
5000	1050	31.35	212.8	
10000	750	24.55	243.4	
10000	810	25.99	225.5	
10000	870	27.43	215.4	
10000	930	28.87	212.0	
10000	990	30.31	207.5	
10000	1050	31.75	213.6	
15000	750	24.73	242.7	2.1
15000	810	26.18	226.3	1.6
15000	870	27.63	217.6	1.3
15000	930	29.08	213.2	1.2
15000	990	30.53	212.0	1.1
15000	1050	31.98	215.5	3.4
20000	750	24.86	242.9	3.0
20000	810	26.32	223.3	2.1
20000	870	27.78	219.6	2.3
20000	930	29.23	216.1	2.4
20000	990	30.69	211.0	2.1
20000	1050	32.15	214.5	3.5
25000	750	24.96	242.3	2.3
25000	810	26.42	225	2.6
25000	870	27.89	219.5	3.1
25000	930	29.35	214.8	2.7
25000	990	30.81	213.2	3.6
25000	1050	32.28	216.9	3.5
30000	750	25.04	238.1	2.9
30000	810	26.51	225.3	5.3
30000	870	27.98	216.8	4
30000	930	29.45	212.8	2.7
30000	990	30.91	209.4	2.6
30000	1050	32.38	218	3.5

Creep tested				
DKZ	110.1	650	20.34	237.8
DKY	1637.5	650	21.43	245.8
DKX	6576.0	650	21.98	248.4
DLA	18159.0	700	23.60	246.6
DLB	4995.0	700	23.06	243
DLC	582.5	700	22.15	241.8
DLD	156.5	700	21.60	239.5
ELM	761.0	700	22.26	239.5
12722	206.3	750	22.83	248.3
12784	164.9	750	22.73	243.3
DLE*	8059.0	750	24.46	235.5
DLF*	9907.0	800	25.75	228.7
DLG*	6549.0	850	26.75	218.5
CNZ	124.6	900	25.92	227.9
COA	389.1	900	26.50	217.5
COB	951.0	900	26.95	215.4
COC	2415.5	900	27.43	212.9
DLH	28775.0	900	28.69	216.5
COD	50874.0	950	30.22	215.1
COG	5366.0	1000	30.21	208.8
COE	64.0	1000	27.76	210.8
COF	221.0	1000	28.44	214.1

9.4 MICROHARDNESS STUDIES

Table 9.2 The comparison and the review of all microhardness values: load 50g, loading time 15s.

	d1 (μm)	d2 (μm)	EYEPIECE	d1 (μm)	d2 (μm)	d (μm)	FEGSEM
matrix	21,4	22,3	194	19,4	19,2	19,3	249
matrix	19,4	20,1	238	17,4	16,8	17,1	317
2	15,7	15,7	376	13,6	13,3	13,45	513
3	15,7	16	369	12,9	13,3	13,1	540
4	15,6	15,1	393	13	12,9	12,95	554
5	12,3	11,8	638	10,2	9,6	9,9	946
6	10,3	10,3	874	7,3	7,8	7,55	1625
7	13	12,7	561	10,3	10,2	10,25	882
8	10,5	10,5	841	8,5	8,1	8,3	1346
average			730				1200

9.5 NANOHARDNESS STUDIES

Table 9.3 Input parameters for nanohardness studies

Percent To Unload	%	90
Surface Approach Velocity	nm/s	10
Delta X For Finding Surface	um	-50
Delta Y For Finding Surface	um	-50
Maximum Load	gf	5/10/25/50
Load Rate Multiple For Unload Rate		1
Number Of Times To Load		1
Allowable Drift Rate	nm/s	0.05
Approach Distance To Store	nm	1000
Peak Hold Time	s	10
Time To Load	s	15
Surface Approach Distance	nm	1000
Surface Approach Sensitivity	%	25
Poissons Ratio		0.2/0.3

9.6 STATISTICAL ANALYSIS

The test hypotheses are:

1. Do the two sets of data ('Thermal' and 'Creep') come from the same population?

F-test (R.A.Fisher) – [147] is a statistical test consisting of the ratio of two independent random variables (e.g. sum of squares), each divided by the corresponding degrees of freedom. It is used to compare statistical models in order to identify the one which has the best fit for the sampling population, and assumes that the null hypothesis is true.

Cubic model:

$$E(Y_i) = aph^3 + bph^2 + cph + d + \epsilon_i \quad \text{Equation 9.12}$$

$\epsilon_i \dots$ independent random variables with the Normal distribution $\epsilon_i \sim N(0, \sigma^2)$ (the expectation is 0, the variance is σ^2)

$$ph = xh1 + C * xh2 \quad \text{Equation 9.13}$$

ph represents LMP equation for hardness for $C = 20$, where

$$xh1 = \frac{\log(t) * (273 + T)}{1000} \quad \text{Equation 9.14}$$

$$xh2 = \frac{273 + T}{1000} \quad \text{Equation 9.15}$$

where t is time in hours and T is temperature in degrees of Celsius.

The sum of the squares of the deviations for a set of observation is

$$SS = \sum_{i=1}^n (y_i - \mu_i)^2. \quad \text{Equation 9.16}$$

Let the observations be Y_{ij} , where $j=1$ if the observation belongs to the 'thermal' set and $j=2$ for the 'creep' set. There are n_1 observations in the 'thermal' set and n_2 observations in the 'creep' set. Then let the null hypothesis H_0 be such that

$$\mu_{ij} = E(Y_{ij}) = aph_i^3 + bph_i^2 + cph_i + d. \quad \text{Equation 9.17}$$

Also let the alternative hypothesis H_1 be such that

$$\mu_{ij} = E(Y_{ij}) = a_j p h_i^3 + b_j p h_i^2 + c_j p h_i + d_j, \text{ for } j=1,2. \quad \text{Equation 9.18}$$

Then

$$SSE_0 = \sum_{j=1}^2 \sum_{i=1}^{n_j} (y_{ij} - \hat{\mu}_{ij})^2 \quad \text{Equation 9.19}$$

with $\hat{\mu}_{ij}$ the estimate of μ_{ij} in Equation 9.17.

$$SSE = \sum_{j=1}^2 \sum_{i=1}^{n_j} (y_{ij} - \hat{\mu}_{ij})^2 \quad \text{Equation 9.20}$$

with $\hat{\mu}_{ij}$ the estimate of μ_{ij} in Equation 9.18.

Now use an F test with the null hypothesis (preferred model) H_0 with SSE_0 , and alternative hypothesis H_1 with SSE satisfying the following condition: $SSE_0 > SSE$. The F statistic with $(l - l_0)$ and $(n - l)$ is given by

$$F = \frac{\frac{SSE_0 - SSE}{(l - l_0)}}{\frac{SSE}{(n - l)}} \quad \text{Equation 9.21}$$

where n = number of combined observations ($n=102$); l_0 = number of parameters in μ_{ij} in Equation 9.17 ($l_0=4$); l = number of parameters in μ_{ij} for both sets in Equation 9.18 ($l=8$). The results give

$$F = \frac{\frac{((4.184^2 * 98) - (4.052^2 * 94))}{(8 - 4)}}{\frac{4.052^2 * 94}{(102 - 8)}} = 2.62$$

The probability that the random variable F exceeds the value $f_{n,p}$ (the percentage point of the F distribution) is

$$P(F > f_{\alpha,n,p}) = \int_{f_{\alpha,n,p}}^{\infty} f(x) dx = \alpha \quad \text{Equation 9.22}$$

$$P(F > f_{0.05,102,4}) = P(F > 2.474) = 0.05 \quad \text{Equation 9.23}$$

$$f_{102,4} = 2.62 \quad P(f_{102,4}) = 0.04 \sim 4\%$$

2. 95% Confidence and Prediction Intervals ($\pm 2SE$)

Standard Error (SE) - 'thermal' set (80 values): standard error $\hat{\sigma}_{80} = 4.138$ is estimate of σ using Equation 9.17.

- 'combined' set (102 values): standard error $\hat{\sigma}_{102} = 4.184$ is estimate of σ using Equation 9.17.

95% Confidence Interval '*thermal*': $\hat{\mu}_{i1} \pm 2SE(\hat{\mu}_{i1})$

$$\text{max width} = 4 SE(\hat{\mu}_{i1}) = 3.7$$

'*combined*': $\hat{\mu}_{ij} \pm 2SE(\hat{\mu}_{ij})$ for $j=1,2$

$$\text{max width} = 4 SE(\hat{\mu}_{ij}) = 3.6$$

95% Prediction Interval '*thermal*': $\hat{\mu}_{i1} \pm 2 * \sqrt{(SE(\hat{\mu}_{i1}))^2 + \hat{\sigma}_{80}^2}$

$$\text{max width} = 4 * \sqrt{(SE(\hat{\mu}_{i1}))^2 + \hat{\sigma}_{80}^2} = 17$$

'*combined*': $\hat{\mu}_{ij} \pm 2 * \sqrt{(SE(\hat{\mu}_{ij}))^2 + \hat{\sigma}_{102}^2}$

$$\text{max width} = 4 * \sqrt{(SE(\hat{\mu}_{ij}))^2 + \hat{\sigma}_{102}^2} = 17.1$$

3. The estimation of LMP constant C.

$$\log - \text{likelihood} (C) = -\frac{n}{2} \log(SSE_C) \quad \text{Equation 9.24}$$

$$\log - \text{likelihood ratio}(C) = \frac{n}{2} \log\left(\frac{SS_{min}}{SS_C}\right) \quad \text{Equation 9.25}$$

$$\text{e.g. } \log - \text{likelihood ratio}_{LMP=20}(20) = \frac{102}{2} * [\log(1703.27) - \log(1717.2)] = -0.4153$$

for the combined sample.

The optimum C is the intercept point with the y axis at 0 with a confidence interval of the two unit log-likelihood interval.

9.7 TEM

Table 9.4 List of calculations of the lattice parameters from the electron diffraction patterns using the lattice parameter of the matrix as the calibration of the phases precipitated in the specimen thermally exposed for 15000 hours at 1050°C (in-situ lift out specimen).

	lattice parameter 3.573 Å	distance - mm	1/d 0.4848	d-spacing calculated	angles	Lattice parameter (calculated)
DP4 matrix						
110				1mm~x		
d-spac 111	2.0629	21.1	0.0230	2.063		3.57
d-spac 200	1.7865	24.5		1.777		3.55
d-spac 220	1.2632	34		1.280		3.62
d-spac 311	1.0773					
DP5b matrix						
220		32		1.360	65	3.85
114		311	37.75	1.153	115	3.82
DP1 WC						
220		10.5		4.145	64	11.72
114		311	12.5	3.482	80	11.55
DP2 WC						
220		10.5		4.145	73	11.72
113		422	18.75	2.321	34	11.37
DP3 WC						
220		11.5		3.785	34	10.71
116		331	17	1.47	90	11.16
		511	20	1.74	56	11.31
DP6 phase						
200		6.75		6.448	50	12.90
210		420	16	2.720	40	12.17
		422	17	2.560	20	12.54

Table 9.5 List of calculations of the lattice parameters from the electron diffraction patterns using the lattice parameter of the matrix as the calibration of the phases precipitated in the specimen creep tested COD (H-bar specimen).

	lattice parameter 3.573 Å	distance - mm	1/d 0.4848	d-spacing calculated	angles	Lattice parameter (calculated)
COD 120x 23						
			1mm~x			
d-spac 111	2.0629	16	0.0303	2.063		3.57
d-spac 200	1.7865	18.5		1.784		3.57
d-spac 220	1.2632	26		1.269		3.59
d-spac 311	1.0773					
COD 120x 29 mat						
111		16.25		2.031	58	3.52
112		26.5	1.63	1.246	64	3.52
		30.75	1.89	1.073	32	3.56
COD 120x 31 mat						
220		26.5	1.16	1.246		3.52
114		30.75		1.073		3.56
COD 120x 33 mat						
311		30.75		1.073	86	3.56
521		41	1.37	0.805	47	3.60
		45	1.5	0.733	43	3.59
COD 120x 13						
111		7		4.715	56	8.17
123		17.5	2.5	1.886	20	8.22
		18	2.57	1.834	22	8.20
COD 120x 17						
220		9		3.667	60	10.37
111		15.75		2.096	30	10.27
COD 120x 18						
111		4.75		6.949	54	12.04
112		7.5	1.5	4.401	36	12.45
		9	1.8	3.667	90	12.16
COD 120x 21						
200		5		6.601	< 2-3	13.20
210		11.25	2.25	2.934	< 1-2	13.12
		12.25	2.45	2.694	< 1-3	13.20

9.8 XRD

9.8.1 PHASE EXTRACTION

14 carbide extractions from bulk material (Haynes 230 Alloy) were carried out:

1. As-received material -1 sample
2. Material thermally exposed for 3000 and 20000 hours at 6 different temperatures -12 samples
3. Material cut out from transition duct -1 sample

The solution: 20ml of Br₂+ 180ml of EtOH (10% Bromine in analar ethanol)

Samples: ~ 3g of chippings

The procedure was optimised as follows:

1. Degrease a known amount of chippings (10 min) in a suitable solvent (petroleum ether 40-60°C).
 - 100ml Erlenmeyer (EM) in an ultrasonic bath.
2. Dry in an oven at 80°C (30min). Weigh the chippings.
3. Make up a 200 ml solution of 10% bromine in ethanol. Exothermic reaction!
 - Ice bath, 500ml EM with a magnetic stirrer, pour EtOH and slowly add Bromine (20ml over 20 min)
4. Leave the chippings in the solution until all metal has been dissolved. (~24 hours)
 - Put the chippings into a rounded flask with a magnetic stirrer, add the solution, protect against the air moisture.

When dissolution of the metal is completed:

5. Centrifuge the solution
 - Pour the solution into 8 tubes (balanced them ±0.1g), 15000rpm for 30min at 4°C.
6. Pour off the solution (= supernatant liquid, preserved for ICP-OES).
7. Wash the residue
 - Rinse out the residue with EtOH into a 500ml EM (~100ml) and add the same amount of deionised water.
8. Wash in an ultrasonic bath for 15 min.
9. Centrifuge

- Pour the solution into 8 tubes (balanced them $\pm 0.1g$), 15000rpm for 30min at 4°C.
10. Pour off the solution and wash the residue.
 - Rinse out the residue with deionised water into two glass tubes.
 11. Wash in an ultrasonic bath for 2 min.
 12. Centrifuge
 - 2 glass tubes (balanced), 4200rpm for 10min at RT
 13. Pour off the liquid.
 14. Dry in the oven at 80°C (overnight).

The products:

1. Extract/powder analysed by XRD and ESEM
2. Scum/phases not centrifuged filtrated – ESEM
3. Supernatant liquid - ICP

9.8.2 CALIBRATION OF THE DIFFRACTOMETER

A corundum standard specimen was used for the calibration of the diffractometer before the analysis. The data and values are shown in Figure 9.4.

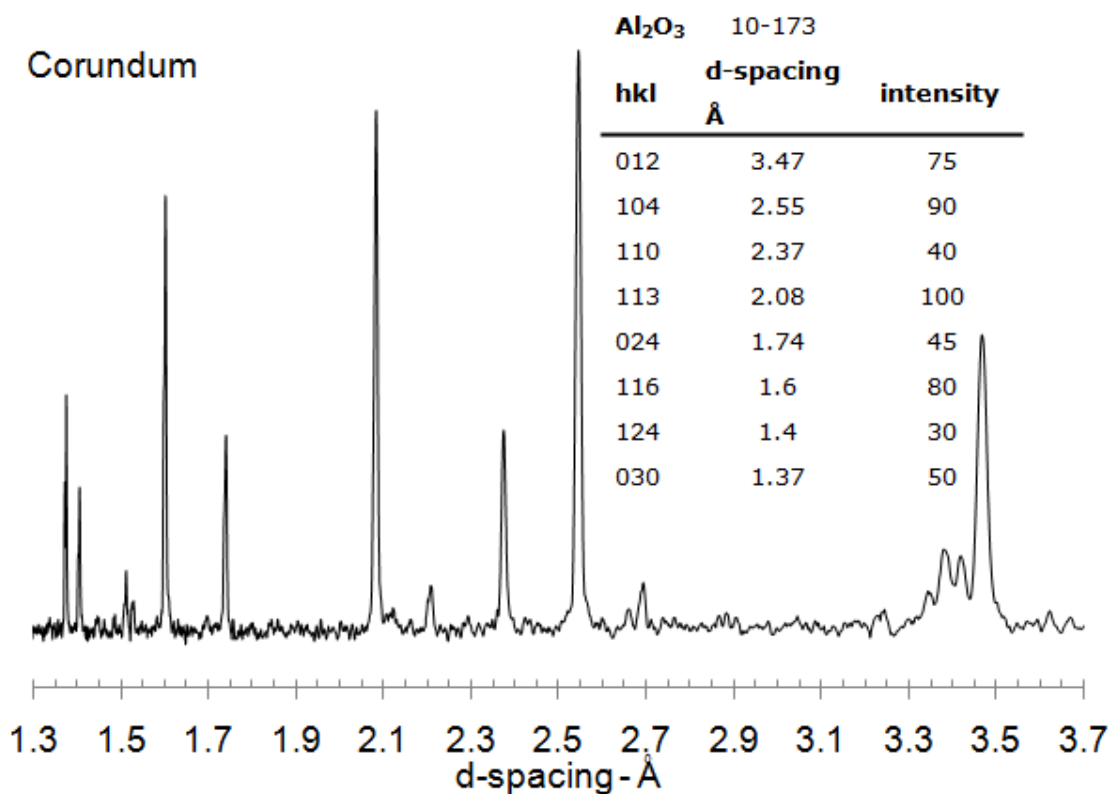


Figure 9.4 XRD spectra of corundum used as calibration standard.

10 LIST OF PUBLICATIONS

Veverková, J., Strang, A., Marchant, G., Atkinson, H.V. *Effects of Long -Term High Temperature Exposure on the Microstructure of Haynes Alloy 230*. in **Materials for Advanced Power Engineering**, 2010. Liège (Belgium). in preparation.

Veverková, J., Strang, A., Marchant, G.R., Atkinson, H.V., *Examination of a HA230 Turbine Transition Duct*, **Materials Science and Technology** (in press)

Veverková, J., Strang, A., Marchant, G.R., McColvin, G.M., Atkinson, H.V., *High Temperature Microstructural Degradation of Haynes Alloy 230*, in **Superalloys 2008**, ed. R.C. Reed et. al., 2008. TMS: Warrendale, PA, USA.

Veverková, J., Strang, A., Marchant, G., McColvin, G., Atkinson, H.V., *Microstructural evolution in high temperature creep and thermally aged HA230*. in **PARSONS 2007**. 2007. Glasgow, UK.

11 REFERENCES

1. Doucet, J., *Oxidation Characteristics of Haynes Alloy 230*. 2008, MSc Project Report, Department of Engineering, University of Leicester: Leicester.
2. Veverková, J., Atkinson, H.V., Strang, A. and Marchant, G.R., *Examination of a HA230 Turbine Transition Duct*. Materials Science and Technology, 2010. **in print** (special issue).
3. Veverková, J., Strang, A., Marchant, G.R., McColvin, G.M., Atkinson, H.V. *Microstructural evolution in high temperature creep and thermally aged HA230*. in *PARSONS 2007*. 2007. Glasgow, UK:p.161-172
4. Veverková, J., A. Strang, G.R. Marchant, G.M. McColvin, and H.V. Atkinson. *High temperature microstructural degradation of Haynes Alloy 230*. in *Proceedings of the International Symposium on Superalloys*. 2008:p. 479-488.
5. Veverková, J., Atkinson, H.V., Strang, A. and Marchant, G.R. *Effects of Long -Term High Temperature Exposure on the Microstructure of Haynes Alloy 230*. in *Materials for Advanced Power Engineering*. 2010. Liège (Belgium). in preparation:p.
6. Sims, C.T., Hagel, W.C., *The superalloys*. 1972, New York: Wiley.
7. Bowman, R. Available from: <http://www.tms.org/Meetings/Specialty/Superalloys2000/SuperalloysHistory.html>.
8. Sims, C.T.S., Norman S.;Hagel, William C., *Superalloys II: high-temperature materials for aerospace and industrial power*. 1987, New York: Wiley & sons.
9. Davis, J.R., *Heat-Resistant Materials*. 1997: ASM International.
10. Donachie, M.J., *Superalloys: A Technical Guide*. 2002: ASM International.
11. Bhadeshia, H.K.D.H. Available from: <http://www.msm.cam.ac.uk/phase-trans/2003/Superalloys/superalloys.html>.
12. Sabol, G.P., Stickler, R., *Microstructure of nickel-based superalloys*. *Physica status solidi*, 1969. **35**(11): p. 11.
13. Reed, R.C., *Superalloys*. 2006: Cambridge: Cambridge University Press.
14. Durand-Charre, M., *The Microstructure of Superalloys*. 1997: CRC Press.
15. Pearson, W.B., *Handbook of Lattice Spacings and Structures of Metals and Alloys*. 1958, London: Pergamon Press Ltd.
16. Corey, C.L. and B. Lisowsky, *The Ni₃Al Ordering System*, in *Technical Rep. Prepared under Contract NONR-4520 (00)*. 1966, Wayne State Univ.
17. Lund, C.H., *Physical Metallurgy of Nickel-Based Superalloys*, in *DMIC Rep.153*. 1961.
18. Nordheim, R., Grant, N.J., *Trans AIME*, 1954. **200**: p. 211.
19. Callister, W.D., *Materials science and engineering: an introduction*. 4 ed. 1997, New York; Chichester: John Wiley & Sons.

20. Haynes International. *HAYNES 230 Alloy Product Brochure, H-3000*. Available from: www.haynesintl.com.
21. Tawancy, H.M., Klarstrom, D. L., Rothman, M. F., *Development of a New Nickel-Base Superalloy*. Journal of Metals, 1984. **36**(9): p. 58-62.
22. Klarstrom, D.L., *The Development of Haynes 230 Alloy*. Corrosion, 1994: p. 407/1-407/12.
23. Klarstrom, D.L. *The Thermal Stability of a Ni-Cr-W-Mo Alloy*. in *NACE Corrosion 94*. 1994. Houston, TX, USA:p. Paper No. 407.
24. Klarstrom, D.L. *Heat treatment/Property Relationships for Solid-Solution Strengthened Heat Resisting Alloys*. in *1st International Conference on Heat Resistant Materials*. 1991. Lake Geneva:p.
25. Klarstrom, D.L. *The development of HAYNES® 230® alloy*. 2001. Indianapolis, IN, USA: TMS - Miner., Metals & Mater. Soc:p. 297-307.
26. Tiearney, T.C., Grant, N.J., *Measurement of structural parameters important in creep of Ni-Mo and Ni-W solid solutions*. Metallurgical Transactions A, 1982. **13**(10): p. 1827-36.
27. Tawancy, H.W., *On the role of lanthanum, silicon and manganese during high-temperature oxidation of a wrought nickel-base alloy*. Journal of Materials Science Letters, 1993. **12**(13): p. 1015-1019.
28. Seeley, R.R., Srivastava, S.K. *The Effect of Long-Term Thermal Exposure on the Mechanical Properties of Four Modern High-Temperature Nickel-Base Alloys*. in *The 1999 TMS Annual Meeting & Exhibition*. 1999. San Diego, California, USA:p. 93-108.
29. Whittenberger, J.D., *77 to 1200K Tensile Properties of Several Wrought Superalloys after Long-term 1093K Heat Treatment in Air and Vacuum*. Journal of Materials Engineering and Performance, 1994. **3**(1): p. 91-103.
30. Lara-Curzio, E., Trejo, R., More, K. L., Maziasz, P. J., Pint, B. A., *Evaluation and characterization of iron- and nickel-based alloys for microturbine recuperators*, in *ASME Turbo Expo*. 2005: Reno-Tahoe (USA). p. 945-961.
31. Gleeson, B., Harper, M.A., *The Long-Term, Cyclic-Oxidation Behavior of Selected Chromia-Forming Alloys*. Oxidation of Metals, 1998. **49**: p. 373-399.
32. Tawancy, H.M., *High Temperature Creep Behaviour of a Ni-Cr-W-B Alloy*. Journal of Material Science, 1992. **27**: p. 6481-6489.
33. Klarstrom, D.L., Hoback, G.L., Ishwar, V.R., Qureshi, J.I. *Rejuvenation Heat Treatment and Weld Repairability Studies of HAYNES 230 alloy*. in *International Gas Turbine Conference*. 2000. Munich, Germany:p. ASME Paper 2000-GT-629.
34. Vecchio, K.S., Fitzpatrick, M.D., Klarstrom, D.L., *Influence of Subsolvus Thermomechanical Processing on the Low-Cycle Fatigue Properties of HAYNES 230 Alloy*. Metallurgical and Materials Transactions A: Physical Metallurgy and Materials Science, 1995. **26**(3): p. 673-689.
35. Meyer-Olbersleben, F., Kasik, N., Ilchner, B., Rézai-Aria, F., *The thermal fatigue behavior of the combustor alloys In 617 and HAYNES 230 before and after welding*. Metallurgical and Materials Transactions A, 1999. **30**(4): p. 981-989.

36. Lu, Y.L., Brooks, C.R., Chen, L.J., Liaw, P.K., Wang, G.Y., Benson, M.L., Thompson, S.A., Blust, J.W., Browning, P.F., Bhattacharya, A.K., Aurrecochea, J.M., Klarstrom, D.L., *A technique for the removal of oxides from the fracture surfaces of HAYNES 230 alloy*. Materials Characterization, 2005. **54**(2): p. 149-155.
37. Lu, Y.L., Chen, L.J., Liaw, P.K., Wang, G.Y., Brooks, C.R., Thompson, S.A., Blust, J.W., Browning, P.F., Bhattacharya, A.K., Aurrecochea, J.M., Klarstrom, D.L., *Effects of temperature and hold time on creep-fatigue crack-growth behavior of HAYNES® 230® alloy*. Materials Science and Engineering A, 2006. **429** (1-2): p. 1-10.
38. Lu, Y.L., P.K. Liaw, G.Y. Wang, M.L. Benson, S.A. Thompson, J.W. Blust, P.F. Browning, A.K. Bhattacharya, J.M. Aurrecochea, and D.L. Klarstrom, *Fracture modes of HAYNES® 230® alloy during fatigue-crack-growth at room and elevated temperatures*. Materials Science and Engineering A, 2005. **397**(1-2): p. 122-131.
39. Chen, L.J., W. Wu, and P.K. Liaw, *Creep-fatigue interaction behaviors and life predictions for three superalloys*. Acta Metallurgica Sinica, 2006. **42**(9): p. 952-958.
40. Chen, L.J., He, Y.H., Liaw, P.K., Blust, J.W., Browning, P.F., Seeley, R.R., Klarstrom, D.L. *High-Temperature Low-Cycle Fatigue Behaviour of Haynes 230 Superalloy*. in *Superalloys 2000*. 2000. Seven Springs, PA (USA): TMS:p. 573-581.
41. Saleh, T.A., *Nondestructive Evaluation of Loading and Fatigue Effects in Haynes 230 Alloy*. 2006, University of Tennessee: Knoxville.
42. Lee, S.Y., Liaw, P.K., Lu, Y.L., Fielden, D., Pike, L.M., Klarstrom, D.L., *Elevated-temperature creep-fatigue crack-growth behavior of nickel-based HAYNES® R-41, HAYNES® 230® and HASTELLOY® X alloys*, in *Proceedings of the International Symposium on Superalloys*. 2008.
43. Rothman, M.F., Lai, G.Y., Lewis, B.E., *Long-term thermal stability of solid-solution-strengthened superalloys*.
44. Birks, N., Meier, G.H., *Introduction to high temperature oxidation of metals*. 1983, London: Edward Arnold.
45. Evans, U.R., *The corrosion and oxidation of metals*. 1968, London: Edward Arnold.
46. Lu, Y.L., Chen, L.J., Wang, G.Y., Benson, M.L., Liaw, P.K., Thompson, S.A., Blust, J.W., Browning, P.F., Bhattacharya, A.K., Aurrecochea, J.M., Klarstrom D.L., *Hold time effects on low cycle fatigue behavior of HAYNES 230® superalloy at high temperatures*. Materials Science and Engineering A, 2005. **409** (1-2): p. 282-291.
47. Lu, Y.L., Liaw, P.K., Sun, Y., Wang, G.Y., Thompson, S.A., Blust, J.W., Browning, P.F., Bhattacharya, A.K., Aurrecochea, J.M., Klarstrom, D.L., *Hold-time effect on the elevated-temperature crack growth behavior of solid-solution-strengthened superalloys*. Acta Materialia, 2007. **55** (3): p. 767-775.
48. Pop, D., Wolski, K., *Surface segregation in HAYNES 230 alloy*. Applied Surface Science, 2006. **253**(4): p. 2244-2250.
49. Bai, C.-Y., *Effects of electrical discharge surface modification of superalloy Haynes 230 with aluminum and molybdenum on oxidation behavior*. Corrosion Science, 2007. **49**(10): p. 3889-3904.
50. Kim, D., Jang, C., Ryu, W. S., *Oxidation characteristics and oxide layer evolution of Alloy 617 and Haynes 230 at 900°C and 1100°C*. Oxidation of Metals, 2009. **71**(5-6): p. 271-293.

51. Peter, I., Zago, A., Actis Grande, M., Ugues, D., *Thermo-mechanical and oxidation behaviour of high temperature advanced metallic alloys*. Surface and Coatings Technology, 2009. **203**(13): p. 1776-1784.
52. England, D.M., Virkar, A.V., *Oxidation kinetics of some nickel-based superalloy foils and electronic resistance of the oxide scale formed in air. I*. Journal of the Electrochemical Society, 2001. **146** (9): p. 3196-202.
53. Deodeshmukh, V.P., Srivastava, S.K., *Long-term cyclic oxidation behaviour of selected high temperature alloys*, in *Superalloys*. 2008: Seven Springs, PA (USA).
54. Lai, G.Y. *Nitridation attack in a simulated gas turbine combustion environment*. in *Materials for Advanced Power Engineering*. 1994. Liège, Belgium:p.
55. Lai, G.Y., *High-temperature corrosion and materials applications*. 2007: ASM International.
56. Cabet, C., Rouillard, F., *Corrosion of high temperature metallic materials in VHTR*. Journal of Nuclear Materials, 2009. **392**(2): p. 235-242.
57. Clauss, F.J., *Engineer's guide to high-temperature materials*. 1969: Addison-Wesley.
58. Lupton, D.F., Ennis, P.J., *Influence of carburisation on the ductility of four high temperature alloys*. Res mechanica letters, 1981. **1**(6): p. 245-252.
59. Quadackers, W.J., Schuster, H., *Corrosion of High Temperature Alloys in the Primary Circuit Helium of High Temperature Gas Cooled Reactors. - Part I: Theoretical Background*. Werkstoffe und Korrosion, 1985. **36**: p. 141-150.
60. Wright, R., Simpson, J., Wertsching, A., Swank, W.D., *High temperature behavior of candidate VHTR heat exchanger alloys*, in *Topical Meeting on High Temperature Reactor Technology*. 2008: Washington (USA).
61. Whittenberger, J.D., *Effect of long-term 1093 k exposure to air or vacuum on the structure of several wrought superalloys*. Journal of Materials Engineering and Performance, 1993. **2**(5): p. 745-758.
62. Wu, Q., Shingledecker, J.P., Swindeman, R.W., Vasudevan, V.K., *Microstructure characterization of advanced boiler materials for ultra supercritical coal power plants*, in *Advances in Materials Technology for Fossil Power Plants*. 2004. p. 748-761.
63. Stefanuto, A., Pojaghi, M., *Comportamento a creep della superlega a base nichel HA230*. 2008, MSc Project Report, Politecnico di Milano: Milano, (It).
64. Brandis, H., Haberling, E., Weigand, H. H., *Metallurgical aspects of carbides in high speed steels*. Thyssen Edelstahl Technische Berichte, 1983: p. 5-12.
65. Casellas, D., Caro, J., Molas, S., Prado, J.M., Valls, I., *Fracture toughness of carbides in tool steels evaluated by nanoindentation*. Acta Materialia, 2007. **55**(13): p. 4277-4286.
66. Buytoz, S., *Microstructural properties of M7C3 eutectic carbides in a Fe-Cr-C alloy*. Materials Letters, 2006. **60**(5): p. 605-608.
67. Tawancy, H.M., *Long-term ageing characteristics of Hastelloy alloy X*. Journal of Materials Science, 1983. **18**(10): p. 2976-2986.

68. Kirchhoefer, H., Schubert, F., Nickel, H., *Precipitation behaviour of Ni-Cr-22 Fe-18 Mo (HASTELLOY-X) and Ni-Cr-22 Co-12 Mo (INCONEL-617) after isothermal aging*. Nuclear Technology, 1984. **66**(1): p. 139-148.
69. Zhao J.-C., L.M., Ravikumar V., *Phase precipitation and time-temperature-transformation diagram of Hastelloy X*. Materials Science and Engineering A, 2000. **293** (1): p. 112-119.
70. Raghavan, M., Berkowitz, B.J., Scanlon, J.C., *Electron Microscopic Analysis of Heterogeneous Precipitates in Hastelloy C-276*. Metallurgical Transactions A, 1982. **13**(6): p. 979-984.
71. Rideout, S., Manly, W.D., Kamen, E.L., Lement, B.S., Beck, P.A., J. Metals, 1951. **191**: p. 872-876.
72. Tanabe, T., Abe, F., Sakai, Y., Okada, M., *Effect of boron addition on the creep rupture properties of Hastelloy XR in an impure helium environment*. Transactions of the Iron and Steel Institute of Japan, 1986. **26**(11): p. 968-976.
73. Li, C.C., Johnson, W.R., Thompson, L.D., *Effects of controlled impurity helium on the mechanical behaviour of Hastelloy Alloy X*. Nuclear Technology, 1984. **66**(2): p. 439-464.
74. Kazdal Zeytin, H., Arslan Kaya, A., Tekin, A., *Microstructural evolution in a Ni-Cr-Co based superalloy during cooling from the melt*. Materials Characterization, 2006. **57**(2): p. 86-93.
75. Knotek, O., Lugscheider, E., Tschech, F., *The formation of tungsten carbide in cobalt-base wear-resistant coating alloys*. Thin Solid Films, 1976. **39 (C)**: p. 263-268.
76. Svistunova, T.V., Tsvigunov, A.N., Stegnukhina, L.V., Sakura, N.D., *Influence of composition and heat treatment on carbide phases in Ni-Mo alloys*. Metal Science and Heat Treatment, 1984. **26**(2): p. 119-124.
77. Newsam, J.M., Jacobson, A.J., McCandlish, L.E. and Polizzotti, R.S., *The structures of the η -carbides Ni₆Mo₆C, Co₆Mo₆C, and Co₆Mo₆C₂*. Journal of Solid State Chemistry, 1988. **75**(2): p. 296-304.
78. Muddle, B.C., *Interphase boundary precipitation in liquid phase sintered W-Ni-Fe and W-Ni-Cu alloys*. Metallurgical transactions. A, Physical metallurgy and materials science, 1983. **15A**(6): p. 1089-1098.
79. Posthill, J.B., Edmonds, D.V., *Matrix and interfacial precipitation in the W-Ni-Fe system*. Metallurgical Transactions A, 1986. **17**(11): p. 1921-1934.
80. Kuo, K., *Ternary laves and sigma-phases of transition metals*. Acta Metallurgica Sinica, 1953. **1**(6): p. 720-724.
81. Kikuchi, M., Kajihara, M., Kadoya, Y., Tanaka, R., *Decomposition of sigma phase in a NiCrW system*. Scripta Metallurgica, 1983. **17**(4): p. 475-478.
82. Kikuchi, M., Usuki, H., Kajihara, M., Tanaka, R., *Precipitation of sigma phase in nickel-rich NiCrW alloys as an intermediate precipitate*. Scripta Metallurgica, 1985. **19**(4): p. 421-424.
83. Rolland, A., Montagono, M.M., Cabane, J., *Kinetics of S and Mo surface cosegregation in Fe-Mo alloys*. Surface Science, 1996. **352**: p. 206-210.

84. Hille, V., Viljoen, E.C., Uebing, C., *Cosegregation of tungsten and nitrogen on Fe-9%W-N(100)*. Surface Science, 1996. **367**(2): p. L54-L60.
85. Davis, J.R., ed. *Nickel, Cobalt, and Their Alloys*. 2000, ASM International: Materials Park, Ohio.
86. Maldini, M., *Personal communication*. 2009: CNR IENI, Milan, (It).
87. Srolovitz, D.J., Grest, G.S., Anderson, M.P., *Computer simulation of grain growth-V. Abnormal grain growth*. Acta Metallurgica, 1985. **33** (12): p. 2233-2247.
88. Courtney, T.H., *Mechanical behavior of materials*. 2000, New York; London: McGraw-Hill.
89. Instron. Available from:
http://www.instron.co.uk/wa/applications/test_types/hardness/vickers.aspx.
90. Larson, F.R., Miller, J., *A Time-Temperature Relationship for Rupture and Creep Stresses*. Trans. ASME, 1952. **74**: p. 765-775.
91. Fischer-Cripps, A.C., *Nanoindentation*. 2004, New York: Springer.
92. Oliver, W.C., Pharr, G.M., *An improved technique for determining hardness and elastic modulus using load and displacement sensing indentation experiments*. Journal of Materials Research, 1992. **7**(6): p. 1564-1580.
93. Wheeler, J.M., *Nanoindentation under Dynamic Conditions*, in *Department of Materials Science and Metallurgy*. 2009, University of Cambridge: Cambridge.
94. Lawes, S.D.A., *The Application of Surface for Low-Wear and Low-Friction Performance Between Valve-train Components*. 2009, PhD thesis, University of Leicester: Leicester.
95. Čtvrtlík, R., Stranyánek, M., Boháč, P., Jastrabík, L., *NanoTest™ NT600 - A Device for Analyses of Mechanical Properties of Materials*. Materials Structure, 2006. **13**(2).
96. Zheng, S., *Nano-indentation studies on thermally exposed and creep rupture tested Haynes Alloy 230*. 2009, University of Leicester: Leicester.
97. <http://micro.magnet.fsu.edu/primer/anatomy/reflected.html>.
98. Goldstein, J.I., *Scanning electron microscopy and X-ray microanalysis*. 3 ed. 2003, New York: Springer.
99. Goodhew, P.J., Humphreys, J., Beanland, R., *Electron microscopy and analysis*. 3 ed. 2001, London: Taylor & Francis.
100. <http://mse.iastate.edu/microscopy/path2.html>.
101. University of Iowa. Available from:
<http://www.uiowa.edu/~cemrf/methodology/sem/index2.htm>.
102. Williams, D.B., Carter C. B., *Transmission electron microscopy: a textbook for materials science*. 1996, New York: Springer.
103. <http://www.mete.metu.edu.tr/Facilities/Service/TEM/TEMtext/TEMtext.html>.
104. <http://www.jeol.com/Default.aspx?tabid=119>.

105. Warren, B.E., *X-ray diffraction*. 1969: Addison-Wesley.
106. <http://www.doitpoms.ac.uk/tlplib/xray-diffraction/bragg.php>.
107. Lipson, H., *Interpretation of X-ray powder diffraction patterns*. 1970: Macmillan.
108. Cullity, B.D., Stock, S.R., *Elements of X-Ray Diffraction*. 2001, Upper Saddle River, N.J.: Prentice Hall.
109. <http://pubs.usgs.gov/of/2001/of01-041/htmldocs/images/xrdtube.jpg>.
110. <http://www.ifw-dresden.de/institutes/ikm/organisation/dep-31/methods/auger-electron-spectroscopy-aes>.
111. <http://www.chem.wisc.edu/~newtrad/CurrRef/BDGTopic/BDGtext/BDGGraph.html>.
112. Giannuzzi, L.A., Stevie, F. A., ed. *Introduction to focused ion beams: instrumentation, theory, techniques, and practice*. 2005, Springer.
113. Orloff, J., Utlaut, M., Swanson, L., *High Resolution Focused Ion Beams: FIB and its Applications*. 2003: Kluwer Academic/ Plenum Publishers.
114. Omniprobe. Available from: <http://www.omniprobe.com/pdf/sp1.pdf>.
115. Patterson, R.J., Mayer, D., Weaver, L. & Phaneuf, M.W., "*H-Bar Lift-Out*" and "*Plan-View Lift-Out*": Robust, re-thinnable FIB-TEM preparation for ex-situ cross-sectional and plan-view FIB specimen preparation. *Microscopy and Microanalysis*, 2002. **8**: p. 566-567.
116. Li, J., Malis, T., Dionne, S., *Recent advances in FIB-TEM specimen preparation techniques*. *Materials Characterization*, 2006. **57**(1): p. 64-70.
117. Reed, S.J.B., *Electron Microprobe Analysis and Scanning Electron Microscopy in Geology*. 2nd ed. 2005: Cambridge University Press.
118. Sibilia, J.P., ed. *A guide to Materials Characterization and Chemical Analysis*. 2nd ed. 1996, Wiley-VCH.
119. Ashby, M.F., Jones, D.R.H., *Engineering materials I. - an introduction to properties, applications and design*. 3rd ed. 2005: Elsevier Butterworth-Heinemann.
120. *Annual book of ASTM standards*. Vol. 03.01. 1996: ASTM.
121. Struers Ltd, *LaboPress-3 - Instruction manual*. 1998.
122. Aggag, G., Abu-Elezz, A. *Effect of loading rate and duration time on indentation hardness measurements*. in *IMECO*. 2006. Rio de Janeiro, Brazil:p.
123. Hermann, K., Germak, A., Menelao, F., Barbato, G., Brondino, G. *Indentation velocity effect on Martens hardness measurements*. in *IMECO*. 2002:p.
124. Marriner, R.S., *The precision and accuracy of the Vickers, Rockwell and. Brinell Hardness Tests*. 1964, Acta IMEKO.
125. Goodhew, P.J., *Specimen preparation for transmission electron microscopy of materials*. 1984: Oxford University Press for the Royal Microscopical Society.

126. Goodhew, P.J., *Thin Foil Preparation for Electron Microscopy, Practical methods in electron microscopy*. Vol. 11. 1985: Elsevier Science Publications.
127. Vodárek, V., *Personal communication*. 2007: Technical University of Ostrava, Czech Republic.
128. Angella, G., *Personal Communication*. 2008: CNR-IENI, Milano, Italy.
129. Svoboda, M., *Personal Communication*. 2008: IPM of the ASCR, Brno, Czech Republic.
130. Jairath, S., *Analysis of high temperature solid solution nickel-based alloys for gas turbine combustion components*. 2008, 3rd Year MEng Project Report, University of Leicester: Leicester.
131. Kaye, G.W.C., Laby, T.H., *Tables of Physical & Chemical Constants*, <http://www.kayelaby.npl.co.uk/>.
132. Sneddon, I.N., *The relation between load and penetration in the axisymmetric bousinesq problem for a punch of arbitrary profile*. International Journal of Engineering Science, 1965. **3**(1): p. 47-57.
133. Korsunsky, A.M., M.R. McGurk, S.J. Bull, and T.F. Page, *On the hardness of coated systems*. Surface and Coatings Technology, 1998. **99**(1-2): p. 171-183.
134. Jönsson, B. and S. Hogmark, *Hardness measurements of thin films*. Thin Solid Films, 1984. **114**(3): p. 257-269.
135. Taljat, B. and G.M. Pharr, *Development of pile-up during spherical indentation of elastic-plastic solids*. International Journal of Solids and Structures, 2004. **41**(14): p. 3891-3904.
136. Bolshakov, A. and G.M. Pharr, *Influences of pileup on the measurement of mechanical properties by load and depth sensing indentation techniques*. Journal of Materials Research, 1998. **13**(4): p. 1049-1058.
137. Xu Z.-H., A.J., *An analysis of piling-up or sinking-in behaviour of elastic-plastic materials under a sharp indentation*. Philosophical Magazine, 2004. **84**(23): p. 2367-2380.
138. Bhanu Sankara Rao, K., Schiffers, H., Schuster, H., Nickel, H., *Influence of time and temperature dependent processes on strain controlled low cycle fatigue behavior of alloy 617*. Metallurgical and Materials Transactions A, 1988. **19**(2): p. 359-371.
139. Klarstrom, D.L., *Personal communication*. 2007: Haynes International, Kokomo, USA.
140. Edington, J.W., *Electron Diffraction in the Electron Microscope*. 1975: Macmillan.
141. Fletcher, D.A., McMeeking, R.F., Parkin, D. *The United Kingdom Chemical Database Service*. Available from: <http://cds.dl.ac.uk/>.
142. Zuo, J.M., Mabon, J.C. *Web Electron Microscopy Applications Software*. Available from: <http://emaps.mrl.uiuc.edu/>.
143. Koloušek, D., *Personal communication*. 2009: Institute of Chemical Technology, Prague, Czech Republic.

144. Wang, T., L.Q. Chen, and Z.K. Liu, *Lattice parameters and local lattice distortions in fcc-Ni solutions*. Metallurgical and Materials Transactions A: Physical Metallurgy and Materials Science, 2007. **38**(3): p. 562-569.
145. Jordan, C.E., Raserfske, R.K., Castagna, A., *Thermal Stability of High Temperature Structural Alloys, Long Term Stability of High Temperature Materials*. Proceedings of TMS Annual Meeting, 1999: p. 55-67.
146. Maldini, M., *Personal Communication*. 2008.
147. Montgomery, D.C., Runger, G.C., *Statistical Inference for Two Samples*, in *Applied Statistics and Probability for Engineers*. 2007, John Wiley & Sons, Inc.